Advanced Ceramic Materials Series 15

edited by Aleksander Gurlo

Julien Gonthier

Kinetics of reversible deformations during the evaporative drying of silica aerogels

David Karl | Segerkegel | 2017

ISSN (online) 2569-8338

Technische Universität Berlin

Kinetics of reversible deformations during the evaporative drying of silica aerogels

vorgelegt von
Julien Gonthier, M. Sc.
ORCID: 0000-0001-5257-4688

an der Fakultät III – Prozesswissenschaften
der Technischen Universität Berlin
zur Erlangung des akademischen Grades

Doktor der Ingenieurwissenschaften
– Dr.-Ing. –

genehmigte Dissertation

Promotionsausschuss:

Vorsitzende:	Prof. Dr.-Ing. Claudia Fleck
Gutachter:	Prof. Dr. Aleksander Gurlo
Gutachter:	Dr. habil. Wolfgang Wagermaier
Gutachter:	Dr. Wim Malfait

Tag der wissenschaftlichen Aussprache: 24. Mai 2024

Berlin 2024

Abstract

Silica aerogels are highly porous, translucent materials with the lowest thermal conductivities among solids. They are produced via sol-gel process and subsequent drying to replace the pore liquid by air without significant alterations of the silica skeleton. During ambient-pressure drying (APD), evaporation generates capillary forces that put the liquid under tension, which is balanced by the compression of the silica skeleton. This results in substantial drying shrinkage that is made partially reversible by surface modification of silica gels. Past a critical shrinkage, the gels re-expand through the spring-back effect (SBE), demonstrating a remarkable elasticity for a silica-based material. However, the description of the evaporation and deformation mechanisms remains mostly theoretical and few experiments were performed to investigate the APD process in-operando.

This thesis aims to provide an empirical description of the evolution of silica gels properties during drying, thermal treatment and mechanical compression. The main motivation is to unveil the underlying mechanisms of the drying shrinkage and spring-back by addressing the kinetics of the gels' phase composition during APD. Another incentive is to quantify the capability of silica aerogels to recover large deformations related to drying shrinkage and uniaxial compression and evaluate the corresponding changes in the aerogels' nanostructure.

Silica gels were prepared by a sol-gel process from tetraethyl orthosilicate and were casted as 16 mm tall cylinders, followed by modification with trimethylchlorosilane. Specimen were dried at ambient-pressure to produce monolithic aerogels. The average phase composition of the gels during APD was successfully computed by developing a novel quantitative imaging workflow based on in-operando X-ray micro-computed tomography (μCT). The emergence of the SBE was correlated to an equal volume fraction of silica skeleton, hexane and gas in the gels. To this regard, the re-expansion was arguably caused by a local relaxation of the drying stress, indicating a depletion of solvent in some pores. Simulations on unmodified gels supported the incidence of condensation reactions during drying.

Further analysis of μCT data allowed to map the distribution of liquid and vapor in the gels during drying, which notably uncovered evidence of evaporation of the pore liquid by cavitation. This was supported by estimations using classical nucleation theory, and by separate in-operando wide-angle X-ray scattering experiments showing a significant volume of gas in the gels prior to the SBE. The onset of evaporation by meniscus recession was manifested by a drying front travelling across the specimen and was correlated to a heterogeneous SBE.

Initially limited after drying, the spring-back was completed by thermal annealing resulting in a "two-step" SBE. The related nanostructural changes were evaluated by small-angle X-ray scattering, giving insights on the causes of partial re-expansion after drying. Annealed silica aerogels showed significant compressibility and a plastic behavior under uniaxial compression, and it was found that residual deformations were completely recovered by a second thermal annealing at the macro- and nano-scale. The deformation mechanisms upon compression were addressed by analyzing changes in fractal dimension and mean cluster size, which supported a phenomenology of compaction by sequential shrinkage of large pores.

To this day, the size of monolithic silica aerogels produced by APD remains limited due to the susceptibility of silica gels to mechanical failure. This thesis contributes to a better understanding of the evaporation mechanisms, which is relevant to evaluate and predict the stress state in gels during drying. Moreover, the occurrence of cavitation brings new aspects on the APD process and highlights the potential of reducing the drying stress and thus the risk of cracks by tuning the gels' preparation and drying conditions to promote cavitation. Re-expansion of silica aerogels can be controlled by thermal activation thus qualifying aerogels as programmable materials, which broadens their potential utilization in several fields such as thermal insulation.

Kurzfassung

Siliziumdioxid-Aerogele sind hochporöse, lichtdurchlässige Materialien mit den niedrigsten Wärmeleitfähigkeiten unter den Feststoffen. Sie werden durch ein Sol-Gel-Verfahren und anschließendem Trocknen hergestellt, bei dem die Porenflüssigkeit durch Luft ersetzt wird, ohne dass sich das Gerüst aus Siliziumdioxid (engl.: Silica) wesentlich verändert. Bei der Trocknung bei Umgebungsdruck (engl.: ambient-pressure drying, APD) entstehen durch die Verdampfung Kapillarkräfte, die die Flüssigkeit unter Spannung setzen, was durch die Kompression des Siliziumdioxidgerüsts ausgeglichen wird. Dies führt zu einer beträchtlichen Schrumpfung beim Trocknen, die durch eine Oberflächenmodifizierung der Silica-Gele teilweise reversibel gemacht werden kann. Nach einer kritischen Schrumpfung dehnen sich die Gele durch einen Rücksprung-Effekt (engl.: spring-back effect, SBE) wieder aus, was eine bemerkenswerte Elastizität für ein Material auf Siliziumdioxidbasis darstellt. Die Beschreibung der Verdampfungs- und Verformungsmechanismen ist jedoch bis heute weitgehend nur theoretisch beschrieben, und nur wenige Experimente wurden durchgeführt, um den APD-Prozess in-operando zu untersuchen.

Ziel dieser Arbeit ist es, eine empirische Beschreibung der Entwicklung der Eigenschaften von Silica-Aerogelen während der Trocknung, der thermischen Behandlung und der mechanischen Kompression zu liefern. Eine zentrale Motivation der Arbeit besteht darin, die zugrundeliegenden Mechanismen der Trockenschrumpfung und des SBE aufzudecken, indem die Kinetik der Phasenzusammensetzung der Gele während der APD untersucht wird. Des Weiteren wird untersucht, wodurch Silica-Aerogele in der Lage sind große Verformungen, verursacht durch Trockenschrumpfung bzw. einachsige Kompression, rückgängig zu machen und wie sich dabei die Nanostruktur der Aerogele ändert.

Silica-Aerogele wurden durch ein Sol-Gel-Verfahren aus Tetraethylorthosilikat hergestellt und in 16 mm hohe Zylinder gegossen, die anschließend mit Trimethylchlorsilan modifiziert wurden. Die Proben wurden bei Umgebungsdruck getrocknet, um monolithische Aerogele herzustellen. Die durchschnittliche Phasenzusammensetzung der Gele während der APD wurde erfolgreich durch die Entwicklung eines neuartigen quantitativen Bildgebungsverfahrens auf Grundlage eines In-Operando-Ansatzes mit Röntgen-Mikro-Computertomographie (μCT) berechnet. Das Auftreten des SBE korrelierte mit einem gleichen Volumenanteil von Silikaskelett, Hexan und Gas in den Gelen. Die Ausdehnung während des SBE wurde durch eine lokale Relaxation der Trocknungsspannungen verursacht bedingt durch eine Leerung einiger Poren von Lösungsmittel. Simulationen an unmodifizierten

Gelen bestätigten das Auftreten von irreversiblen Kondensationsreaktionen während der Trocknung.

Eine weitere Analyse der μCT-Daten ermöglichte es, die Verteilung von Flüssigkeit und Dampf in den Gelen während der Trocknung abzubilden, was insbesondere Hinweise auf eine Verdampfung der Porenflüssigkeit durch den Prozess der Kavitation ergab. Diese Erkenntnis wurde durch Einschätzungen anhand der klassischen Keimbildungstheorie und durch In-Operando-Weitwinkel-Röntgenstreuungsexperimente gestützt, die ein erhebliches Gasvolumen in den Gelen vor dem SBE zeigten. Der Beginn der Verdampfung durch Meniskus-Rezession zeigte sich in einer Trocknungsfront, die sich quer über die Probe bewegte, und wurde mit einem heterogenen SBE in Verbindung gebracht.

Die nach dem Trocknen zunächst begrenzte Wiederherstellung der ursprünglichen Form durch den SBE wurde durch Tempern vervollständigt und die nanostrukturellen Veränderungen wurden durch Röntgenkleinwinkelstreuung ausgewertet, was Einblicke in die Ursachen der teilweisen Wiederausdehnung nach dem Trocknen lieferte. Getemperte Silica-Aerogele zeigten eine signifikante Komprimierbarkeit und ein plastisches Verhalten bei einachsiger Kompression, und es wurde festgestellt, dass Restverformungen durch Tempern sowohl auf der Makro- als auch auf der Nanoskala wieder vollständig zurückgebildet werden konnten. Die Verformungsmechanismen bei der Kompression wurden durch die Analyse der Veränderungen der fraktalen Dimensionen und der mittleren Clustergröße untersucht, die insbesondere auf eine Verdichtung durch Schrumpfung der großen Poren hindeuteten.

Bis heute ist die Probengröße der durch APD hergestellten monolithischen Silica-Aerogele aufgrund der Anfälligkeit von Silica-Gelen für mechanisches Versagen begrenzt. Diese Arbeit trägt zu einem besseren Verständnis der Verdampfungsmechanismen bei, was für die Bewertung und Vorhersage des Spannungszustands in Gelen während der Trocknung von Bedeutung ist. Darüber hinaus zeigt das Auftreten von Kavitation neue Aspekte des APD-Prozesses und verdeutlicht das Potenzial, den Trocknungsstress und damit das Risiko von Rissen zu verringern, indem die Präparations- und Trocknungsbedingungen des Gels so abgestimmt werden, dass Kavitation gefördert wird. Die Wiederausdehnung von Silica-Aerogelen kann durch thermische Aktivierung kontrolliert werden, wodurch sie als programmierbare Materialien eingestuft werden können. Diese Eigenschaft erweitert ihr Potenzial für verschiedene Anwendungen wie beispielsweise Wärmedämmung.

Table of Contents

1 Introduction

1.1 Motivation and goals

We spend a significant portion of our life indoors: buildings, houses and residences. In temperate climates, those environments are kept warm by diverse heating installations (fire stove, radiators, and central heating). In Europe, the residential sector accounted for about 28 % of the total energy consumption in 2021,[1] among which 64 % was dedicated to household space heating.[2] This results in a total of 18 % of the yearly energy input spent solely for heating buildings, creating incentives for the reduction of the associated greenhouse emissions. The fundamental reason for the high amount of energy spent in space heating is that it is difficult to keep the warmth: heat flows from hot to cold regions.

Buildings' walls, roofs, floors and ceilings alleviate heat losses by slowing down the diffusion of the heat across their thickness, which is greatly improved throughout the incorporation of interlayers of thermal insulating materials. The performance of an insulating material can be represented by its thermal conductivity. Whereas concrete[3] typically has a thermal conductivity of 1.5 W m^{-1} K^{-1}, conventional insulation materials[4] (e.g. mineral wool and glass wool) show much lower values at 0.031 – 0.045 W m^{-1} K^{-1}, highlighting the importance of thermal insulation in buildings. Even though it is possible to increase the thickness of thermal insulation layers to reduce heat losses, a more desirable solution consists in using materials with lower thermal conductivities to achieve the same insulation while saving space and raw materials.

Aerogels stand out as inert, light and superinsulation materials with thermal conductivities[5] of about 0.015 W m^{-1} K^{-1}, making them ideal candidates for improving the thermal insulation in old and new buildings. The thermal insulation properties of aerogels arise from their unique porous network combining small pores (in nanometer range) and high porosity, resulting in a lower thermal conductivity than air at ambient temperature.[6] Among aerogels, silica systems are particularly suited for thermal insulation as they show among the lowest thermal conductivities[5] and are well-known in terms of processing and properties.[7,8] Furthermore, silica aerogels can be manufactured into transparent/translucent products, enabling their incorporation in glazed windows[9,10] and even in load-bearing translucent bricks.[11] However, the majority of commercially available products rely on silica aerogel granules that show lower thermal insulation properties and lower transmittance compared to monolithic

("single piece") aerogels.[9,12] The reason for that is that it remains demanding to manufacture silica aerogel monoliths with the current methods.

Producing silica aerogels requires exchanging the pore liquid of a gel for air without significant alteration of the silica skeleton structure,[13] which is achieved by drying. Ambient-pressure drying (APD, also called evaporative drying) is the most feasible process in terms of cost[14] and can produce both silica aerogels monoliths and granules. Upon evaporation of the liquid that is confined in nanometer-sized pores, the liquid enters in tension due to the capillary pressure and is balanced by the compression of the silica skeleton, resulting in drying shrinkage of the gel.[15] Drying shrinkage is made reversible via surface modification using silylating agents,[16] which enables the gel re-expansion during drying called the spring-back effect (SBE). The SBE of silica gels illustrates a surprising deformation of the gels' solid matrix for a ceramic material that is not observed in other forms of silica like glass or quartz and remains mostly unexplored. Unveiling the origin and phenomenology of the SBE -and thus the mechanisms of the evaporative drying process - not only represents a fundamental research question, but may also bring substantial progress in the production of large aerogel monoliths by APD, which remains the main limitation of this process.

The current dissertation is part of a joined project between the Max Planck Institute of Colloids and Interfaces and the Chair of Advanced Ceramic Materials at Technische Universität Berlin, with the primary objective of studying the phenomenology of the SBE in ambient-pressure dried silica aerogels. This topic was tackled with different research questions, approaches and methods throughout this collaboration. Within this joined project, Fabian Zemke recently made valuable contributions to the aerogel community, issuing a PhD dissertation[17] and three publications[18–20] on the nanostructural characterization of the SBE. A notable outcome of that work was the impact that different silylating agent had on the nanostructural features of the gels during drying such as fractal dimension, mean cluster size and particle size, which was achieved by the development of an experimental protocol and modeling workflow based on in-situ X-ray scattering measurements.

The research questions that build the framework of this thesis relate to the conditions of emergence of the SBE, the underlying evaporation mechanisms of the APD process and the deformation mechanisms associated to the compression and re-expansion of the solid silica network. These questions are used to outline the goals of the dissertation in consideration to the technical capabilities that may be needed to investigate them. To this regard, part of this thesis is dedicated to the development of a new methodology based on the quantitative imaging analysis of in-operando X-ray micro-computed tomography (μCT) measurements. A workflow

is developed aiming at generating spatial and temporal phase composition maps of materials undergoing dynamic shape and composition changes, such as silica gels.

The **first goal** of this dissertation is to reveal the kinetics of the ambient-pressure drying process by evaluating the evolution of the solid, liquid and gas volumes in monolithic silica gels, which remains mostly unknown. In practice, it should be assessed if these parameters can be derived by modeling data collected on a lab-source μCT instrument using a quantitative imaging approach. Differences between silylated and non-silylated silica gels will notably be addressed.

The **second goal** is to explore cavitation as a potential evaporation mechanism during the ambient-pressure drying of silica gels. The motivation of this study lies in the conclusions drawn from the first goal, which align with the hypothesis of evaporation by cavitation proposed by Scherer and Smith nearly 30 years ago.[21] Cavitation is known to occur in other mesoporous materials, but has never been observed in silica gels. An advanced workflow based on μCT data will be established with the purpose to calculate the vapor/air distribution within the gels during drying, which may uncover experimental evidence of solvent cavitation.

The **third goal** is to evaluate the compressibility of dry and annealed silica aerogel monoliths, and to assess whether residual deformations can be recovered at a macro- and nano-scale via thermal treatment at mild temperatures. The interest of this goal is dual, as it may unveil the cause(s) of the incomplete spring-back effect during the drying of silica gels and provide information on the deformation mechanisms of the solid silica network. Parallels between evaporative drying and uniaxial compression tests will also be discussed.

1.2 Structure of the thesis

This dissertation is organized as follows:

Chapter 1 introduces the motivation and main goals of this dissertation, how they were addressed and describes the structure of the thesis.

Chapter 2 covers the state-of-the-art of the research on silica aerogels with an emphasis on the evaporative drying, spring-back efficiency, and thermal treatment and stability of silylated silica gels.

Chapter 3 describes the materials synthesized in this thesis, the methods used to characterize them and how the generated data were managed. This chapter outlines the impact of the synthesis and preparation conditions on the quality and spring-back of the produced silica gels. A short review on each method is also presented, covering the basics and how it can be applied to aerogel materials. Concrete application of the methods are described in chapters 4, 5 and 6.

Chapter 4 presents the synthesis route used to produce silica gels samples for μCT experiments. The findings of the μCT quantitative imaging workflow and the associated drying model applied to the APD of silylated silica gels are described. The emergence of the spring-back effect is correlated to the average phase composition of the drying gels and the limitations of the model are discussed by performing simulations based on μCT data collected on unmodified gels. The content of this chapter is published as: Gonthier, J.; Rilling, T.; Scoppola, E.; Zemke, F.; Gurlo, A.; Fratzl, P.; Wagermaier, W. In Operando μCT Imaging of Silylated Silica Aerogels during Ambient Pressure Drying and Spring-Back. *Chem. Mater.* **2023**, *35* (18), 7683–7693.

Chapter 5 revisits the evaporation mechanisms of silylated silica gels during APD using a spatially resolved μCT quantitative imaging approach enabling to generate composition maps. It presents experimental evidences of evaporation by cavitation and discusses the possible consequences on the production of monolithic aerogels by evaporative drying. The content of this chapter is published as: Gonthier, J.; Scoppola, E.; Rilling, T.; Gurlo, A.; Fratzl, P.; Wagermaier, W. Solvent cavitation during Ambient Pressure Drying of Silica Aerogels. *Langmuir* **2024**, *40* (25), 12925–12938.

Chapter 6 reports the synthesis and post-drying treatment used to prepare silica gels and aerogels' samples for SAXS/WAXS measurements. This chapter is dedicated to the interpretation on the structural changes of silica aerogels upon annealing and mechanical compression, highlighting the recovery capabilities of silica aerogels by thermal treatment. The content of this chapter has been submitted in Journal of Sol-Gel Science and Technology on the 15th of April 2024 and is currently under review.

Chapter 8 summarizes the major findings of this work and suggests directions for further investigations and applications.

In addition to the aforementioned manuscripts, I have contributed in the following publication related to the topic of this thesis but not included: Zemke, F.; Gonthier, J.; Scoppola, E.; Simon, U.; Bekheet, M. F.; Wagermaier, W.; Gurlo, A. Origin of the Springback Effect in Ambient-Pressure-Dried Silica Aerogels: The Effect of Surface Silylation. *Gels* **2023**, *9* (2), 160.

The graphs in this thesis were generated using the scientific color maps batlow, lapaz, lisbon, oslo and tokyo[22] to prevent visual distortion of the data and exclusion of readers with color-vision deficiencies.[23]

2 State-of-the-art

2.1 Overview

It is surprisingly difficult to find a consensus on a unique definition of aerogels. Some definitions rely on the extrinsic properties of the material itself such as the one proposed by Liebner et al.: "*Aerogels are solids that feature very low density, high specific surface area and consist of a coherent open-porous network of loosely packed, bonded particles or fibers*".[24] Such a definition has the advantage of being inclusive as it does not restrict the kind of compounds that can be prepared as aerogels, neither does it restrict the preparation methods. It also gives an overview of the properties that can be expected from an aerogel. Alternative definitions are based on the process used to produce them. To quote Hüsing and Schubert: "[aerogels are] *materials in which the typical structure of the pores and the network is largely maintained* […] *while the pore liquid of a gel is replaced by air* ".[25] This definition -although more restrictive- gives more insights on the process used to produce aerogels.

The first aerogels were made out of silica[26] which remains nowadays the most studied system with the highest potential of commercialization for its thermal insulation properties.[7,8] Other systems include ceramics (titania,[27] alumina,[28] zirconia[29]), cellulose,[30] carbon[31] and hybrid compounds.[32–34] Besides applications in the thermal insulation sector, aerogels can be prepared to promote their photocatalytic activity,[32] they can be used as biocompatible carriers for drug delivery[35] and as reusable sorbent to clean-up organic liquids[36] and water contaminants.[37]

The extrinsic properties of aerogels arise from their characteristic porous network that combines high porosity (> 80 %), large specific surface area (200 – 1000 $m^2 g^{-1}$) and a pore size distribution ranging from a few nm to about hundred nm,[13] making aerogels a subclass of mesoporous materials. Their extremely low thermal conductivity is a consequence of the small pore size that alleviates energy exchange of the gas molecules confined in the gel.[5] Aerogels mechanical properties are intimately related to their porosity[38] and also depend on the intrinsic properties of the solid matrix. Cellulose aerogels are rather compressible and show a near-zero Poisson's ratio[39] while silica aerogels are generally described as elastic but brittle.[40,41] This fragile behavior under mechanical stimuli is a limiting factor for their applications in some fields[9] and also in their production (chapter 2.3). The brittle nature of silica aerogels can notably be circumvented by fiber reinforcement[42] or by creating architectured structures.[43] More details on the mechanical properties of silica aerogels will be given in chapter 6.

2.2 Sol-gel process

This section gives a brief summary on the synthesis of aerogels by sol-gel processes, focusing on silica systems. The sol-gel process is well described in the literature, and its description here is mainly inspired from three excellent references on that topic: the book Sol-Gel Science by Brinker and Scherer[44] and the chapters "Overview of the Sol-Gel Process"[45] and "Gel-Phase Processing and Solvent Exchange"[46] from the Springer Handbook of Aerogels. Statements related to other references than those are explicitly cited in the text.

Sol-gel processes consist in the preparation of ceramics, organics and composite materials via the synthesis of a sol and the gelation of the sol. A sol is a colloidal suspension of solid or liquid particles in another liquid, where the particle size is typically 1 – 1000 nm. Blood and paint are examples of sols. The sol-gel transition corresponds to the point where a sol loses the properties of a suspension and becomes a solid phase (see Figure 2.1), which is represented by a sharp increase in viscosity. That transition is the result of chemical bonds forming between the particles of the sol that create clusters, which then grow by aggregation and eventually become large enough so that they extend throughout the solution. The resulting material is called a gel. Following the formal definition from IUPAC, a gel is a "*non-fluid colloidal network that is expanded throughout its whole volume by a fluid*".[47] Using a less rigorous phrasing, a gel is an object composed of a solid matrix whose pores are filled with a continuous fluid phase. Jellies and mucus are examples of gels. Moreover, a gel whose dimensions exceed a few millimeters can be called a monolith.

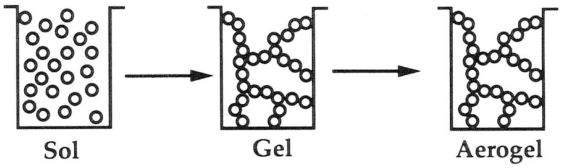

Figure 2.1 Sketch of the sol-gel process to produce an aerogel. Reprinted from ref.[44] with permission from Elsevier.

The sol-gel process for the production of silica aerogels can be broken down into three steps: synthesis, aging and drying. Drying will be detailed in chapter 2.3, being the most critical part in the production of aerogels. The synthesis step consists in the creation of a sol and in the gel formation via chemical reactions of a precursor within a medium. There are mainly two classes of precursors used to produce silica gels: silicon alkoxides and sodium silicate. Silicon alkoxides are molecules consisting of a metal (here silicon) surrounded by organic compounds (ligands) with the formula $Si(OR)_4$, where R is an alkyl group. They are hydrophobic and

immiscible in water. Tetraethyl orthosilicate (TEOS) is a common silicon alkoxide and has the chemical formula: $Si(OC_2H_5)_4$, but several other silicon alkoxides are also used,[48] and the reactivity highly depends on the alkoxy group. Sodium silicate (Na_2SiO_3), also commonly referred to as waterglass, is a low-cost precursor used as an alternative to silicon alkoxides.[49] Silicon alkoxides are usually preferred for the synthesis of silica gels because of the more lengthy process involved in the sol-gel process using waterglass that notably requires additional steps to eliminate sodium salts generated during the reaction.[50,51]

The preparation of silica gels from silicon alkoxides is carried out by mixing the precursor with an alcohol (e.g. ethanol) and water. Under these conditions, there are two reactions happening: hydrolysis and condensation. Hydrolysis reaction replaces an alkoxide group $-OR$ from the precursor by a hydroxyl group $-OH$ and releases an alcohol molecule according to eq. (2.1). Condensation reaction corresponds to the formation of a siloxane bond ($Si-O-Si$) between two metal centers. Condensation can occur between two silanol groups ($SiOH$), in which case it releases a water molecule (eq. (2.2)), or between a silanol and a silicon alkoxide group, releasing an alcohol molecule (eq. (2.3)).

$$\equiv Si-OR + H_2O \rightleftharpoons \equiv Si-OH + ROH, \tag{2.1}$$

$$\equiv Si-OR + HO-Si \rightleftharpoons \equiv Si-O-Si\equiv + ROH, \tag{2.2}$$

$$\equiv Si-OH + HO-Si \rightleftharpoons \equiv Si-O-Si\equiv + H_2O. \tag{2.3}$$

The rate of hydrolysis and condensation reactions has a significant influence on the structure of the sol and is dictated by the pH of the solution: hydrolysis occurs faster than condensation under acidic conditions and the trend is reversed under basic conditions. Acid-catalyzed reactions result in chain-like polymeric sols (low degree of cross-linking) while base-catalyzed reactions generate highly branched colloidal particles (high degree of cross-linking). Adjusting the pH during the sol-gel process allows to control the morphology of the sol, which ultimately influences the structure of the aerogel. As the reactions go on, the particles in the sol collide and condense with each other leading to the formation of the gel, which in the case of alkoxide precursors can be called an alcogel. Gels formed under acidic conditions have a branched silica skeleton that is relatively compact, whereas basic environments creates a skeleton made of rather porous silica clusters. As it will be discussed in section 2.3, the drying stress and shrinkage highly depend on the gels' pore size and on the compliance of the silica skeleton. Therefore, the structures formed in acid- and base-catalyzed gels have a critical impact during the drying of the gels. Two-step acid/base catalyzed procedures can produce highly porous silica gels featuring a "pearl-necklace" structure while keeping a reasonable

gelation time.[49] In the two-step procedures, the hydrolysis of a silicon precursor (e.g. TEOS) is carried out in a solvent (e.g. ethanol) and is promoted by adding an acid (e.g. HCl) and sub-stoichiometric amounts of water. In a second step, further water and a base (e.g. NH_4OH) are added to the silica sol to enhance condensation reactions and activate the gelation of the sol. The two-step acid/base catalyzed procedure is commonly used to produce translucent, monolithic aerogels from TEOS and tetramethyl orthosilicate (TMOS) precursors.[16,51–54]

Gelation is usually followed by aging to strengthen the silica skeleton and improve the mechanical properties of silica gels, which is required prior to drying. Cross-linking and aggregation of the silica clusters does not stop at the sol-gel transition and the diffusion of residual oligomers (small alkoxide chains or clusters) through the porous network leads to further condensation reactions. This process is enhanced by exposing the gels to temperatures of ca. 50 – 75 °C to promote the diffusion of species through the pores[55] and the dissolution-precipitation process of surface silica groups (typically silanol).[56,57] It results in the growth of the necks in between the silica nanoparticles. Syneresis is another consolidation mechanism that can occur during aging and more generally during the storage of gels in a solvent, where the pore liquid is forced out of the solid network resulting in shrinkage of the gels. This mechanism is arguably driven by condensation reactions.[58] The shrinkage caused by syneresis in silica gels is not well documented, but some authors reported a linear shrinkage of 10 %[59] and 14 %[14] upon gelation and Bisson et al. mentioned a volume shrinkage as high as 20 vol %.[57] Another factor influencing the structure of the silica gels is the size of the alkoxy groups attached to the metal center, as the steric hindrance is more pronounced in large molecules and can affect the degree of cross-linking during polymerization.

Most sol-gel processes include an additional step after aging that is the surface modification and is required if the gel is to be dried at ambient-pressure. Moreover, the pore liquid is usually exchanged for another solvent/liquid regardless of the drying procedure. These aspects will be covered in the next chapter.

In conclusion, the synthesis of gels by a sol-gel process is well documented for the silica systems and the two-step acid/base procedures stand out among other synthesis routes to synthesize gels suitable for the preparation of aerogels. The structure of silica gels produced from silicon alkoxide can be tuned in a numerous ways by adjusting the precursor:water:solvent ratio, the solution pH and the aging conditions. Steiner et al. recently compiled detailed protocols on the synthesis of aerogels from a multitude of starting materials (silica, cellulose, carbon),[60] which gives useful details to researchers unfamiliar with the sol-gel process.

2.3 Evaporative drying and monolithic aerogels

This chapter covers the evaporative drying process of silica aerogels with an emphasis on the production of monolithic specimen. The reason why drying is the most critical step in the synthesis of aerogels can be explained with an example and a single equation. Let us consider a capillary dipped into a liquid: an interface (a meniscus) forms between the liquid and the vapor inside of the capillary. At the capillary walls, the contact point between the solid and liquid phases forms an angle θ whose extent depends on the total surface energy balance. For example, a straw dipped in water will generate a concave meniscus ($\theta < 90°$), corresponding to a slight rise of the water at the capillary walls because the surface energy of the solid-liquid interface is lower than the one of solid-vapor (see Figure 2.2). The water "wets" the capillary. The curvature of the meniscus corresponds to a pressure difference across the liquid-vapor interface called capillary pressure, which is given by the Young-Laplace equation:[61,62]

$$\Delta p = p_0 - p_l = \frac{2\gamma_{LV}\cos\theta}{r_c}, \tag{2.4}$$

where Δp is the capillary pressure, p_0 is the vapor pressure, p_l is the pressure in the liquid, γ_{LV} is the surface tension of the liquid-vapor interface and r_c is the capillary radius and is set as $r_c > 0$. For wetting fluids ($\theta < 90°$), p_l can be negative: the liquid is under tension.[63,64] The smaller the capillary radius, the higher the tension. In the case of stiff solids (e.g. a glass capillary), the tension in the liquid is balanced by the rise of water in the capillary to reach an equilibrium between the capillary pressure and the atmospheric pressure, as illustrated in Figure 2.2.

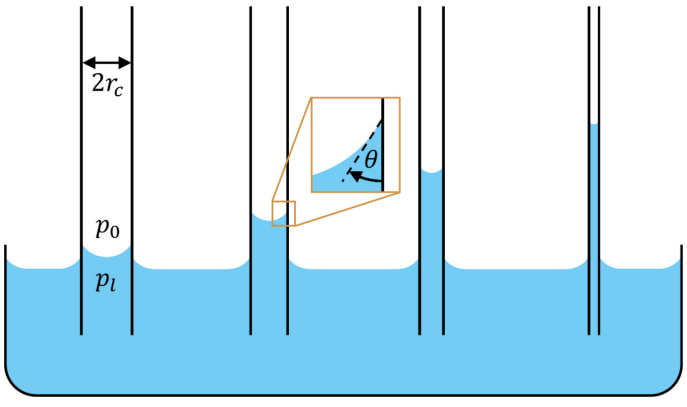

Figure 2.2 Rise of a liquid in capillary tubes of decreasing radii r_c. The vapor pressure p_0 and the pressure in the liquid p_0 are depicted in the figure, and the contact angle θ is shown in the inset (orange box).

Let us now replace the capillary by a porous media with open pores filled with a solvent: upon evaporation of the solvent, a meniscus forms in the pores at the surface of the material. Most solvents fully wet gels,[65] thus the contact angle is $\theta \approx 0$. For small pores, the liquid is under tension according to eq. (2.4) but unlike the example of the capillary tubes, the tension in the liquid cannot be balanced by capillary rise and is instead balanced by the compression of the solid network embedding the liquid.[66] The small pore size of silica gels results in capillary pressures that can reach 100 MPa.[21,66] This, combined with the rather compliant and compressible matrix of silica gels[40,67,68] generates a substantial shrinkage of the gel. This has two detrimental effects on the final structure of the dry gels: 1) the drying stress and the stress gradients can create cracks, thus the difficulty of producing large monolithic aerogels by APD,[15,69] and 2) the shrinkage creates contact points between the silica clusters covered with silanol groups, which can undergo further condensation reactions resulting in irreversible compaction of the gels upon evaporative drying.[57] To this regard, dry gels that underwent irreversible shrinkage have degraded properties due to the collapse of the pores, and are called xerogels.[13,47] Drying shrinkage is the main limitation of the APD process and requires finding approaches to alleviate the drying stress and related deformations. One approach consists in tuning the sol-gel synthesis to produce gels with a skeleton made of larger particles to improve the gels' stiffness and with larger pores to reduce the capillary pressure. As previously stated, gels synthesized via a two-step acid/base procedure have been shown to withstand the APD process and to enable the production of monolithic products. The other two main approaches to improve the APD process are solvent exchange and surface modification, which are performed after the aging of the gels.

Exchanging the pore liquid by a solvent with a lower surface tension directly decreases the capillary pressure according to eq. (2.4). In alkoxide-based silica gels, ethanol is usually exchanged for n-hexane that has a surface tension against air of only 18.2 mN m^{-1} at 20 °C.[70] In comparison, the surface tension of water is 73 mN m^{-1} at 20 °C and that of liquid nitrogen is 9.1 mN m^{-1} at -196 °C.[71] It has also been shown that the solvent used to dry the gels has an impact on the dry gels transparency, surface area and hydrophobicity.[72] Solvent exchange is performed after aging of the gel. In practice, it is done by moving a specimen from its initial solution to another container, the exchange occurring by diffusion.[46] A similar procedure is used to prepare cement pastes for microstructural characterization.[73]

Chemical surface modification or derivatization consists in replacing the silanol groups at the surface of the silica nanoparticles (that are hydrophilic) by hydrophobic groups to prevent condensation reactions to occur during drying shrinkage. The advent of surface

modification using trimethylchlorosilane (TMCS) uncovered the reversible shrinkage of silica gels dried by APD, resulting in partial recovery of the gel volume that is referred to as the spring-back effect (SBE).[16,74,75] Surface modification is carried out similarly as solvent exchange by immersing gels in a solution containing a silylating agent. Typical silylating agents used in the modification of silica gels are TMCS, hexamethyldisilazane (HMDS or sometimes HMDZ), and hexamethyldisiloxane (HMDSO).[49] The effect of the silylating agents on the SBE and on the aerogels' properties is a major topic in the research on evaporative drying,[72,76–80] and still receives attention.[19,20,81,82] Zemke et al. notably emphasized the importance of a complete surface modification to enable the SBE, as traces of residual silanol groups could still significantly affect the gels re-expansion.[19] On the other hand, excess modification can also alter the mechanical properties of the gels and increase the risk of cracks developing during APD.[59,83] The completeness of the surface modification relies on the diffusion of the silylating species through the porous network and their reactivity with the silanol groups. For these reasons, TMCS is the most used silylating agent as it is highly reactive and has a relatively small molecular size compared to other compounds, allowing it to diffuse through small pores and it also alleviates pore blocking effects upon reaction.[19,78]

The extent of the SBE dictates the final properties of aerogels and can be quantified by the relative change in volume throughout drying as V_d/V_0, with V_d and V_0 the dry gel and alcogel volume, respectively. This ratio is sometimes referred to as the spring-back efficiency[59,83] or volume shrinkage,[51,84] but is not systematically reported in the literature, arguably due to the challenges related to measuring the alcogels dimensions and the dry gels volume that break into smaller pieces. Additionally, the method used to measure the gels dimensions is often not reported. Different silylating agents result in different extents of the SBE. TMCS-modified gels stand out with the highest average spring-back efficiency.[17] Some authors claim very high spring-back efficiencies (> 99 vol %,[51] 94.5 vol %[59]), but at this point it is important to differentiate the volume recovery of the gels upon drying, and the volume recovery upon heat-treatment.

Post-drying thermal annealing is often performed to complete the SBE and increases the porosity and surface area of dry gels.[85] Annealing is usually done at mild temperatures within 150 – 230 °C.[59,74–76,83,84,86,87] The thermal stability of TEOS-based silica aerogels modified with TMCS is around 400 °C,[19,78,82,84] although values of 260 °C[85] and 350 °C[80] have been reported. Beyond ca 400 °C, the methyl groups at the surface of the silica nanoparticles are oxidized,[19] leading to a degradation of the aerogel properties and notably the loss of hydrophobicity. Thus, annealing temperatures of ~200 °C should not lead to any chemical

decomposition of the silica skeleton. Heat-treatments at high temperatures (> 400 °C) lead to severe densification of the gel,[88] an increase of the pore size and possibly mechanical failure.[89] Annealing or drying at mild temperatures also seems to conserve the monolithicity of silica aerogels,[59,74,83,85,86] but is also used to produce granules.[68,87,90]

Monolithic aerogels have higher optical transmittance and insulating properties than granules, thus the interest of preventing mechanical failure during the APD process. Fracture can occur during drying shrinkage but also during the SBE,[18] the fragments re-expand individually resulting in highly porous granules[4,68,80] (Figure 2.3). Cracking of the gel happens when the stress on the silica skeleton exceeds its fracture toughness, which can be alleviated by tuning the gel structure (synthesis, aging) and by optimizing the drying conditions. The deformation of porous materials during drying or upon mechanical action is a wide research topic[38,66,91] and is not only relevant to sol-gel materials,[65] but also ceramics,[92,93] in geology[94] and cementitious materials.[95] Slower drying rates generate a more homogeneous distribution of stress, which reduces the risk of cracks. The duration of the APD process to produce aerogel monoliths varies largely in the literature, it can last between a few hours[86] to a few days.[19,51,59,80,83–85,96] Interestingly, it has recently been shown that highly porous monolithic silica gels can be produced by evaporative drying without surface modification, provided that the gels are dried slowly enough (up to 18 days).[14] The gels dried by that manner did not spring-back, but also did not show a significant drying shrinkage. The authors reported that the dry gel height was 94 % of alcogel height, whereas gels commonly shrink down to ca 20 vol % of their original volume before spring-back.[59,74] This suggests that the drying-related stress in mesoporous gels is not yet fully understood. The evaporation mechanisms during the APD process of porous materials will be reviewed in chapter 5.

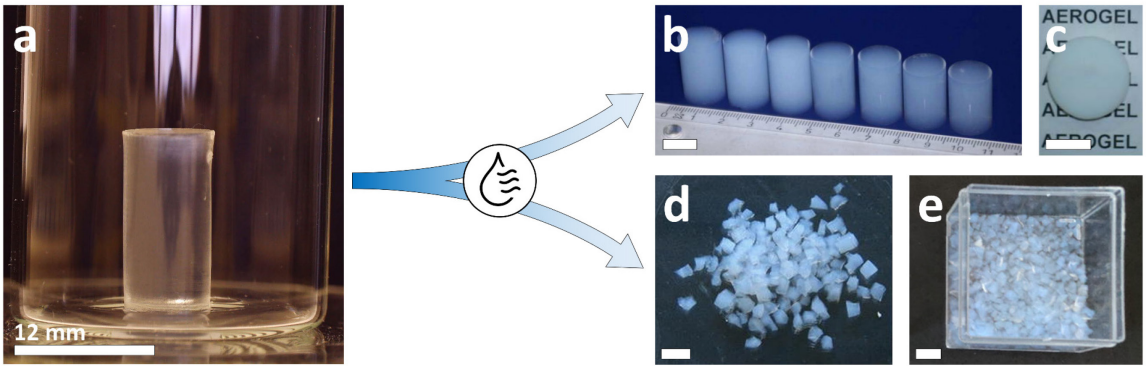

Figure 2.3 Illustration of the ambient-pressure drying of a silica alcogel (**a**) to produce monolithic aerogels (**b**[41], **c**[59]) and aerogel granules (**d**[4], **e**[68]). The scale bar in all panels is 12 mm. Panels (**b**,**c**) reprinted from refs.[41,59], respectively, with permission from Elsevier. Panel (**d**) reprinted from ref.[4] with permission from Springer Nature. Panel (**e**) reprinted from ref.[68], CC BY 4.0 (https://creativecommons.org/licenses/by/4.0/).

Besides APD, supercritical drying (SCD) and freeze-drying (FD) are alternatives methods that circumvent capillary pressure by replacing the pore liquid by air without any liquid-vapor interface. In SCD, the pore liquid is brought to a supercritical state by increasing its pressure and temperature and is then evacuated, effectively bypassing the liquid-vapor transformation. In FD, the pore liquid is frozen and evacuated by sublimation. Solvent exchange is also needed with these alternative drying methods, as well as surface modification when producing hydrophobic aerogels. Additionally, for SCD performed with supercritical CO_2, the miscibility of different solvents must be taken into account. Gels filled with water for example require an additional solvent exchange step as CO_2 and water are immiscible.[97] The disadvantage of SCD methods resides in the initial investment and manufacturing costs related to the instrumental setup,[8,98] especially compared to APD processes. FD methods seem yet unable to produce monolithic aerogels reliably especially for silica-based gels, usually resulting in cracked or powder product.[8,57] Nevertheless, it is worth noting the efforts of some researchers to go in that direction.[99]

Solvent exchange, aging and surface silylation are key steps in the production of silica aerogels by APD. The spring-back effect is enabled by chemical modification of the gels and can be completed by thermal annealing at mild temperatures. This is notably emphasized by ongoing efforts on the optimization of silylation procedures to produce high-quality aerogels by APD.[81] On the other hand, the improvement of APD processes is directly linked to the spring-back efficiency, which highlights the importance of better understanding the emergence of the SBE and the deformation mechanisms of the silica skeleton. Recent studies have paved the way towards that goal by assessing the macroscopic and structural deformations upon spring-back of silica gels.[18,20,68] Further investigation on the kinetics of the APD process is yet required, as recently illustrated by the relations between drying rate and drying shrinkage.[14] To this regard, further efforts should be directed towards a systematic evaluation of the drying conditions (evaporation rate and temperature) and the drying-related deformations of the gels. This could unveil the kinetics of the SBE and may allow surpassing the current size limitations of monolithic aerogels produced by APD.

3 Materials and methods

3.1 Specimens

This section summarizes the synthesis procedures that were performed throughout this thesis to produce silica aerogels and discusses the impact of the synthesis conditions, casting and thermal annealing on the quality and spring-back of the silica gels. It also highlights the learning process that permitted to produce aerogels with satisfying properties.

13 batches were produced; the main parameters of each batch are described in Table 3.1. The first four synthesis batches (A1–B2) were adapted from the work of our collaborator Zemke, which is itself adapted from the synthesis of Wei et al.[51] All batches were produced from a two-step acid/base catalyzed sol-gel synthesis with the same total TEOS:EtOH:H_2O molar ratio at 1:8:3.6, where EtOH stands for ethanol. The pH was controlled with solutions of hydrochloric acid (HCl) in EtOH and ammonium hydroxide (NH_4OH) in water. In a first step, a mixture of TEOS:EtOH:H_2O at a molar ratio of 1:3:1 was prepared and the pH was adjusted by adding $2.6 \cdot 10^{-4}$ moles of HCl per mole of TEOS. In a second step, further ethanol and water were added to the mixture: 5 moles of EtOH and 2.6 moles of H_2O per mole of TEOS, along with different amounts of NH_4OH (Table 3.1). After gelation, the pore liquid (ethanol) was exchanged for n-hexane by rinsing the gels with solutions of n-hexane in ethanol of 0/100, 25/75, 50/50 and 75/25 vol % every 24 h, followed by rinsing in pure n-hexane four times every 24 h. The gels were then silylated by immersing them in solutions of TMCS in n-hexane at 3, 3, 6 and 6 vol % every 24 h for batches A1 – C1, D1, D2, D4 and D5. The TMCS:TEOS molar ratio was varied depending on the batch (Table 3.1). Less TMCS was used in batches D3 and E1 – E3, thus the concentration of the silylation solutions was 1.5, 1.5, 3 and 3 vol %. After surface modification, the gels were finally rinsed in pure n-hexane four times every 24 h. The total volume of the rinsing and silylation solutions differed among the batches (Table 3.1). In batches C1 and E1 – E3, some gels were not silylated and kept as unmodified references. Unless mentioned otherwise, the spring-back efficiency was evaluated by measuring the diameter and height of the gels with a micrometric caliper at three locations (3x diameter, 3x height).

Three generations of molds were produced to cast the solution into cylindrical samples: M1, M2 and M3 (Figure 3.1). The M1 series refers to a set of five single-part molds made from PTFE consisting in 8 cylindrical slots. Each mold of the set had a different depth:diameter of

Table 3.1 Summary of the synthesis batches. All quantities other than (*) are expressed as a molar ratio versus TEOS that is fixed at one. (*) is a volume of solvent (L) per mol of TEOS for a single solvent exchange step, the solvent being a mixture of EtOH and n-hexane. The amount of TMCS reported corresponds to the total amount of TMCS used over the four modification steps. (1) The samples from C1 are used in chapters 4 and 5. (2) The samples from E2 and E3 are used in chapter 6.

	1st step				2nd step			3rd step		Mold
Batch	TEOS	EtOH	H_2O	HCl	EtOH	H_2O	NH_4OH	Solv.(*)	TMCS	
A1	1	3	1	$2.6 \cdot 10^{-4}$	5	2.6	$1 \cdot 10^{-3}$	-	-	M1
A2	1	3	1	$2.6 \cdot 10^{-4}$	5	2.6	$1 \cdot 10^{-3}$	-	-	M1
B1	1	3	1	$2.6 \cdot 10^{-4}$	5	2.6	$1 \cdot 10^{-3}$	3.7-6.4	5.3-9.0	M2
B2	1	3	1	$2.6 \cdot 10^{-4}$	5	2.6	$4 \cdot 10^{-3}$	3.7-6.4	5.3-9.0	M2
C1(1)	1	3	1	$2.6 \cdot 10^{-4}$	5	2.6	$4 \cdot 10^{-3}$	1.2	1.7	M3
D1	1	3	1	$2.6 \cdot 10^{-4}$	5	2.6	$4 \cdot 10^{-3}$	2.3	1.7	M3
D2	1	3	1	$2.6 \cdot 10^{-4}$	5	2.6	$4 \cdot 10^{-3}$	2.3	1.7	M3
D3	1	3	1	$2.6 \cdot 10^{-4}$	5	2.6	$4 \cdot 10^{-3}$	2.3	1	M3
D4	1	3	1	$2.6 \cdot 10^{-4}$	5	2.6	$4 \cdot 10^{-3}$	2.3	4.5	M3
D5	1	3	1	$2.6 \cdot 10^{-4}$	5	2.6	$4 \cdot 10^{-3}$	2.3	1.7	M3
E1	1	3	1	$2.6 \cdot 10^{-4}$	5	2.6	$4 \cdot 10^{-3}$	-	-	M3
E2(2)	1	3	1	$2.6 \cdot 10^{-4}$	5	2.6	$4 \cdot 10^{-3}$	2.3	1	M3
E3(2)	1	3	1	$2.6 \cdot 10^{-4}$	5	2.6	$4 \cdot 10^{-3}$	2.3	1	M3

16:8, 12:8, 8:8, 12:6 and 9:6, in mm. The motivation behind the different geometries was to test if larger monoliths (i.e. 16:8 mm) could be produced. The M2 series is a set of five two-part molds with the same slot dimensions as the M1 series, but each mold consists in a top PTFE part and a bottom part out of PEEK joined together by 10 screws. The M3 series consist in five identical two-part molds made from PEEK with slots at a depth:diameter ratio of 16:8 mm. PTFE and PEEK materials were chosen for the molds given their chemical resistance against n-hexane.

The first three synthesis attempts (batches A1, A2, B1) failed to produce gels that sprung back. The sol produced in batch A1 did not gel, which was possibly due to the use of an HCl 1M solution that had deteriorated due to improper storage conditions or that was expired. A new acidic solution was produced and used for batch A2, which led to a successful gelation. However, extracting the gels from the molds M1 required using a tweezer as they were blocked in the slots. The extraction was not possible without substantial damage to the samples, which were discarded. The molds design was then improved by manufacturing the M2 mold series as two-part molds using PEEK at the bottom. The reason to use PEEK for the bottom part instead of PTFE lies in its higher resistance to creep compared to the later,[100,101] which may be an issue when assembling two parts with screws. The effectiveness of the molds M2 was tested

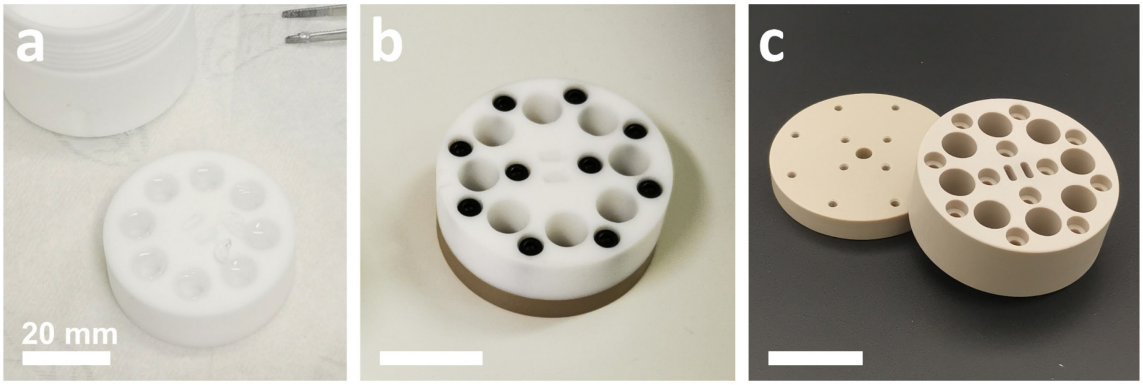

Figure 3.1 (**a**) Mold from the M1 series (PTFE, one-part) with 8 slots each at a depth and diameter of 16 and 8 mm, respectively. The slots are filled with water. (**b**) Mold from the M2 series (PTFE in white, PEEK in green, two-part) with slots at a depth and diameter of 12 and 8 mm, respectively. (**c**) Mold from the M3 series (PEEK, two-part) with slots at a depth and diameter of 12 and 8 mm, respectively. The scale bar is 20 mm in each panel. Panel (**c**) reprinted from ref.[102], CC BY 4.0 (https://creativecommons.org/licenses/by/4.0/)

with batch B1. This time, the molds permitted a flawless extraction of the gels that underwent a following solvent exchange and surface modification procedure. The amount of solvent was not controlled in batch A2, but was between 3.7 and 6.4 L per mol of TEOS (or per mol of SiO_2). The amount of TMCS was between 5.3 and 9.0 mol per mol of TEOS. The gels were dried at ambient-pressure and the resulting dry gels are shown in Figure 3.2a. The gels showed no SBE and their final volume was about 13 vol % of the mold volume in which they were casted. Small air inclusions (bubbles) were observed at the surface of the gels. The gels' outer surface and core were hydrophobic, suggesting a successful modification by TMCS. The absence of SBE in batch B1 was attributed to an incorrect concentration of the ammonia solution added in the 2nd step of the sol-gel process.

Batch B2 was produced using a corrected ammonia solution that was consistent with ref.[19] and all other quantities were kept the same as in B1. This time, the gels from B2 showed a non-negligible SBE during drying, resulting in bluish dry gels with a final volume about 21 vol % of the molds volume (Figure 3.2b). Small air inclusions were still visible at the bottom of the gels, which corresponded to the contact between the two parts of the molds. At the same location, some gels showed a reduced diameter that was possibly due to the deformation of the top part of the mold (PTFE) upon assembling the molds. All gels were monolithic and those casted in the mold with a depth:diameter ratio of 16:8 mm showed the overall highest quality among the five geometries. According to these results, the M3 set of molds was manufactured as 5 molds with the same depth:diameter ratio at 16:8 mm. Both parts of the molds were made from PEEK.

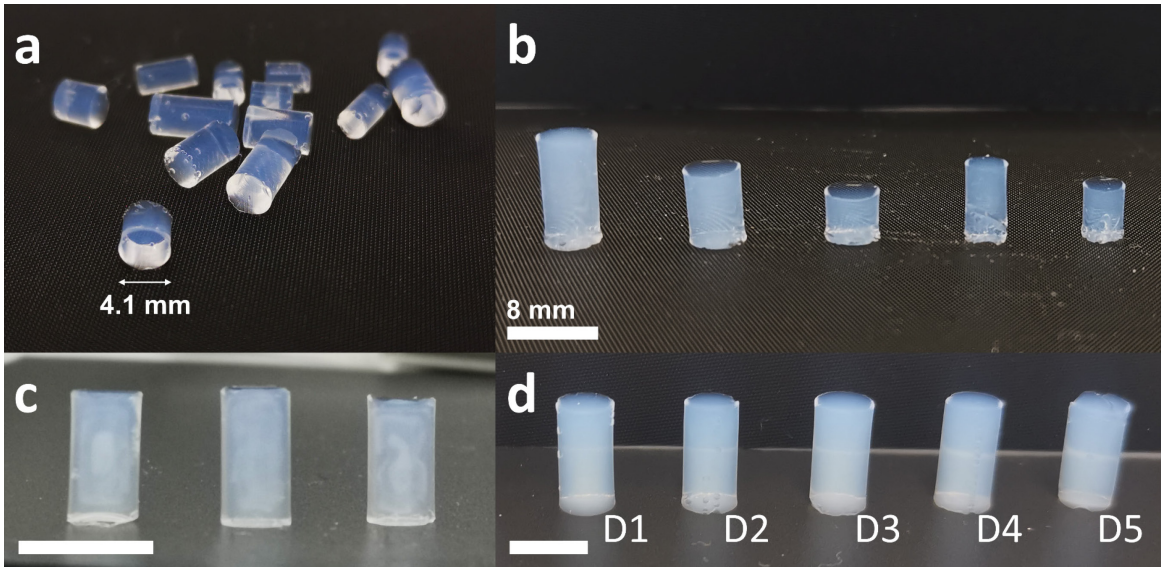

Figure 3.2 Digital pictures of dry gels prepared from different batches. (**a**) Several gels from batch B1 that did not spring-back. Air bubbles can be seen at the surface of the samples. The length scale is indicated for only one gel due to the perspective. (**b**) Five gels from batch B2. From left to right, the height:diameter ratio of the slots used to cast the gels is 16:8, 12:8, 8:8, 12:6, 9:6 in mm. (**c**) Three of the dry gels from batch C1 casted with the molds M3 (depth:diameter of 16:8 mm) that displayed a cloudy core. (**d**) Five gels from the batches D1 – D5 casted with the molds M3. The gel from D3 showed the highest spring-back and quality among this set with no cracks nor bubbles. The scale bar is 8 mm in panels (**b**-**d**).

Batch C1 was produced using the M3 molds with the objective to improve the SBE compared to batch B2. Two changes were made to the synthesis and casting steps in accordance to the experimental procedures reported by Hwang et al.[59,83] It was proposed that air bubbles form during gelation due to the vaporization of air dissolved in the gel at higher temperatures.[83] Thus, the solution was defoamed under slight vacuum after casting as an attempt to avoid that effect. This was done by inserting the molds in a desiccator and by pumping air out until the bubbling of the solution. The amount of solvent in the solvent exchange steps was also controlled, and the total TMCS content was adjusted to reach a TMCS:TEOS molar ratio of 1.7:1 as it has been shown that excess modification can have a detrimental effect.[59] The other synthesis conditions were identical to B2. The spring-back efficiency of five gels was evaluated by segmentation of in-operando μCT measurements (chapter 4) and was calculated as the ratio between the dry gel and the alcogel volume. It was on average 29.4 vol %. The gels still had air inclusions, but less than in batches B1 and B2. Some gels displayed a cloudy texture in their core (Figure 3.2c) that could not be explained or linked to a specific parameter of the synthesis. Finally, a large disk of 47 mm of diameter and ~10 mm of height was casted in a PTFE bottle to assess if it can produce a monolithic gel but the disk cracked already during the surface modification steps, and collapsed during drying.

TEM micrographs were acquired on one modified and one unmodified gel from batch C1 to assess the difference in re-expansion at the nanoscale upon silylation. The samples were ground into a fine powder and dry loaded onto TEM grids (Cu 300-mesh covered by a lacey carbon film) following the recommendation of ref.[103] The morphology of the ground specimen was observed using a JEM-F200 microscope (JEOL, Tokyo, Japan) at an accelerating voltage of 80 kV. Bright-field image were acquired by limiting a maximum the exposure of an area to the electron beam to alleviate beam damage. Figure 3.3 shows the TEM micrographs of the silylated and unmodified gels. A pear-necklace structure could clearly be seen in the silylated gel, consistent with previous observations in silica aerogels.[103–105] The micrographs of the unmodified gels revealed rather dense aggregates caused by the irreversible compaction of the structure during drying. The size of the silica nanoparticles in the modified gel was estimated in the software Fiji[106] by measuring the diameter of 40 particles in Figure 3.3a-c. An average diameter of 2.7 ± 0.7 nm was found.

Batches D1 – D5 were achieved in parallel with the motivation to investigate the influence of some parameters on the quality and spring-back of the gels. The synthesis route for those five batches were the same as C1 to the exception of the following points: D1 was not stirred during casting, while D2 – D5 were. D1 – D4 were not defoamed during casting, while D5 was. The TMCS:TEOS molar ratio of D3 and D4 was 1:1 and 4.5:1, respectively. D5 was produced the same way as C1 and was used as a control. Five dry gels issued from D1 – D5 are shown in Figure 3.2d. Stirring the solution during casting did not have an effect on the re-expansion and quality of the gel by comparing D1 and D2. The defoaming of the solution did not seem to have a significant impact on the amount of air bubbles in the gels by comparing D2 and D5. Gels produced at a TMCS:TEOS ratio of 1:1 (D3) showed the highest re-expansion and overall quality, compared to the higher ratios (D2 and D4). However, D3 dry gels did not show a substantial improvement of the SBE, as the gels volume was about 27 vol % of the molds volume.

Batch E1 was produced with the same procedure as D3, but the two parts of the M3 molds were attached more loosely together. The motivation was to asses if it results in a larger extent of air inclusions in the gel, since defoaming did not prevent the apparition of bubbles. Some molds leaked during gelation, and visual inspection of some gels revealed significantly more air inclusions than in batch D3. The samples from E1 were discarded.

Batches E2 and E3 had the same procedure as D3 and were achieved in parallel to create 2x40 gels. Upon casting, the two parts of the molds were assembled very tightly to prevent air bubbles in the gels. Overall, the dry gels from E2 and E3 were of the highest quality among all

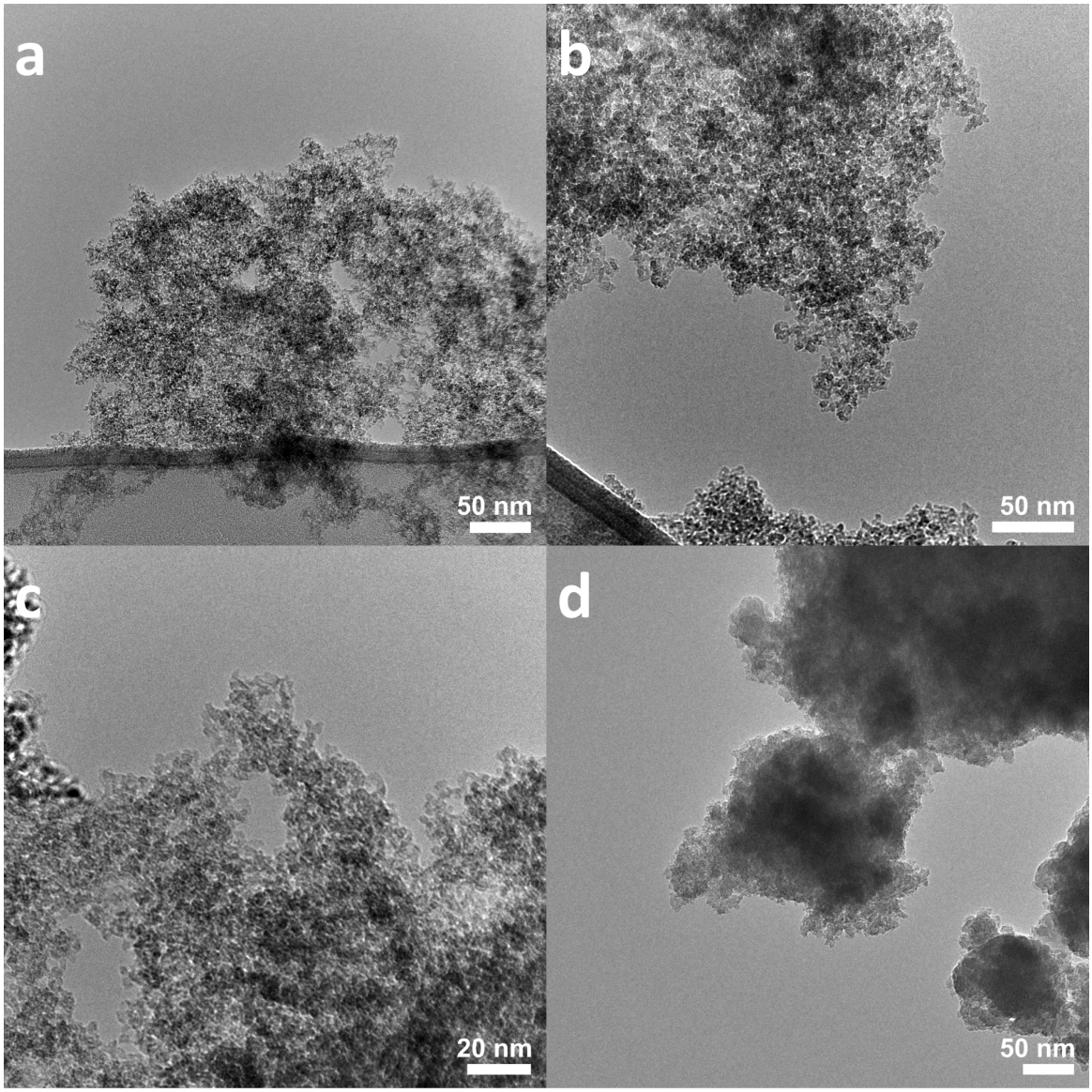

Figure 3.3 TEM micrographs of a modified gel from batch C1 (**a**-**c**) and of an unmodified gel from batch C1 (**d**). The porous structure of the modified gel is clearly visible, as well as the silica particles. In comparison, the unmodified gel appears much denser and the particles cannot clearly be distinguished. The scale bar is displayed at the bottom of each panel.

batches, although some samples still had air inclusions (Figure 3.4). Some samples also showed a reduced diameter at their bottom, it was believed to be caused by the deformation of PEEK upon too strong tightening of the mold parts together. Five gels from E2 and E3 were used for the experiments reported in chapter 6, and the spring-back efficiency of one gel was assessed by in-operando μCT at 26.5 vol %. An annealing treatment at 230 °C for 1 h of the gels from E2 and E3 did not degrade the quality of the gels and resulted in significant re-expansion (Figure 3.4). The total spring-back efficiency after annealing was assessed on one gel by μCT at 85.5 vol % (chapter 6).

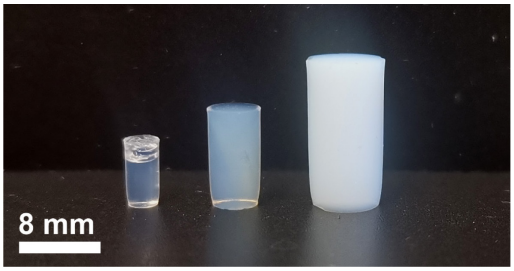

Figure 3.4 Digital picture of three samples produced from batch E2. From left to right: an unmodified dry gel, a dry gel and an annealed gel. Cracks are visible on the top of the unmodified gel, while the other two samples are monolithic without any visible defects. A slight reduction of diameter can be seen at the bottom of the three gels, presumably caused by the deformation of the molds during gelation.

This paragraph summarizes miscellaneous notes about the improvement of the synthesis procedure throughout the 13 batches. Before gelation at 50 °C, it was very important to close tightly the PTFE bottles in which the molds were inserted, otherwise the solution may evaporate significantly. To this regard, it was found best to add about 1 mL of EtOH in the PTFE bottles before inserting the molds, which acted as a buffer to prevent evaporation of the solution. Another good practice was to cast a precise amount of solution in the molds to create a convex meniscus at the top of the mold. Some amount of solution irremediably evaporated upon gelation and the gels shrank slightly due to syneresis. As a result, the convex surface at the top of the gel flattened to a relatively even surface that was optimal for mechanical tests. Note that this was relatively difficult to achieve since very slight tilting of the molds during the procedure led to the spilling of the solution. Moreover, forming a convex meniscus was easier to do with the PEEK molds than with the PTFE ones, as the contact angle between the solution and PTFE was rather low, leading to spreading of the solution on the mold surface. Lastly, disassembling the two-part molds after gelation takes 1–2 min and to prevent premature drying of the gels in the meantime, ethanol was splashed regularly on the top surface of the molds to keep the samples wet.

Despite the attempts to improve the spring-back efficiency upon APD, the maximum re-expansion was relatively low when compared to the synthesis route employed by Zemke et al.[19] While the spring-back efficiency was not explicitely reported in Zemke's publications, it could be estimated to be at least 60 vol % based on the volume of a dry TMCS-modified gel (542.4 mm^3) and on the volume of the molds (1.5 x 1 x 0.6 cm) reported in ref.[19] Batches B2 – E3 were achieved using the same procedure in the 1st and 2nd step of the synthesis as in ref.[19] (Table 3.1), suggesting the difference in SBE was not related to the sol-gel synthesis. The different shape and dimensions of the specimen was also not believed to be responsible for such a difference in the re-expansion. One possible explanation could be different temperature

and humidity conditions during the sol-gel synthesis. Another explanation could reside in the TMCS:TEOS molar ratio, which was not controlled in the original procedures.[18–20] However, the investigations on the effect of the TMCS content from batches D2 – D4 suggested that it did not have a large impact on the SBE within the tested values.

The substantial re-expansion of the gels upon annealing allows to rule out the possibility that the SBE was hindered by insufficient silylation of the gels, since siloxane bonds created by condensation between surface silanol groups would not be affected by heat treatment. On the contrary, this volume recovery suggested the presence of residual hexane and/or entanglement of the silica clusters (see chapter 6). Residual liquid would likely be confined in the smallest pores where it could not evaporate completely during drying, resulting in residual stress on the solid networks that would prevent a complete re-expansion. To this regard, a possible explanation for the different SBE behaviors could lie in the pore size of the gels, the samples produced in this thesis having a smaller pore size than those produced in Zemke's work.

In conclusion, high quality silica aerogels could be produced by an iterative process throughout several batches produced with different synthesis conditions, molds, surface modifications and post-drying thermal treatment. Although the spring-back efficiency of the dry aerogels was limited, the samples endured the drying shrinkage adequately resulting in monolithic and almost flawless pieces. Moreover, the aerogels conserved their monolithicity upon further re-expansion by thermal annealing. While air inclusions could not be completely avoided, they were reduced by developing better molds and by adapting the casting procedure. In this thesis, defoaming the solution prior to gelation did not seem to have a significant impact on the presence of air inclusions. Further improvement of the molds could help increasing even more the aerogels quality and should be of general interest. The effect of the TMCS:TEOS or TMCS:SiO_2 molar ratio on the spring-back effect was not major for the produced samples but should be systematically reported in the literature to enhance reproducibility of the experiments.

3.2 Data management

All samples and measurements were digitally reported in the internal sample database of the Max Planck Institute of Colloids and Interfaces: https://webdb02.mpikg.mpg.de/sampledb/ in accordance to the rules of the institute. This database is not in open access. The samples recorded on the database consist of a unique sample ID, a custom sample tag, the creator of

the sample, group leader, record creation date, sample creation date, the species of the sample, the storage location and a short description of the sample. The measurements recorded on the database share a similar structure with additional details on the device used for the measurement.

While the sample database contains all the official records, I have documented all my research throughout my PhD on another medium, due to the limitations of the sample database and other tools. I chose to work on a OneNote notebook as it proved to be, in my opinion, the most versatile digital tool to organize text, tables and images into sections and pages. During the first part of my PhD, I documented most of my work on a physical notebook that I then reported in my digital notebook. The second part of my PhD being mostly computational, I reported directly my observations and findings in the digital notebook. The notebook is organized into the following sections:

1) README: information for external readers, list of abbreviations.
2) Meetings: content and outcomes of each meeting.
3) Samples: synthesis routes and created samples.
4) Experiments: measurements/tests with limited significance.
5) Measurements: parameters, conditions and some discussion on the main measurements.
6) Analysis: discussion, interpretation and general notes on the results of the syntheses or measurements. Overall organized by method.
7) Python: external documentation on the python scripts developed during my research, the changes and updates of each script is organized by versions of the code. The pages in this section also contain some extent of discussion.
8) Conferences: reports of conferences/seminars/workshops.
9) Others: miscellaneous notes notably on some admin, hardware and some life-pro-tips.

Each section contains a set of pages that are labelled with the creation date and a custom identifiant. When a sample or measurements appears on a page, its link to the sample database is provided. Additionally, the records of all samples and measurements on the database point towards the latest version of my digital notebook via a link to a directory internally available on the institute servers.

All data are stored and archived on different internal servers of the institute. This includes data generated by any measurement and data generated by processing or modeling a dataset. In accordance to the code of good scientific practice, all data linked to a given

publication are grouped and archived on a data repository. The data linked to the first[102] and second[107] publication are archived on the Edmond repository here: https://doi.org/10.17617/3.OYI3T9. The data linked to the submitted manuscript in chapter 6 are archived on the Edmond repository here: https://doi.org/10.17617/3.MAZXUW.

3.3 AI tools

The author discloses the limited use of DeepL translator in this dissertation to translate some words from French to English, and to assist on the translation of the abstract from English to German. No other artificial intelligence tools were used.

3.4 Review of characterization methods

3.4.1 X-ray micro-computed tomography

This section provides the basic working principle of X-ray micro-computed tomography (μCT), giving an overview on the underlying physical mechanisms, its applications and limitations. An emphasis is given on lab-source μCT instruments. X-ray computed tomography (CT) is an imaging method providing morphological information of an object, allowing to investigate its shape and internal structure via the use of penetrating radiations. The final data generated by such method consists of a stack of consecutive digital images called slices that form the 3D volume of the measured object. CT takes advantage of the low absorption of X-ray radiations through materials made of elements with a low to medium atomic number.[108] Thus, one predominant field of application is the characterization of biologic materials (invertebrates,[109] teeth,[110] bone,[111] fungi,[112] biofilms[113]), but CT also sees applications in geology,[114] batteries[115] and cement-based materials.[116] CT methods are distinguished by their achievable resolution: conventional CT provides a resolution in the millimeter range (0.1 mm and above), μCT refers to resolutions in the micron range (0.1 μm and above) and nanoCT goes down to resolutions at ca 10 nm.[108] The working principle of the three CT methods is similar, and unless mentioned otherwise, the rest of this section details these methods indifferently. CT generally consist of three steps: acquisition, reconstruction and segmentation.

The acquisition step is the measurement by itself where images of a specimen are recorded. A typical CT instrument consists of an X-ray source, a rotating stage and a detector (Figure 3.5). An alternative configuration also exists, in which the X-ray source and detector

rotate around a stationary sample stage. During acquisition, a series of images are taken at different angles by shooting X-rays at a target. The images are called projections or radiographs and are formed by the light transmitted through the specimen upon irradiation. There are two configurations of CT instruments, the parallel beam and the cone beam geometry, the latter is shown in Figure 3.5. Generally, parallel beams can only be achieved using synchrotron radiations, which is normally associated with nanoCT methods as it permits to reach higher resolutions.[117] Cone-beam geometry is achieved with lab-source CT instruments relying on X-ray tubes as a source of radiation, which comprises a cathode and an anode in a vacuum chamber. Upon application of a voltage, electrons are emitted and accelerated from the cathode towards the anode. The resulting emission of X-rays from the anode target (e.g. tungsten) are narrowed down by collimators into a conical beam directed at the sample.[108] The resolution of a CT measurement relying on the cone-beam geometry depends on the source-to-object distance (SOD) and the source-to-detector distance (SDD). Higher resolutions are achieved upon decreasing the SOD and increasing the SDD.[118]

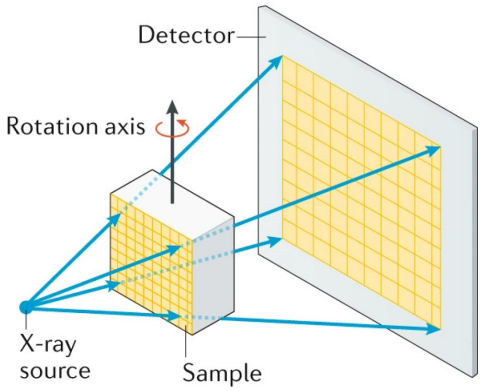

Figure 3.5 Illustration of the acquisition of a CT scan using a cone beam setup. The X-ray source is directed at a sample under rotation and the projections are acquired on a detector. Reprinted from ref.[108] with permission from Springer Nature.

The detector of a CT instrument records the transmitted intensity and transforms it into a digital image (e.g. in 16-bit tiff format). This is typically achieved through the use of a scintillator that converts X-rays into visible light, which is then converted into an electric signal for image generation.[108] A projection thus consists in a 2D array of pixels, each pixel having a certain intensity referred to as the gray level or gray value.

When light is shined at an object, its transmission through that object depends on the light energy and on the properties of the material. That relationship is given by Lambert-Beer's law:[118]

$$I(E) = I_0(E)e^{-\mu(E)d}, \tag{3.1}$$

where I is the transmitted intensity of the incident beam, E is the beam energy, I_0 is the initial intensity of the incident beam, μ is the linear attenuation coefficient of the material and d is the thickness of the material along the beam path. The gray value in the projections is proportional to the transmitted intensity I. The transmission of light through an object does not only depend on its thickness, but on the intricate property of the material to absorb light, which is measured by the attenuation coefficient μ. The latter depends on the energy of the beam and on the materials composition, notably on the apparent density and atomic weight[119] and its values are tabulated in the literature.[120] According to eq. (3.1), the CT projection of a pure specimen (e.g. water) with a constant thickness would be seen as a monochrome image (constant gray value). However most specimen show variations in both thickness and composition. In multi-component materials, the average linear attenuation coefficient along the beam path is given by the weighted sum of the attenuation coefficient of each individual component. The Lambert-Beer's law becomes:

$$I(E) = I_0(E)e^{-\sum_i \mu_i(E)d_i}, \tag{3.2}$$

with μ_i the attenuation coefficient of the species i and d_i the length of the corresponding species along the beam path.

The variations in attenuation coefficient and thickness result in different brightness and contrast in the projections, as illustrated in Figure 3.6 with the example of a walnut. In the walnut projections, the area surrounding the walnut appears bright (high gray value) because the attenuation coefficient of air in the energy range of X-ray light is essentially zero. The shell and flesh of the walnut appear darker (low gray value) because of a partial absorption of X-rays. While CT projections already provide some extent of morphological information via the contrast in transmission from the different parts of the walnut, the reconstruction of the scan enables the recovery of the spatial distribution of the attenuation coefficients of the sample.

The reconstruction step corresponds to the computation of a stack of slices from the series of projections. The mathematical relation between the projections and the slices is described by the Radon transform.[121] The description of Radon transform and the reconstruction algorithms go beyond the scope of this section and will thus not be discussed. A summary of the corresponding computational approaches can be found in the excellent review of CT by Withers et al.[108] The reconstructed stack of slices forms a 3D array of voxels (cubic volume elements) with the voxel size corresponding to the resolution of the CT measurement. The gray value of a voxel is independent of the specimen thickness and is directly proportional to the attenuation coefficient of the part of the sample located within that

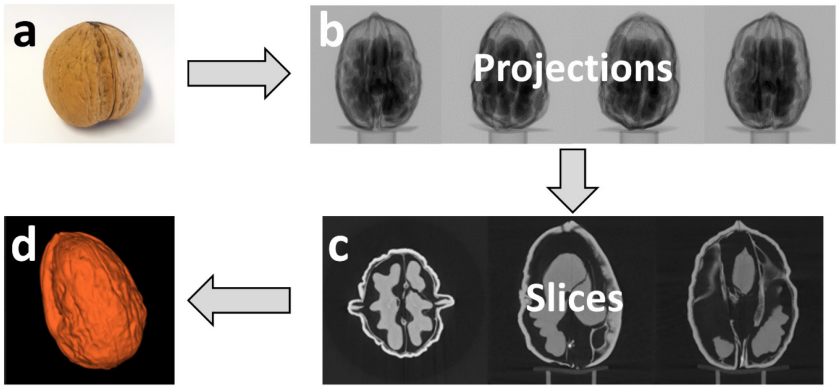

Figure 3.6 Example of a complete μCT procedure on a walnut sample (**a**). Acquisition of a series of projections (**b**), reconstruction into slices (**c**) and segmentation in a 3D visualization software to generate a 3D volume (**d**). The three slices shown in panel (**c**) correspond to three perpendicular cross-section planes across the sample. Panels (**b**-**d**) reprinted from ref.[122], CC BY 4.0 (https://creativecommons.org/licenses/by/4.0/).

voxel. Given the relationship between the transmitted intensity and the attenuation coefficient, the contrast in the slices is essentially inverted compared to the projections (Figure 3.6c).

At this point, it is important to clarify the differences between monochromatic and polychromatic radiations. Besides the geometrical configuration of the beam, synchrotron-source and lab-source CT instruments differ by the energy spectrum of the associated radiations. Whereas synchrotron enables the production of highly monochromatic X-rays,[123] X-ray tubes generate radiations with a broad range of wavelengths (polychromatic).[108] Therefore, the data generated using a monochromatic source are related to the physical attenuation coefficient of the material, which notably allows elemental analysis by correlating the data with tabulated values.[120] This is generally not possible with laboratory CT instruments, due to polychromatic radiations. The majority of detectors do not allow the differentiation of photons energy, thus the transmitted intensity recorded on the detector represents a mix of the intensity of light at different wavelengths.[124] In that case, the gray values in the reconstructed slices are proportional to the reconstructed attenuation coefficient (RAC), which is not a physical value. However, recent advances in CT detectors have uncovered the possibility of performing 3D chemical analysis using laboratory μCT instruments.[125] This method is referred to as spectral CT and can essentially generate a 4D dataset with three spatial dimension and one energy dimension. In 2021, the first commercial spectral CT instrument was brought to the market by TESCAN.[126]

Image segmentation can be considered as the last step of a CT experiment and allows to extract quantitative information from the reconstructed volumes. Segmentation is the process of creating one or more masks from an image, where a mask is a binary image with the same dimensions as the original image. In tomography measurements, a mask is a 3D image and is

more commonly referred to as a region of interest (ROI). Taking the example of the walnut (Figure 3.6d), the ROIs could be: 1) the background (air), 2) the sample holder, 3) the walnut shell and 4) the walnut flesh.

Segmentation can be performed via manual labelling of the voxels, automatic techniques or deep learning algorithms. Automatic segmentation techniques are based on different features of the dataset and ROIs. A popular method is the Otsu thresholding,[127] which proceeds by separating the gray values of the dataset into two classes by minimizing the variance of the gray value histogram. Other techniques are based on the connectivity of the labeled voxels, allowing for example to split the voxels belonging to the surface of the walnut flesh from those belonging to the core. The advent of deep learning algorithms for image processing has substantially facilitated the segmentation of large and complex dataset,[128] which beneficiates from the steady improvements of computational power and algorithms efficiency.

Basic morphological information that can be computed from the derived ROIs includes the ROI volume, its surface area, and the minimum/maximum thickness of the volume. Examples of advanced morphological characterization are distance maps (minimal distance between a labeled voxel and the background) and porous microstructure analysis to derive e.g. pore size distributions. The segmentation and related analyses can be performed with custom image processing routines, but is usually carried out using 3D visualization software such as Amira,[129] Dragonfly[130] and Fiji.[106]

Several artifacts can appear upon reconstruction of μCT projections and it is important for the users to be aware of them to differentiate real and artificial features in the specimen. Some CT artifacts can be avoided by selecting suitable acquisition parameters and by ensuring the sample remains static during scanning.[108] Geometrical correction routines are generally included in reconstruction software and allow to correct for small displacements of the sample and axes.[131] Beam hardening is the most common artifact in lab-source CT instruments and is relatively difficult to correct completely (Figure 3.7a). It is caused by the non-linear attenuation of radiations with different wavelengths across the specimen thickness.[132] Within the energy range of radiations emitted from X-ray tubes (30 – 300 keV),[108] the attenuation coefficient of most materials decreases as the light energy increases, not accounting for absorption edges.[132] Therefore, soft X-rays (low energy) are absorbed preferentially which results in a shift of the energy spectrum of the transmitted light to higher energies: the beam hardens.[131] Beam hardening depends on the thickness of the material along the beam path as in eq. (3.1), leading to a relatively higher intensity recorded along the sample's core than along its edges.[132] Upon reconstruction, this effect is propagated to the slices and results in an apparent lower

attenuation coefficient in the specimen core (Figure 3.7a). Another common artifact in lab-source CT systems is the anode heel effect, which is manifested by the presence of an intensity gradient along one axis of the cone beam.[133] As electrons accelerated from the cathode reach the anode material, they interact with the latter at different depths. The X-rays generated deeper in the anode are more attenuated by the anode material than those generated close the anode surface.[134] This creates X-rays with different energy spectra along the cathode-anode axis, resulting in apparent variations of the gray values in μCT projections as illustrated in Figure 3.7b, which are also propagated to the slices. The variations in the slices' gray values caused by CT artifacts could be misinterpreted as a density change, and can affect negatively the segmentation procedures relying on thresholding methods.

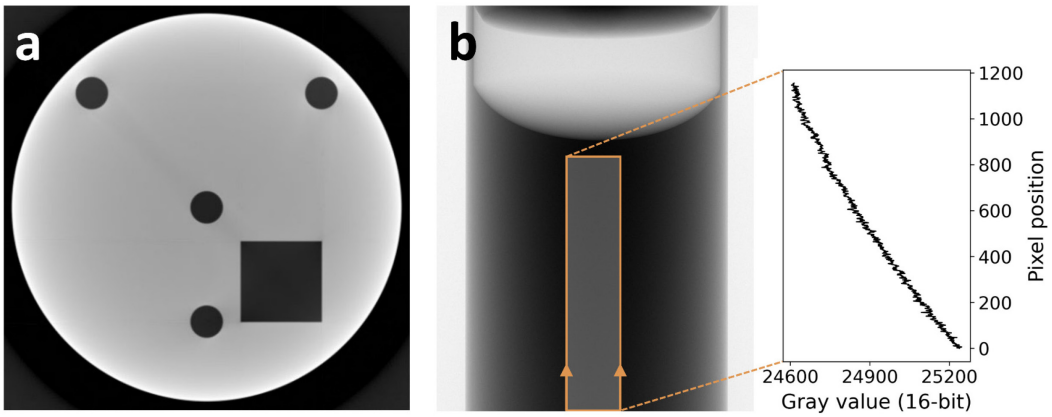

Figure 3.7 (**a**) Beam hardening artifact in a vertical slice. (**b**) Anode heel effect in a μCT projection of a water tube, the inset graph shows the gray values vertical profile within the depicted box. Panel (**a**) reprinted from ref.[131] with permission from SAGE Publications.

Although CT and μCT methods are interesting to characterize materials with structural features in the millimeter to micrometer range, they are unable to resolve the structure of silica aerogels whose characteristic size is below one micron. There is little literature on μCT measurements applied to aerogels. Zhang et al. performed μCT scans at a 20 μm resolution to characterize the macropores size distribution in hybrid manganese oxide aerogels.[135] Partow et al. also evaluated the macropores in lignin-based aerogels.[135] It is worth noting that in the latter study, the authors reported performing nano-CT measurements while the maximum resolution of the CT instrument used in that study is 0.5 μm,[136] thus qualifying the technique as μCT.

Quantitative imaging analysis of μCT data is also possible –to some extent– using lab-source CT instruments. Phillips et al. could notably calculate approximate density values of ceramics by analyzing the gray values in the slices.[137] Similarly, Borisenko evaluated density gradients in divinyl benzene aerogels[138] and during the gelation of TEOS-based gels[139] for applications as laser targets. Despite the polychromatic nature of X-ray radiations, some extent

of chemical analysis can be performed with lab-source μCT instruments. This will be further explored in chapters 4 and 5, which describes the application of μCT to silica gels during drying.

3.4.2 Small-angle x-ray scattering

Small-angle X-ray scattering (SAXS) is a non-destructive method used to probe the structure of materials at the nanoscale[140] and can notably complement CT methods when higher resolution is required. It sees applications for several materials and is especially well-suited for investigating disordered or hierarchical materials and two-phase systems.[141] Notable examples include macromolecules[142] and colloidal suspensions,[143] bone,[111] microporous ceramics[144] and aerogels.[145–147] Synchrotron-source provides the possibility to perform measurements at ambient pressure thanks to the high flux of X-ray radiations that mitigate air absorption.[123] This aspect, combined with the non-destructive nature of X-ray radiations, enable in-operando nanostructural characterization of materials under different stimuli and processes such as polymerization[148] or mineralization.[149] In the aerogel community, in-operando SAXS has been used to evaluate the evolution of specimens' structure during gelation,[150] drying[18,20] and during mechanical tests.[39]

X-ray scattering is the interaction of light with the electrons within a material. SAXS and wide-angle X-ray scattering (WAXS) are more precisely based on the elastic scattering process (without energy loss) of X-ray radiations with the electrons of an atom.[141] Upon irradiation of an object with an X-ray beam, each scatterer (electrons) in the beam path can interact with the incident light and emit a spherical wave. The interference of each individual spherical waves generates a 2D scattering pattern that is recorded on a detector (Figure 3.8).

The difference between the incident beam direction and the scattered beam is expressed as a function of an angle 2θ and is characteristic of the distances between the scattering centers,[140] which in a two phase system can be understood as the distance between basic structural units.[147] The intensity recorded on the detector is proportional to the density of the scattering centers within the probed volume and to a property of the material called scattering length density.[141] In the case of X-ray scattering, the scattering length density is proportional to the electron density of the material,[151] which corresponds to the probability of finding an electron at a given position. The scattering intensity in multicomponent materials arises from the different electron densities of its individual components.

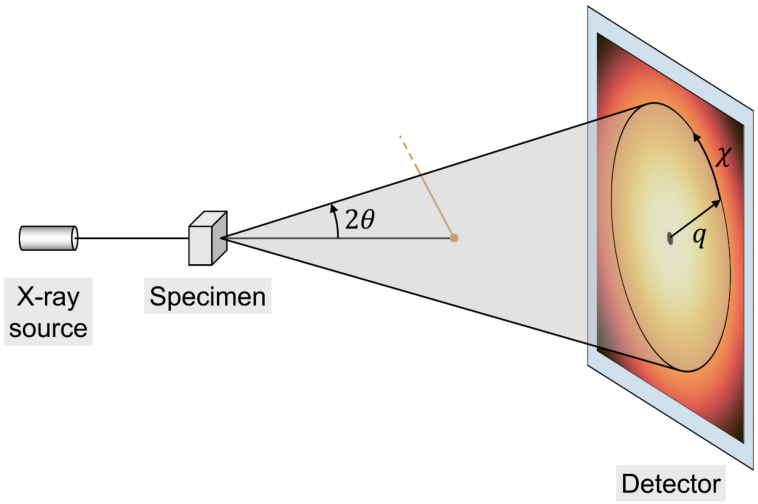

Figure 3.8 Illustration of a SAXS experiment. A focused X-ray beam is emitted from a source towards a specimen. The beam interacts with the specimen, generating a cone of scattered X-rays that are recorded on a detector. Transmitted radiations are blocked with a beamstop (in orange). The scattering angle 2θ, scattering vector q and azimuthal angle χ are depicted.

The change in direction of the beam upon scattering is expressed with the modulus of the scattering vector q rather than the angle 2θ, which is defined as:[152]

$$q = \frac{4\pi \sin(\theta)}{\lambda} \tag{3.3}$$

where λ is the incident light wavelength. The scattering vector is a coordinate in the reciprocal space, thus the inverse of the scattering vector represents a distance in the real space. Specimen with an isotropic structure generate scattering patterns with a rotational symmetry, as the one illustrated in Figure 3.8. Anisotropic structures result in intensity variations along the azimuthal direction of the scattering patterns. A typical example is the orientations of the chains in polymers under tensile test, which create a strong anisotropy at the nanoscale.[153] In order to analyze X-ray scattering data, the q spacing need to be calibrated from the detector's pixels array, which is achieved by measuring standards.[141] In a similar manner, the scattering intensity can be absolutely calibrated using a standard[154] and by normalizing the intensity by the specimen thickness among other things, in which case the scattering intensity is expressed in absolute units (cm^{-1}).[155] Absolute calibration allows to extract more quantitative information from SAXS data and also allows comparison with data acquired with different instruments.[141] After calibration, the intensity in the scattering patterns is expressed as $I(q, \chi)$, where χ is the azimuthal direction in the scattering patterns.

Aerogels created by sol-gel process have an isotropic structure,[151] thus the analysis of SAXS measurements is performed on the scattering profiles $I(q)$ that are derived by integrating $I(q, \chi)$ over χ. Figure 3.9 shows a scattering profile characteristic of an aerogel. The variations

of intensity over q arise from the electron density difference between the aerogel solid skeleton and the air confined in the pores at different length scales.[140] The small q region (small-angle) corresponds to large objects and the high q region (wide-angle) corresponds to small objects. The scattering profile of aerogels can be divided into three characteristic length scales. At small q values, the aerogel structure is essentially homogeneous, resulting in a constant scattering signal (plateau in the small-angle region in Figure 3.9).[145] At an intermediate q range after the plateau, structural inhomogeneities are evidenced by a decrease in the scattering intensity with increasing q values. In silica aerogels, the scattering intensity over this q range is described by a power-law decay with an exponent $-D_f$ called the fractal dimension. Over the corresponding length scale, the structure of silica aerogels is representative of a fractal geometry with a dimension D_f.[156] Fractals are geometric shapes that appear similar at different length scales.[143] Romanesco broccoli is a good example of an everyday item displaying a fractal geometry. The fractal dimension gives information on the distribution of the silica skeleton in space, and can be related to the aggregation mechanisms during the gelation.[143,146] The fractal range extends from $q \approx \xi^{-1}$ to $q \approx a^{-1}$, where ξ is called the mean cluster size or correlation length and a corresponds to the size of the primary particles constituting the clusters. The mean cluster size is the critical length above which the local density is constant (homogeneous structure).[156] The crossover at $q \approx a^{-1}$ marks the end of the fractal region as the scattering intensity drops at larger q values. This scattering region is called the Porod's region and the corresponding signal arises from the abrupt interface between the particles and the gas phase in the pores.[147] Within this q range, the scattering intensity typically evolves as $I(q) \propto q^{-4}$, where the -4 exponent

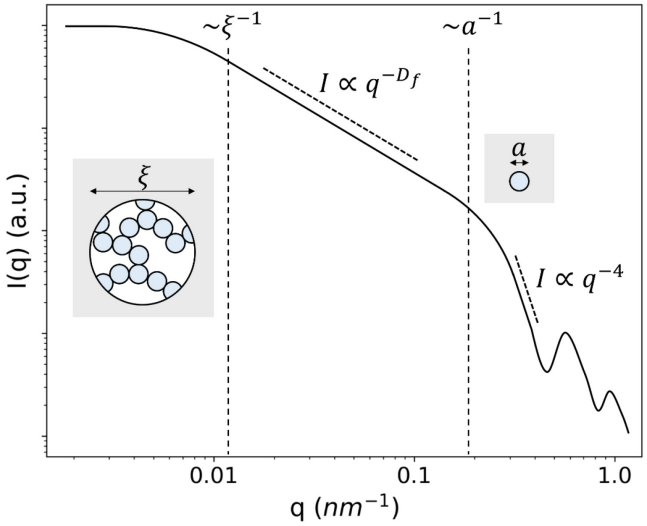

Figure 3.9 Log-log plot of the scattering profile $I(q)$ typical for an aerogel displaying a fractal structure. The insets depict the mean cluster size ξ and the particle size a. The fractal and Porod regions are highlighted. Adapted from ref.[156], CC BY 4.0 (https://creativecommons.org/licenses/by/4.0/).

indicates a sharp surface of the particles.[152] At larger q values ($q \approx 10$ nm^{-1}), the signal arises from the molecular structure of the material[145] which is defined as wide-angle X-ray scattering (WAXS).

The analysis of scattering data can be particularly complex, especially in in-operando measurements that create time-series of scattering profiles $I(q)$. Alternatively, modeling of the SAXS data has been shown to be a valuable way to compute advanced information on the nanostructure of aerogels. By modeling SAXS data of silylated silica gels dried in-operando, Zemke et al. notably found non-negligible variations in the primary particle size during drying and spring-back possibly pointing towards a contraction and relaxation of the structure beyond the fractal range.[20] Omote & Iwata were able to simulate the 3D structure of a silica aerogel from ex-situ SAXS modeling.[157] SAXS measurements are sometimes complemented with atomic force microscopy (AFM)[158] and TEM[105,150,157,159] to visualize the morphology of the structure with a resolution down to a few nanometers and even lower. Chapter 6 reports the application of SAXS/WAXS to silica aerogels under uniaxial compression.

3.4.3 Uniaxial compression tests

In materials science, the mechanical properties of a material have to be considered in the conception, processing and application of a component. When measuring the mechanical properties, the choice of the solicitation method is always driven by the component's design: a jute rope is measured under tension (tensile test), a steel beam under flexion (flexural test), a concrete cube under compression (compression test).[160] In the literature, monolithic aerogels are most often manufactured as cylinders[41,67,68,161,162] or disks.[53,59,89] Their mechanical properties are thus commonly measured uniaxial compression tests, though three-point bending tests are sometimes used.[40] This section will discuss the basics of uniaxial compression tests and present some characteristics of materials during deformation.

The specimen shape has a substantial influence on the stress distribution and fracture mode, which is particularly well-known for concrete samples.[163,164] In general, cylindrical samples with an aspect ratio (length over diameter) of 2 are best suited for compression.[163–165] Samples with such a geometry tend to experience mechanical failure by cracking,[163] while cylinders with a smaller aspect ratio and cubes are subject to shear fracture or crushing.[163,165] To this regard, Darvell emphasized the difficulty of comparing the compressive strength of materials measured under different conditions, with different specimen designs.[165]

Compression tests like tensile tests can be carried out in two modes: force controlled or displacement controlled. The latter seems to be exclusively used in the aerogel community, [40,54,68,90] although there does not seem to be a specific reason. Andreev et al. reported in cyclic fatigue tests that displacement controlled mode led to a less brittle failure in silica refractories than the force controlled mode.[166] It will be assumed for the rest of this section that measurements are performed on a cylindrical sample in the displacement mode.

In uniaxial compression tests, a specimen is placed between two plates whose displacement is controlled by a motor and the force on the plates is monitored by a load cell. Most commercial instruments allow to perform compression, tensile and flexural tests with a single machine. The values computed during a compression test are the stress and strain that are defined as follows. The engineering stress in the material is $\sigma = F/A_0$, where F is the force and A_0 is the initial cross-section area of the specimen. The axial strain is $\varepsilon_{\mathrm{ax}} = (h - h_0)/h_0$, where h is the height of the specimen during the test and h_0 is its initial height. The initial height is usually defined by pre-loading a specimen until a noticeable change in the force is recorded. The transverse strain is $\varepsilon_{\mathrm{tr}} = (d - d_0)/d_0$, where d is the sample diameter and d_0 is its initial diameter. The force and height of the specimen are given by the load cell and motor displacement from which the stress-strain curve can be calculated. If the material is subject to large deformations, it is preferable to calculate the true stress $\sigma = F/A$ by using the actual cross-section area A of the specimen during loading, as it may vary significantly.

Mechanical properties of a specimen are derived by interpreting the stress-strain curves. At small deformation, the relationship between stress and strain is given by Hook's law: $\sigma = E\varepsilon$, where E is Young's modulus and ε is the axial strain. Young's modulus is a measure of the deformation of a material under stress in the elastic regime and is an important property to consider in materials selection process. It is generally measured upon applying small load or strain. Stiff materials such as ceramics and metals have a Young's modulus within 10 – 10 GPa, while elastomers have much lower values at 0.1 – 100 MPa.[160] When compressed, a specimen may exhibit a lateral contraction or expansion that can be characterized by Poisson's ratio: $\nu = -d\varepsilon_{\mathrm{tr}}/d\varepsilon_{\mathrm{ax}}$. Most materials have a positive Poisson's ratio, i.e. expand laterally when compressed axially, but can also have negative ratios depending on materials macro- and micro-structure.[43,167] The strength of a material is defined as the stress at which mechanical failure occurs and is referred to as compressive strength in compression tests. Accordingly, the maximum deformation at the rupture is called the fracture strain.

Materials can have different response upon unloading that are characterized as elastic, viscoelastic or plastic behaviors. The deformation is said elastic if a specimen returns to its

original shape upon removing the load, as illustrated in Figure 3.10a.[160] In that case, the final strain is 0 % and the path along the stress-strain curve during unloading is the same as during loading. On the other hand, the presence of a hysteresis (closed loop) in the stress-strain curve is characteristic of viscoelastic deformations and indicates that energy was dissipated in the material during the deformation (Figure 3.10b). This energy dissipation can notably occur through friction (in rocks)[168] or dislocations (in plastics and metals).[169] If the specimen does not recover its original shape upon unloading, the deformation is said plastic and is illustrated in Figure 3.10c.

Silica aerogels display viscoelastic or plastic responses in uniaxial compression tests.[41,68] Some authors have investigated the impact of silica aerogels' apparent density on their mechanical properties, like Young's modulus,[40,41,68] compressive strength,[40,170] fracture strain,[67,68] and strain recovery.[68,171] In general, less dense aerogels are more compressible (higher fracture strain), show higher compressive strength and lower Young's modulus. Interestingly, Sivaraman et al.[68] observed a non-linear dependency of the strain recovery with aerogels' density that was the highest for gels at around 0.1 g cm^{-3}. The application of uniaxial compression tests to silica aerogels is presented in chapter 6.

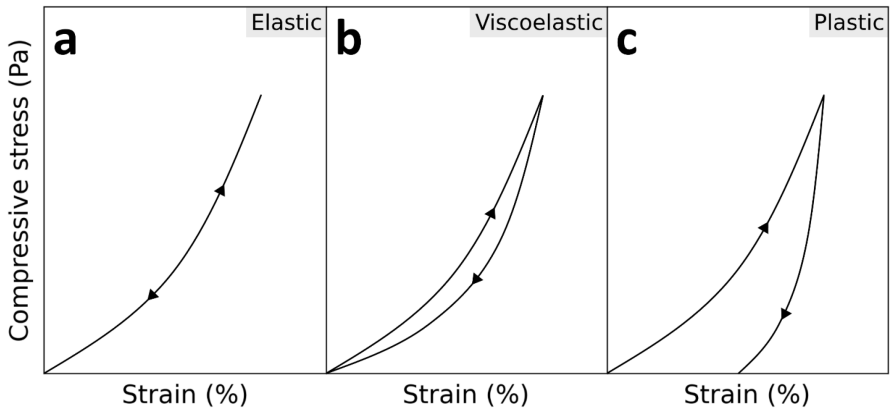

Figure 3.10 Illustration of different kind of deformations in the stress-strain curves from uniaxial compression experiments without fracture. (**a**) In elastic deformation, the loading and unloading paths are confounded and the specimen returns to its original shape after unloading. (**b**) Viscoelastic deformations are characterized by a hysteresis in the stress-strain curve.[168] (**c**) Plasticity corresponds to irreversible deformations after unloading.

4 In operando μCT imaging of silylated silica aerogels during ambient pressure drying and spring back

The content of this chapter is based on the published article:

Title	In Operando μCT Imaging of Silylated Silica Aerogels during Ambient Pressure Drying and Spring-Back
Authors	Julien Gonthier, Tilman Rilling, Ernesto Scoppola, Fabian Zemke, Aleksander Gurlo, Peter Fratzl, Wolfgang Wagermaier
Journal	Chemistry of Materials
Publisher	ACS Publications
Publication date	11th of September 2023
Reference	Chem. Mater. **2023**, *35* (18), 7683–7693
DOI	https://doi.org/10.1021/acs.chemmater.3c01451
Author contributions	Conceptualization and methodology: J.G., P.F., and W.W.; design of the experimental setup: J.G., F.Z., and W.W.; software: J.G. and E.S.; formal analysis: J.G.; investigation and data curation: J.G. and T.R.; writing−original draft and visualization: J.G. and W.W.; writing−review and editing: J.G., T.R., E.S., F.Z., A.G., P.F., and W.W.; supervision: P.F. and W.W.; project administration: J.G., W.W., and P.F.; funding acquisition: A.G. and W.W.

The following co-authors made notable contributions: Tilman Rilling performed the μCT acquisitions for half of the samples; Ernesto Scoppola wrote a python code to compute the height and diameter of the specimen based on cross-section area profiles.

4.1 Background

Only few studies have tackled the conditions of emergence of the spring-back effect and result in structural and compositional changes, while the impact of the synthesis, aging, surface modification, and drying on the spring-back efficiency has been exhaustively studied.[14,49,56,76,77,79,81,83] It is difficult to quantitatively track structural and compositional variations during drying as it generally requires a controlled environment under ambient conditions and the use of non-destructive methods. To this regard, X-ray imaging techniques like SAXS and μCT are well suited for measuring dynamic processes at ambient conditions and provide enough space for experiments on gels contained in a drying chamber. Where SAXS provides structural information from 2 to 500 nm,[147] μCT can generate 3D volumes of samples of various sizes with a maximum resolution of about 1 μm. Although elemental analysis is technically not possible with lab-source CT instruments (chapter 3.1), it is possible to extract some quantitative compositional information of a specimen from the collected data.[137]

This chapter reports the principles and results of an in-operando μCT quantitative imaging workflow to investigate the changes in the shape and average composition of TMCS-modified and unmodified silica gels during APD. The calculated silica skeleton, pore liquid and gas during drying provide valuable information on the kinetics of the APD process and spring-back. The drying shrinkage and SBE are correlated to the porosity and composition of the pores during drying. The skeletal density calculated by μCT quantitative imaging is compared to typical values determined by helium pycnometry, and the reliability of the method is discussed. The data on the xerogels resulting from the drying of unmodified gels are challenged by simulating condensation reactions related to drying shrinkage. A mixture of gaseous and liquid phases is already present in the gels before the maximum shrinkage, which challenges the common assumptions that gas penetrates the pores in parallel to the SBE.

4.2 Materials and Methods

Synthesis. Silica alcogels were produced by a two-step sol–gel synthesis adapted from refs.[19,51] A silica sol (53 mL) was prepared by mixing 14.58 g (0.07 mol) of tetraethyl orthosilicate (98%, Sigma-Aldrich) with 6.130 mL of ethanol (99.96%, VWR Chemicals), 6.130 mL of a solution of hydrochloric acid (37%, Carl Roth) in ethanol (2.449×10^{-4} vol %), and 1.260 mL of water. The sol was covered and stirred for 90 min. Ethanol (16.13 g) was added, and 3.285 mL of a

solution of ammonium hydroxide (25%, Merck) in water (6.678×10^{-3} vol %) was introduced dropwise to promote the gelation. The sol was covered and stirred slowly for 30 min and was then casted into two-part molds made of polyether ether ketone (PEEK) using a micropipette. The molds have eight cylindrical slots with a depth and diameter of 16 and 8 mm, respectively (Figure A.1a), and each slot was filled with 785 μL of solution, resulting in cylindrical samples each containing 1.04×10^{-3} mol of SiO_2. After casting, the sol was defoamed at room temperature by applying a light vacuum for 2 min in a desiccator to remove the air dissolved in the sol. Each mold was inserted in a closed polytetrafluoroethylene (PTFE) container and left to gel at 50 °C for 24 h. Upon unmolding, the silica gels were splashed with ethanol to prevent drying and were stored in 1.2 L of ethanol per mole of SiO_2 at room temperature for 24 h. Ethanol was exchanged for n-hexane (99%, Carl Roth) stepwise by replacing the initial volume of ethanol for an equivalent volume of mixtures of 25/75, 50/50, and 75/25 vol % of n-hexane in ethanol every 24 h. The gels were rinsed four times with the same volume of n-hexane every 24 h. Some gels were then modified with trimethylsilyl chloride (TMCS; 99%, Sigma-Aldrich). The surface modification was conducted in four steps successively replacing n-hexane by the same volume of a TMCS in n-hexane solutions of 3, 3, 6, and 6 vol % every 24 h. The total TMCS/SiO_2 molar ratio was 1.7. The modified gels were finally rinsed with the same volume of n-hexane every 24 h four times and were stored in n-hexane. The samples were stored for different durations before drying, up to 6 months.

In operando APD by μCT. Five modified and two unmodified silica gels were dried at ambient pressure using an in operando μCT method for a total of seven samples. The modified gels are labeled M1–M5 and the unmodified gels U1–U2. Prior to μCT experiments, a sample was transferred from its n-hexane storage solution into a tailored PEEK chamber closed with a lid (Figure A.1b). The chamber was inserted in an EasyTom 160/150 CT system (RX Solutions, Chavanod, France) equipped with a micro-focus tube (tungsten filament) and a flat panel detector (cesium iodide scintillator). The PEEK chamber has a 0.4 mm wall thickness to limit X-ray absorption. The distance between the chamber and the tube was minimized to reach a voxel size of 11 μm while keeping the sample in the field of view during drying. During the APD of a single sample, a series of 141 μCT scans were acquired at a voltage and current of 135 kV and 200 μA, respectively. One scan consisted of 64 projections captured in the step and shot mode without reference images in only 1 min. Each scan was preceded by a black and gain calibration of 1 and 3 min, respectively. The time step between each tomography was about 6 min, and the total duration of the experiment was ca. 14 h. The first scan was done with the chamber closed, and then, the lid of the chamber was exchanged for a second lid with

a 6 mm diameter opening to begin the drying. The moment of the lid exchange was defined as $t = t_0$. The timestamp of each scan was defined as the difference between the average time of the 64 projections and t_0. The reconstruction was performed with a cone beam algorithm in the software XAct (RX Solutions). Back-projection parameters of the first scan were adjusted manually and were used as a template for the 140 remaining scans from the same specimen. Each reconstruction generated a vertical stack of about 1,000 slices in the 8-bit tiff format along the vertical axis of the cylinder. The slices were segmented in the software Dragonfly[130] using an in-house written python script. The segmentation procedure is described in appendix A.1 and generated the following outputs: the volume of the gel: $\tilde{V}_k$, the cross-sectional area of the gel along the z-axis of the cylinder: $A_{i,k}$, and the gray value averaged over that area: $\tilde{g}_{i,k}$, with $i, k \in \mathbb{N}$. i is the vertical voxel coordinate (or the slice number), and k is the scan number. At each scan number corresponds a timestamp t_k. The volume of the gel was corrected, as described in appendix A.2 resulting in V_k. We then defined the spring-back efficiency as the ratio between final volume $V^d = V_{k=140}$ and initial volume $V^0 = V_{k=0}$ of the gel. The maximum shrinkage was defined as $V^{\min}/V^0$, with $V^{\min}$ as the minimum volume of the gel. To evaluate the accuracy of the automated segmentation procedure, a manual segmentation was performed on 11 randomly selected tomographies among the seven gels at different drying times. The results are presented in appendix A.2. After a few more days of drying, the gels were weighed on a PCE-AB 100 (PCE Deutschland GmbH, Meschede, Germany), and the apparent density was calculated as $\rho_a = m^d/V^d$ with m^d as the mass of the dry gel. Fourier transform infrared (FTIR) spectra were recorded on an IRAffinity-1S spectrometer (Shimadzu Corp., Kyoto, Japan) to confirm the surface modification of the aerogels. One modified and one unmodified gel were ground into a fine powder and were analyzed in the attenuated total reflection mode (ATR). In addition to the scans on the silica gels, two additional measurements were carried out on pure n-hexane and deionized water with the same parameters as for the silica gels. A total of 141 μCT scans were recorded on n-hexane and 16 scans on deionized water.

The drying of TMCS-modified and unmodified gels resulted in monolithic aerogels and monolithic xerogels, respectively (Figure 4.1). Some gels had sub-millimeter gas bubbles trapped in them, which presumably came from a mismatch between the two parts of some molds during the gelling of the gels at 50 °C, allowing some air to enter the sol without consequences on the overall μCT analysis. The aerogels show a bluish taint under a black background characteristic of Rayleigh scattering as some air-filled pores were large enough to scatter blue light (ca. 400 nm), whereas the xerogels gels appear more transparent.

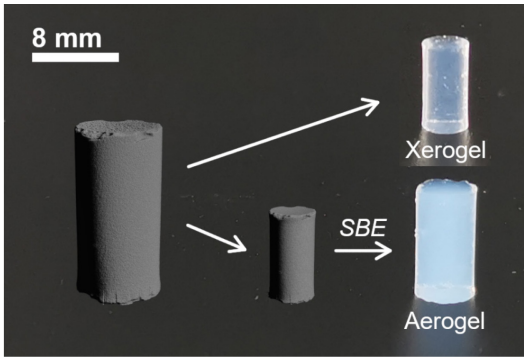

Figure 4.1 3D rendering of a gel's volume generated by the automated segmentation procedure at the beginning of drying (left) and at the maximum shrinkage (middle). Visualization done in Dragonfly software. Digital photographs of a xerogel and an aerogel after drying (right). Reprinted from ref.[102], CC BY 4.0 (https://creativecommons.org/licenses/by/4.0/).

Quantitative Imaging. The gray value profiles $\tilde{g}_{i,k}$ were corrected for the anode heel effect[133] with the procedure described in appendix A.3, resulting in the corrected gray value profiles $g_{i,k}$. A unique gray value of the gel at a given drying stage was calculated by averaging $g_{i,k}$ along the slice number i with eq. (4.1):

$$G_k = \frac{1}{\tilde{V}_k} \sum_{i=0}^{N} g_{i,k} \cdot A_{i,k} \tag{4.1}$$

where G_k is called the "global gray value" and N is the total number of slices. The conversion between the gray value of a voxel and the reconstructed attenuation coefficient (RAC) of the scanned material at that voxel was given by

$$g = \frac{\mu - a}{b - a} \cdot 255. \tag{4.2}$$

where g is a gray value in 8-bit, μ is the RAC, and a and b are, respectively, the minimum and maximum attenuation values within the volume and are called contrast parameters. In all measured samples, a and b were set at −0.90185 and 1.14111, respectively. These values were chosen so that the gray values corresponding to the voxels belonging to the sample were binned between 0 and 255 in the reconstructed images at any point of drying. The global RAC of the gel during drying $\bar{\mu}_k$ was calculated with eq. (4.2) from the global gray values G_k. $\bar{\mu}_k$ can be expressed as the sum of the RAC of each individual phase composing the gel, weighted by their respective volume fractions

$$\bar{\mu}_k = \frac{\mu_{\mathrm{hex}} V_{\mathrm{hex},k} + \mu_{\mathrm{skel}} V_{\mathrm{skel}}}{V_k} \tag{4.3}$$

where μ_{hex} and μ_{skel} are the RACs of n-hexane and of the silica skeleton and $V_{\mathrm{hex},k}$ and V_{skel} are the corresponding volumes, respectively. In eq. (4.3), the contribution of gas phases to the global RAC, notably hexane vapor, was neglected. The contribution of hexane vapor to X-ray

absorption was considered negligible compared to the one of liquid hexane. The RACs of the silica skeleton μ_{skel} and of hexane μ_{hex} as well as the skeleton volume μ_{skel} were assumed to remain constant during drying. The global gray value of hexane G_{hex} was computed from the μCT scans done on a reference n-hexane sample. μ_{hex} was then calculated using eq. (4.2) with G_{hex} averaged over the 134 last scans. At any time, the gel volume V_k reads:

$$V_k = V_{\mathrm{hex},k} + V_{\mathrm{skel}} + V_{\mathrm{air},k} \tag{4.4}$$

with $V_{\mathrm{air},k}$ as the volume of air or gas in the gel. At the end of drying for $k \geq k_d$, the hexane content was assumed to be zero and eq. (4.3) becomes:

$$\bar{\mu}_{k \geq k_d} = \frac{\mu_{\mathrm{skel}} V_{\mathrm{skel}}}{V_{k \geq k_d}}. \tag{4.5}$$

In practice, the product $\mu_{\mathrm{skel}} V_{\mathrm{skel}}$ was computed by taking the average of the product between the global RAC and the volume of the gel:

$$\mu_{\mathrm{skel}} V_{\mathrm{skel}} = \frac{1}{M} \sum_{k \geq k_d} \bar{\mu}_k V_k, \tag{4.6}$$

where M is the number of scans between the scan k_d and the final scan. The hexane volume was calculated by substituting eq. (4.6) in eq. (4.3). At the beginning of the drying for $k \leq k_2$, the air content was assumed to be zero and with the knowledge of V_{hex}, the skeleton volume can be calculated with eq. (4.7):

$$V_{\mathrm{skel}} = \frac{1}{N} \sum_{k_1 \leq k \leq k_2} V_k - V_{\mathrm{hex},k}, \tag{4.7}$$

where N is the number of scans between scans k_1 and k_2. k_1 corresponds to the scan number from which the X-ray tube was assumed stable. k_d, k_1, and k_2 were chosen manually and may be different for each sample (Table A.1). The air volume was directly given in eq. (4.4) since $V_{\mathrm{hex},k}$ and V_{skel} are known. Eqs. (4.3), (4.4), (4.6) and (4.7) form a four-equation invertible system with four unknowns: $V_{\mathrm{hex},k}$, $V_{\mathrm{air},k}$, V_{skel}, and μ_{skel}. The error propagation was calculated numerically and is documented in appendix A.4. The error bands of all graphs correspond to the 95th percentile. The skeletal density of the gels was calculated with $\rho_{\mathrm{skel}} = m^d / V_{\mathrm{skel}}$.

Numerical simulations were carried out by considering a modified drying model allowing μ_{skel} and V_{skel} to vary over time and the creation of water with the term V_{H_2O}. The global gray value of water G_{H_2O} was computed from the μCT scans done on a reference deionized water sample, and μ_{H_2O} was calculated using eq. (4.2) with G_{H_2O} averaged over the nine last scans. The details on the modified model, the assumptions, and the solving of the equations for the simulations are reported in appendix A.5.

4.3 Results and Discussion

Synthesis. In the surface modification process, the reaction between a silanol group and TMCS resulted in a trimethylsilyl group via eq. (4.8):

$$\equiv \mathrm{Si-OH} + (\mathrm{CH_3})_3\mathrm{SiCl} \rightarrow \equiv \mathrm{Si-O-Si(CH_3)_3} + \mathrm{HCl}. \quad (4.8)$$

A sufficient surface modification was necessary to prevent condensation of the silanol groups and promote the spring-back effect.[57] The surface coverage of the trimethylsilyl and silanol groups was evaluated qualitatively by FTIR on a modified and unmodified gel after APD, and the spectra are shown in Figure 4.2. The broad peak at 1050 cm^{-1} was characteristic of Si–O–Si vibrations and was present in both types of gels.[48] The band at 3370 cm^{-1} and the peak at ~960 cm^{-1} originated from O–H and SiO–H vibrations, which were significant in the unmodified gel.[172] The absence of the O–H vibration band in the modified gel along with the presence of the peaks at ~2970 ($C–H_3$), 1255 (C–H), 845 (Si–C), and 756 (Si–C) cm^{-1} indicated a successful silylation of the silica skeleton.[18,48] H–O–H vibrations can be seen in the unmodified gel at ~1640 cm^{-1}, which was expected due to the hydrophilic nature of silanol groups. These results confirmed the presence of silicon–carbon and methyl bonds in the gels modified with TMCS, which was attributed to trimethylsilyl groups.

μCT Acquisition, Reconstruction, and Segmentation. Before presenting the details of the results, we present in this section the accuracy of the workflow related to the μCT data acquisition and processing. The combination of voltage, current, and framerate of the μCT

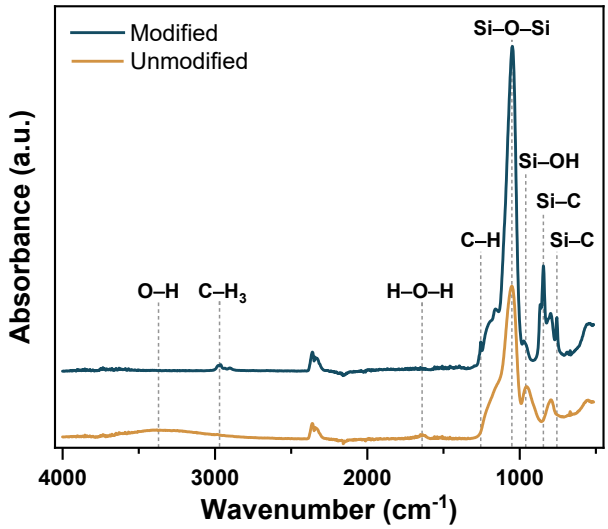

Figure 4.2 FTIR spectra of a modified and unmodified gel. Relevant vibration frequencies are indicated by a dashed line. Reprinted from ref.[102], CC BY 4.0 (https://creativecommons.org/licenses/by/4.0/).

scans produced well-contrasted projections (Figure 4.3 and Figure A.10a) leading to reasonable signal-to-noise ratio and spatial resolution in the reconstructed slices (11 μm voxel^{-1}), allowing to resolve details of 40–50 μm. The drying of the gels could be accurately monitored with a 6 min time step between each scan and allowed to capture accurately the maximum shrinkage (Figure 4.3). Some of the μCT scans lasted longer than 1 min due to instrument errors, resulting in a lower temporal resolution especially for M1 (Figure A.11). The temperature in the μCT chamber slightly increased throughout the duration of the experiment but remained within 23–25 °C (Figure A.12). The low number of projections used for the reconstruction with the cone-beam algorithm introduced under-sampling artifacts in the slices.[132] This generated line patterns in the reconstructed slices (Moire patterns), which were easily visible around the sample in the background (Figure A.10b). These artifacts had a negligible impact on the segmentation procedure except at the bottom of the gel close to the chamber. The ROIs obtained by automated segmentation were representative of the gel geometry (Figure A.13) and were comparable to the ROIs obtained by manual segmentations independently of the sample and of the drying stage of the gel. Because of undersampling, the gray values of the voxels belonging to the sample were broadly distributed (Figure A.10c).

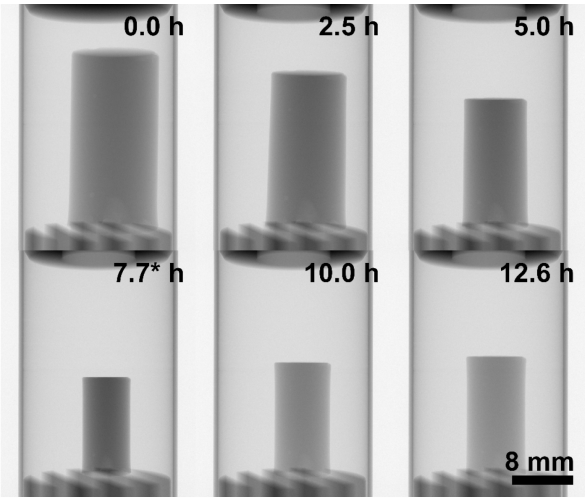

Figure 4.3 μCT projections of the modified gel (M4) at six stages of drying. The drying time is indicated on the top right of each projection, and the maximum shrinkage is highlighted by an asterisk. Reprinted from ref.[102], CC BY 4.0 (https://creativecommons.org/licenses/by/4.0/).

Resolving local changes in the structure was excluded given that the size of the details that can be resolved in the μCT scans was much larger than the typical size of the structure of silica aerogels (40–50 μm vs 100 nm).[173] No cracks nor pores were noticed in the μCT reconstructions of the dry gels. However, cracks smaller than 40–50 μm cannot be excluded and the under-sampling artifacts may also prevent to resolve larger cracks. Some gels moved

in the chamber during drying, but the impact on the volume V_k and gray values $g_{i,k}$ computed after segmentation was negligible.

Geometric characterization. The geometric parameters of the gels during drying were computed based on the results from the automated segmentation procedure. Figure 4.4 shows the volume, height, and diameter profiles versus time of a modified and unmodified gel during drying (see Figure A.14 for the profiles of all seven gels). While the volume was given directly from the segmentation, the height h_k and the diameter D_k of the gel were calculated from the cross-sectional area of the gel along the z-axis of the cylinder: $A_{i,k}$.

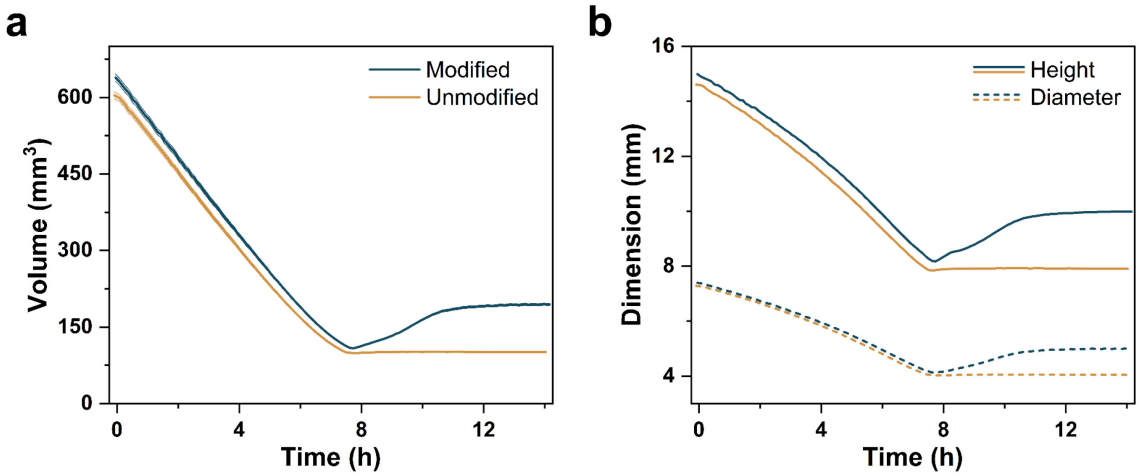

Figure 4.4 (**a**) Volume of a modified gel: M4 and an unmodified gel: U2 during ambient pressure drying. (**b**) Height (full line) and diameter (dashed line) of the same gels. The error bands of the height and diameter profiles are not shown. Each curve consists of 141 data points. Reprinted from ref.[102], CC BY 4.0 (https://creativecommons.org/licenses/by/4.0/).

At the beginning of the drying, the volume was slightly different between the seven produced alcogels (Figure A.14). However, the overall evolution was remarkably similar in both kinds of gels, suggesting a good reproducibility of the synthesis and drying process. For all gels, the aspect ratio h/D was rather stable throughout drying at around 2.0 (Figure A.15). The initial volume of the alcogels was on average 20% smaller than the volume of the molds (785 μL). This difference was attributed to syneresis.[55,59] All samples reached the maximum shrinkage after 7–8 h of drying, and those with a higher initial volume took longer to dry. The maximum shrinkages, defined as $V^{\min}/V^0$, were about 16.6 and 15.9 vol % for the five modified and two unmodified gels, respectively. A small difference in the maximum shrinkage of modified and unmodified gels was already reported by Smith et al. in a similar material.[74] That difference was attributed to a real feature rather than a measurement error given the time and spatial resolution of the μCT measurements and could be due to different volumes of the silica skeleton and/or different repulsive forces within the silica network between the two types

of gels. The SBE in the modified gel can be seen in Figure 4.4 at t = 7.7 h in the volume and height/diameter profiles. The spring-back efficiency was very similar between the five modified gels and was on average 29.4 vol %. Surprisingly, the two unmodified gels slightly re-expanded and recovered about 0.3% of their original volume within 2 h following the maximum shrinkage followed by a shrinkage of 0.2 vol %. Although the amount of reversible shrinkage was negligible, this confirmed that unmodified gels can relax drying-related stresses to some extent. The apparent density of the modified gels was on average 0.391 g cm^{-3}, and it was very reproducible within the five samples. The lowest and largest densities recorded were 0.384 and 0.397 g cm^{-3}, respectively. As a consequence of the limited spring-back efficiency, the produced aerogels were denser than those reported in the literature for similar synthesis and drying conditions.[18,51] This effect can arise from one or more of the following: condensation reactions (chemical lock), plastic deformation, entanglement of the solid network, and residual liquid phase (mechanical locks). It is notably possible that differences in the TMCS/SiO_2 molar ratio affected the capability of the gels to spring-back.[83] To this regard and complementary to FTIR, quantitative evaluation by thermogravimetric analysis (TGA) could reveal whether the extent of trimethylsilyl groups was similar compared to aerogels produced with similar synthesis conditions.[19] The two unmodified gels showed higher discrepancies with apparent densities of 0.708 and 0.648 g cm^{-3}. In fact, a variation of room humidity in combination with the hydrophilic character of unmodified gels would result in a different water intake for the two gels at the time the μCT scans were measured and until the gels were weighted. Additional μCT scans performed after a few days of further drying did not show a significant difference of the volume for both modified and unmodified gels, suggesting no residual liquid phase in the samples. The SBE was heterogeneous; on the μCT projections, it was observed that the expansion began from the top of the gel and continued downward over roughly 30 min. Further analysis of the spatial evolution of the SBE would require a local analysis of the μCT data, a procedure not conducted in this work. To further understand the emergence of the SBE, the solid, liquid, and gas volumes during the drying of the gels were calculated using μCT quantitative imaging.

Quantitative Imaging Results. In this section, the quantitative imaging procedure and intermediate results are reported and its necessary assumptions are discussed. The μCT experiments generated two time-dependent parameters, the volume of the gel V_k and the global gray value G_k; the latter was converted into the global reconstructed attenuation coefficient $\bar{\mu}_k$ using eq. (4.2). To calculate the volumes of the silica skeleton, hexane, and gas in the gels, the following assumptions were made: (i) at the beginning of drying, the gel consists only of the

silica skeleton and hexane; (ii) at the end of drying, the gel consists only of the silica skeleton and a gas phase; (iii and iv) the hexane and silica skeleton RACs were constant during drying; (v) the skeleton volume was constant during drying. As previously mentioned, the combination of the equations and constraints allowed us to generate an invertible system with a unique solution for the parameters of interest. The intermediate data produced by the quantitative imaging procedure are shown in Figure 4.5 for one modified and unmodified gel (see Figure A.16 for the data on all seven gels).

The global gray values were reported instead of the RACs since these are the quantities generated by the μCT reconstruction. Figure 4.5a,b shows the global gray values of a modified and unmodified gel. During drying, the gray values increased and reached a maximum at 7–8 h (Figure 4.5a,b and Figure A.16) and this time corresponded exactly to the point of maximum shrinkage in both kinds of gels (Figure 4.4 and Figure A.14). After the maximum shrinkage, the gray value decreased and stabilized. Since the volume of the unmodified gels did not change significantly after the maximum shrinkage, the decrease in the gray value was only related to the replacement of liquid hexane for a gaseous phase. In the modified gels, the decrease in gray values originated from both the evaporation of hexane and the re-expansion of the volume. Figure 4.5c shows the gray values of a reference hexane sample from which an average gray value of 131.9 was calculated, equivalent to an RAC of 0.155. Instabilities of the X-ray tube

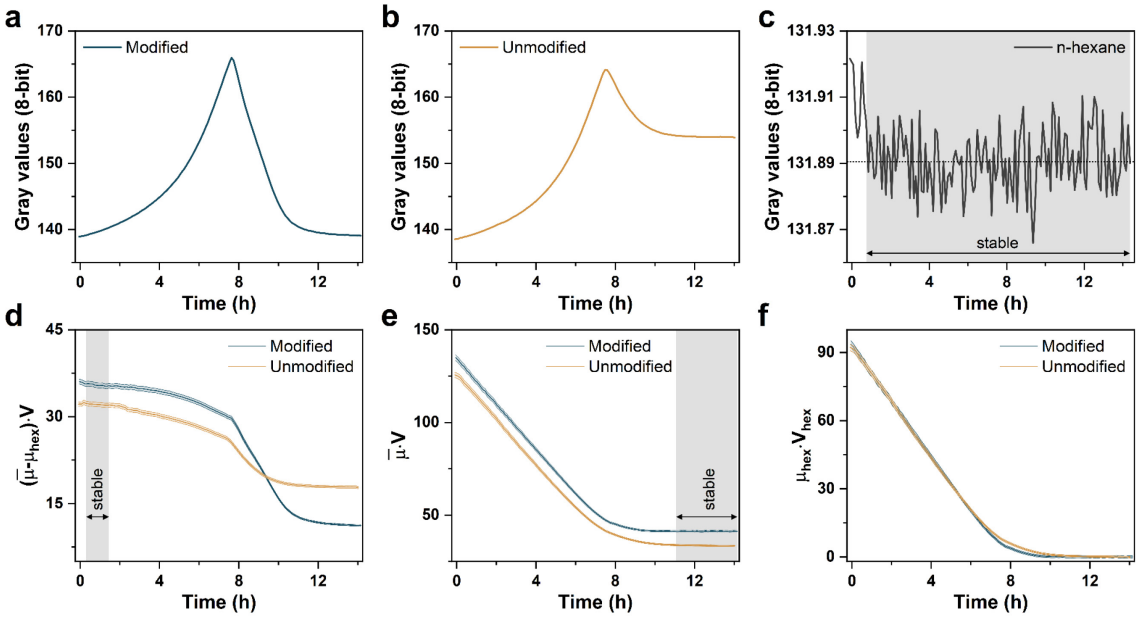

Figure 4.5 Intermediate data from the μCT quantitative imaging procedure. (**a**,**b**) Global gray values of a modified gel: M4 and an unmodified gel: U2 during drying. The error of the global gray values is 0.018. (**c**) Global gray value of an n-hexane reference sample. (**d**) $(\bar{\mu} - \mu_{\mathrm{hex}}) \cdot V$ profiles of the two gels. (**e**) $\bar{\mu} \cdot V$ profiles. (**f**) $\mu_{\mathrm{hex}} \cdot V_{\mathrm{hex}}$ profiles. The stable region of the profiles in panels (**c**−**e**) is highlighted in gray only as indicative values. Each curve consists of 141 data points. Reprinted from ref.[102], CC BY 4.0 (https://creativecommons.org/licenses/by/4.0/).

tube were observed at the beginning of every in operando μCT experiment. As a result, slightly higher gray values were observed in the reconstructed slices for the first few μCT scans, which is notably visible in the reference hexane sample.

The skeleton volume was calculated as the average of the difference between the total volume and the hexane volume at the beginning of the drying between the lower and upper thresholds k_1 and k_2 as shown in eq. (4.7). These thresholds allowed us to exclude the effect of the beam instabilities at the beginning of the experiment and also to provide better statistics. k_1 and k_2 were set by analyzing the quantity $(\bar{\mu}_k - \mu_{\mathrm{hex}})V_k$, which could be seen as a mass conservation equation. Besides hexane evaporation, a gel could be considered as a closed system as long as there is no gaseous phase present. This assumption permits to write the conservation of the quantity:

$$[\bar{\mu}V - \mu_{\mathrm{hex}}V_{\mathrm{hex}}]_{k_1 \le k \le k_2} = \text{constant.} \tag{4.9}$$

Combining eq. (4.9) with eq.(4.4) and recalling the assumption that μ_{skel} and V_{skel} are set as constants and that the volume of gas is $V_{\mathrm{air},k_1 \le k \le k_2} = 0$ during drying lead to:

$$[(\bar{\mu} - \mu_{\mathrm{hex}})V]_{k_1 \le k \le k_2} = \text{constant.} \tag{4.10}$$

The quantity $(\bar{\mu}_k - \mu_{\mathrm{hex}})V_k$ is shown in Figure 4.5d for a modified and unmodified gel and in Figure A.16b for all gels. The plateau region where eq. (4.10) was stable at the beginning of the drying was different between the samples, ranging from 6 to 120 min ($k_2 - k_1$ in Table A.1). A plateau region at the end of the drying was also defined for the calculation of the product $\mu_{skel}V_{skel}$ calculated in eq. (4.6) at $k \geq k_d$. k_d was determined from the $\bar{\mu}_k V_k$ profiles and was set at about 13.7 h (Figure 4.5e, Figure A.16c and Table A.1). Figure 4.5f and Figure A.16d also show the quantity $[\mu_{\mathrm{hex}}V_{\mathrm{hex}}]_k$ before the division by the RAC of hexane calculated from the hexane reference sample. From these intermediate results, the remaining parameters needed to solve the system of four equations were determined, allowing the evaluation of the amount of silica skeleton, hexane, and gas of the gels during drying.

Phase Composition during Drying. The quantitative imaging procedure coupled with the underlying model of drying silica gels was used to calculate their phase composition throughout APD. Figure 4.6 shows the time-dependent volume profiles of the skeleton, hexane, and gas in a modified gel and unmodified gel (see Figure A.17 for the other gels). The results for the five modified gels were compiled in a ternary plot showing the volume fraction of each phase (Figure 4.7). The phase composition analysis seemed to provide reproducible results between the different modified gels with the exception of M1, which seemed to be off-trend. At the beginning of drying, the porosity of all modified gels was about 95%. In some gels, the calculated air volume was negative over the first few scans due to beam instabilities

and it should not be considered as a physical feature. The steady decrease in the hexane profile showed that the evaporation rate was constant for the first 6 h (Figure 4.6 and Figure A.17), suggesting that the slight increase in temperature in the instrument had no impact on the drying dynamic as the temperature stabilized at 4–6 h (Figure A.12). The hexane profiles were similar between modified and unmodified gels. In parallel to the evaporation, there was a decrease in the gel surface area where the mass transfer occurs (in Figure 4.4 and Figure A.14 from the height and diameter profiles assuming a perfect cylinder). Therefore, the evaporation rate per surface area increased until the maximum shrinkage as already reported elsewhere,[74] which implied that the mass transfer at the outer surface of the gel was not the limiting factor in the drying rate. This suggested that the drying rate was only limited by the convection of hexane vapor within the drying chamber for the first 6 h. A previous study reported an increasing evaporation rate in similar gels, which may be related to a difference in the ambient conditions compared to this study.[18]

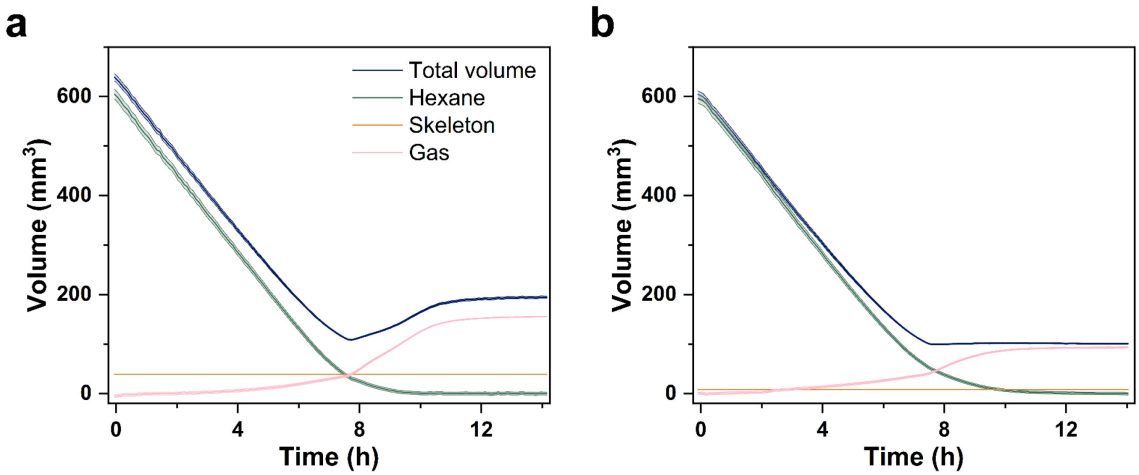

Figure 4.6 Total volume along with hexane, skeleton, and gas volumes of (**a**) a modified gel: M4 and (**b**) an unmodified gel: U2 during drying. Each curve consists of 141 data points. Reprinted from ref.[102], CC BY 4.0 (https://creativecommons.org/licenses/by/4.0/).

Interestingly, we calculated a significant amount of gas phase in all gels already before the maximum shrinkage, making for up to 37 vol % of the gel's volume (Figure 4.6, Figure 4.7 and Figure A.17). This suggested that the liquid–gas interface already receded into the pores, whereas common drying models predict that the liquid recedes in the pores once shrinkage stops.[65] This finding was supported by the small decrease in the hexane evaporation rate before maximum shrinkage (Figure 4.6 and Figure A.17), indicating that the transport of hexane vapor became limited by its diffusion through the pore network rather than by the convection within the drying chamber. It is worth noting that upon visual inspection of modified gels dried ex situ in glass containers they remained transparent until the maximum shrinkage and only turned

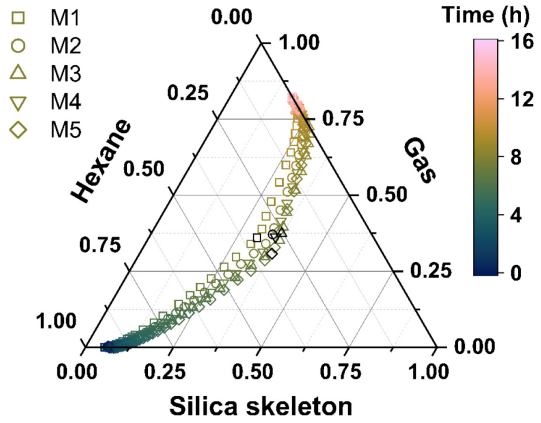

Figure 4.7 Ternary plot of the volume fraction of hexane, skeleton, and gas in the five modified gels during drying. The drying stage of the gel is indicated on each symbol with a color scale. The maximum shrinkage is highlighted by black symbols at the center of the graph. Only half of the data points are represented to enhance readability (71 in total). Reprinted from ref.[102], CC BY 4.0 (https://creativecommons.org/licenses/by/4.0/).

opaque afterward. Although the drying conditions were different compared to the μCT drying chamber, we can reasonably assume that the gels underwent similar changes in the in operando μCT experiments. This could mean that the volume occupied by gas/air in the pores was too small to scatter light prior to the SBE.[65]

The emergence of the SBE could be related to a particular state of the gel, composed of nearly equal volume fractions of silica skeleton, hexane, and gas phases (Figure 4.6, Figure 4.7 and Figure A.17). This composition arguably corresponds to a critical drying stage where some pores get completely depleted in hexane. Consequently, the silica skeleton was able to relax the drying-related stresses, generating a spring-back visible on a macroscopic level. Such critical composition would depend on the morphology and structure of the silica network and thus on the synthesis conditions. Given that the quantitative imaging approach only provided the average volume of hexane and gas, it could not be ruled out that this critical composition was a consequence of heterogeneous phase composition in the gels, e.g., that the top part of the gel dried faster than the bottom part. To exclude heterogeneities would require investigating the local phase composition of the gels during drying. However, μCT projections revealed a homogeneous evolution of the diameter and height prior to the SBE, suggesting a homogeneous phase composition. Moreover, the gray value profiles along the vertical axis of the gel only changed significantly after the SBE (Figure A.5). The SBE seemed to happen in two regimes: at first, the volume expansion rate was rather steady, and after about 80 min, it slightly increased. The moment of increasing rate corresponded to the point where the fraction of hexane went below ~5 vol % of the pore volume for all modified gels (Figure 4.6a and Figure A.17). Nevertheless, the analysis of the average phase composition of the gels after

spring-back was limited due to the slightly heterogeneous SBE. The abrupt change of hexane and gas volume profiles at the maximum shrinkage may be an artifact related to the correction of the anode heel effect as it was difficult to fit the gray value profiles during the SBE (appendix A.3). In the unmodified gels, the shrinkage stopped once the hexane and gas volumes were roughly equal followed by a decreasing evaporation rate (Figure 4.6b and Figure A.17e).

The skeleton volume of the modified gel shown in Figure 4.6 was about 39 mm^3 and varied from 33 to 38 mm^3 in the other gels (Figure A.17). The average skeletal density for the five modified gels was 1.97 ± 0.14 g cm^{-3}, showing consistent reproducibility between the five samples. The calculated densities were in the range of typical values for silica aerogels reported in the literature by helium pycnometry.[18,76] These findings emphasized the reliability of the μCT quantitative imaging procedure and the accuracy of the underlying model for the modified gels. It is pertinent to be aware about the impact of potential closed pores in the calculation of the skeleton volume. Closed pores being inaccessible by helium lead to an overestimation of the skeleton volume and thus to an underestimation of the skeleton density. Using μCT, closed pores still filled with hexane at the end of drying would result in an overestimated global RAC and thus in an overestimation of the skeleton volume as well. The remaining amount of hexane in the aerogels may be quantified by comparing the weight of the gels before and after heat treatment, which can also enable further volume recovery.[59] It must also be noted that small changes in the hexane volume (and hexane RAC) had a large impact on the skeleton volume since it was calculated as the difference between two large quantities: the total volume and the hexane volume as shown in eq. (4.7). Finally, eventual unresolved cracks in the μCT volumes appearing during drying would essentially be interpreted as "pores" in the drying model. These would result in a higher gas content but would not have consequences on the skeleton or hexane volumes since the quantity $[\bar{\mu}V]_{k\geq k_d}$ in eq. (4.5) is independent of the gas volume.

The quantitative imaging procedure applied to unmodified gels resulted in substantially underestimated skeleton volume, which led to very different skeletal densities of the xerogels at 3.7 and 8.4 g cm^{-3}, much higher than the density of silica glass (2.2 g cm^{-3}). Given the dependency of the skeleton, hexane, and gas volumes in eq. (4.4), the hexane and gas volume profiles of the unmodified gels reported in Figure 4.6b were affected by the underestimated skeleton volume and were thus erroneous. A difference between unmodified and modified gels was also observed in the raw data from the quantitative imaging procedure. The profiles $\bar{\mu}_k V_k$ of U1 and U2 started at a similar value as M3 and M5 at the beginning of the drying but reached a lower plateau at the end of the drying (Figure A.16c). That difference could not be caused by the residual amount of hexane in the unmodified gels since it would increase the RAC. We

propose that the abnormal quantities calculated for the unmodified gels were due to limitations in the modeling of the phase composition evolution. More specifically, the assumption of a constant skeleton RAC and volume may not be valid in the unmodified gels due to condensation reactions occurring during the drying shrinkage. To complement the phase composition analysis, we performed simulations based on the quantitative imaging results including potential condensation reactions between surface silanol groups in the model.

Condensation during Shrinkage. Water condensation reactions between surface silanol groups results in the creation of siloxane bonds, which leads to irreversible shrinkage of the silica network.[57] The assumptions of the model were modified to include in the equations a change in skeleton volume and RAC as well as a term corresponding to the created water. For simplicity, the simulations were not performed over time but only comparing the state of a gel at the beginning and at the end of drying. The derivation of the modified model and corresponding solution of the simulations are reported in appendix A.5.

By taking into account the condensation reactions, the number of unknowns in the four-equation system increased from four to seven. The skeletal density was fixed and set at 1.9 g cm^{-3} for the modified gels and at 2.4 g cm^{-3} for the xerogels.[18] Despite the additional constraint, the resulting system had two more unknowns than equations and the simulations generated an infinite number of solutions as 2D surfaces. We chose to evaluate the change of the following quantities: $C_V = V^d_{\text{skel}}/V^0_{\text{skel}}$, $C_\mu = \mu^d_{\text{skel}}/\mu^0_{\text{skel}}$, and $C_H = V^d_{H_2O}/V^d_{\text{skel}}$. C_V and C_μ represent the relative change of the skeleton volume and RAC between the dry gel (superscript d) and the alcogel (superscript 0), respectively. C_H represents the intake of water in the dry gel relative to the final skeleton volume V^d_{skel}. For the sake of visualization, we assumed that the change in skeleton volume and RAC would not exceed 20% and that the final water intake would not be larger than 10% of the dry skeleton volume. Therefore, the simulations were performed for $0.8 \leq C_V \leq 1.0$, $1.0 \leq C_\mu \leq 1.2$, and $0 \leq C_H \leq 0.1$.

The results from the simulations are shown in Figure 4.8 for an unmodified and modified gel, and simulations on the other gels are shown in Figure A.18. The domain over which $0 \leq C_H \leq 0.1$ was valid corresponds to the slightly curved band in Figure 4.8. In the unmodified gel, the band was considerably distant from the point $(C_V, C_\mu, C_H) = (1,1,0)$, which corresponded to a model excluding condensation reactions. Simulations suggested that a skeleton volume shrinkage of at least 13 vol % of its original value, corresponding to $C_V = 0.87$, would be necessary for reaching a target density of 2.4 g cm^{-3} for the dry silica skeleton in unmodified gels. Although all points on the curved surface were theoretically valid in the

simulation framework, only part of them was physically relevant, e.g., a decrease in skeleton volume without water intake would not be a physical feature.

In the modified gels, the point of no condensation reactions was included in the curved surface with $0 \leq C_H \leq 0.1$ (Figure 4.8b). Therefore, a target dry skeletal density of 1.9 g cm^{-3} could theoretically be possible without any condensation reactions. This emphasizes the successful modification by TMCS. These results also support the fact that the relatively low spring-back efficiency was not due to a chemical lock of the silica network by condensation reactions but possibly by mechanical locking of the silica network. The simulations on the condensation reactions based on the quantitative imaging analysis showed that the change of skeleton volume was potentially significant during APD of unmodified gels, while it was potentially negligible in the modified gels. Table 4.1 summarizes the key quantities computed by μCT segmentation and quantitative imaging for all gels.

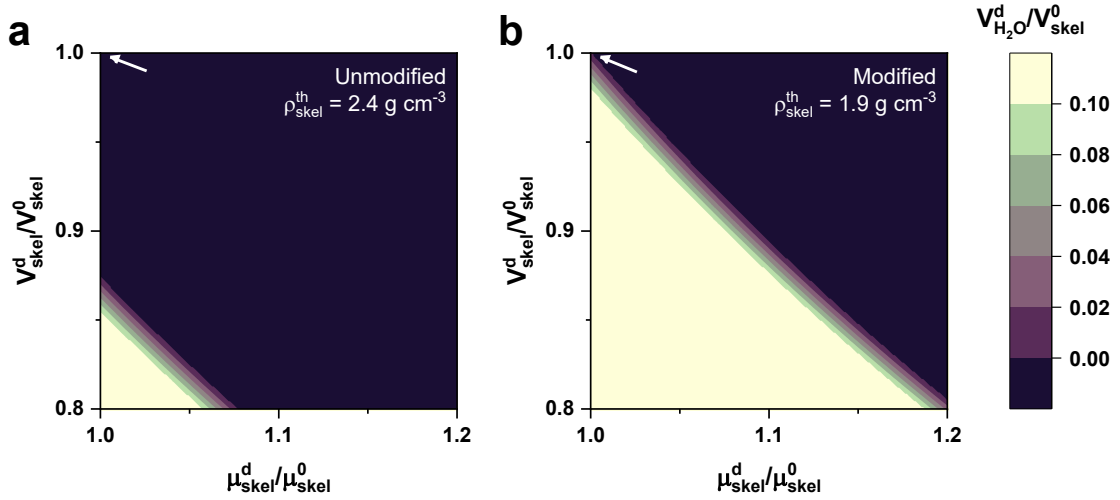

Figure 4.8 Maps resulting from numerical simulations implementing condensation reactions during the drying of (**a**) an unmodified gel: U2 and (**b**) a modified gel: M4 assuming theoretical skeleton densities of 2.4 and 1.9 g cm^{-3} for the unmodified and modified gel, respectively. The x axis corresponds to the relative change in the skeleton RAC between the end and the beginning of the drying. The y axis corresponds to the relative change in the skeleton volume. The colored scale bar shows the relative volume of water in the gel at the end of the drying. Each trio of values located on the contour surfaces within $0 \leq V^d_{H_2O}/V^0_{skel} \leq 0.1$ satisfies $\rho_{skel} = \rho^0_{skel}$. Points located outside of this range are not shown. The arrows highlight the theoretical point corresponding to no condensation reactions. The maps resolution is 100 × 100 data points. Reprinted from ref.[102], CC BY 4.0 (https://creativecommons.org/licenses/by/4.0/).

Table 4.1 Main properties of the five modified and two unmodified gels dried at ambient-pressure. The values with a (*) superscript were calculated from the underestimated skeleton volume in the unmodified gels and are thus not representative. Adapted from ref.[102], CC BY 4.0 (https://creativecommons.org/licenses/by/4.0/).

Sample	Volume change upon gelation or syneresis (vol %)	Maximum shrinkage (vol %)	Spring-back efficiency (vol %)	Alcogel porosity (vol %)	Dry gel porosity (vol %)	Apparent density (g cm^{-3})	Dry skeletal density (g cm^{-3})
M1	14.8	16.2	28.5	95.9	82.4	0.394	2.251
M2	17.0	16.4	29.1	95.4	80.1	0.397	2.025
M3	22.8	16.5	29.0	94.8	80.0	0.391	1.853
M4	18.6	16.9	30.5	94.7	80.0	0.384	1.922
M5	24.4	16.9	29.8	93.4	78.7	0.387	1.820
U1	21.9	15.5	15.5	97.4*	81.4*	0.708	3.741*
U2	23.0	16.4	16.7	98.6*	93.0*	0.648	8.443*

4.4 Summary

This study addressed the phase composition evolution of silylated silica aerogels during ambient pressure drying by an in operando μCT approach. The quantitative imaging workflow was more reliable to characterize modified gels than unmodified gels, which was attributed to the drying-related condensation reactions occurring in the latter.

The emergence of the spring-back effect in the silylated gels coincided with volume fractions of the skeleton, hexane, and gas reaching roughly one-third each during drying. We proposed that at this threshold composition, some pores got locally depleted in hexane, which enabled the relaxation of the capillary stresses by the silica skeleton, thus enabling the SBE. At first, the re-expansion was slow due to significant amounts of hexane remaining in the pores. Once the hexane went below roughly 5 vol % of the total pore volume, the expansion rate increased slightly as more of the silica skeleton was able to relax. The expansion stabilized, and the gels volume plateaued at 29 vol % of their initial volume, resulting in monolithic aerogels. The results suggest that this relatively low spring-back efficiency could be attributed to an irreversible plastic deformation and/or remaining stress in the solid network. We anticipate that further expansion was mostly hindered by the entanglement of the silica network and that the structure could be unlocked by overcoming some activation energy. Further analysis of the data collected by μCT would provide more insights on the dynamic of the SBE in silica aerogels, in particular by evaluating the local phase composition of drying gels rather than the overall phase composition. We also emphasize the potential of lab-source CT instruments as

a tool for materials scientists to perform phase compositional analysis of materials undergoing geometric and compositional transformations over time.

5 Solvent cavitation during ambient pressure drying of silica aerogels

The content of this chapter is based on the published article:

Title	Solvent Cavitation during Ambient Pressure Drying of Silica Aerogels
Authors	Julien Gonthier, Tilman Rilling, Ernesto Scoppola, Aleksander Gurlo, Peter Fratzl, Wolfgang Wagermaier
Journal	Langmuir
Publisher	ACS Publications
Publication date	12th of June 2024
Reference	Langmuir **2024**, *40* (25), 12925–12938
DOI	https://doi.org/10.1021/acs.langmuir.4c00497
Author contributions	Conceptualization: J.G., E.S., P.F., and W.W.; methodology: J.G. and E.S.; software: J.G. and E.S.; formal analysis: J.G., E.S. and P.F.; investigation and data curation: J.G., E.S., and T.R., writing–original draft: J.G., E.S., and W.W.; writing–review and editing: J.G., E.S., T.R., A.G., P.F., and W.W.; visualization: J.G.; supervision: P.F. and W.W.; project administration: J.G., P.F., and W.W.; funding acquisition: A.G. and W.W.

The following co-authors made notable contributions: Tilman Rilling performed the μCT acquisitions for half of the samples; Ernesto Scoppola assisted in the acquisition of the X-ray scattering measurements, performed the calibration and integration of the generated data, developed the WAXS drying model and computed the corresponding average phase composition.

5.1 Background

This chapter gives the theoretical background of the evaporative drying of porous media and gives a more thorough overview on the drying of silica gels. In general, evaporation of a liquid confined in a porous media can occur by three mechanisms: evaporation by recession of the liquid−vapor interface, drying shrinkage, and cavitation (Figure 5.1). Drying starts with the formation of a meniscus at the outer surface of the pores. As introduced in chapter 2.3, this liquid-vapor interface is subject to capillary pressure that is described by Young-Laplace equation: $\Delta p = p_0 - p_l = 2\gamma_{LV}\cos\theta / r_c$.

Evaporation by the recession of the meniscus will occur, provided that the tension in the liquid remains under the elastic limit of the solid matrix. This is typically the case for porous materials with a large pore size or a stiff matrix. With water as the pore liquid ($\gamma_{\text{water}} \approx 72$ mN m^{-1}) and a pore size of 1 μm, the capillary pressure would be around 0.15 MPa, which is about the yield strength of polyurethane foams[169] (found in, e.g., kitchen sponges). The meniscus recedes in the larger pores first, resulting in a heterogeneous drying front inside the porous medium where evaporation is limited by the diffusion of the vapor phase.[93,174] Under certain conditions, evaporation by the recession of the meniscus may also proceed by a sudden conversion of liquid to vapor referred to as adiabatic burst events.[175]

Evaporation by drying shrinkage takes place in porous materials with a compliant matrix and a smaller pore size, eventually preceded by an initial stage of evaporation by meniscus recession. As the meniscus reaches smaller pores, the tension in the liquid increases and can overcome the elastic limit of the solid matrix, which then contracts onto the liquid.[176] The flow

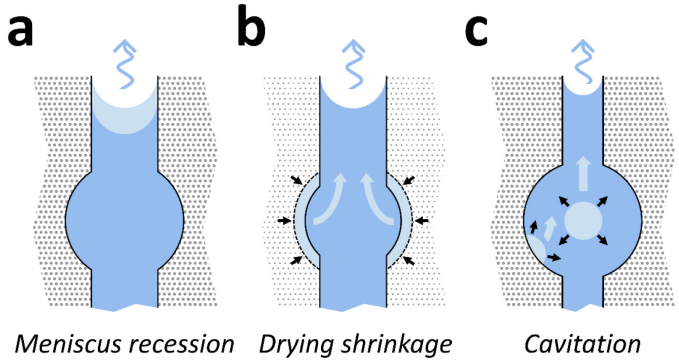

Figure 5.1 Illustration of the three evaporation mechanisms in a simplified cylindrical pore with an ink-bottle-shaped geometry confined by a solid matrix (in gray). (**a**) Evaporation by recession of the meniscus. (**b**) Evaporation by drying shrinkage. (**c**) Evaporation by homogeneous (center bubble) and heterogeneous (edge bubble) cavitation. The black arrows depict the tension in the liquid and the light blue arrows indicate the liquid flow. The gray background represents the stiffness of the matrix, a denser background stands for a higher stiffness. The wavy arrow on top illustrates the evaporated liquid. Reprinted from ref.[107], CC BY 4.0 (https://creativecommons.org/licenses/by/4.0/).

of liquid resulting from the pore volume shrinkage sustains the evaporation at the meniscus through poromechanical coupling.[38] The capillary pressure can be as high as 150 MPa for a pore radius of 1 nm considering water as a pore liquid, resulting in a significant compressive stress on the solid matrix.

Evaporation by cavitation may take place in porous materials with a stiff matrix and "ink-bottle"-shaped pores (Figure 5.1c), that is, large pores constricted by smaller pore necks.[177] Unlike evaporation by drying shrinkage, the tension in the liquid is not compensated by a contraction of the solid matrix and keeps rising, making the liquid metastable and susceptible to cavitation. Cavitation occurs by the nucleation of vapor bubbles in larger pores ahead of the pore constriction, where the effects of confinement by the matrix are less strong.[178–180] The evaporation proceeds at the meniscus and is sustained by the liquid flow toward the pore constriction at the expense of the formation and growth of the bubbles. The onset of cavitation depends on the state of the liquid: its saturation vapor pressure, surface tension, and temperature;[181–184] and on the properties of the porous media: the pore size distribution,[177,181,182,185] the stiffness of the solid matrix,[178,180] and the presence of defects.[186]

Evaporative drying of gels is commonly described as a succession of evaporation by drying shrinkage and meniscus recession.[65] Because the matrix of the gels is initially rather compliant, evaporative drying first proceeds by drying shrinkage, and the menisci remain mostly located on the outer surface of the gel. The decrease in the pore volume causes a progressive stiffening of the gel. As the tension in the liquid increases, it reaches a maximum once the radius of curvature of the meniscus becomes equal to the radius of the smallest pores. At this point, the liquid tension cannot overcome the stiffening of the solid matrix, marking the end of drying shrinkage and the beginning of evaporation by meniscus recession. This threshold is known as the maximum shrinkage. As the meniscus recedes into the pores, the compressive stress on the solid matrix related to capillary forces is released. In silica gels modified with a silylating agent, this coincides with a re-expansion of the solid matrix through the spring-back effect and results in hydrophobic aerogels.[25]

In addition to the two known evaporation mechanisms, it is theoretically possible that cavitation also plays a central role during the drying of gels at ambient pressure as suggested by Scherer & Smith.[21] Using classical nucleation theory (CNT), they estimated that homogeneous nucleation of vapor bubbles may happen before maximum shrinkage provided a small enough pore size (1−2 nm). Cavitation events are particularly intriguing in gels as they stabilize the tension in the liquid, which in turn would reduce the stress on the silica matrix and potentially prevent mechanical failure. A systematic literature review of publications citing

the Scherer & Smith paper revealed the absence of experimental evidence of cavitation events in the drying of gels to produce aerogels. Only three papers were found reporting visual observations of an opaque phase growing in the core of gels dried at ambient pressure that could possibly be associated with cavitation bubbles.[187–189] The lack of investigation on cavitation is presumably due to experimental limitations: monitoring the evaporative drying of gels requires non-destructive in operando methods at ambient pressure and with enough resolution and/or contrast to resolve cavitation events.

In the previous chapter, the volume of gas in silylated gels was up to 37 vol % of the gels' volume at the maximum shrinkage. This appeared inconsistent with a drying model based on dual-evaporation mechanisms although the spatial distribution of gas was not evaluated. This finding echoed with the theoretical study of Scherer & Smith and motivated the current work with the aim of evaluating cavitation as an additional evaporation mechanism. μCT records changes in the absorption of an irradiated specimen and allows the reconstruction of a 3D volume, in which the contrast is proportional to the attenuation coefficient of the specimen.[108] Quantitative imaging of the reconstructed volumes correlates the temporal variations in the attenuation coefficients of a specimen with changes in composition by image processing and subsequent modeling. Spatially resolved quantitative imaging can produce composition maps notably showing the distribution of vapor/air inside of the gels and provide information on the evaporation mechanisms. Besides absorption, changes in gels' composition can also be evaluated from the scattering of X-rays upon irradiation of a gel. In the wide-angle X-ray scattering (WAXS) region, the scattering signal arises from the molecular structure of the pore liquid and solid silica skeleton.[18,145] Deconvolution of these two signals and subsequent modeling allow us to calculate the average phase composition of the gels within the incident beam path.

The μCT data from the five silylated silica gels presented in chapter 4 were reanalyzed based on a spatially resolved μCT quantitative imaging workflow to test for the hypothesis of cavitation. While the workflow presented in the previous chapter only permitted to calculate the average phase composition, the procedure presented in this chapter generates composition maps of pore liquid and vapor/air within silica gels during drying. This computational approach consists in reducing and interpolating 4D reconstructed volumes, along with a systematic evaluation of instrumental and computational artifacts. Despite the resolution of the μCT scans (11 μm) being much larger than the size of the cavitation bubbles as postulated by Scherer & Smith (2 nm), the present approach was able to capture the spreading of a vapor/air phase in the gels well ahead of the maximum shrinkage. That gas phase appeared

and grew homogeneously across the sample, suggesting it was created by cavitation of the solvent. WAXS measurements and CNT estimations consolidated the results on the evaporation mechanisms. This chapter reports indirect evidence of evaporation by cavitation in silica gels by two methods, opening new aspects to the understanding and improvement of the evaporative drying process to produce high-performance, monolithic aerogels

5.2 Materials and Methods

µCT data reduction. The motivation behind the reduction of the reconstructed µCT data was to simplify the geometry of the gels during drying, taking advantage of their cylindrical symmetry. Doing so allowed us to work on a 2D or 3D data set instead of a 4D data set (three spatial dimensions and one temporal dimension). It also improved the presentation of the results that can be shown against different axes of the cylinders independently. The ROIs generated upon segmentation of the reconstructed µCT were used to overwrite the gray values of all background voxels in the slices by zero, generating masked slices that were exported as 8-bit tif images. For a single sample, 141 series of 1000+ masked slices were created, corresponding to the segmented volume of the gel over time. The latter was reduced by integrating the data over one or more axes of the samples. The raw gray values in the masked images were corrected for the anode heel effect[133] using a similar procedure as reported in appendix A.3. The resulting gray values were referred to as $g_{i,p,q,k}$ with i,p,q the z,x,y coordinates in the reconstructed volume, respectively and k the time index. $i,p,q,k \in \mathbb{N}$. Formally, $i = i_k$, $p = p_k$ and $q = q_k$ because the shape of the sample was changing over time. Three reduction procedures were used to generate different spatial and temporal representations of the reconstructed gray values during drying (Figure 5.2):

a) Azimuthal integration (3D, Figure 5.2a): the masked slices were integrated over the azimuth of the cylinder, resulting in 141 2D gray value maps along the height and radius of the cylinder: $g_{i,p,q,k} \rightarrow g_{i,j,k}$, where j represents the radial distance to the center of a masked slice. $j \in \mathbb{N}$. The azimuthal integration was computed with the Python DIPlib library[190] and the center of a slice was defined as the center of mass of the image. The domain of pixels in the maps belonging to the sample was referred to as Ω_k with $(i,j) \in \Omega_k$. This representation was referred to as the maps of the gray values along the height and radius (GHR maps).
b) Azimuthal and vertical integration (2D, Figure 5.2b): the GHR maps were further integrated over the vertical axis of the cylinder resulting in a single gray value map

along the radius of the gel and the scan number: $g_{i,j,k} \rightarrow g_{j,k}$. $j \in \Omega_k^r$ where Ω_k^r is the domain of pixels in the map belonging to the sample. This representation was referred to as the radial gray value map (GR map).

c) Slice integration (2D, Figure 5.2c): the masked slices were integrated over p and q, resulting in a single gray value map along the height of the gel and the scan number: $g_{i,p,q,k} \rightarrow g_{i,k}$. $i \in \Omega_k^h$ where Ω_k^h is the domain of pixels in the map belonging to the sample. This representation was referred to as the vertical gray value map (GH map).

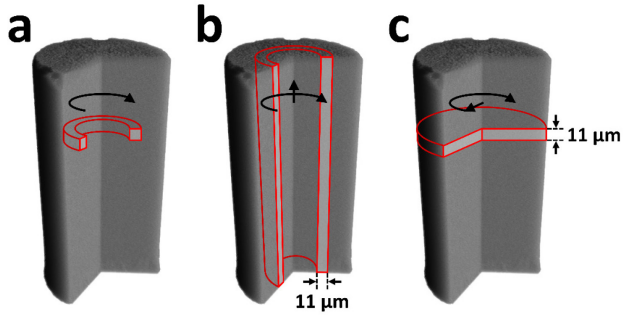

Figure 5.2 Illustration of the three data reduction procedures on the 3D segmented volume of gel M4 at the beginning of drying. (**a**) Azimuthal integration (GHR maps). (**b**) Azimuthal + vertical integration (GR map). (**c**) Slice integration (GH map). The black arrows indicate the direction of integration and the red contours depict an integrated volume element. The integration step was equal to the voxel size: 11 µm. Reprinted from ref.[107], CC BY 4.0 (https://creativecommons.org/licenses/by/4.0/).

A complete description of the reduction procedures can be found in appendix B.1. After data reduction, RAC maps were generated using eq. (4.2): $\mu = g(b-a)/255 + a$ and were referred to as MHR, MR and MH maps. These data were then used to model the phase composition of the drying silica gels.

µCT drying model. The spatial and temporal phase composition of the drying gels was computed by applying a local drying model to the reduced RAC maps, where local refers to calculation applied to each individual voxel. The construction of the drying model consists in (1) derive the main equations, (2) make assumptions to express additional equations, and (3) solve the system of equations using bilinear interpolation and correction factors. The model presented in this section applies to the MHR maps resulting from the azimuthal integration, but the notation can easily be extended to the two other data reduction procedures. At any time during drying, the silica gels were composed of three phases: solid silica skeleton, liquid n-hexane, and vapor/air. In the MHR maps, the RAC can thus be written as

$$\mu_{i,j,k} = \frac{\mu_{\mathrm{hex},i,j,k} V_{\mathrm{hex},i,j,k} + \mu_{\mathrm{skel},i,j,k} V_{\mathrm{skel},i,j,k} + \mu_{\mathrm{air},i,j,k} V_{\mathrm{air},i,j,k}}{V_{\mathrm{voxel}}}, \tag{5.1}$$

where $\mu_{\varphi,i,j,k}$ and $V_{\varphi,i,j,k}$ are the RAC and volume of a phase φ respectively at a vertical and radial coordinate (i,j) and at scan k for the hexane, skeleton and vapor/air phases, and V_{voxel} is the voxel volume. The attenuation of the vapor/air phase was set to zero, thus: $\mu_{\text{air},i,j,k} = 0$. The RAC of the silica skeleton and of liquid n-hexane phases was assumed constant and homogeneous throughout drying: $\mu_{\text{hex},i,j,k} = \mu_{\text{hex}}$ and $\mu_{\text{skel},i,j,k} = \mu_{\text{skel}}$. μ_{hex} was calculated from the reference n-hexane measurements, $\mu_{\text{hex}} = 0.155$. Eq. (5.1) can be rewritten as a function of the volume fraction of each phase at a given voxel rather than the total volume, leading to the first equation of the drying model:

$$\mu_{i,j,k} = \mu_{\text{hex}} f_{\text{hex},i,j,k} + \mu_{\text{skel}} f_{\text{skel},i,j,k}, \tag{5.2}$$

where $f_{\varphi,i,j,k} = V_{\varphi,i,j,k}/V_{\text{voxel}}$ for a phase φ. Additionally, the volume conservation implies:

$$f_{\text{hex},i,j,k} + f_{\text{skel},i,j,k} + f_{\text{air},i,j,k} = 1. \tag{5.3}$$

The volume fraction maps were referred to as the HEXHR, SKELHR, AIRHR maps for $f_{\text{hex},i,j,k}$, $f_{\text{skel},i,j,k}$ and $f_{\text{air},i,j,k}$, respectively. Solving the equation system required taking assumptions on the composition of the gels throughout drying. First, the HEXHR maps were computed by assuming that the hexane content was zero at the end of drying. To do so, a RAC map representative of the dry gel was generated:

$$\mu^{\text{dry}}_{i,j,k_f} = \frac{1}{N_d}\left(\mu_{i,j,k_f} + \sum_{k_d \le k < k_f} \mu^{\text{F}}_{i,j,k\to k_f} \cdot \gamma_{k\to k_f}\right), \tag{5.4}$$

where $\mu^{\text{dry}}_{i,j,k_f}$ is an artificial MHR map defined over the domain Ω_{k_f}, $k_f = 140$ is the final scan, k_d is a threshold scan number from which the hexane content is assumed to be zero, N_d is the number of scans in $k_d \le k \le k_f$, $\mu^{\text{F}}_{i,j,k\to k_f}$ is a map generated by bilinear interpolation of a map from scan $k \ge k_d$ onto the domain of the map at scan $k = k_f$ and $\gamma_{k\to k_f}$ is a scaling factor. The scaling factor was defined as the volume ratio between a source scan k_1 and a target scan k_2 as: $\gamma_{k_1\to k_2} = V_{k_1}/V_{k_2}$. Bilinear interpolation was required so that a map defined over a domain Ω_1 can match the domain Ω_2 of another map, because the change in the sample volume throughout drying implied that the domain Ω_k was different for all scans. The map $\mu^{\text{dry}}_{i,j,k_f}$ was then interpolated from source scan k_f onto target scan $0 \le k < 140$, resulting in the maps $\mu^{\text{dry,F}}_{i,j,k_f\to k}$ defined over Ω_k at any scan. The HEXHR maps of any scan could be computed by replacing the product $\mu_{\text{skel}} f_{\text{skel},i,j,k}$ in eq. (5.2) by $\mu^{\text{dry,F}}_{i,j,k_f\to k}$ with a scaling factor:

$$f_{\mathrm{hex},i,j,k} = \frac{\mu_{i,j,k} - \mu^{\mathrm{dry,F}}_{i,j,k_f \to k} \cdot \gamma_{k_f \to k}}{\mu_{\mathrm{hex}}}. \tag{5.5}$$

The SKELHR maps were computed by assuming a zero vapor/air content at the beginning of drying from scan number k_1 to k_2. The maps at $k_1 < k \leq k_2$ were rescaled onto the domain of target scan k_1 and were then averaged over $k_1 \leq k \leq k_2$ to compute an artificial map representative of the alcogel $\mu^{\mathrm{alco}}_{i,j,k_1}$:

$$\mu^{\mathrm{alco}}_{i,j,k_1} = \frac{1}{N_a}\left[\mu_{i,j,k_1} + \sum_{k_1 < k \leq k_2} \mu^{\mathrm{F}}_{i,j,k \to k_1} \gamma_{k \to k_1} + \mu_{\mathrm{hex}}\left(1 - \gamma_{k \to k_1}\right)\right] \tag{5.6}$$

where $\mu^{\mathrm{F}}_{i,j,k \to k_1}$ is the map interpolated from scan $k_1 < k \leq k_2$ to scan $k = k_1$ and N_a is the number of scans in $k_1 \leq k \leq k_2$. k_d, k_1, and k_2 were evaluated using the global quantitative imaging approach reported in chapter 4. The rightmost product in eq. (5.6) was an additional scaling factor. An artificial hexane map representative of the alcogel at scan $k = k_1$ was computed as:

$$f^{\mathrm{alco}}_{\mathrm{hex},i,j,k_1} = \frac{\mu^{\mathrm{alco}}_{i,j,k_1} - \mu^{\mathrm{dry,F}}_{i,j,k_f \to k_1} \cdot \gamma_{k_f \to k_1}}{\mu_{\mathrm{hex}}}. \tag{5.7}$$

The skeleton map at $k = k_1$ was then calculated by substituting $f_{\mathrm{hex},i,j,k}$ by $f^{\mathrm{alco}}_{\mathrm{hex},i,j,k_1}$ in eq. (5.3), resulting in $f_{\mathrm{skel},i,j,k_1}$. The SKELHR maps for the other scans were computed by interpolating and rescaling the SKELHR map from scan k_1 to scan $k \neq k_1$:

$$f_{\mathrm{skel},i,j,k} = f^{\mathrm{F}}_{\mathrm{skel},i,j,k_1 \to k} \cdot \gamma_{k_1 \to k}, \tag{5.8}$$

where $f^{\mathrm{F}}_{\mathrm{skel},i,j,k_1 \to k}$ is the skeleton map interpolated from source scan $k = k_1$ to target scan $k \neq k_1$. The AIRHR maps were finally calculated with eq. (5.3). The complete derivation of the drying model is reported in appendix B.2 and the bilinear interpolation algorithm is reported in appendix B.3. Sample M3 had a large meniscus at its bottom (Figure B.5) leading to complications in the data reduction procedure and was thus discarded. Similar equations were derived for the MR and MH maps (not shown), and the resulting volume fraction maps were referred to as the HEXR, SKELR and AIRR and HEXH, SKELH and AIRH maps, respectively. The GR and GH maps and the corresponding volume fraction maps were interpolated from scan number to time to create profiles monotonically increasing with time. Finally, all maps were saved as 2D float arrays, which were then converted into images to create the figures. The data processing, modeling and the creation of the figures were carried out in Python with the DipLib,[190] Matplotlib,[191] NumPy,[192] Pillow[193] and Scipy[194] libraries.

In operando X-ray scattering. X-ray scattering experiments were performed to monitor the structure of the gels during drying at a wide angle, which corresponds to the molecular structure of the silica skeleton and n-hexane. The general idea was to correlate the evolution of scattering intensity in the wide-angle region with the change in the specimen composition within the volume probed by the beam. X-ray scattering measurements were performed at the BESSY II synchrotron of the Helmholtz-Zentrum für Materialien and Energie (Germany, Berlin) at the μSpot beamline.[195] One silylated silica gel (labeled M6) was dried at ambient pressure in a tailored measurement cell adapted from ref.[18] The cell was constructed from anodized aluminum with a silicon wafer and a silicon nitride window (NORCADA low-stress SiNx membrane, 10 mm length/width, 1000 nm thickness) placed in the direction of the X-ray beam. The top of the cell was sealed with a valve (1/8 in., PN63/1.4408, shortened with an adapter to ca. 26 mm), and a museum glass was placed on the side to allow the collection of digital pictures of the sample with a digital microscope camera (TOOLKRAFT USB microscope, 5 MP). The cell was mounted on a rotary stage that could host up to five cells. At the time of measurement, sample M6 was transferred from its n-hexane storage solution to the measurement cell, whereas an empty cell was used for background correction. The valve was opened fully before the measurement

Experiments were performed using a monochromatic X-ray beam at 18 keV and a B4C/Mo Multilayer (2 nm period) monochromator. A spot size of 30 × 30 μm^2 was adjusted by a series of pinholes. The cell position was set so that the beam hits the sample at a fixed location, 4 mm from the bottom of the sample. The scattering data were collected on an Eiger 9 M detector with a 75 × 75 μm^2 pixel size. A quartz reference was fixed at the same distance from the beam source as the sample and was used to determine the sample−detector distance, beam center, tilt, and rotation. A glassy carbon Standard Reference Material 3600 (SRM 3600) of the National Institute of Standards and Technology (NIST) was measured for absolute intensity calibration.[154] The transmission through the sample was calculated from the X-ray fluorescence signal collected from a lead beamstop by using a RAYSPEC Sirius SD-E65133-BE-INC detector equipped with an 8 μm beryllium window, while the primary beam intensity was monitored and normalized by using an ion chamber. Each data frame was collected by exposing the sample to radiation for 1 s every 27 s, with the rotary stage alternating between an empty cell and the sample cell. The resulting data were preprocessed/previewed using the DPDAK software package[196] and a custom Python script utilizing pyFAI library.[197] The preprocessing steps involved integration to 1D scattering curves and subtraction of an instrumental background (i.e., the empty cell). The scattering data were corrected for

transmission and primary beam intensity and corrected for a "container background". To normalize the data with the sample thickness, the diameter of the gel was determined from the optical images collected during drying (see appendix B.4). As a final step, data were scaled to absolute units (i.e., cm^{-1}) by sample thickness normalization and by the scaling factor of the glassy carbon.

The azimuthal integration of X-ray scattering measurements provided scattered intensity $I(q)$ as a function of the momentum transfer q, using the wavelength of the synchrotron beam λ and the scattering angle 2θ (eq. (3.3)), resulting in an accessible q range of ca. 0.07 nm^{-1} to 40 nm^{-1}. Collected data were analyzed in a wide-angle diffraction region (3−30 nm^{-1}) to obtain time-dependent volume fraction profiles. To this end, diffraction data of liquid hexane in a borosilicate glass capillary were collected. The latter was reduced following the same procedure described above (i.e., monitor and transmission normalization, empty capillary subtraction, radial integration) but not scaled by sample thickness or corrected by glassy carbon scaling factor.

To compute the hexane, skeleton and vapor/air volume fraction profiles of the gel at each data frame, the diffraction 1D profiles of the hexane reference: $I_{\mathrm{hex}}(q,t)$ and of the dry aerogel (i.e. last collected data frame): $I_{\mathrm{dry}}(q,t)$ were modeled using a baseline function and a function sum of three pseudovoigts:

$$I_{\varphi}(q,t) = I_{\varphi}^{(\mathrm{base})}(q,a,t) + \sum_{j=1}^{3} I_{\varphi}^{(\mathrm{PV})}\left(q, A_j, q_{0,j}, \Gamma_j, r_j\right), \tag{5.9}$$

where $I_{\varphi}(q,t)$ stands for $I_{\mathrm{hex}}(q,t)$ or $I_{\mathrm{dry}}(q,t)$ and the parameters A_j, $q_{0,j}$, Γ_j, r_j of the pseudovoigt represent the area, the center, the full width at half maximum and the Gaussian-Lorentzian ratio respectively. Similarly to the μCT drying model, the hexane content in the gel at the end of drying was assumed to be zero, so that the scattered intensity of the dry gel arose only from the skeleton and vapor/air. The baseline function for the hexane reference: $I_{\mathrm{hex}}^{(\mathrm{base})}(q,a,t)$ was set as a linear polynomial with slope a:

$$I_{\mathrm{hex}}^{(\mathrm{base})}(q,a,t) = a(t)\cdot q \tag{5.10}$$

and the baseline function for the dry aerogel was set as a power law decay with a constant a representing the law's exponent:

$$I_{\mathrm{dry}}^{(\mathrm{base})}\left(q,a,t=t_f\right) = q^{a(t_f)}, \tag{5.11}$$

where $t = t_f$ is the time of the last data frame. During the modeling of the hexane and dry aerogel diffraction profiles, an additional parameter representing the data background was used. To obtain volume fraction profiles of each phase, two more steps were necessary. At

first, the volume fraction of the skeleton in the dry aerogel was calculated by assuming a composition: $Si_{23}O_{40}C_9H_{28}$ and a skeletal density of approximately 1.9 g cm^{-3}. That composition was estimated by comparing the weight of fully dried silylated gels with fully dried unmodified gels and by assuming that the weight difference was only due to the silyl groups in the modified gels: $Si(CH_3)_3$. Moreover, the unmodified gels were left in a desiccator for 24 h before being weighed to complete drying.

Subsequently, by mean of the Python library xraylib[198,199] and the Beer-Lambert equation, it was possible to compare the experimental transmission of the dry aerogel T_{dry} and the volume fraction-dependent theoretical transmission:

$$T_{\mathrm{dry}} = \exp\left(-f_{\mathrm{skel}}^{\mathrm{dry}}\mu_{\mathrm{skel}}d_{\mathrm{dry}}\right), \tag{5.12}$$

with $f_{\mathrm{skel}}^{\mathrm{dry}}$ the skeleton volume fraction of the dry gel, μ_{skel} its attenuation coefficient for an 18 keV X-ray beam and d_{dry} the sample diameter obtained with the optical microscope at the corresponding time. The model functions $I_{\mathrm{hex}}(q)$, $I_{\mathrm{dry}}(q)$ and $f_{\mathrm{skel}}^{\mathrm{dry}}$ were combined and used for fitting the time-dependent scattering profiles $I(q,t)$ of the drying gel as follows:

$$I(q,t) = s_{\mathrm{hex}}f_{\mathrm{hex}}(t)I_{\mathrm{hex}}(q) + \frac{f_{\mathrm{skel}}(t)}{f_{\mathrm{skel}}^{\mathrm{dry}}}I_{\mathrm{dry}}(q) + b(t), \tag{5.13}$$

with $f_{\mathrm{hex}}(t)$ and $f_{\mathrm{skel}}(t)$ the hexane and skeleton time dependent volume fractions, $b(t)$ a background independent of q, and s_{hex} a constant factor to scale the hexane data to absolute units (i.e. cm^{-1}). s_{hex} was calculated by assuming that at $t = 0$, the vapor/air content in the gel was zero, leading to:

$$1 = s_{\mathrm{hex}}f_{\mathrm{hex}}(t=0) + f_{\mathrm{skel}}(t=0). \tag{5.14}$$

At $t > 0$, the time dependent vapor/air volume fraction $f_{air}(\mathrm{t})$ was calculated by modifying eq. (5.14):

$$f_{air}(t) = 1 - \left(s_{hex}f_{hex}(t) + f_{hex}(t)\right), \tag{5.15}$$

which implies $f_{\mathrm{air}}(t=0) = 0$. All data modeling was performed using the Scipy optimize library provided by Python.[194] In order to improve performance and result reliability, fits were performed by providing analytical functions and jacobians. Best-fit parameter uncertainties were therefore calculated by evaluating the Jacobian at the minimum of the penalty function distribution.

5.3 Results and Discussion

Hexane and Vapor/Air Spatial and Temporal Distributions. This section reports and discusses the spatial distribution and evolution of the gels phase composition generated by μCT quantitative imaging. The azimuthal integration of the masked slices produced well-defined GHR maps shown in Figure 5.3a for sample M4 at different drying stages. The drying shrinkage can be seen with the decrease in height and maximum radius of the gel up to the maximum shrinkage at 7.6 h, together with an increase of the average gray values. The maximum shrinkage was followed by the re-expansion of the gel (spring-back effect) and by a decrease in the gray values. Silica gels dried in the fume hood under similar conditions remained transparent until the maximum shrinkage and only turned opaque upon re-expansion. The hexane, skeleton and vapor/air volume fractions along the height and radius of sample M4 are shown in Figure 5.3b-d. At the start of drying, the hexane and skeleton phases were uniformly distributed in the gel at an average volume fraction of 94 and 6 vol %, respectively, suggesting a homogeneous gelation process. The fraction of vapor/air was 0 vol %, as it was set in the drying model. Up to the maximum shrinkage, the hexane content decreased while the skeleton and vapor/air contents increased, each phase being still relatively homogeneously distributed across the entire gel's volume. The emergence of the vapor/air phase in the gel was not clearly depicted in the AIRHR maps due to the noise in the data, but Figure 5.3d shows a non-negligible amount of vapor/air before the maximum shrinkage. Near the end of drying, the skeleton and vapor/air spatial distributions were homogeneous, and after 14 h of drying, the gel was composed of about 22 and 78 vol % of skeleton and vapor/air, respectively. Heterogeneities in the repartition of hexane and vapor/air appeared at the maximum shrinkage where the hexane volume fraction abruptly dropped to ca. 0 vol % at the top of the gel (Figure 5.3b). However, the fact that each map corresponds to a single drying stage and the presence of noise in the maps limited the analysis. The spatial and temporal distribution of the hexane and vapor/air phases was thus analyzed based on the vertical and radial volume fraction maps derived by modeling the GH and GR maps, which had the advantage of depicting the gel state at all drying stages along the two main axes of the cylindrical samples. The results are shown in Figure 5.4.

The noise in the gray values of the vertical and radial maps in Figure 5.4a was significantly lower compared to the corresponding GHR maps, resulting in smoother volume fraction maps, which permitted a more accurate evaluation. Slight variations in the vertical distribution of hexane were observed before the maximum shrinkage, with a higher concentration of

hexane at the bottom of the gel than at the top (Figure 5.4b). The top of the gel was composed of relatively more vapor/air than at the bottom before the maximum shrinkage (Figure 5.4d), whereas the skeleton spatial distribution remained static throughout the entire drying process,

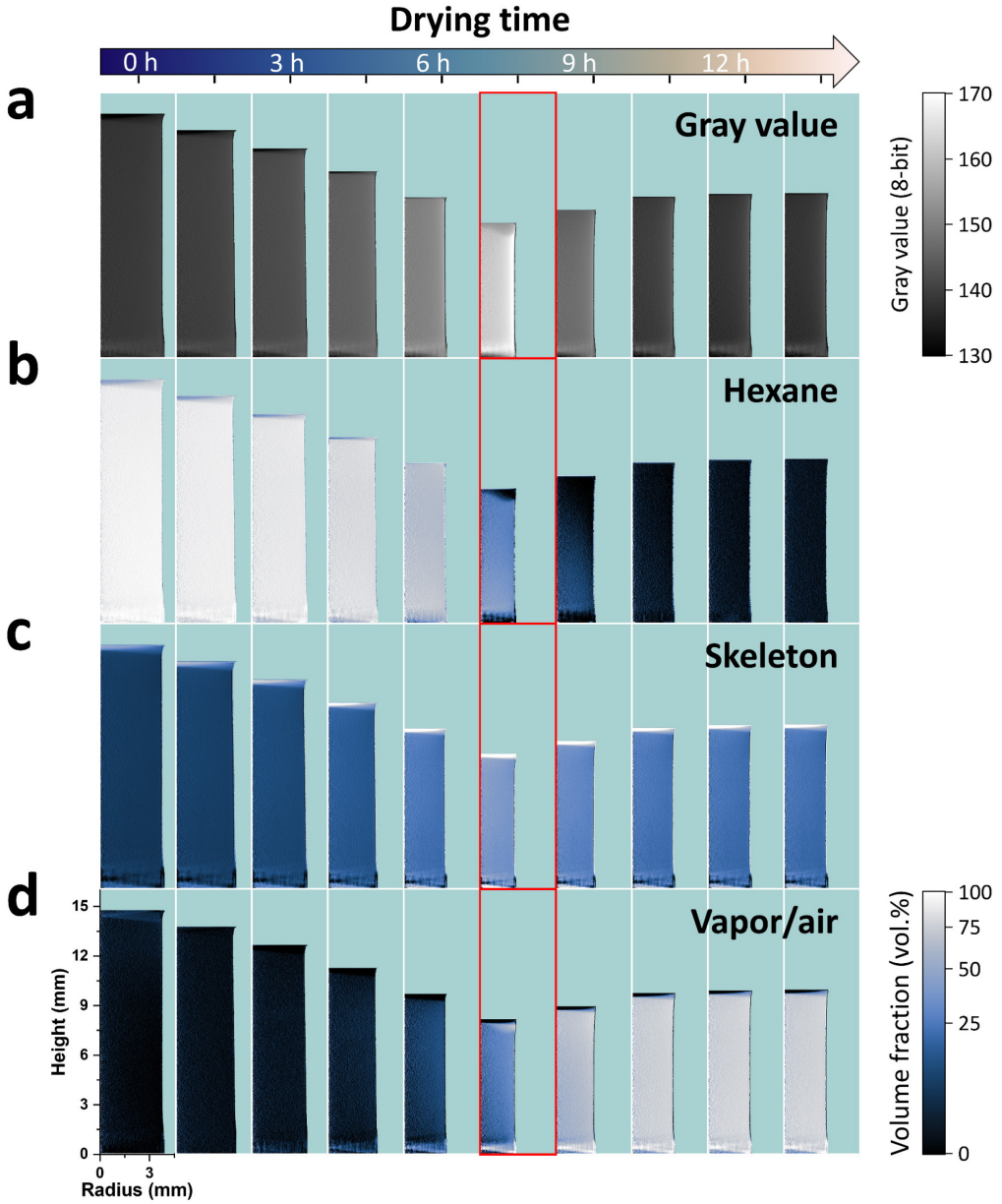

Figure 5.3 GHR and volume fraction maps of sample M4 at 10 selected drying stages on top of a cyan background. (**a**) GHR maps with the corresponding gray value scale on the right. The brightness and contrast in the images of the GHR maps are adjusted to improve visualization. (**b**) HEXHR maps. (**c**) SKELHR maps. (**d**) AIRHR maps. The color scale of the volume fraction maps is shown at the bottom right of the figure. The volume fraction maps are normalized between 0 and 100%. The images of the volume fraction maps are encoded with a gamma value of 0.5 to improve the visualization. The time scale is illustrated with an arrow on top of the figure, and the time gap between the maps in a given panel is 1.56 ± 0.05 h. The length scale of all maps is indicated in the first map of panel (**d**). The maps corresponding to the maximum shrinkage are outlined in red. Each map consists of 410 × 1455 noninterpolated data points. Reprinted from ref.[107], CC BY 4.0 (https://creativecommons.org/licenses/by/4.0/).

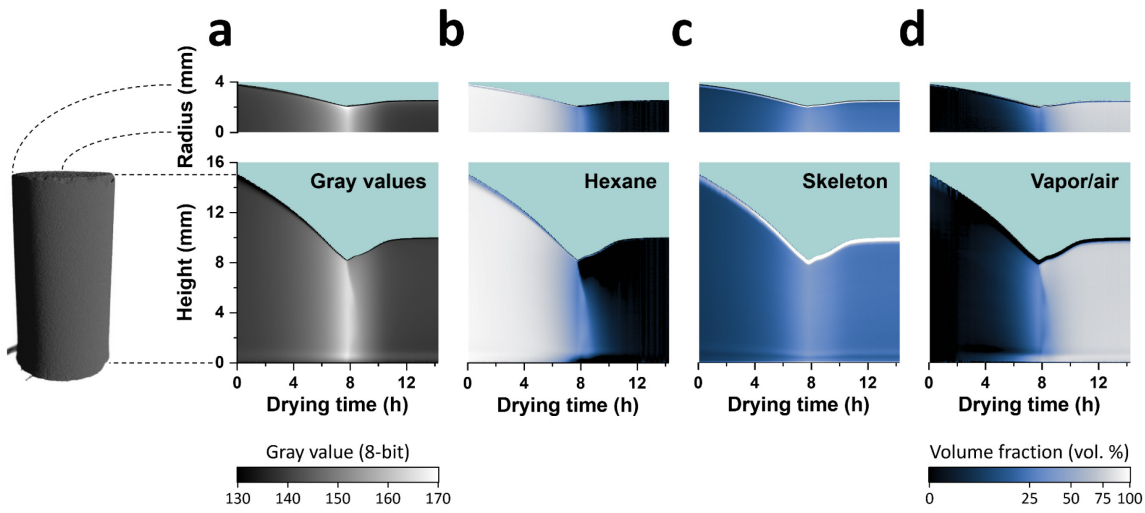

Figure 5.4 Radial and vertical maps of the gray values and volume fraction of sample M4 on top of a cyan background. The 3D image on the left of the figure depicts the segmented volume of M4 at the beginning of drying, and the dashed lines illustrate the radial and vertical axes of the cylinder against which the radial and vertical maps are shown. (**a**) GR and GH maps. The gray value scale is shown at the bottom of panel (**a**). The brightness and contrast in the images of the GR and GH maps are adjusted to improve visualization. (**b**) HEXR and HEXH maps. (**c**) SKELR and SKELH maps. (**d**) AIRR and AIRH maps. The images of the volume fraction maps are encoded with a gamma value of 0.5 to improve visualization. The time axis is shown in each vertical map, and the length scale is shown in the radial and vertical maps of panel (**a**). The radial maps consist of 1460 × 410 data points and the vertical maps consist of 1460 × 1455 points. In all maps, the horizontal time resolution is interpolated from 141 time stamps onto 1460 points. Reprinted from ref.[107], CC BY 4.0 (https://creativecommons.org/licenses/by/4.0/).

as set in the drying model (Figure 5.4c). Upon spring-back, significant variations in the repartition of hexane and vapor/air appeared along the height of the gel. The top region of the gel got depleted in hexane first, leading to an increase in the vapor/air volume fraction in the same region (Figure 5.4b,d).

Hexane and vapor/air vertical profiles were extracted from the HEXH and AIRH maps to quantify the variations before and after maximum shrinkage (Figure 5.5). At the maximum shrinkage (7.6 h), the vapor/air content abruptly increased from 30 to 52 vol % near the top of the gel within 6 min (Figure 5.5a) and was followed by a wave-like drying front traveling downward in the sample as the gel started re-expanding (Figure 5.5b). At 7.9 h, the vapor/air content rose at the bottom of the gel, which corresponded to another drying front traveling upward. At 8.5 h, those heterogeneities along the gel height stabilized, although a gradient of vapor/air was still present from the top to the bottom of the gel (Figure 5.5b). Similar but opposite features were noted in the hexane vertical profiles (Figure 5.5c,d). It was worth noting that at 8.5 h, there was still a significant fraction of hexane remaining with up to 29 vol % in the bottom regions of the gel (Figure 5.5c,d). At ca. 10 h of drying, the re-expansion of the gel slowed down and the variations in the hexane and vapor/air content along the gel height

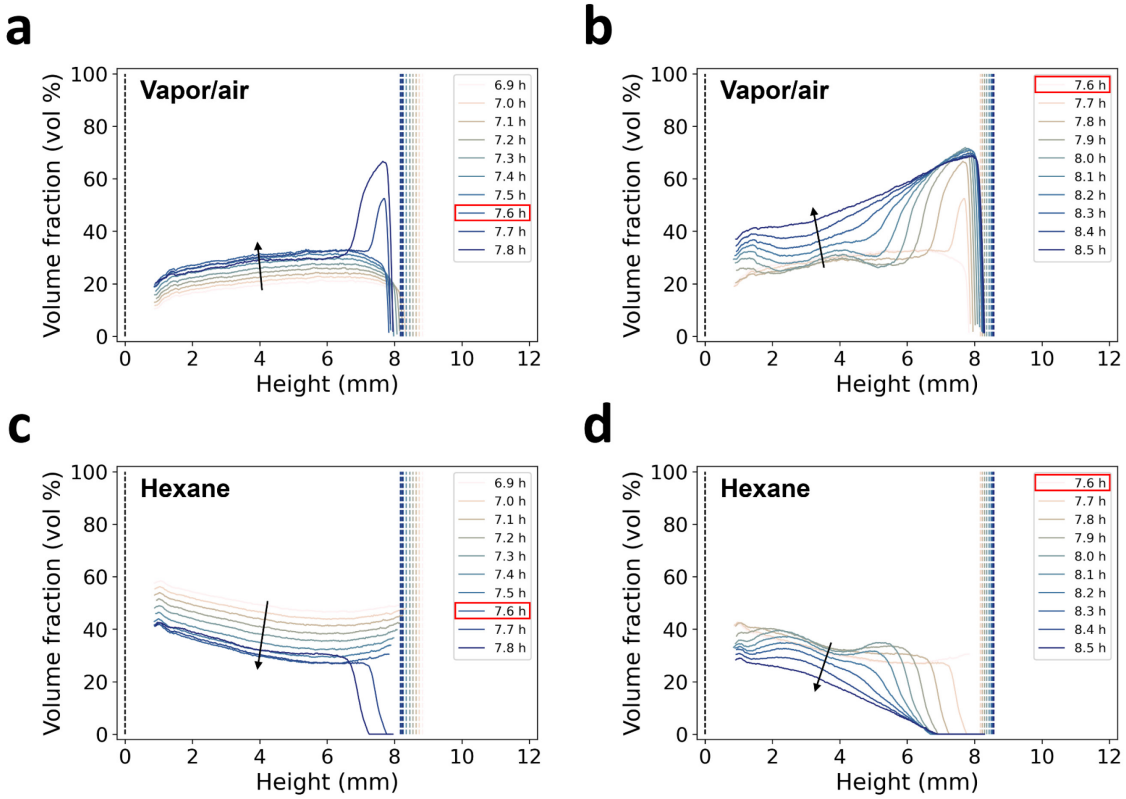

Figure 5.5 Volume fraction profiles of hexane and vapor/air along the height of sample M4 at selected time stamps. Vapor/air profiles between 6.9 and 7.8 h (**a**) and between 7.6 and 8.5 h (**b**). Hexane profiles between 6.9 and 7.8 h (**c**) and between 7.6 and 8.5 h (**d**). The profiles in panels (**a**) and (**c**) correspond to the μCT scans before the maximum shrinkage and shortly after, while the profiles in panels (**b**) and (**d**) correspond to the μCT scans at the maximum shrinkage and after. The dashed lines correspond to the bottom (h = 0 mm) and to the top of the sample. The time of maximum shrinkage is highlighted in red in the legends. The spacing between the profiles in each panel corresponds to a single μCT scan. The profiles were extracted from the AIRH and HEXH maps by excluding the values affected by the artifacts at the edges for better visualization. Reprinted from ref.[107], CC BY 4.0 (https://creativecommons.org/licenses/by/4.0/).

dissipated with an average hexane volume fraction close to zero and an average vapor/air volume fraction at 73 vol %. Between 10 and 14 h, the volume fraction of vapor/air slightly increased as the gel re-expanded to reach a final value of 78 vol % (Figure 5.4d).

The emergence of the vapor/air phase in the gels was referred to as the "cavitation onset" and was evaluated from the AIRH maps by extracting vertical volume fraction profiles near the start of drying (Figure 5.6). The vertical profiles indicated a nonzero amount of vapor/air from 2.0 h of drying in sample M4, with a higher concentration in the middle of the gel. Similar conclusions were drawn from the analysis of samples M1, M2, and M5. The only notable difference was a shift in the timing and duration of specific events such as the spring-back effect and the emergence of the vapor/air phase (especially in sample M1) due to slightly different starting volumes of the gels and possibly drying conditions (Figure B.9 – Figure B.18).

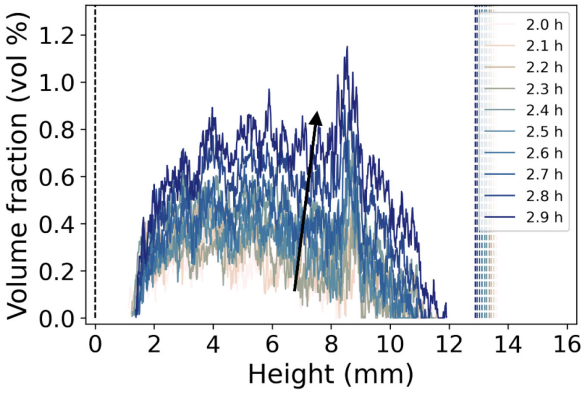

Figure 5.6 Vertical vapor/air profiles extracted from the AIRH maps of sample M4 between 2.0 and 2.9 h. The dashed lines correspond to the bottom (h = 0 mm) and to the top of the sample. The spacing between each profile corresponds to a single μCT scan. Reprinted from ref.[107], CC BY 4.0 (https://creativecommons.org/licenses/by/4.0/).

As an attempt to quantify the cavitation onset, the AIRH maps (Figure 5.4d and Figure B.12 – Figure B.14d) were integrated over the height of the gel, giving an average vapor/air volume fraction. The cavitation onset was then defined as the drying time at which the average vapor/air volume fraction rose above an arbitrary volume fraction of 1 vol %. The time of cavitation onset for samples M1, M2, M4, and M5 was 2.93, 3.50, 3.64, and 3.43 h respectively. Additionally, the pore volume shrinkage was calculated at the cavitation onset. It was defined as $\nu_{p,k_{\mathrm{cav}}} = V_{p,k_{\mathrm{cav}}}/V_{p,0}$ where $V_{p,k_{\mathrm{cav}}}$ and $V_{p,0}$ is the pore volume at the cavitation onset and at the start of drying, respectively. The pore volume shrinkage was 64.1, 55.3, 52.7, and 51.8 vol % for samples M1, M2, M4, and M5, respectively. The time and pore volume shrinkage of sample M1 seemed to deviate compared to those of the three other samples. The global μCT quantitative imaging analysis on that sample also showed deviations compared to the other samples (chapter 4). This sample put apart, the proximity of the results between the three other samples suggested that the cavitation onset was related to a particular state of the gel. Figure 5.5a and Figure 5.6 showed a steady growth of the fraction of the vapor/air phase in the gel from the cavitation onset until the maximum shrinkage throughout drying, which was also observed in the other samples. Table 5.1 summarizes the properties of the gels upon the cavitation onset.

To corroborate the observations made from the μCT measurements, the phase composition derived by modeling of the WAXS data was compared with the results from μCT modeling at a representative location in the gel. Although WAXS did not allow spatial resolution of the vapor-air phase, it could detect the emergence of a vapor-air phase prior to the maximum shrinkage. Figure 5.7 shows the hexane, skeleton, and vapor/air volume fraction profiles computed from both methods against a normalized time scale. The evolution of the

Table 5.1 Properties of all samples at the cavitation onset. t_{cav} and t_{MS} stand for the time of cavitation onset and the time of maximum shrinkage, respectively. The volume shrinkage is the ratio of the gel volume over the gel initial volume at the start of drying. Reproduced from ref.[107], CC BY 4.0 (https://creativecommons.org/licenses/by/4.0/).

Sample	t_{cav} (h)	t_{cav}/t_{MS}	Pore volume shrinkage at t_{cav} (vol %)	Volume shrinkage at t_{cav} (vol %)
M1	2.93	0.360	64.1	66.5
M2	3.50	0.436	55.3	58.8
M4	3.64	0.471	52.7	55.8
M5	3.43	0.482	51.8	54.9

scattering profiles in the 3−30 nm^{-1} region and examples of the data fit can be found in Figure B.19 and Figure B.20, respectively. The volume fraction profiles corresponded to the composition of the gels 4 mm above their bottom (where the X-ray beam probed the sample during the in operando X-ray scattering experiment). The profiles generated by these two methods were relatively consistent. The WAXS modeling results suggested a content of 14 vol % of vapor/air in the gel before the maximum shrinkage, supporting the μCT results. The initial and final compositions of the gels were similar between both methods with variations of ca. 2 vol %. In the probed location, the fraction of vapor/air raised above 1 vol % at $t/t_{MS} \approx$ 0.3 from the μCT measurement, and at $t/t_{MS} \approx 0.63$ in the WAXS measurements (Figure 5.7). This cavitation onset in the gels dried in the μCT setup was lower than the values reported in Table 5.1 because it only accounted for the gas volume detected at a specific height in the gels. The differences observed between μCT and WAXS results during drying could be due to the different environments in the two experiments. Sample M6 dried faster in the scattering setup and reached the maximum shrinkage after ca. 4.3 h of drying versus ca. 7.5 h for the samples

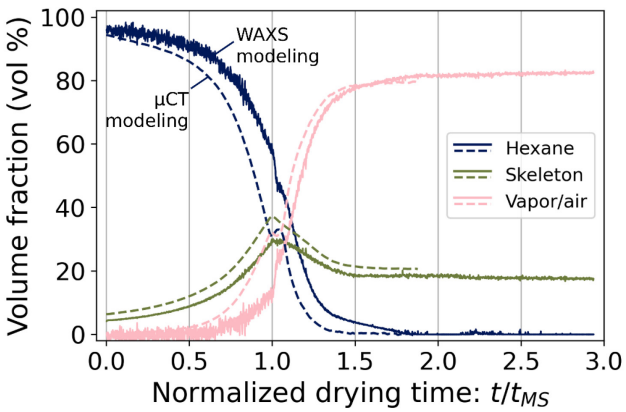

Figure 5.7 Average phase composition of gel M6 computed by WAXS modeling (full lines) along with the phase composition computed by μCT modeling, averaged over gels M1, M2, M4 and M5 (dashed lines) at the same location in the gel. The time scale is normalized by the time of maximum shrinkage t_{MS}, which was 4.3 h for the WAXS modeling and ca. 7.5 h for the μCT modeling. Reprinted from ref.[107], CC BY 4.0 (https://creativecommons.org/licenses/by/4.0/).

dried in the μCT setup. This could suggest that the gel composition and the cavitation onset have a nonlinear dependency on the drying rate. Additionally, the lower skeleton volume fraction from WAXS modeling compared to μCT modeling could be related to the assumptions on the chemical composition and density of the silica skeleton set in the WAXS drying model.

Evaporation Mechanisms. The spatial and temporal phase composition of the gels was interpreted in terms of evaporation mechanisms with an emphasis on cavitation. Based on the distribution and evolution of the hexane and vapor/air phases, it can be proposed that the evaporative drying of the silica gels prepared in this study proceeded in three distinct stages:

(1) Evaporation by drying shrinkage from 0 to ca. 3.5 h.
(2) Evaporation by a combination of cavitation and drying shrinkage from ca. 3.5 h to 7.5 h (maximum shrinkage).
(3) Evaporation by meniscus recession from ca. 7.5 h until complete evaporation of the remaining hexane.

During stage (1), the hexane content decreased homogeneously without any vapor/air inclusions (Figure 5.4d) and the volume of hexane evaporated matched the volume shrinkage of the gel, which was consistent with the drying shrinkage model.[65,176] During stage (2), the drying shrinkage proceeded until the maximum shrinkage was reached in parallel with the growth of a vapor/air phase in the gels. Both the μCT and WAXS results showed that vapor/air appeared ahead of the maximum shrinkage and increased steadily, and μCT volume fraction maps revealed a relatively homogeneous distribution of vapor/air across the whole gel's volume (Figure 5.3d, Figure 5.5a, Figure 5.6), which suggested it was created by cavitation of hexane. In stage (3), the gel sprung back and a drying front was observed growing vertically through the sample (mostly downward). This stage was associated with the recession of the hexane-vapor interface into the pores and corresponded exactly to the re-expansion of the gels. Gels dried in the fume hood turned opaque upon re-expansion and gradually shifted toward a bluish color under a dark background, the latter being caused by Rayleigh scattering.[200] The time resolution of the μCT experiments did not allow us to distinguish potential adiabatic burst events. Presumably, no additional cavities were created ahead of the drying front in stage (3) as the vapor/air volume fraction did not increase at those locations (Figure 5.5a). The gradient in the hexane and vapor/air volume fraction along the height of the gel during the re-expansion confirmed the heterogeneous nature of the spring-back effect, which was attributed to the design of the drying chamber used the μCT drying experiments.

The hypothesis of cavitation was indirectly supported by two experimental observations. First, the vapor-air phase grew uniformly without any visible drying front. This was inconsistent with an evaporation mechanism by recession of the meniscus, which would proceed by the ingress of the liquid−vapor interface into the pores, forming a drying front. It also seemed unfeasible that evaporation by drying shrinkage and meniscus recession occurred simultaneously in the gels, given that the recession of the meniscus would result in local relaxation of the capillary stress, whereas the drying shrinkage kept proceeding steadily throughout stage (2). The absence of a drying front supports evaporation by cavitation although it must be noted that this feature might also be associated with other mechanisms, such as fractal-like penetration of the vapor phase.[201,202] Second, the gels turned opaque only upon re-expansion and not at the cavitation onset. The change of transparency during stage (3) arguably corresponded to the apparition of pores filled with vapor/air that showed a characteristic size large enough to scatter visible light (400− 700 nm). As such a change was not observed during stage (2), it suggested the absence of a continuous medium of vapor/air in the gels larger than 400 nm. This observation would be consistent with the growth of vapor/air within the gels by cavitation with cavities smaller than the wavelength of visible light. Nevertheless, it may be possible for gels to turn opaque upon cavitation.[187–189] Those elements suggested that the vapor/air phase in the gel prior to the maximum shrinkage was not caused by meniscus recession but by cavitation of the solvent. Additionally, the cavitation onset coincided with a pore volume shrinkage of 51−64 vol % (Table 5.1). Because cavitation in porous materials depends on the porous media stiffness,[178,180] which is closely related to the pore volume, the pore volume shrinkage is a critical parameter for the emergence of cavitation in the gels. As vapor/air bubbles appeared at the start of stage (2), they grew steadily and uniformly as shown by the vapor/air vertical distribution (Figure 5.4d, Figure 5.5a, Figure 5.6). This growth was consistent with the phenomenology of evaporation by cavitation and drying shrinkage. The first cavities were presumably created in large pores ahead of the outer surface of the gel, where the liquid confinement by the solid matrix was the smallest.[178] At this stage, there was no deceleration of the volume shrinkage upon the emergence of vapor/air in the gel (chapter 4) As the drying shrinkage proceeded, the tension in the liquid rose, which enabled the nucleation of additional cavities in smaller pores and possibly the growth of already-created bubbles. Shortly before maximum shrinkage, the volume shrinkage decreased (chapter 4), which could indicate a stress release by cavitation.

To assess whether cavitation can actually occur in silica gels filled with hexane, the pressure and required pore size were estimated following the arguments of ref.[203] The energy

change associated with the creation of a spherical cavity of radius R is $4\pi R^3 p_l/3 + 4\pi R^2\gamma$, with $p_l < 0$ the pressure in the liquid.[64,204] A bubble with a critical radius larger than $R^* = -2\gamma/p_l$ will spontaneously grow, and the corresponding energy barrier is $\Delta E = 16\pi\gamma^3/3p_l^2$.[204] Cavitation can occur only in pores larger than R^*. According to the classical nucleation theory, the nucleation rate is[203]

$$J = J_0 e^{-\Delta E/k_B T} \tag{5.16}$$

where J_0 is a prefactor in cm^{-3} s^{-1}, k_B is the Boltzmann constant, and T is the temperature. Silica gels display a fractal structure[156] with a wide size distribution of pores (1−100 nm).[13] In silica gels, cavitation will occur in sufficiently large pores if the pressure generated at the meniscus (in smaller pores within the network) is large enough to generate a reasonable nucleation rate, as shown in eq. (5.16). At the meniscus, the pressure in the liquid is given by $p_l = p_0 - 2\gamma/r$ (chapter 2.3) assuming that hexane fully wets the gel ($\theta = 0$), where r is the smallest pore radius blocking the recession of the meniscus in the gel. In nanometric pores, $|p_l| \gg |p_0|$ and the vapor pressure can be neglected.[21] The energy barrier for the nucleation of a bubble can be rewritten as a function of the smallest pore radius: $E = 4\pi\gamma r^2/3$. Ref.[203] provides an estimate for the prefactor J_0 for cavitation conditions: $J_0 = (2\gamma\rho^2 N_A^3/\pi M_w^3)^{0.5}$, with ρ being the liquid density, N_A being Avogadro's constant, and M_w being the molar mass of the liquid.

The nucleation rate of hexane in silica gels was then numerically estimated as a function of the smallest pore radius in the gel using eq. (5.16). The dependence of n-hexane surface tension on the temperature was taken into account using a modified van der Waals equation reported in ref.[70] The results are shown in Figure 5.8. The nucleation rate showed an extreme dependence on the radius of the smallest pores. The liquid temperature also has a strong influence on the nucleation rate, promoting cavitation at higher temperatures as already reported elsewhere.[181,182,184]

To evaluate what would be a reasonable nucleation rate for cavitation in silica gels, the numerical estimates of J were compared with the experimental growth rate of vapor/air from the μCT analysis. The growth rate per unit volume and per unit time was calculated as $J_{\mathrm{exp}}(r) = \Delta\bar{f}_{\mathrm{air}}/(\Delta t \cdot 4\pi r^3/3)$, where $\Delta\bar{f}_{\mathrm{air}}$ is the difference of the average volume fraction of vapor/air in gel M4 taken between t_{cav} and t_{MS}, with t_{cav} the time of cavitation onset and t_{MS} the time of maximum shrinkage, and $\Delta t = t_{\mathrm{cav}} - t_{\mathrm{MS}} = 4.1$ h. $\Delta\bar{f}_{\mathrm{air}}/\Delta t$ was a good approximation of the vapor/air growth rate (Figure B.21). The profile $J_{\mathrm{exp}}(r)$ corresponds to the creation of spherical vapor bubbles of radius r that neither grow nor collapse during the time lapse Δt. The intersection between the profiles J from the CNT estimations and J_{exp} in Figure 5.8 gives

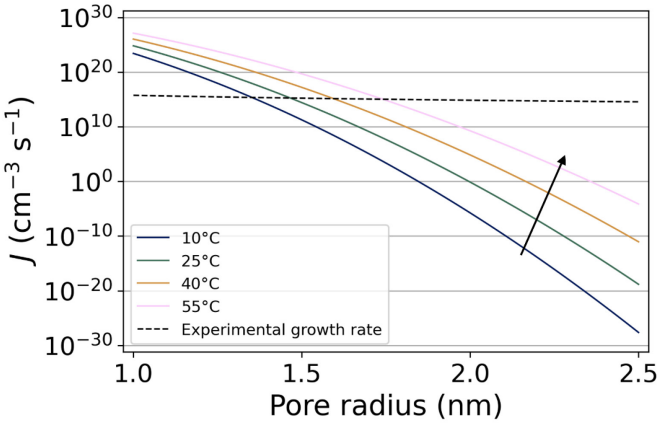

Figure 5.8 Calculated rate (full lines) of the formation of hexane bubbles J as a function of the smallest pore radius r blocking the recession of the meniscus at different liquid temperatures. Vapor/air growth rate (dashed line) was calculated from the μCT experiments on sample M4, assuming the creation of spherical bubbles of radius r. The black arrow depicts the temperature increase. Reprinted from ref.[107], CC BY 4.0 (https://creativecommons.org/licenses/by/4.0/).

an approximation of the nucleation rate that would correspond to the growth rate of the vapor/air phase in gel M4. At 25 °C (average temperature in the μCT instrument), a nucleation rate of about $2{\cdot}10^{15}$ cm^{-3} s^{-1} was found for a pore radius blocking the meniscus recession of $r = 1.47$ nm. Under these conditions, the liquid pressure would be $p_l \approx -24$ MPa, which was in good agreement with the values found by optical measurements of hexane desorption in alumina membranes.[177] These results supported that hexane cavitation can occur in silica gels, which have a small enough pore size for the liquid to reach the negative pressure required to form hexane bubbles at a reasonable rate. However, those results did not consider the dynamic of hexane bubbles over time. The spontaneous growth of already formed bubbles could notably produce the vapor/air volume in sample M4 at a much lower nucleation rate; thus, cavitation might also occur at larger pore radii. On the other hand, the hexane temperature during drying was likely lower than 25 °C due to the latent heat of vaporization, and this would reduce the nucleation rate at a fixed pore radius.

The timing and extent of cavitation could largely differ in gels resulting from different synthesis routes, depending on the porous network, stiffness of the solid matrix, and the nature of the solvent. Notably, in certain systems, cavitation may be absent. Cavitation in the silica gels synthesized in this study could have been facilitated by the presence of a thicker layer of silica on the outer surface of the gels, which may have formed during gelation in the molds. Such a shell with a smaller pore size would have a pore-blocking effect,[183] generating a stronger capillary pressure during drying that enables nucleation of vapor/air bubbles ahead of the gel surface. Additionally, cavitation of solvents with a low surface tension (such as hexane) is facilitated since the free energy of cavitation bubbles is proportional to γ^3 at a given liquid

pressure.[64,203] As shown by the CNT estimations, the temperature at which hexane evaporation occurs has a significant influence on the cavitation rate. Performing ambient-pressure drying at higher temperatures may therefore reduce the drying stress and possibly allow the production of larger monolithic aerogels with higher spring-back efficiencies, which may be investigated in the future. To our knowledge, the effect of the drying temperature on the spring-back efficiency and size of monolithic aerogels has not been investigated, though sometimes temperatures of 50 °C and more have been used. The surface chemistry of the silica network may also play a role: defects on the silica surface (e.g., remaining silanol groups due to incomplete silylation) can enable heterogeneous nucleation of vapor/air bubbles which require less energy than homogeneous nucleation,[186,205] meaning that cavitation can occur at a reduced liquid pressure. However, recent investigations in porous silicon suggest that desorption exclusively takes place through homogeneous cavitation in that system.[177,181] This is attributed to the complete wetting of silicon and most surfaces by hexane, liquid nitrogen, and liquid helium, owing to their exceptionally low surface tension. Cavitation in silica gels could also be detected by complementary measurements and analyses, such as acoustic measurements[206–208] and Small-Angle X-ray Scattering (SAXS),[209] which were not conducted in this work.

Reliability and Limitations. This section discusses the reliability of the μCT data reduction procedures and modeling and lists the artifacts generated experimentally and computationally. The GR maps of all samples indicated a heterogeneous distribution of the gray values along the gel radius at all drying stages (Figure 5.4a, Figure B.12a – Figure B.14a). This feature was also visible in the GHR maps to a lesser extent (Figure 5.3a, Figure B.9a – Figure B.11). Those variations were more pronounced near the maximum shrinkage. A spatial variability analysis revealed an exponential dependency of the gray values on the gel radius (appendix B.5). The relative increase of the gray values along the radius was correlated to the gel diameter and attributed to beam hardening,[108] although potential heterogeneities in the skeleton concentration along the gel radius could not be excluded. A spatial variability analysis on the gray values across the gel's height showed no sign of beam hardening. A similar analysis of the distribution of the gray values along the azimuth of the cylinders revealed slight variations that were caused by reconstruction artifacts rather than being a physical feature of the samples (appendix B.5). Darker lines can be seen on the top and bottom of the gel and its outer radius in the GHR maps (Figure 5.3a). These were caused by background inclusions in the masked images due to imperfect segmentation. Locally higher gray values were observed at a height of ca. 0.7 mm from the bottom of the gels (Figure 5.3a), which were reconstruction

artifacts due to the proximity of the sample to the bottom of the PEEK drying chamber and the low number of CT projections used for reconstruction. The artifacts in the GHR maps were propagated to the GR and GH maps, where similar features were observed at the vertical and radial edges of the samples. Despite these artifacts, the overall kinetics of the gray values in the GHR, GR, and GH maps were consistent with the results of the global quantitative imaging analysis (appendix B.6). This confirmed the reduction procedures could generate accurate representations of the shape-changing samples. The histograms of the GHR maps also showed a narrower distribution of the gray values compared to the histogram of the masked slices, as a result of the azimuthal integration (Figure B.31). Lastly, the gray values in the raw reconstructed slices were affected by the anode heel effect,[133] which was corrected by the procedure reported in appendix A.3.

The volume fraction maps were affected by the artifacts in the gray value maps. The abnormally high/low volume fraction of a given phase at the edges of the gel (Figure 5.3b–d and Figure 5.4b–d) corresponded to the locations where the segmentation included the background in the masked slices, which was interpreted in the drying model as a change in the composition. The abrupt changes at the top, bottom, and radial edges of the gels were thus treated as artifacts. The radial variations of the gray values were also propagated to the volume fraction maps, which can be seen, for example, in the increasing vapor/air volume fraction with the gel radius in the AIRR map of sample M4 before the maximum shrinkage (Figure 5.4d). Those variations, being partially attributed to beam hardening, prevented making reliable interpretations of the radial distribution of hexane, skeleton, and vapor/air during drying. The vertical maps were the most reliable representations to quantify the phase composition of the gels as they appeared to be free of beam hardening artifacts. Nonetheless, the HEXHR, SKELHR, and AIRHR maps depicted qualitative aspects of the composition evolution during drying despite the artifacts in the radial direction. The kinetics of the hexane, skeleton, and vapor/air volumes were consistent with the results from the global quantitative imaging approach reported in chapter 4 besides some irregularities near the maximum shrinkage that were possibly related to the additional computational steps required in the presented method (appendix B.6).

At the beginning of stage (3), as the drying front emerged on the top of the gel, an increase in the hexane concentration was observed in regions ahead of the drying front in all samples (Figure 5.5c, Figure B.16c – Figure B.18). A similar but opposite feature was observed in the vapor/air phase with a decrease in the vapor/air volume fraction at those locations. This phenomenon can also be seen in Figure 5.7, where the hexane and vapor/air volume fractions

were computed at a constant height in the gel. Most likely this phenomenon was related to an artifact arising from the assumption of a temporally static skeleton distribution throughout drying. This assumption seemed valid for most of the drying process, as the volume shrinkage appeared to be uniform along the height and radius of the gel (Figure 5.3), but may present limitations at the onset of stage (3) due to the heterogeneous nature of the spring-back effect in this study. The HEXHR maps were computed based on an artificial MHR map representative of the dry gel, which was rescaled toward a target scan. That artificial MHR map was stretched by bilinear interpolation to fit the target scan domain and corrected by a scalar scaling factor given by the volume ratio between the source scan and the target scan. The overall volume of the gel increased at the spring-back, which decreased the rescaling factor $\gamma_{k_f \to k}$ used to compute the local hexane volume fraction (see eq. (5.5)), resulting in an effective increase of the local hexane volume fraction that did not account for the heterogeneous re-expansion of the gel. This also resulted in an overall decrease of the vapor/air volume fraction ahead of the drying front, as it was calculated from eq. (5.3). Nevertheless, it could not be excluded that part of the observed variations were a physical feature of the sample. The sudden relaxation of the liquid tension could notably destabilize the equilibrium of the vapor/air bubbles close to the drying front and possibly result in a collapse of the cavities. This would increase again the tension in the liquid, which may pull more hexane ahead from the drying front, resulting in an effective increase of the hexane volume fraction at the corresponding location. Including the local re-expansion of the gel in the bilinear interpolation routine would require generating a dynamic mesh depending on both the shape changes and local gray values, which was out of the scope of this study.

5.4 Summary

This study addressed the evaporation mechanisms during the evaporative drying of silica gels by evaluating the spatial and temporal phase compositions modeled by μCT quantitative imaging. A noteworthy discovery was made, as the observed evolution of vapor/air content in the gels aligned with the concept of evaporation by cavitation initially theorized by Scherer and Smith in 1995. The presence of vapor and air in the gels before the maximum shrinkage was confirmed by WAXS modeling. The repartition of hexane and vapor/air in the gels was successfully computed by an in operando μCT workflow, which also demonstrated the potential of μCT quantitative imaging to generate local phase composition maps of the shape and composition of evolving materials. Based on these results, we proposed that the

evaporative drying of silylated silica gels proceeded in three stages: (1) evaporation by drying shrinkage; (2) evaporation by drying shrinkage and by cavitation; (3) evaporation by the recession of the meniscus, challenging the common drying model associated with sol−gel processes. The use of classical nucleation theory also permitted to derive the nucleation rate and smallest pore radius required to create the vapor/air volume computed by μCT quantitative imaging, which supported that cavitation can occur in silica gels. The emergence of cavitation was correlated with a pore volume shrinkage of about 50 vol % that was attributed to the critical point where the silica matrix stiffened enough to enable the nucleation of cavities. Cavitation started as early as 3.4 h of drying time, whereas the maximum shrinkage occurred at 7.6 h of drying.

In general, this discovery highlights cavitation as a new potential mechanism for evaporation in silica gels and makes a valuable contribution to understanding drying processes in porous materials. Tailoring the evaporative drying process by cavitation could be advantageous in the production of monolithic aerogels as it would reduce the pressure gradients in the gels and alleviate the rise of the capillary pressure, which would in turn reduce the risk of cracks appearing during drying. This could be done by precise modulation of gel properties (specifically pore size and matrix stiffness) and optimization of drying conditions and may represent a promising route for substantial advancements in the fabrication of monolithic aerogels through ambient-pressure drying, a process currently constrained in its application. The study notably highlighted the potential of carrying out evaporative drying at temperatures higher than room temperature, which may promote cavitation. The characterization of cavitation in the drying process of silica gels could be expanded through the application of alternative nondestructive methodologies, including acoustic detection and SAXS.

6 Plastic deformation and heat-enabled structural recovery of monolithic silica aerogels

The content of this chapter has been submitted to Journal of Sol-Gel Science and Technology on the 15th of April 2024:

Title	Plastic deformation and heat-enabled structural recovery of monolithic silica aerogels
Authors	Julien Gonthier, Ernesto Scoppola, Aleksander Gurlo, Peter Fratzl, Wolfgang Wagermaier
Journal	Journal of Sol-Gel Science and Technology
Publisher	Springer
Publication date	-
Reference	-
DOI	-
My contribution	Conceptualization: J.G., E.S., P.F., and W.W.; methodology: J.G. and E.S.; software: J.G. and E.S.; formal analysis: J.G. and E.S.; investigation and data curation: J.G. and E.S., writing–original draft: J.G. and W.W.; writing–review and editing: J.G., E.S., A.G., P.F., and W.W.; visualization: J.G.; supervision: P.F. and W.W.; project administration: J.G., P.F., and W.W.; funding acquisition: A.G. and W.W.

Ernesto Scoppola notably contributed to the acquisition of the X-ray scattering measurements, performed the calibration, integration and fit of the generated data and calculated the fractal dimension, Q invariant and Porod's constant.

6.1 Background

The drying shrinkage, spring-back effect and re-expansion by annealing represent substantial deformations for a ceramic material, as silica gels can recover a shrinkage down to 17 – 20 % of their original volume (chapter 4 and ref.[59]). From a fundamental materials science standpoint, investigating the phenomenology of the deformations associated with these processes provides insights into the underlying principles governing the manufacturing process of aerogels. While the two previous chapters uncovered the phase composition changes and other work investigated nanostructural changes[18,20] of silylated silica gels during drying and spring-back, the deformation mechanisms during the SBE and annealing remain mostly unexplored. It was recently proposed that the spring-back efficiency was correlated with the strain recovery of aerogels compressed uniaxially.[68] This parallel opens the possibility of evaluating the deformation of silica aerogels in a controlled manner under a stable environment and on a two-phase material (silica-air). The latter aspect is especially interesting for the structural characterization of aerogels by X-ray or neutron scattering methods, which allow only limited interpretations when performed on drying gels due to the convolution of the signal arising from three different interfaces (silica-air-solvent).[20]

The motivation behind the present study is twofold. Firstly, from an application perspective, there is a growing demand for structurally robust monolithic aerogels that can be utilized in various applications, including construction and insulation. Developing efficient production methods for such aerogels is essential for meeting the increasing demand for advanced insulation materials. Secondly, investigating the mechanical properties and annealing behavior of aerogels provides insights into the underlying mechanisms governing their structure-property relationships. To do so, uniaxial compression experiments are performed on native and annealed silica aerogels produced by a conventional APD process to characterize the macro- and nano-structural evolution during the deformations. This is achieved by monitoring the gels in-operando using synchrotron SAXS/WAXS measurements. The aim is to provide a systematic understanding of the deformation mechanisms in silica gels upon mechanical stimuli, as well as to draw parallels with the deformations related to the drying process.

6.2 Materials and Methods

Synthesis. 30+ silica gels were prepared by a two-step sol-gel process with a TEOS precursor adapted from chapter 4. A sol was created by mixing TEOS, ethanol, water and hydrochloric acid. Additional ethanol, water and ammonium hydroxide was introduced to promote gelation. The solution was casted into cylindrical molds with a diameter and depth of 8 and 16 mm, respectively. The solvent exchange was conducted using a mixture of ethanol and n-hexane with a volume of 2.3 L of per mol of SiO_2 and was done four times at intervals of 24 h. The surface modification was done in four steps, using a TMCS in hexane solution of 1.5, 1.5, 3 and 3 vol % that was replaced every 24 h. The volume of the solution used was 1.4 L per mol of SiO_2 at each step, resulting in a total TMCS/SiO_2 molar ratio of 1.0. The gels were finally rinsed with 2.3 L of hexane per mol of SiO_2 four times and were stored in hexane until drying. The reader is referred to chapter 4 for a complete description of the synthesis procedure.

Evaporative drying and annealing. One sample was dried in-operando in a μCT instrument and the four other samples were dried at ambient pressure in a fume hood. The in-operando drying procedure by μCT was adapted from chapter 4. The gel was transferred from its hexane solution and inserted in a tailored drying chamber placed in an EasyTom 160/150 CT instrument (RX Solutions, Chavanod, France). 160 scans were acquired using a micro-focus tube (tungsten filament) at 135 kV and 200 μA and a flat panel detector (cesium iodide scintillator). 64 projections were acquired in each scan for a duration of 1 min. Accounting for black and gain calibrations and motor displacements, a scan was taken every 6 min and the experiment lasted for a total of 16 h, corresponding to 161 scans. At the end of drying, the gel was taken out of the drying chamber. A hexane reference sample was measured immediately after by filling the chamber with hexane and closing it. 10 scans were acquired with the same parameters. In the meantime, the dry gel was weighted on a PCE-AB 100 (PCE Deutschland GmbH, Meschede, Germany) and was annealed in an oven at 230 °C for one hour. The gel was weighted again and was transferred back to the μCT drying chamber where a single scan was taken with the same parameters as before. The scans were done sequentially with no pause in between to prevent the build-up of instabilities in the X-ray tube. The sample dried in-operando was referred to as HT1. The evolution of the average phase composition of HT1 was computed by a μCT quantitative imaging approach with minor adaptations (appendix C.1). The apparent density, skeletal density and the porosity of the annealed gel were computed as $\rho_{\mathrm{HT}} = m_{\mathrm{HT}}/V_{\mathrm{HT}}$, $\rho_{\mathrm{skel,HT}} = m_{\mathrm{HT}}/V_{\mathrm{skel}}$ and $\phi_{\mathrm{HT}} = 1 - V_{\mathrm{skel}}/V_{\mathrm{HT}}$, respectively, where m_{HT} is

the mass of HT1 after annealing, V_{HT} is the total volume of the gel after annealing and V_{skel} is the silica skeleton volume.

The four other gels were transferred from their hexane solution into individual glass bottles with a lid in which a ~5 mm hole was drilled. The drying was carried out in a fume hood over 16 hours and the dry gels were then weighted. Three of the four gels were stored at ambient pressure and temperature; those samples were referred to as nHT1, nHT2 and nHT3. One sample was annealed at 230 °C for one hour and was weighted again. This sample was referred to as HT2. Samples HT1-2 and nHT1-2 were used for in-operando mechanical tests and sample nHT3 was used for ex-situ SAXS/WAXS measurements. The remaining gels were dried and annealed the same way as HT2 to characterize the weight loss upon annealing.

Mechanical tests combined with X-ray scattering. Uniaxial compression of the specimen was conducted in-operando with a simultaneous acquisition of X-ray scattering data frames and digital pictures. The SAXS/WAXS measurements were conducted at the synchrotron BESSY II of the Helmholtz-Zentrum für Materialien und Energie (Germany, Berlin) at the μSpot beamline.[195] The uniaxial compression tests were performed on a micromechanical device that was constructed specifically for in-operando experiments. The device consisted of a motor (PI C-863 M-403.1DG) augmented with stainless steel arms, on which were mounted a 250 N load cell (Althensensors) and two 8.5 mm wide cylindrical plates (Figure C.2). The micromechanical tester was installed on a moving stage at the beamline and was aligned such that the x-ray beam probed a fixed location at 3 mm below the top plate of the tester, while the bottom plate was actuated by the motor. A digital camera (TOOLKRAFT USB microscope, 5 MP) was placed perpendicular to the beam to monitor the sample geometry. Windows with a 7.5 μm thick kapton film were placed before and after the sample to protect the beamline equipment of eventual flying debris. Figure C.2b shows the experimental setup.

Four samples were compressed at different maximum strains: 43 and 30 % for HT1, HT2, respectively, and 30 and 18 % for nHT1 and nHT2, respectively. The tests were carried out in displacement control mode at a loading and unloading rate of 5 and 1 strain % min^{-1}, respectively, in accordance to ref.[68] The height of the sample was defined at a pre-load of -0.5 N. The unloading ended once the load went above -0.5 N, upon which the relaxation of the sample was monitored at a constant force of -0.5 N. The compression experiments were stopped after 50 min. X-ray scattering data frame were acquired every 5 sec, with an exposure of 1-2 sec depending on the specimen, and the background (including the kapton foils) was measured every 5 min by moving the sample laterally out from the beam. The force and

displacement values were recorded every 0.2 sec and digital pictures were taken every 2 sec. The data from those three methods were synchronized by interpolation on the time scale of the SAXS/WAXS measurements to enable a correlative analysis.

The projected area of the samples was determined by segmenting the digital pictures in the software Dragonfly.[130] The average diameter was then calculated by dividing the projected area by the height of the sample taken from the motor position of the micromechanical instrument. By assuming a perfect cylinder, the cross-section area was calculated from the average diameter and the gel volume was calculated from the height and diameter. The uncertainties were not calculated. The true stress was $\sigma = F(\varepsilon_z)/A(\varepsilon_z)$ with F the force, ε_z the axial strain and A the cross-section area. The apparent density during uniaxial compression was calculated as $\rho(\varepsilon_z) = m/V(\varepsilon_z)$, with m the sample mass. As the skeleton volume of HT1 is known from μCT quantitative analysis, the porosity of HT1 could be computed during compression as $\phi(\varepsilon_z) = 1 - V_{\mathrm{skel}}/V(\varepsilon_z)$ by assuming that the sample remained monolithic throughout the mechanical test. After compression, sample HT1 was annealed a second time for one hour at 230 °C in an oven at the synchrotron facilities, and was scanned again afterwards. Sample nHT3 was scanned before and after one hour of annealing, and its height and diameter were measured using a micrometric caliper.

The accessible q range was ca 0.1 – 30 nm^{-1}. The beam energy was 18 keV. Pinholes were 30 and 70 μm of diameter, leading to a beam size of 30 μm. The beam stop was a lead rod of 125 μm diameter. The scattering data were normalized over the intensity of the primary beam, the transmission of the sample and a glassy carbon reference, and the background was subtracted accordingly. Furthermore, the scattering data were absolutely normalized over the specimen diameter. The scattering patterns were radially and azimuthally integrated to generate the profiles $I(\chi)$ and $I(q)$, respectively, where I is the scattered intensity, q is the momentum transfer in nm^{-1} and χ is the azimuth in degree. The radial integration was performed over 0.1 – 0.2 nm^{-1} for the heat-treated gels, and over 0.1 – 0.6 nm^{-1} for the dry gels. The azimuthal integration was calculated over three domains: (1) for $\chi \in [0{,}360]$, (2) for $\chi \in [80{,}100] \cup [260{,}280]$ referred to as the axial integration (along the load), and (3) for $\chi \in [-10{,}10] \cup [170{,}190]$ referred to as the transverse integration (perpendicular to the load). The calculations of the fractal slope and Porod's constant were performed in agreement with previous studies.[20] The Porod's slope was set constant at -4. The Q invariant was calculated as:

$$Q = \int_{q_{\min}}^{q_{\max}} I(q) q^2 dq + \int_{q}^{\infty} K q^{-2} dq, \tag{6.1}$$

where q_{min} is the lowest accessible q value in the data, q_{max} represents the lower limit of the Porod region and K the Porod constant. The wide-angle signal past the Porod region was fitted with a sum of Pseudo-Voigt functions as reported in chapter 5. The scattering length density of the air-filled pores was 0, therefore the scattering length density difference between the silica skeleton and air was reduced to the one of the skeleton: ρ_{SLD}, which was calculated on the first data frame of sample HT1 before compression and was then set constant:[152]

$$Q = 2\pi^2\phi(1-\phi){\rho_{\mathrm{SLD}}}^2, \tag{6.2}$$

with ϕ the porosity of HT1 computed by μCT quantitative imaging, which is known. The specific surface area (SSA) of this sample was calculated with:

$$\mathrm{SSA} = \frac{\pi K\phi}{\rho_s Q}, \tag{6.3}$$

where K is the Porod constant and ρ_s is the skeletal density. The mean chord length was $\bar{l} = 4Q/\pi K$, and the mean chord length of the pores l_p and the mean chord length of the silica skeleton l_s were computed using $l_p = \bar{l}/(1-\phi)$ and $l_s = \bar{l}/\phi$, respectively.[145] The same quantities were also calculated for the other samples measured at the synchrotron by assuming they all shared the same skeletal density ρ_{skel} and scattering length density ρ_{SLD} of the silica skeleton. This also enabled to compute the porosity of the samples by reversing eq. (6.2).

6.3 Results and Discussion

In this section, we present the results of our investigation on the expansion and structural changes of the aerogel samples induced by annealing, as well as their compressibility and strain recovery properties. We begin by discussing the observed alterations in structure following annealing, elucidating the impact on the overall morphology and pore architecture. Subsequently, we present the mechanical properties obtained from uniaxial compression tests, highlighting the differences between the behavior of dry and annealed samples under applied stress. Finally, we analyze the structural changes using X-ray scattering techniques, specifically focusing on WAXS data reflecting density changes upon deformation and SAXS data revealing pore structural rearrangements. The discussion part provides insights into the mechanisms governing structural changes during compression and the subsequent full recovery of shape and structure upon annealing.

Expansion and structural changes upon annealing. The evolution of the total volumes of hexane, silica skeleton and vapor/air of HT1 throughout drying and annealing is shown in Figure 6.1a. The kinetics of hexane evaporation and vapor/air content was consistent

with the observations made on the samples from chapter 4, besides a slightly longer drying process due to a larger starting volume of the wet gel. The porosity of the wet gel was 94.3 ± 0.1 vol % (95th percentile). The maximum shrinkage was reached after 8.8 h of drying where the gel volume was 14.4 ± 0.2 vol % of the original volume, and the gel sprung back to 26.5 ± 0.3 vol % of its original volume. Upon annealing, HT1 underwent a significant re-expansion and reached 85.5 ± 1.0 vol % of its original volume (Figure 6.1a) and a final apparent density of 120.4 ± 0.2 mg cm^{-3} and porosity of 93.4 vol %. The ex-situ samples dried slightly faster compared to HT1 as the design of the drying chambers was different. Similar re-expansion was observed for the other annealed samples but was not quantified. During annealing, HT1 lost 0.6 ± 0.1 wt % of its weight. This weight loss was attributed to residual hexane in the dry gel, given that TMCS-modified silica gels are thermally stable (no oxidation) until at least 260 °C.[19,85] The statistical precision of the weight loss was assessed by measuring it on 33 annealed samples (including HT1 and HT2), and the average weight loss was 0.33 ± 0.32 wt %. Although the error of these measurements was relatively high, it could be concluded that the weight loss was statistically significant and thus that it was a real feature of the thermal annealing process. The skeletal density of the annealed HT1 was calculated as 1.830 ± 0.002 g cm^{-3} and was similar to the values reported in chapter 4.

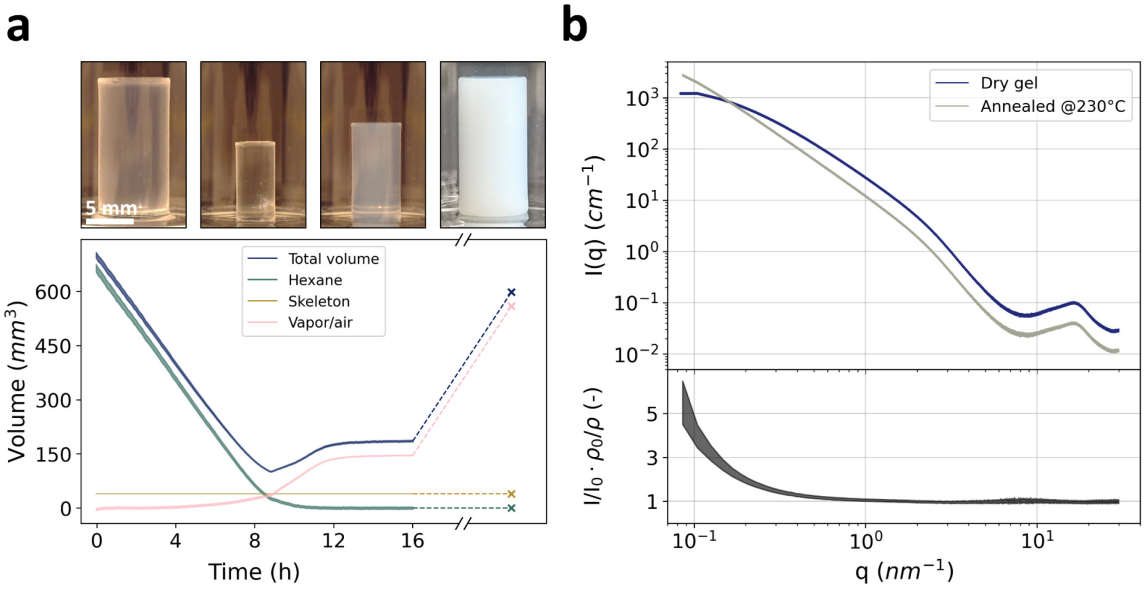

Figure 6.1 (**a**) Total volume of hexane, silica skeleton and vapor/air in gel HT1 during drying (full lines) and after annealing (scatter points). The error bands correspond to the 95th percentile. Dashed lines were drawn as visual aid. The top of the figure displays digital pictures of a gel from the same synthesis dried ex-situ at selected drying stages. From left to right: before drying, maximum shrinkage, after drying, and after annealing. (**b**) Scattering profiles $I(q)$ of gel nHT3 before and after annealing along with the intensity ratio of the annealed profile over the dry profile normalized by the sample apparent density: $I_{HT}(q)/I_d(q) \cdot \rho_d/\rho_{HT}$.

The structural changes at the nanometer scale upon annealing were evaluated by SAXS/WAXS on a different sample to complement the μCT quantitative imaging analysis. The scattering profiles of sample nHT3 before and after annealing are shown in the top graph of Figure 6.1b. The overall decrease of the intensity in the wide-angle region ($q > 8$ nm^{-1}) was consistent with the lower apparent density (higher porosity) of the annealed gel compared to the dry gel. At this scale, the scattering signal arises from the molecular structure of the silica skeleton,[18,145] and as the apparent density decreased there were fewer scattering centers in the volume probed by the beam. This can also be seen in the bottom graph of Figure 6.1b showing the ratio of the annealed and dry gel intensity normalized by the gel apparent density, where the plateau extends down to $q \approx 1$ nm^{-1}. The porosity of nHT3 was calculated from the Q invariant at 75.5 ± 0.0 and 90.7 ± 0.3 % before and after annealing respectively, which was slightly lower than the values calculated for HT1 by μCT quantitative imaging. This can be caused by slight differences in the spring-back efficiency of nHT3 compared to HT1, as the drying setup was different. Additionally, the thermal annealing of nHT3 was performed in a different oven and the heat-treatment may have been insufficient to complete the re-expansion of the specimen. The SSA was calculated at 1260 ± 18 and 1326 ± 19 m^2 g^{-1} before and after annealing, respectively. The SSA of both gels was higher than the values previously reported for similar systems using nitrogen sorption measurements.[19,51] Unlike X-ray scattering methods, nitrogen sorption of mesoporous materials such as silica aerogels can lead to underestimation of the porosity and SSA especially in compliant gels containing micropores,[210] which may explain in the observed differences between the two methods. Although relatively high, the specific surface area was arguably in the range of values for silica-based aerogels.[13,49,57]

Significant changes were observed in the small-angle region with an increase of the intensity after heat-treatment from $q < 0.5$ nm^{-1}. The fractal region in the dry gel was identified from ca 0.4 to 2 nm^{-1} and was characterized by a mass fractal dimension at 2.16 ± 0.04. Upon annealing, the lower q limit of the fractal region extended outside of the accessible q window and the fractal dimension increased to 2.35 ± 0.01, where typical values for silica aerogels are 1.8 – 2.4.[156] The fractal dimension of aerogels is commonly used to describe the aggregation mechanisms during the sol-gel process,[143] but can also be interpreted as the cluster compactness, where the local bulk density of an object of size L is $\rho \propto L^{D_f-3}$, with D_f the mass fractal dimension.[156] The increase of the fractal dimension upon annealing could appear counter-intuitive, as the density of the gel decreased significantly which would rather be associated with less compact fractal clusters. However, these results can be interpreted by considering the pore size distribution in the gels. In chapter 4, it was proposed that the low

spring-back efficiency of the silica gels after drying was caused by a mechanical lock of the gel solid network. Although small, a residual amount of solvent in the dry gels may act as a mechanical locker, which could explain the relatively low spring-back efficiency. Therefore, the dry gel would be in a metastable state where pores were unable to fully re-expand past a critical size, resulting in a narrow range of pores size and a certain fractal dimension.

Thermal annealing at mild temperature enables the evaporation of residual n-hexane and would also make the solid network more compliant, promoting the reordering of the silica skeleton and release entanglement of the silica clusters. These statements were supported by the increase in the specific surface area upon annealing, suggesting that new silica skeleton – air interfaces were created. More importantly, the pores would re-expand freely, which would reduce the density of small pores and create larger pores that were inexistent before annealing. The pore size range would thus be wider, with each pore size being less populated than before annealing. This would be translated into more compact clusters and thus in a larger fractal dimension, given that at any length scale within the fractal region, the density of pores decreased upon annealing.

To test these statements, the correlation between the bulk density of the aerogels and their fractal dimensions was evaluated using a simple fractal model. For aerogels displaying a singular fractal structure, the density of the fractal clusters can be expressed as:[146]

$$\rho(\xi) = \rho(a) \cdot \left(\frac{\xi}{a}\right)^{D_f-3} \tag{6.4}$$

where ξ is the mean size of the fractal cluster and a is the size of the aerogel particles. The parameter a was estimated as the radius of the silica particles, assuming a spherical shape. In this case, the relation between the mean chord length of the skeleton and the radius of the particles is given by $l_s = 4R/3$, with R the particle radius.[145,211] With the knowledge of l_s, the particle size was set as $a = 3l_s/4$ and it corresponded to a radius R. The mean cluster size ξ is the maximum length scale above which the structure can be considered as homogeneous and is thus characterized by a constant density.[212] The mean cluster size is also a quantity representative of the largest pores within the fractal domain. Assuming that the density of the fractal clusters corresponded to the bulk density of the gels allowed to estimate the value of ξ according to eq. (6.4). By doing so, the mean cluster size before and after annealing was calculated at 7.49 ± 0.65 and 47.65 ± 2.50 nm, respectively (Figure C.3). In this case, given the definition of a, ξ would also correspond to a radius. The increase in the mean cluster size upon annealing supported the hypothesis that the pores did not fully re-expand after drying due to some contraption. In the dry gel, the calculated cluster size corresponded approximately to the

start of the plateau at $q \approx 0.1 - 0.2$ nm^{-1} assuming $\xi \approx 1/q$. In comparison, the cluster size of a dry gel produced with a similar synthesis was reported as 6.3 nm by modeling the X-ray scattering data,[20] which is in relatively good agreement with the current estimation. The particle radius before and after annealing was very similar at 1.30 ± 0.02 and 1.24 ± 0.02 nm, in good agreement with the average diameter of gels from a similar synthesis measured by TEM (chapter 3.1). This suggested a negligible impact of the annealing process on the silica nanoparticles.

Compressibility and strain recovery. This section reports the mechanical properties of a dry (nHT1) and an annealed (HT1) sample during uniaxial compression. The true stress – strain curves of both samples are shown in Figure 6.2, along with the transverse vs axial strain. The maximum strain values were chosen based on ex-situ experiments, which showed that the critical strain at which mechanical failure of the samples occurred was about 36 and 48 % for a dry and an annealed gel, respectively (appendix C.2). The maximum strain for the nHT1 and HT1 was then set at 30 and 43 %, respectively to ensure their mechanical stability throughout the in-operando experiment and to prevent any damage to the equipment at the beamline. In all experiments, digital pictures and visual inspection of the samples after compression revealed no cracks and the samples stayed monolithic throughout the experiments. The stress reached in the annealed gel at the maximum strain was significantly lower than in the dry gel, so was the Young's modulus. The Young's modulus of silica aerogels has a power-law dependency on the gel bulk density:[41,68,213] $E \approx \rho^{\alpha}$. An exponent of 4.2 was found by comparing those properties for HT1 and nHT1.

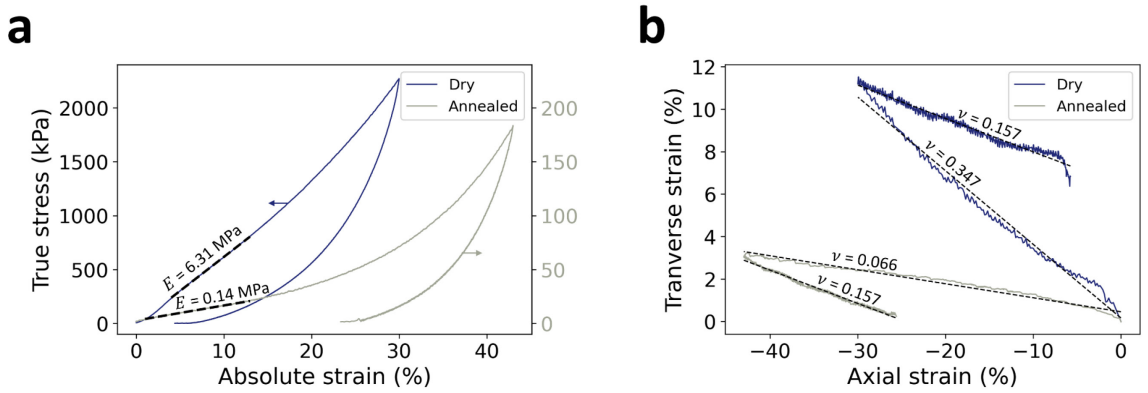

Figure 6.2 (**a**) True stress versus absolute strain for samples nHT1 and HT1 including a relaxation of ca. 20 min. The maximum strain is 30 and 43 % for nHT1 and HT1, respectively. The Young's modulus E is depicted on the corresponding profiles. (**b**) Transverse versus axial strain for nHT1 and HT1 during loading (starts at the point (0,0)) and unloading. The fit of the loading and unloading curves is shown in black dashed lines and the Poisson's ratio ν is depicted on top of the fitting curves. The error on Poisson's ratio is maximum 0.001.

The dry gel displayed a near viscoelastic behavior during uniaxial compression, showing a hysteresis upon unloading going close to a strain of 0 %. This represents a surprisingly high compressibility (30 %) and strain recovery given the rather high density of the dry gel (407 mg cm^{-3}). The residual strain was only 4.4 % after unloading. In comparison, studies have reported a fracture strain of 10 and 17 % for silica aerogels with lower densities at 342[41] and 185[68] g cm^{-3}, respectively. The strain recovery for the annealed gel (bulk density of 119 g cm^{-3}) was much lower with a residual strain of 23.3 % after unloading. This irreversible deformation was indicative of a more plastic behavior of the annealed gel upon compression. Segmentation of the digital pictures taken throughout the mechanical tests (see Figure 6.3) allowed to quantify the transverse deformation and the Poisson's ratio ν. The two gels behaved very differently with a near-zero lateral expansion in the annealed gel ($\nu = 0.066$) whereas the lateral expansion in the dry gel was much higher ($\nu = 0.347$). Silica aerogels typically have Poisson's ratio of about 0.2 – 0.23.[214] Some reports of aerogels with near-zero or negative Poisson's ratio can be found in the literature, but the structure is usually tailored or made of different materials (composites) to achieve such low ratio.[215–217] In comparison, the annealed aerogel produced in this study showed a very low Poisson's ratio considering that it was a pure silica aerogel. Interestingly, the Poisson's ratio calculated during unloading was the same for both gels at 0.157. The uniaxial compression experiments on nHT2 and HT2 gave similar results, besides slightly different unloading Poisson's ratio at 0.143 and 0.117 for nHT2 and HT2, respectively (Figure C.5). The compressibility and strain recovery was then correlated with the associated structural evolution using X-ray scattering.

Orientation changes of nanoscale features during compression. The orientation of the scattering signal from the SAXS/WAXS was first assessed given the anisotropic nature of the deformation in uniaxial compression experiments. Figure 6.3a and c show the X-ray diffraction patterns of HT1 and nHT1 within a q range of 0.33 nm^{-1} at selected compression stages along with the corresponding digital pictures. Throughout the compression of HT1, the diffraction patterns suggested a rather isotropic structure and an anisotropic scattering signal could only be appreciated upon radial integration of the images (Figure 6.3b). Those changes in the radially integrated profiles were smoothed by computing the intensity ratio relative to the unloaded state. The variations of intensity at small-angle were not only related to the structure at that given length scale, but also to the total number of scattering centers in the volume probed by the beam, which increased during loading since the bulk density of the sample also increased. Thus, the evolution in Figure 6.3b could only be interpreted as a slight increase of preferred orientation (texture) of the nanostructure during compression. After

unloading, the annealed gel retained a residual orientation (Figure 6.3b). The texture of the dry gel during loading was comparatively higher and could be seen directly in the diffraction images (Figure 6.3c). The created pattern is referred to as a butterfly pattern, and similar features have already been observed upon compression of native silica aerogels[162] and hybrid silica aerogels,[218] as well as tensile tests in semi-crystalline polymers.[219] After unloading, the dry gel also retained some preferred orientation (Figure 6.3d). Interestingly, the scattering intensity along the axial direction ($\chi = 90°$ and $\chi = 270°$) returned close to its original value before compression for both specimen. This may however be due to different final bulk densities in the two samples after unloading, since the annealed gel showed much a larger irreversible deformation (Figure 6.2). The results from Figure 6.3 confirmed that the evolution of nanostructural features of both gels was anisotropic during compression. Splitting the axial and transverse contributions of the diffraction patterns allowed to assess the respective changes in the aerogels' structure.

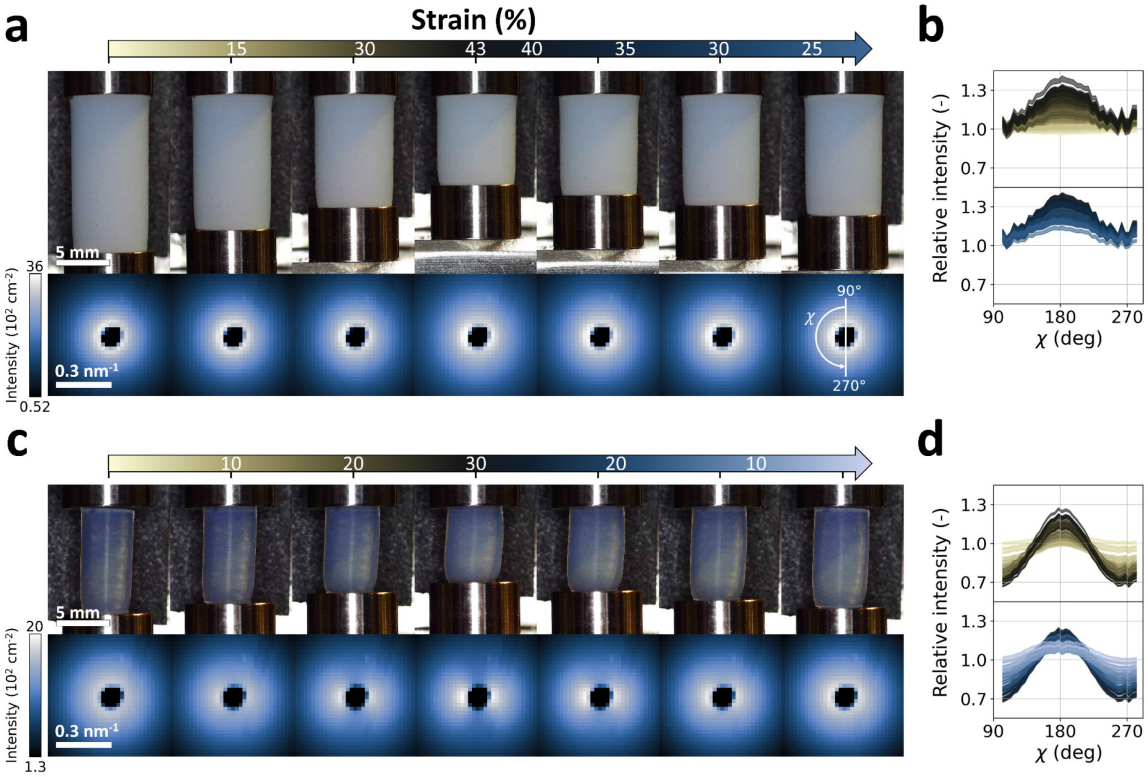

Figure 6.3 Pictures and diffraction patterns (**a**) and radially integrated scattering intensity ratio (**b**) of sample HT1 during uniaxial compression. Panels (**c**) and (**d**) show the same features for sample nHT1. The relative intensity is: $I(\chi, \varepsilon)/I(\chi, \varepsilon = 0)$. The color scales above panels (**a**) and (**c**) depicts the strain of the sample at the corresponding pictures and diffraction patterns for HT1 and nHT1, respectively. The color scale for the intensity of the diffraction patterns is shown on the bottom left of panels (**a**) and (**c**) and is logarithmic. The length scales and angular directions are depicted in panels (**a**) and (**c**).

Correlations between uniaxial compression and drying. The scattering profiles resulting from the azimuthal integration in the axial and transverse directions of samples HT1 and nHT1 during uniaxial compression are shown in Figure 6.4, along with the intensity ratio. The same is shown in Figure C.6 for HT2 and nHT2. The ratio was defined as: $I(q,\varepsilon)/I_0(q) \cdot \rho_0/\rho(\varepsilon)$, with I and I_0 the scattering intensity at a strain ε and at zero strain, respectively, and with ρ and ρ_0 the corresponding bulk density. First, an increase of the intensity was observed during loading independently of the q value (from brown to black), and a corresponding decrease (from black to blue) was observed during unloading (Figure 6.4a-d). This trend in the transverse direction has been reported elsewhere,[218] though limited interpretations on the correlation with the nanostructure were provided notably due to experimental restrictions. The strain-dependent evolution of $I(q)$ was difficult to visualize due to the superposition of the profiles. As mentioned when discussing Figure 6.1b, the change of intensity in the wide-angle was correlated to the number of scattering centers in the region probed by the beam, and thus to the relative change in the gels density. A very good agreement has been found between the intensity ratio of the profiles in the wide-angle region and the relative increase of the gels density (appendix C.3). Thus, to enhance the changes in the nanostructure at the small-angle, the scattering profiles were normalized by the gel bulk density at a given strain and the ratio between the profiles relative to the unloaded state was computed. This allowed to omit the contribution of the increased material amount in the beam path. Additionally, the intensity ratios were split to separate the changes associated to the loading (Figure 6.4e-h) and unloading (Figure 6.4i-l) steps.

During loading, the intensity in the small-angle region gradually decreased in the axial direction for both gels (Figure 6.4e,g). That evolution was consistent with the phenomenology of the compression of porous media where large pores are compressed first resulting in a shift of the pore size distribution to smaller lengths.[114,220,221] Here an interesting parallel can be drawn with the drying of silica gels where a decrease in the intensity in the low q region has also been observed during drying shrinkage.[20] Similarly to compression, drying shrinkage proceeds by the depletion (and contraction) of larger pores first, followed by smaller pores.[15,21] This suggested similarities between the strain recovery after compression and the spring-back efficiency of ambient-pressure dried silica aerogels, as proposed by Sivaraman et al.[68] This correlation could be further evaluated with the experiments performed on sample nHT2, which was compressed to a maximum strain of 18 % to mimic the linear strain that the gels experienced during drying (Figure C.5). The latter was assessed from the μCT analysis on HT1: the height of the gel at the maximum shrinkage was 82 % of the height after spring-back

(without annealing), corresponding to a strain of 18 %. The uniaxial compression experiments on nHT2 revealed an almost complete recovery of the deformation with a residual strain of only 1.87 % (Figure C.5), supporting the relationship between strain recovery and spring-back efficiency. nHT1 showed a slightly higher residual strain at 4.42 % when compressed to 30 % strain (Figure 6.2). X-ray scattering experiments suggested a significant recovery of the nanostructure in the axial direction for both dry samples within the accessible q range (Figure 6.4k, Figure C.6k), strongly highlighting the reversible nature of the deformation.

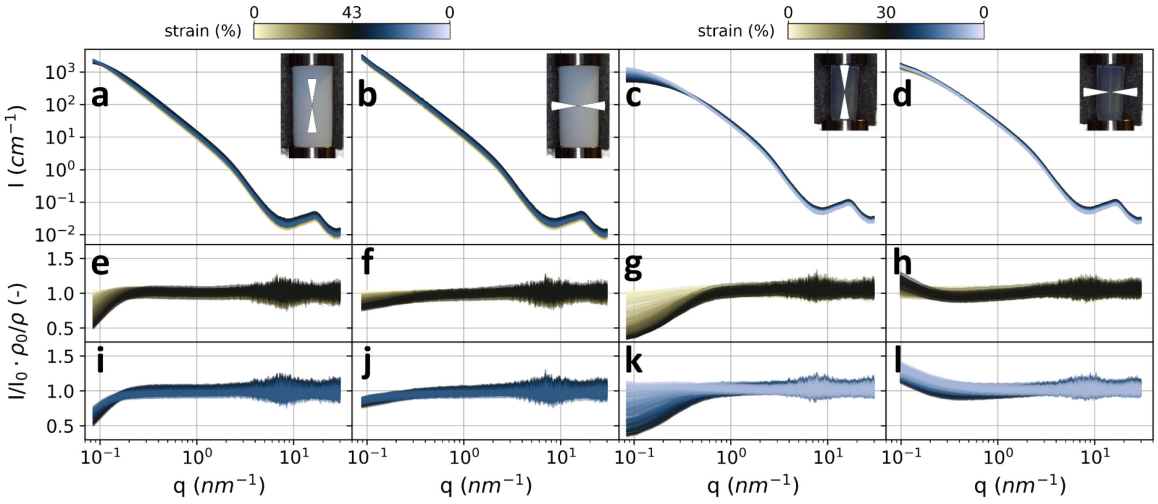

Figure 6.4 Scattering profiles of HT1 in the axial (**a**) and transverse (**b**) directions to the load and scattering profiles of nHT1 in the axial (**c**) and transverse (**d**) directions. Panels (**e**-**j**) display the ratio of the intensity at a given strain $I(q)$ relative to the native intensity before compression $I_0(q)$, and normalized by the apparent density of the sample by multiplying the scalar ρ_0/ρ. The intensity ratio plots are split into the loading (**e**-**h**) and unloading (**i**-**l**) parts of the mechanical test corresponding to the HT1 and nHT1 samples in both axial and transverse directions. The strain value is indicated with a diverging colormap shown on top of panels (**a**,**b**) for HT1 data, and on top of panels (**c**,**d**) for nHT1 data. The insets in panels (**a**-**d**) are images of the sample depicting the integration cake used to reduce the scattering data (axial or transverse directions).

Nevertheless, care has to be taken when comparing SAXS/WAXS data between a two-phase (as during mechanical deformation) and a three-phase material (as during drying).[18] Moreover, it was shown that the gels synthesized in chapter 5 showed a significant amount of vapor/air before the maximum shrinkage, presumably due to solvent cavitation. The presence of vapor/air phase would alter the signal in the small-angle regime, making the results more difficult to interpret. Lastly, the comparison was limited to the axial deformations of the dry samples, since the scattering patterns showed an incomplete recovery of the nanostructure at low q along the transverse direction (Figure 6.4l, Figure C.6l).

Evolution at the macro- and nanoscale. In this section, the nanostructural changes upon compression are interpreted by correlating the evolution of the scattering intensity and the macroscopic deformations. In the previous section, the in-operando compression of nHT1

revealed that both the strain and the nanostructure were restored along the direction of the load. A different evolution was observed along the transverse direction. While there was virtually no change of the nanostructure at $q > 0.2$ nm^{-1}, the scattering intensity increased slightly within 0.1 – 0.2 nm^{-1} and was not recovered upon unloading (Figure 6.4h,l). This suggested that the deformation perpendicular to the load was accommodated by the displacement of relatively large objects ($q < 0.2$ nm^{-1}) whose structure remained similar at smaller length scales ($q > 0.2$ nm^{-1}). At the macroscale, the transverse strain was substantial with an increase in the gel diameter of up to 11.5 % that did not return to its original value (Figure 6.2b). That strain was indicative of a lateral stress that is not or little constrained, enabling a lateral expansion in nHT1. By assuming the absence of lateral constraints at the nanoscale as well, the changes at the nanoscale could be interpreted by the sliding of large silica clusters ($q < 0.2$ nm^{-1}) along each other in the axial direction and re-arranging themselves laterally. Such displacement would increase the population of these large objects in the transverse direction, which would be consistent with the observed evolution of the scattering profiles at the small-angle (Figure 6.4h,l). The residual nanostructural deformations after unloading would suggest an irreversible displacement of the silica clusters in the transverse direction. This was supported by the effectively larger diameter of the gels after uniaxial compression (Figure 6.2b). Interestingly, that feature was somehow similar to the re-expansion of the structure enabled by annealing, where the macroscopic re-expansion was accompanied by an increase of the scattering signal at the small-angle (Figure 6.1b). One could argue that the mechanical stimuli promotes the unlocking of the silica skeleton in a similar fashion as thermal activation, but to a lessened extent.

In the annealed sample (HT1), the evolution of the scattering patterns during compression suggested that deformation of the nanostructure occurred at larger length scales than in the dry gel beyond the accessible q range (Figure 6.4e,f). The interpretation of the changes at the small-angle was thus limited, but a residual deformation of the nanostructure along the axial direction could clearly be identified after unloading, as the scattering profiles were not recovered in the small-angle (Figure 6.4i). Along the transverse direction, the intensity decreased slightly in the small angle but remained mostly identical as they were in the unloaded state (Figure 6.4j). This trend was very similar to the transverse strain of HT1 during compression as the diameter of the gel remained mostly identical with a near-zero Poisson's ratio (Figure 6.2). By relating those features at the macroscopic and nanoscopic scales, one could argue that except for the increase in the density during loading, the arrangement of the silica skeleton in the perpendicular direction to the load did not change, at least within the

accessible q range. By considering the substantial compressibility of HT1, the deformation mechanisms in the annealed gel could occur mostly through the shrinkage of large pores possibly beyond the fractal range. This hypothesis would be supported by the optical properties of the annealed gels that were almost completely opaque, suggesting a pore size within the range of visible light (400 – 700 nm). It may thus be possible for the silica clusters to displace themselves along the axial direction without generating force perpendicular to the load. Key features of the scattering patterns were quantified to bring more insights on the deformation mechanisms of HT1 and nHT1.

Figure 6.5 shows the porosity, mean chord length of the pores l_p, fractal dimension and mean size of the clusters ξ for HT1 and nHT1 during mechanical deformation. The mean size of the clusters was calculated with eq. (6.4) setting the density as $\rho(\xi) = \rho(\varepsilon)$ and the size of the particles as the radius $a = R(\varepsilon)$ with ε being the strain. The particle radius was rather constant for both samples throughout deformation (Figure C.8), so was the specific surface area (Figure C.9). All other properties showed variations throughout compression. Overall, nHT1 recovered its nanostructural characteristics after unloading and even showed a slight increase in l_p and ξ, which was consistent with the expansion of the gel after unloading. On the contrary, l_p and ξ of HT1 were significantly reduced after compression, supporting irreversible nano-structural deformations. However, it must be noted that the mean cluster size ξ computed in HT1 was likely non-representative of the real mean cluster size, as the assumption that the cluster density equals the bulk density may be invalid in the annealed gel. As mentioned previously, the visual opacity of the annealed gels suggested the presence of pores large enough to scatter light, and those pores' characteristic size may be beyond the fractal range.

Interpretations on the fractal dimension. The evolution of the fractal dimension throughout uniaxial compression can be interpreted in a similar fashion as it was done for the annealing process. During the loading of the dry sample, the fractal dimension decreased in both directions, with more pronounced variations along the vertical loading direction (Figure 6.5b). In parallel, the density of the sample increased from 403.6 to 470.0 mg cm^{-3} at the maximum strain (30 %). These observations were coherent with those made when comparing a dry and annealed gel (Figure 6.1): the fractal dimension decreased as the density increased. It is worth noting that the opposite trend has been observed in aerogels prepared with different synthesis conditions,[146] but in that case it was correlated with the different growth mechanisms of the sol-gel synthesis. As discussed in literature, the change of the fractal behaviors of dynamically evolving systems (e.g. during drying) cannot be interpreted in terms of aggregation

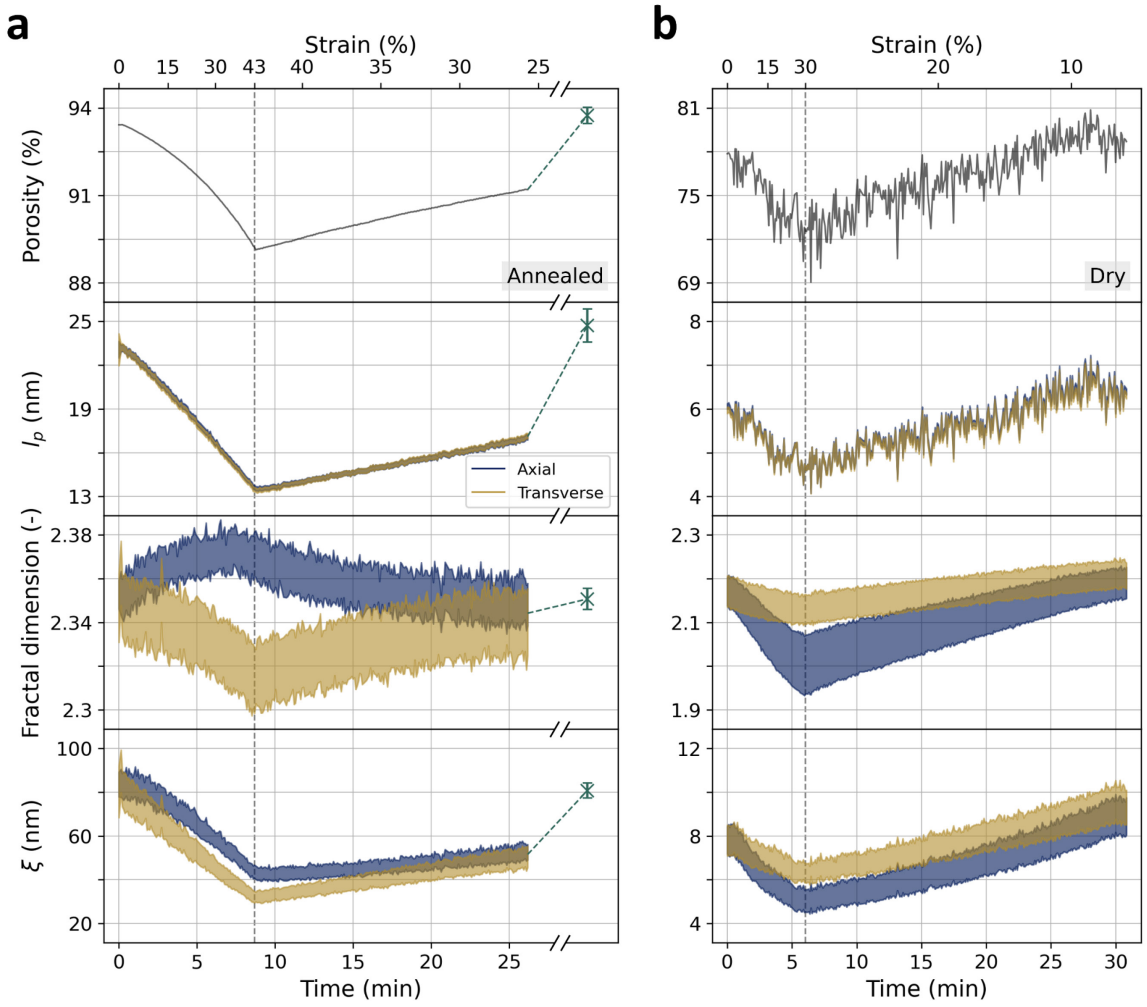

Figure 6.5 Porosity, mean free path within the pores (l_p), fractal dimension and mean length of the fractal cluster (ξ) of samples (**a**) HT1 and (**b**) nHT1 during uniaxial compression. Time is represented on the bottom x-axis and the corresponding strain is depicted on the top x-axis with a non-linear scale. All data are shown in the axial and transverse directions except for the porosity. The error of the HT1 porosity during compression was not calculated, and the error of nHT1 porosity is lower than 0.08 %. The scatter points in each graph of panel (**a**) correspond to the properties of sample HT1 after the 2nd annealing and are connected with dashed lines for visual aid. The data points corresponding to the relaxation are not shown for clarity.

mechanisms.[20] During unloading, the fractal dimension increased and reached back slightly higher values than at the start of the experiment, similarly to other parameters (Figure 6.5b).

We propose that the evolution of the fractal dimension in the dry gel was driven by a heterogeneous deformation of pores depending on their characteristic size. By assuming the compression of large pores during loading, the population of smaller pores must necessarily increase. Consequently, the fractal clusters within the corresponding length scale become less compact, which would be reflected by a lower fractal dimension. Based on this interpretation, the different evolution of the fractal dimension along the axial and transverse direction in the dry gel suggested an anisotropic shrinkage of pores upon compression. This was also

supported to some extent by a Poisson's ratio of 0.35 during loading as the gel expanded laterally (Figure 6.2). Morphologically, this could correspond to the contraction of a sphere onto an ellipsoid with the shortest axis pointing in the direction of the load, which would also be supported by the more pronounced reduction in mean cluster size axially (Figure 6.5). Such anisotropic deformation of the pores would be consistent with the deformation mechanism of the silica clusters proposed when discussing Figure 6.4. It has to be noted that this interpretation should lead to an increase in the scattering intensity at intermediate q values in the axial direction due to the vertical shrinkage of the pores, which was not observed (Figure 6.4g). Nevertheless, recalling the considerations on the sliding of the silica clusters along the transverse direction, the increase of the population of small pores might produce a negligible change in vertical intensity compared to the re-arrangement of large pores in the transverse direction.

The change in fractal dimension during loading of the annealed sample HT1 was significantly different than in the dry samples, showing opposite trends in the axial and transverse directions (Figure 6.5a). The variations were relatively small in comparison to the dry samples, and were within the error range in both directions. A similar evolution was observed for sample HT2 (Figure C.10). A sensitivity analysis on the q-range used to fit the fractal slope suggested that the increase of the fractal dimension in the axial direction during loading was a real feature, but also showed substantial fluctuations when changing the q-range (appendix C.4). Assuming that the fractal dimension stayed rather constant throughout loading, the compactness of the clusters remained similar over the fractal region suggesting that the silica clusters retained their structure within the observable q range. This behavior of the annealed gel would be coherent with the compression of pores larger than the mean size of the fractal clusters that was previously stated (Figure 6.4). According to the values of ξ computed with a simple fractal model, those pores would be larger than 100 nm that is beyond the small-angle observation window achieved in the current experiments. Besides the presence of large non-fractal pores, the annealed gels may also form a second fractal structure at a larger-scale, as observed in composite aerogels.[222] In both cases, this would mean that the hypothesis used in the simple fractal model from eq. (6.4) was invalid, as the bulk density would not correspond to the cluster density. The analysis of the same features for HT2 and nHT2 gave similar conclusions (Figure C.10).

Lastly, the evolution of the mean chord length of the pores l_p remained remarkably similar in the axial and transverse direction for both gels (Figure 6.5). This may seem in contradiction with the anisotropic deformation of the pores proposed by evaluating the fractal

dimension of the dry gel. However, that interpretation could remain valid by considering l_p as a diffusion length,[145] which would correspond to the average distance covered by an object driven by Brownian motion within the porous network. As the motion of such object would be statistically isotropic,[223] it could be argued that l_p is not affected by the anisotropic shrinkage of the pores in the axial and transverse direction but by the overall shrinkage of the porous media.

Recovery of plastic deformations by annealing. After a second heat-treatment on HT1 after compression, the sample recovered almost completely the axial deformation and the volume returned to 98.5 % of the volume before compression. The scattering patterns after the 2nd annealing were virtually identical to the ones before the compression experiment, indicating a complete recovery of the nanostructure within the accessible q range (Figure C.12). This was observed in both axial and transverse directions, sign of no preferential orientation after annealing. All other properties (porosity, mean chord length of the pores, fractal dimension, mean size of clusters) also returned to their original values (Figure 6.5a). These observations supported the hypothesis of a mechanical lock of the silica network upon compression, eventually through the entanglement of the silica chains that relaxed when subjected to a thermal treatment. This capability of aerogels to restore macro- and nano-structure upon a thermal treatment is also characteristic of a thermoplastic behavior in polymers, where the materials flexibility highly depends on the temperature.[224,225] Table 6.1 summarizes the properties computed before and after the annealing of a dry (nHT3) and a compressed (HT1) gel.

In terms of applications, a mechanical lock of the silica network after drying or after mechanical compression by residual pore liquid and/or entanglement may be beneficial to prevent the development of stress gradients that can occur if the gel fully re-expands at room temperature. By providing subsequent thermal energy, the solid matrix may become more compliant allowing to complete the SBE while alleviating the risks of mechanical failure. Additionally, the ability to control the aerogel re-expansion by thermal activation could have direct applications, such as facilitating the incorporation of monolithic aerogels in window glazing systems.[9] Tailoring the drying process to promote the occurrence of the SBE in two-steps could also ultimately increase the size of the monoliths that can be produced by APD, which remains the most important limiting factor compared to supercritical drying.

Table 6.1 Summary of the properties of sample nHT3 in the dry and annealed states, and of sample HT1 in the dry, annealed, and annealed after compression states. The properties derived by μCT measurements are depicted with a superscript (*). The properties derived from the volume measured by a caliper are depicted with a superscript (**). HT1 in the dry state was not characterized by SAXS/WAXS, thus some properties could not be calculated.

	Dry (nHT3)	Annealed (nHT3)	Dry (HT1)	Annealed (HT1)	Annealed after compression (HT1)
Apparent density (mg cm^{-3})	419.5 ± 0.6**	168.4 ± 0.2**	387.9 ± 0.5*	120.4 ± 0.2*	119.2 ± 0.2**
Porosity (%)	75.49 ± 0.05	90.73 ± 0.27	78.80 ± 0.24*	93.42*	93.74 ± 0.28
Fractal dimension (-)	2.16 ± 0.04	2.35 ± 0.01	-	2.35 ± 0.00	2.35 ± 0.00
Specific surface area (m^2 g^{-1})	1261 ± 18	1326 ± 19	-	1327 ± 14	1325 ± 15
Particle radius (nm)	1.30 ± 0.02	1.24 ± 0.02	-	1.24 ± 0.01	1.24 ± 0.01
Mean chord length of the pores l_p (nm)	5.34 ± 0.08	16.15 ± 0.53	-	23.40 ± 0.24	24.71 ± 1.13
Mean cluster size ξ (nm)	7.49 ± 0.65	47.65 ± 2.50	-	83.41 ± 3.40	80.76 ± 3.45

6.4 Summary

This study elucidates several key aspects regarding the mechanical behavior and structural characteristics of silica aerogels and contribute to both, a better understanding on the deformation mechanisms in aerogels and on the processing of aerogels. The occurrence of the spring-back effect in two steps plays a crucial role in providing mechanical stability to the solid matrix, thereby preventing the development of stress gradients and subsequent mechanical fracture. The full recovery of both the macro- and nanostructure of silica aerogels through annealing emphasizes the programmable nature of aerogels whose re-expansion after drying or compression can be controlled by thermal activation. It also supports the hypothesis that partial spring-back is caused by the presence of residual solvent and the entanglement of silica clusters, preventing a full re-expansion of the pore volume.

Correlations between long-range nanostructural changes and macroscopical deformations during mechanical tests highlight the intricate relationship between microstructure and mechanical behavior. Different deformation mechanisms were proposed for the dry and annealed gels, the former proceeding by large silica clusters sliding along

themselves in the axial direction and being redistributed laterally. For the annealed gels, deformation was accommodated by a sequential compression of large pores beyond the fractal range, resulting in a near-zero Poisson's ratio.

Overall, these findings contribute to a deeper understanding of the mechanical and structural properties of silica aerogels as well as porous materials in general, paving the way for their enhanced utilization in various engineering and technological applications.

7 Summary and outlook

The preparation of silica aerogels by ambient-pressure drying (APD) faces several challenges due to the difficulty of preserving the structural integrity of the gels upon evaporation of the pore liquid. Although surface modification enables to recover the drying shrinkage through the spring-back effect, silica gels are prompt to mechanical failure during the drying process. This leads to a decrease in thermal conductivity and optical transparency of aerogel products and limits the size of monolithic objects that can be produced, which remains a major limitation of the ambient-pressure drying process. There is thus an incentive to better understand the evaporative drying process, spring-back effect and related deformations of the silica gels.

This thesis tackled these topics by studying two aspects that were interesting and yet unexplored. One aspect was to assess the kinetics and spatial distribution of the liquid and vapor phases in the gels during drying. In a first step, a sol-gel process was established to create silylated silica gels that demonstrated the spring-back effect and created monolithic aerogels. An experimental and analytical procedure based on X-ray micro-computed tomography (μCT) was developed to study the drying kinetics. This was framed into the first goal of this dissertation. In a second step, the μCT workflow was improved to enable spatial resolution of the gels' phase composition and a detailed interpretation of the evaporation mechanisms. This was framed into the second goal of this dissertation. The second aspect addressed the capabilities of silica aerogels to recover residual deformations by thermal activation. The structural changes of aerogels during mechanical compression and after subsequent annealing were characterized by small-angle X-ray scattering (SAXS) to shine light on the causes of causes of residual deformations. This was framed into the third goal of this dissertation.

In the **first goal**, the average volumes of the silica skeleton, hexane and vapor phases in silylated silica gels were successfully computed by a μCT quantitative imaging workflow. The drying kinetic was outlined by a constant evaporation rate for the first 6 h of drying followed by a slight decrease until the maximum shrinkage at ca. 8 h of drying. After the maximum shrinkage, the evaporation rate decreased exponentially as the gels were re-expanding, which was attributed to a diffusion-limited desorption of hexane. The emergence of the spring-back effect (SBE) was correlated to an equal volume fraction of silica skeleton, hexane and vapor/air. On the one hand, this critical composition may correspond to the point where some pores were completely depleted of pore liquid, enabling a local relaxation of the drying stress.

On the other hand, this revealed that there was already a substantial amount of vapor/air in the gels before the maximum shrinkage, which was counterintuitive given the common models for evaporative drying of gels. The limited spring-back efficiency of the gels (ca. 30 vol %) was interpreted as a possible mechanical lock of the silica skeleton due to residual hexane or entanglement of the solid network.

The reproducibility of the results between different samples highlights the potential of lab-source μCT methods to perform phase composition analysis. The method also allowed calculating the gels skeletal density, which was in relatively good agreement to values reported using helium pycnometry. Simulations using the μCT data collected on unmodified gels allowed to explain the surprisingly low values of skeletal density calculated in those samples by considering condensation reactions during drying. As the silica skeleton undergoes chemical transformations, it introduces more variables than equations in the drying model (notably by releasing water molecules), which prevents to compute the phase composition of unmodified gels.

In the **second goal**, composition maps of hexane and vapor/air were successfully generated by further analyzing the μCT data collected during the drying of silylated silica gels. The spatial distribution of the gas phase in the gels combined with the observations made in the first goal allowed to draw a model of the evaporation mechanisms throughout APD. At first, evaporation proceeded by drying shrinkage as the volume loss of hexane perfectly matched the gel volume shrinkage. After about 3.5 h, a vapor/air phase started growing rather homogeneously across the gels volume. The spatial and temporal distribution of this gas phase suggested it was created by cavitation of hexane, which occurred in parallel to the evaporation by drying shrinkage. At ca. 7.5 h, a drying front emerged from the top of the gels and the fraction of vapor/air abruptly increased, which was attributed to the onset of evaporation by recession of the liquid-vapor interface. The presence of vapor/air prior to the maximum shrinkage was verified by modeling wide-angle X-ray scattering (WAXS) data collected in-operando during drying. Estimations based on classical nucleation theory (CNT) were consistent with the growth rate of vapor/air determined experimentally by μCT and supported the hypothesis of hexane cavitation. The experimental observation of evaporation by cavitation in silica gels, as demonstrated in this study, expands our understanding of the APD process for the preparation of aerogels.

The reliability of the results presented in this project was assessed by careful evaluation of the experimental and computational artifacts that may arise throughout the spatially resolved μCT quantitative imaging workflow. It was proposed that beam hardening had a non-negligible

effect on the composition maps, notably preventing to interpret the variations in composition along the gels' radius. Overall, the volume fraction maps derived by the local analysis of the μCT data were consistent with the average volumes computed in the first goal, supporting the validity of the workflow.

In the **third goal**, the spring-back of the dry gels was completed by thermal annealing at 230 °C, resulting in a recovery to about 85 vol % of the alcogel volume. Re-expansion by thermal activation emphasized the reversibility of residual deformations related to drying shrinkage. The changes in fractal dimension, specific surface area and primary particle size of the gels upon annealing of a dry gel were interpreted as a broadening of the pore size distribution past a critical pore size towards larger pores. This strongly suggested that dry gels were in a metastable state where residual compressive stresses prevented the relaxation of the silica skeleton. Moreover, the occurrence of the spring-back in two-steps was shown to produce monolithic aerogels of high quality and reproducibility. Such a two-step SBE may be beneficial for the preparation of silica aerogels, as higher temperatures could reduce the risk of cracks during re-expansion by increasing the flexibility of the silica skeleton. Thermal annealing also enabled the recovery of residual deformations related to uniaxial compression tests. The aerogel structure was completely restored at a macroscale as well as at a nanoscale within the resolution range of the X-ray scattering experiments. The recovery capabilities of silica aerogels by thermal activation is interesting in terms of fundamental research, as it pictures different mechanical behaviors between viscoelasticity and plasticity depending on temperature. This finding notably uncovers the programmable nature of silica aerogels, which could have valuable applications in materials conception and engineering.

In this project, the compressibility and deformation mechanisms of dry and annealed silica aerogels was also investigated. The annealed gel was highly compressible up to a strain of 43 %, but showed a more plastic behavior after unloading with a residual strain of 23.3 %. The dry gels were less compressible (30 %) and showed characteristics closer to viscoelasticity with a residual strain of only 4.4 %. The SAXS data collected in-operando during compression revealed different evolution of the nanostructure in the dry and annealed gels. Although interpretation of the SAXS data was limited, it was proposed that the uniaxial compression in the dry gel was accommodated by the re-arrangement of large silica clusters along the transverse direction. In the annealed gel, deformation could possibly occur through the collapse of large pores beyond the fractal range.

The main findings of this dissertation were on the onset of evaporation by cavitation during APD and on the occurrence of the two-step spring-back controlled by thermal

activation. The author believes that these two aspects have an important role to play in the improvement of the APD process for the production of large monolithic silica aerogels by APD, and should thus be of high interest to investigate further. It should notably be assessed if performing APD at higher temperatures promotes evaporation by cavitation, and if it allows to create larger monolithic aerogels that way. In practice, this can be done by monitoring the APD process using the μCT workflow developed in this thesis, but solvent cavitation in gels should also be verified through other methods such as acoustic detection and light scattering. Additionally, further research could be done on the mechanisms of re-expansion upon annealing by performing in-operando μCT or SAXS/WAXS experiments. To this regard, it should also be assessed if a two-step SBE can produce larger crack-free aerogels than those produced via the one-step SBE.

Prospectively, the μCT procedure could easily be adapted to the study of materials other than silica gels and could be interesting for the several facilities equipped with a lab-source CT instrument. While the local μCT analysis required much more data processing, modeling and careful interpretation of the CT artifacts, the first approach to compute the average phase composition can already provide valuable insights on materials undergoing time-dependent transformations.

Appendix A. In Operando μCT Imaging of Silylated Silica Aerogels

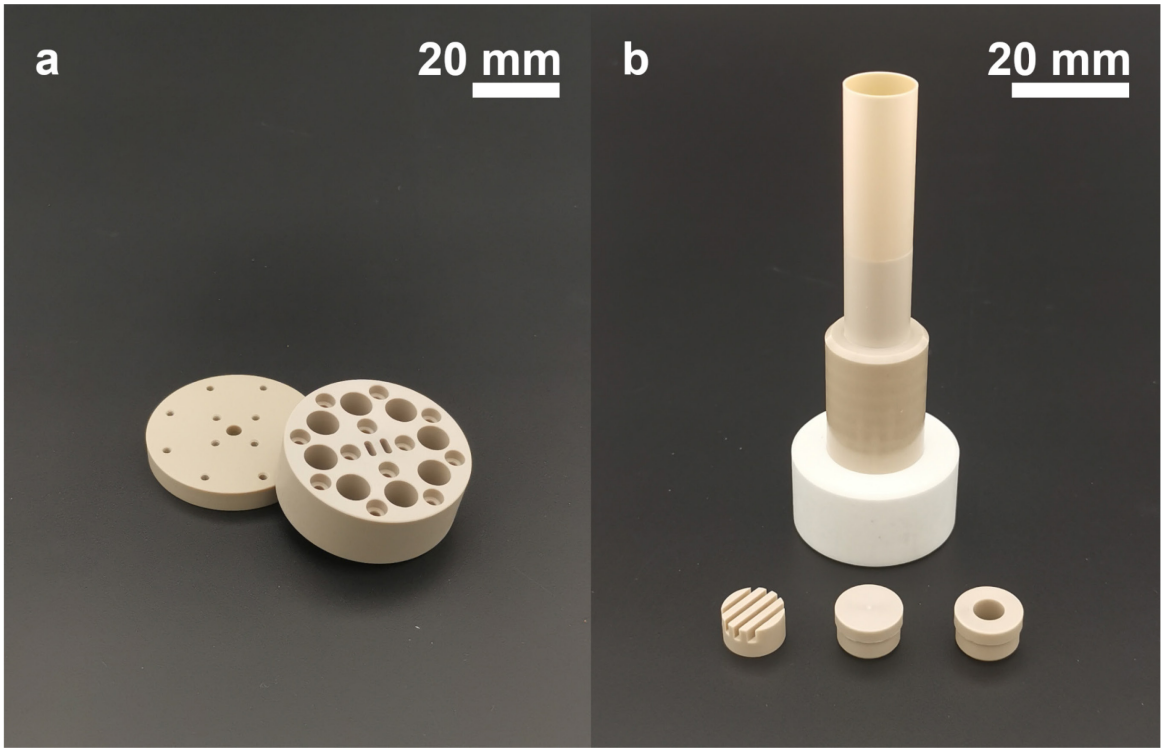

Figure A.1 (**a**) Two-parts mold out of PEEK used for the casting of the gels. Each mold contains eight slots and each slot is 16 mm deep and is 8 mm in diameter. (**b**) Drying chamber used in the in-operando μCT experiments. The inner and outer diameter of the chamber is 12 and 12.8 mm respectively, and the height is 24 mm. The diameter of the hole in the lid is 6 mm. Reprinted from ref.[102], CC BY 4.0 (https://creativecommons.org/licenses/by/4.0/).

A.1 Automated segmentation procedure

Each stack of slices generated by the reconstruction contained the signal of the sample, the chamber and the background (gas). Given the significant amount of datasets to process and the relatively simple geometry of the material, an automated segmentation approach was implemented in the software Dragonfly. Prior to this approach, an ROI separating the sample from the drying chamber was created manually and was unique to each sample. The automated segmentation procedure was run in the python console of Dragonfly. The main steps of the script were:

d) Import of the reconstructed slices in the Dragonfly software.

e) The raw reconstructed images are smoothened with a 2D square median filter (kernel size 7).

f) The manual ROI is loaded.

g) From the filtered images, an ROI foreground is created using the Otsu thresholding method.

h) Intersection of the ROI foreground and the manual ROI.

i) Processing of the ROI:

   1) The noise within the ROI foreground is reduced using the "close" morphological operation (2D, square) at a kernel size of 3.

   2) The background noise outside of the gel is reduced using the "open" morphological operation (2D, square) at a kernel size of 5.

   3) The largest volume of the foreground ROI in terms of voxel count is isolated by connected component labelling (6-connected), resulting in the final ROI.

The different steps of the procedure are illustrated in Figure A.2.

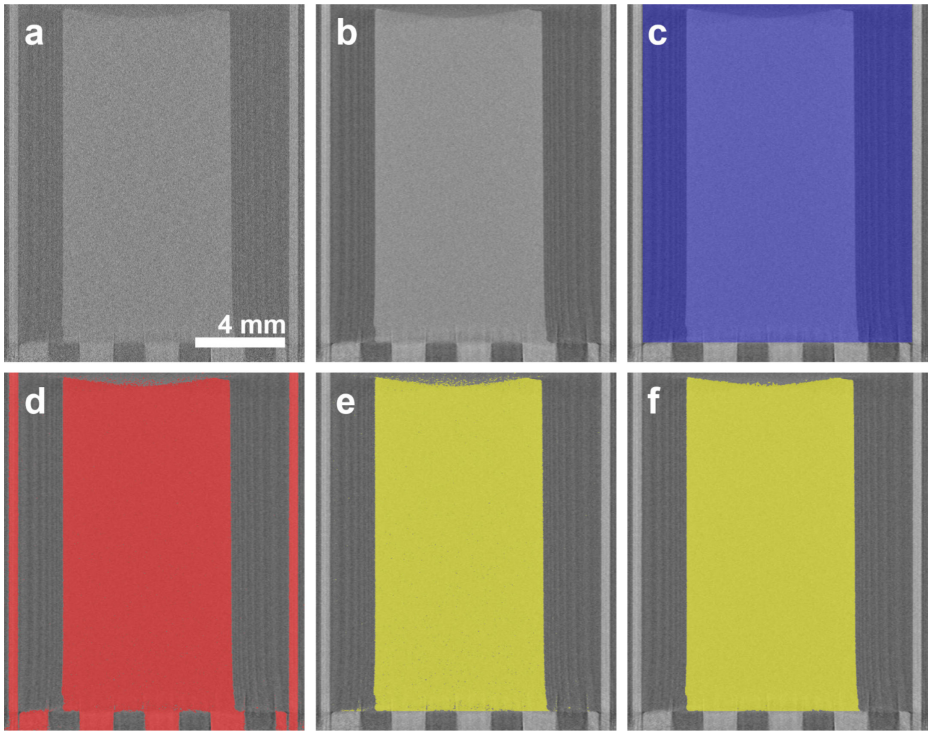

Figure A.2 Reconstructed µCT images of the gel in the chamber at $t = t_0$ along with ROIs at different steps of the segmentation. (**a**) Raw µCT image with a scale bar. (**b**) Filtered image. (**c**) Manual ROI excluding the chamber. (**d**) Foreground ROI from Otsu thresholding. (**e**) Intersection of foreground and manual ROI. (**f**) Final ROI. Reprinted from ref.[102], CC BY 4.0 (https://creativecommons.org/licenses/by/4.0/).

The following quantities were calculated in Dragonfly:

a) The volume of the gel: $\tilde{V}_k$ was given by the voxel count in the final ROI.
b) The surface of the gel in each vertical slice: $A_{i,k}$ was computed on the final ROI using the slice analysis plugin in Dragonfly.
c) The average gray value of the gel in each vertical slice: $\tilde{g}_{i,k}$ was computed on the raw reconstructed slices masked by the final ROI using the slice analysis plugin.

Where i corresponds to the slice number or to the height of the gel and k to the scan number.

A.2 Correction of the gel's volume

The accuracy of the automated segmentation script was assessed by performing manual segmentations on 11 randomly selected μCT scans for different samples and at different drying stages. The manual segmentation was assumed to be flawless and thus provided a reference measurement of the volume of the gel. The difference between automated and manual segmentations was quantified by calculating the relative volume difference obtained by both methods. The relative volume difference was defined as:

$$\delta = \frac{V_{\text{manu}} - \tilde{V}}{\tilde{V}} \cdot 100\%, \tag{A.1}$$

where V_{manu} and $\tilde{V}$ are the volumes computed by manual and automated segmentation respectively. Figure A.3 shows the relative volume difference for the 11 μCT scans.

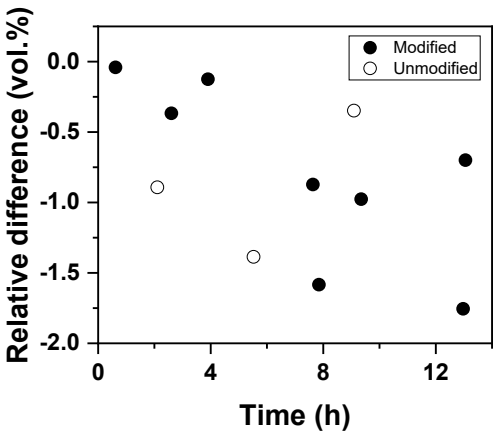

Figure A.3 Relative difference of the gels volume between manual segmentation and automated segmentation on different samples and at different drying time. Reprinted from ref.[102], CC BY 4.0 (https://creativecommons.org/licenses/by/4.0/).

The gel volume computed by automated segmentation was always overestimated compared to the manual segmentation. No trend of the sample, sample type (modified vs unmodified) or drying time was identified. On average, the relative difference was $u_\delta =$

-0.822 vol.%. The volume of the gels computed by automated segmentation was corrected with:

$$V = \left(1 + \frac{u_\delta}{100}\right) \cdot \tilde{V}, \tag{A.2}$$

where V is the corrected volume. The error and error propagation on the volume was calculated in appendix A.4.

A.3 Correction of the anode heel effect

During the first drying stage of the gels, the gray values of the slices decreased linearly from the top to the bottom of the gel (Figure A.4). The bump of gray values at the bottom of the gel was caused by the gel's proximity to lower region of the PEEK chamber, which had a higher X-ray absorption. Potential heterogeneities in the gels were ruled out, since the slope of the linear region kept its sign and magnitude when the gels were flipped upside down. The difference in gray values between the top and the bottom of the gel ranged from 0.9 to 1.4 % of the 255 gray values and had a non-negligible impact in the quantitative imaging analysis. The gray value gradient was due to the anode heel effect,[133] a common phenomenon in X-ray tubes, and was already present in the μCT projections.

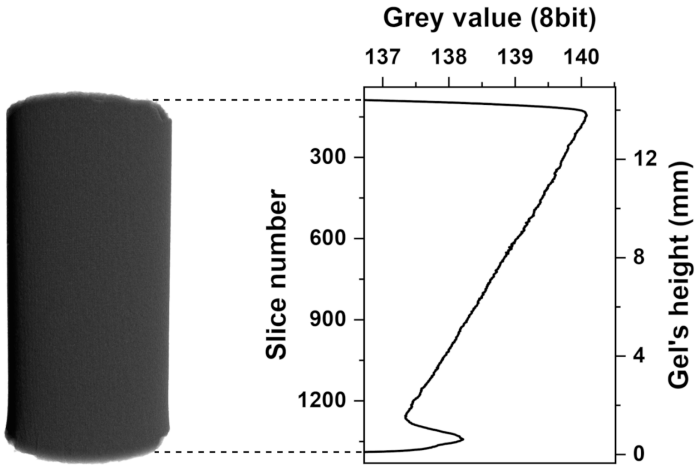

Figure A.4 Example of the anode heel effect in the reconstructed slices of a gel at $t = t_0$ or $k = 0$. (left) 3D volume after segmentation. (right) Gray value profile $\tilde{g}_{i,k=0}$; the left Y axis on the graph represents the position of the voxels in the z-axis of the cylinder, or the slice number i. Reprinted from ref.[102], CC BY 4.0 (https://creativecommons.org/licenses/by/4.0/).

The gray value profiles $\tilde{g}_{i,k}$ from the automated segmentation procedure were corrected by assuming that the phase composition in the gels was homogeneous until a certain scan

number $k = k_c$ near the point of maximum shrinkage. The time values $t_{k=k_c}$ are reported in Table A.1 for each gel. The corrected profiles $g_{i,k}$ were calculated as follows:

a) Linear regression on $\tilde{g}_{i,k}$ versus i, where $i_1 < i < i_2$ and $k < k_c$, with i_1 and i_2 the range over which the fit is performed, resulting in a set of slopes m_k.
b) Tilting of $\tilde{g}_{i,k}$ with m_k and around a pivot i_p:

$$g_{i,k} = \tilde{g}_{i,k} + (i_p - i) \cdot m_k. \tag{A.3}$$

The pivot i_p is the slice number on which the reconstruction corresponds to the horizontal array of pixels of the detector located at mid-height, in alignment with the incoming X-ray beam (Table A.1). i_p could be arbitrary, as long as it stays constant for a given sample. The center of the detector was chosen because it is normally the region where the features of a CT scan are best resolved. After correction, the global gray value G_k was calculated by taking the average of the gray value profiles for $k < k_c$:

$$G_{k<k_c} = \frac{1}{\tilde{V}_k} \sum_{i}^{N} g_{i,k} \cdot A_{i,k}, \tag{A.4}$$

where $\tilde{V}_k$ and $A_{i,k}$ are respectively the gel's uncorrected volume and the area of the slices calculated in appendix A.1 and N is the total number of slices. At $k \geq k_c$, the gray value profiles become more complex due to the heterogeneous spring-back effect (Figure A.5).

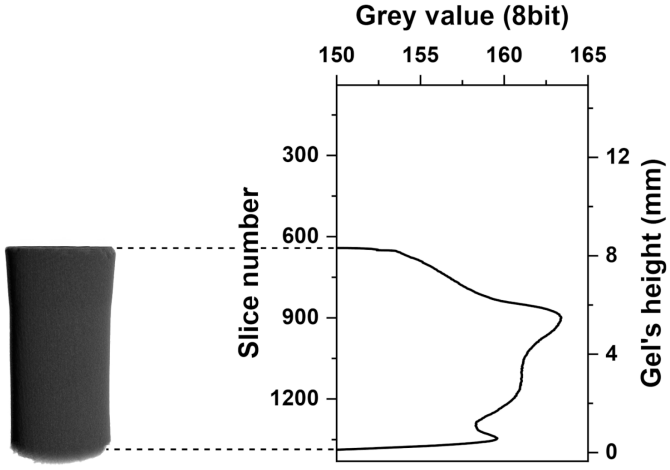

Figure A.5 Example of the anode heel effect in the reconstructed slices of a gel at $k = k_c$. (left) 3D volume after segmentation. (right) Gray value profile $\tilde{g}_{i,k=k_c}$; the left Y axis on the graph depicts the position of the voxels in the z-axis of the cylinder, or the slice number i. Reprinted from ref.[102], CC BY 4.0 (https://creativecommons.org/licenses/by/4.0/).

The gray value profiles $\tilde{g}_{i,k}$ for $k \geq k_c$ can be corrected taking advantage of the slopes calculated at $k < k_c$. To each slope m_k corresponded a global gray value G_k, therefore the

slope can be expressed in function of a gray value: m_{G_k} for $k < k_c$. m_{G_k} was fitted with a decaying exponential function, resulting in a function $m^*(g)$ which allowed to extrapolate the slope for gray values outside the range of $G_{k<k_c}$:

$$m^*(g) = A \cdot e^{-B \cdot g} + C, \tag{A.5}$$

where A, B and C are the parameters resulting from the fit. Figure A.6 shows an example of m_{G_k} and the corresponding fit with $m^*(g)$.

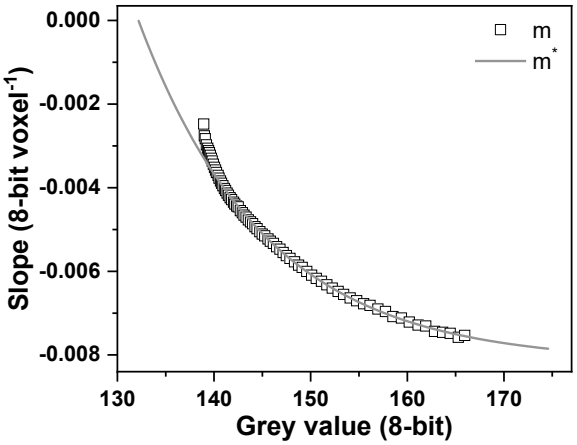

Figure A.6 Example of the original (scatter) slope m_{G_k} from the linear regression on $\tilde{g}_{i,k}$ plotted vs G_k for $k < k_c$ and the fitted (gray line) slope $m^*(g)$. The points m_{G_k} at the lowest gray values G_k were excluded upon fitting due to beam instabilities at the beginning of the drying. Reprinted from ref.[102], CC BY 4.0 (https://creativecommons.org/licenses/by/4.0/).

The correction of the gray value profiles $\tilde{g}_{i,k}$ for $k \geq k_c$ was then done similarly as in eq. (A.3) using:

$$g_{i,k} = \tilde{g}_{i,k} + (i_p - i) \cdot m^*(\tilde{g}_{i,k}). \tag{A.6}$$

After correction, the global gray value G_k was calculated with eq. (A.4). Figure A.7 shows the two gray value profiles of the gel at $k = 0$ and $k = k_c$ (shown in Figure A.4 and Figure A.5) before and after correction.

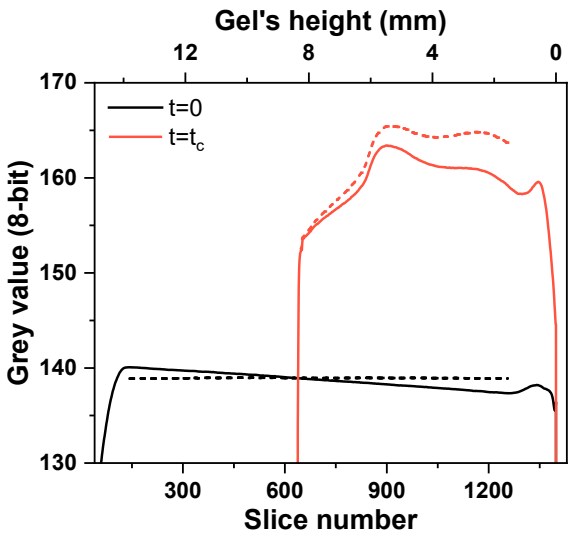

Figure A.7 Original (full line) and corrected (dashed line) gray value profiles at $k = 0$ (black) and $k = k_c$ (red). The correction was done at the pivot $i_p = 628$. The global gray values read $G_{k=0} = 138.9$ and $G_{k=k_c} = 162.1$. Reprinted from ref.[102], CC BY 4.0 (https://creativecommons.org/licenses/by/4.0/).

A.4 Error propagation

Individual error. The quantitative imaging procedure generated two quantities: the volume of the gel V_k and the global gray value G_k. The error on the volume was calculated from the relative volume difference δ between the volume computed by the automated segmentation procedure and the volume resulting from a manual segmentation (appendix A.2). The error on the gray values could not be computed from the µCT scans of the silica gels, as the gray values were changing during drying. Instead, the error of the gray values was calculated from the data on the hexane reference sample (Figure 4.5c) and was also used as the error of the gray values of the drying gels G_k. The distribution of both the volume and the gray value quantities were compared to a normal distribution in a quantile-quantile (Q-Q) plot (Figure A.8). For the volume, the Q-Q plot was constructed on the eleven values of δ and for the gray values it was constructed on the global gray value $G_{\mathrm{hex},k}$ in the last 137 µCT scans.

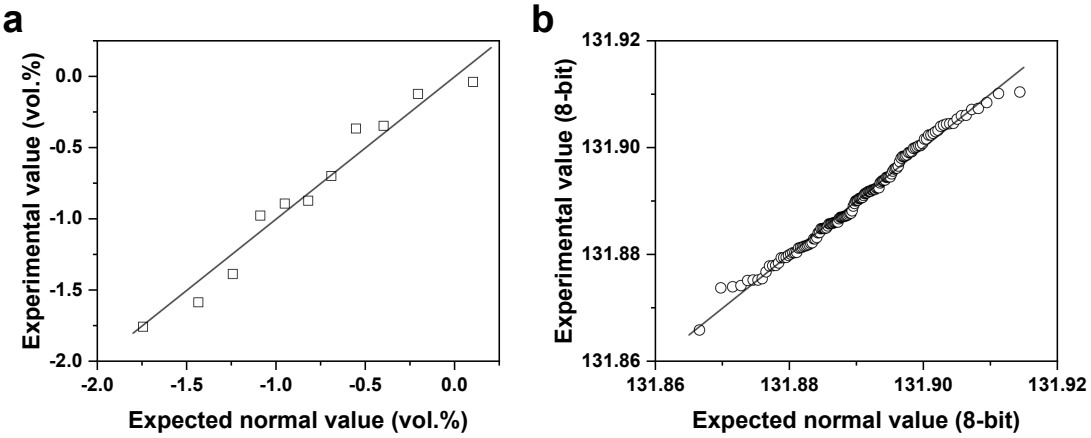

Figure A.8 (**a**) Normal Q-Q plot of the relative volume difference in vol.%. (**b**) Normal Q-Q plot of the global gray values $G_{hex,k}$ of the reference hexane sample. Reprinted from ref.[102], CC BY 4.0 (https://creativecommons.org/licenses/by/4.0/).

In both distributions, the linearity of the points suggested that the data were normally distributed. We can write: $\delta \sim N(u_\delta, \sigma_\delta)$ with a mean of u_δ = -0.822 vol.% and a standard deviation of σ_δ = 0.578 vol.%; $G_{\text{hex}} \sim N\left(u_{G_{\text{hex}}}, \sigma_G\right)$ with a mean of $u_{G_{\text{hex}}}$ = 131.8905 and a standard deviation of σ_G = 0.0092. The error on the volume depended on the volume itself due to the definition of δ in eq. (A.2). Therefore, for $\delta \sim N(u_\delta, \sigma_\delta)$, the volume followed a normal distribution $V_k \sim N\left(u_{V_k}, \sigma_{V_k}\right)$ with:

$$u_{V_k} = \left(1 + \frac{u_\delta}{100}\right) \cdot V_k, \tag{A.7}$$

$$\sigma_{V_k} = \frac{\sigma_\delta}{100} \cdot V_k. \tag{A.8}$$

The global gray values of the gel followed a normal distribution centered around the experimental value of G_k, given by $G_k \sim N\left(u_{G_k}, \sigma_G\right)$, with:

$$u_{G_k} = G_k, \tag{A.9}$$

$$\sigma_G = 0.00923. \tag{A.10}$$

Numerical error propagation. The error propagation was done numerically using the *numpy.random* library from NumPy.[192] It was performed independently for the couples of values $(V_k\,, G_k)$ using populations of 10'000 values for each distribution. At a given scan number k, two populations $V_{k,l}$ and $G_{k,l}$ were generated from $V_k \sim N\left(u_{V_k}, \sigma_{V_k}\right)$ and $G_k \sim N\left(u_{G_k}, \sigma_G\right)$, with $0 \leq l < 10'000$. Since the RAC of hexane was assumed to be constant during drying, a single population $G_{\text{hex},m}$ from $G_{\text{hex}} \sim N\left(u_{G_{hex}}, \sigma_G\right)$ with $0 \leq m < 10'000$ was used for the computation for all 141 points in time and was not regenerated at each iteration. At a given scan number k, the variables of interest were calculated from $V_{k,l}$, $G_{k,l}$ and $G_{hex,m}$ resulting in

10'000 estimates of each of these variables. The error propagation was not performed on quantities that were averaged over a duration, like the skeleton volume V_{skel}. For example, the estimates of V_{hex,k^*} at an arbitrary scan number k^* were calculated as:

$$V_{\mathrm{hex},k^*,n} = \frac{\left(\frac{G_{k^*,n}}{255}(b-a)+a\right)V_{k^*,n} - \mu_{\mathrm{skel}}V_{\mathrm{skel}}}{\left(\frac{G_{hex,n}}{255}(b-a)+a\right)}, \qquad 0 \le n < 10'000. \qquad \text{(A.11)}$$

In eq. (A.11), the RAC was expressed as a gray value with $\mu = g \cdot (b-a)/255 + a$. From the estimates of the variables of interest, the 95$^{\mathrm{th}}$ percentile was computed and was used to show the error bands in Figure 4.4, Figure 4.5, Figure 4.6 and Figure A.14, Figure A.16, Figure A.17.

A.5 Simulations of condensation reactions

Assumptions. The simulations were performed by allowing a variation of μ_{skel} and V_{skel} during drying to translate the condensation reactions resulting in the creation of water in the silica gels. Only the reactions between silanol groups were considered, the condensation reactions between remaining alkoxide and hydroxyl groups were not considered. The assumptions were:

a) At the beginning of drying for $k_1 \le k \le k_2$, the skeleton RAC and volume are constant: $\mu_{\mathrm{skel},k_1\le k\le k_2} = \mu^0_{\mathrm{skel}}$ and $V_{\mathrm{skel},k_1\le k\le k_2} = V^0_{\mathrm{skel}}$.
b) At the beginning of drying for $k_1 \le k \le k_2$, the gel contains: skeleton and hexane.
c) At the end of drying for $k \ge k_d$, the skeleton RAC and volume are constant: $\mu_{\mathrm{skel},k\ge k_d} = \mu^d_{\mathrm{skel}}$ and $V_{\mathrm{skel},k\ge k_d} = V^d_{\mathrm{skel}}$
d) At the end of drying for $k \ge k_d$, the gel contains: skeleton, air and water.
e) The RAC of hexane μ_{hex} and water μ_{H_2O} are constant during drying.
f) The skeletal density is 1.9 and 2.4 g cm^{-3} for the modified and unmodified gels respectively.
g) The water stays in the gels and does not evaporate over time.

Equations and variables. The equations in chapter 4.2 were reworked using the assumptions listed above. Furthermore, simulations were performed on the final state and the initial state of the gel only. The equations for $k_1 \le k \le k_2$ were:

$$\bar{\mu}_k = \frac{\mu_{\mathrm{hex}}V_{\mathrm{hex},k} + \mu^0_{\mathrm{skel}}V^0_{\mathrm{skel}}}{V_k}, \qquad \text{(A.12)}$$

$$V_k = V_{\text{hex},k} + V^0_{\text{skel}}, \tag{A.13}$$

and the equations for $k \geq k_d$ were:

$$\bar{\mu}^d = \frac{\mu^d_{\text{skel}} V^d_{\text{skel}} + \mu_{H_2O} V^d_{H_2O}}{V^d}, \tag{A.14}$$

$$\tilde{V}^d = V^d_{\text{skel}} + V^d_{\text{air}} + V^d_{H_2O}, \tag{A.15}$$

$$\rho_{\text{skel}} = \frac{m^d - m^d_{H_2O}}{V^d_{\text{skel}}}, \tag{A.16}$$

where μ_{H_2O} is the RAC of water, V^d_{air} is the gas volume in the dry gel, ρ_{skel} is the skeletal density of the dry gel and $V^d_{H_2O}$ and $m^d_{H_2O}$ is the volume and the mass of water in the dry gel. μ_{H_2O} was calculated similarly to μ_{hex} from in-operando μCT scans on a reference sample of deionized water. Unlike the reference sample of hexane where 141 scans were performed, only 16 scans were performed for the water sample (Figure A.9). The global gray value of water was corrected for the anode heel effect (appendix A.3) and μ_{H_2O} was computed from G_{H_2O} averaged over the 9 last scans.

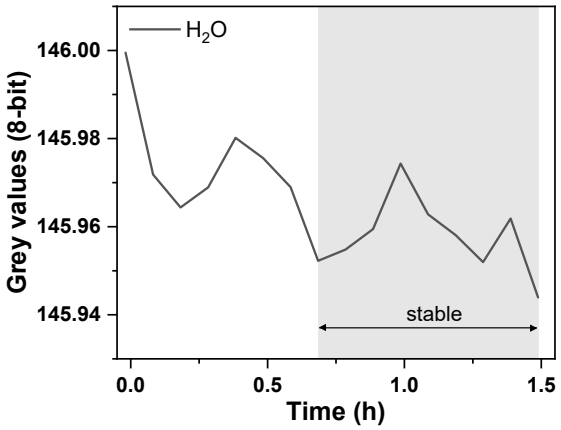

Figure A.9 Corrected global gray value of a water reference sample. The stable region is highlighted in gray. The curve consists in 16 data points. Reprinted from ref.[102], CC BY 4.0 (https://creativecommons.org/licenses/by/4.0/).

The system of five equations built with eqs. (A.12)-(A.16) contained seven unknowns:

$$V_{\text{hex},k_1 \leq k \leq k_2}, V^0_{\text{skel}}, V^d_{\text{skel}}, V^d_{\text{air}}, V^d_{H_2O}, \mu^0_{\text{skel}}, \mu^d_{\text{skel}},$$

where the relation $m^d_{H_2O} = \rho_{H_2O} \cdot V^d_{H_2O}$ was considered trivial. Solving the equations will thus lead to a solution of type $z = f(x, y)$ with two degrees of freedom given by variables x and y. The solution was expressed as a function of the following variables of interest:

$$C_V = \frac{V_{\text{skel}}^d}{V_{\text{skel}}^0}, \tag{A.17}$$

$$C_\mu = \frac{\mu_{\text{skel}}^d}{\mu_{\text{skel}}^0}, \tag{A.18}$$

$$C_H = \frac{V_{H_2O}^d}{V_{\text{skel}}^d}, \tag{A.19}$$

where C_V and C_μ represent the relative change in skeleton volume and RAC compared to the initial state of the gel and C_H represents the relative gain in water volume compared to the final skeleton volume.

Solving the equations. Substitute eq. (A.13) in eq. (A.12) to eliminate $V_{hex,k}$:

$$\bar{\mu}_k = \frac{\mu_{\text{hex}}\left(V_k - V_{\text{skel}}^0\right) + \mu_{\text{skel}}^0 V_{\text{skel}}^0}{V_k}, \tag{A.20}$$

$$\Leftrightarrow (\bar{\mu}_k - \mu_{\text{hex}})V_k = \mu_{\text{skel}}^0 V_{\text{skel}}^0 - \mu_{\text{hex}} V_{\text{skel}}^0. \tag{A.21}$$

Use eqs. (A.17) and (A.18) to eliminate $\mu_{\text{skel}}^0 V_{\text{skel}}^0$ in eq. (A.21):

$$(\bar{\mu}_k - \mu_{\text{hex}})V_k = \frac{\mu_{\text{skel}}^d V_{\text{skel}}^d}{C_V C_\mu} - \frac{\mu_{\text{hex}} V_{\text{skel}}^d}{C_V}. \tag{A.22}$$

Rework eq. (A.14) with eq. (A.19):

$$\bar{\mu}^d = \frac{\mu_{\text{skel}}^d V_{\text{skel}}^d + \mu_{H_2O} C_H V_{\text{skel}}^d}{V^d}. \tag{A.23}$$

Substitute eq. (A.23) in eq. (A.22) to eliminate $\mu_{\text{skel}}^d V_{\text{skel}}^d$:

$$(\bar{\mu}_k - \mu_{\text{hex}})V_k = \frac{\bar{\mu}^d V^d - \mu_{H_2O} V_{\text{skel}}^d C_H}{C_V C_\mu} - \frac{\mu_{\text{hex}} V_{\text{skel}}^d}{C_V}, \tag{A.24}$$

$$\Leftrightarrow (\bar{\mu}_k - \mu_{\text{hex}})V_k = \frac{\bar{\mu}^d V^d}{C_V C_\mu} - \left(\frac{\mu_{H_2O} C_H}{C_V C_\mu} + \frac{\mu_{\text{hex}}}{C_V}\right) V_{\text{skel}}^d. \tag{A.25}$$

2nd part: substitute $m_{H_2O}^d = \rho_{H_2O} \cdot V_{H_2O}^d$ in eq.(A.16) to eliminate $m_{H_2O}^d$:

$$\rho_{\text{skel}} = \frac{m^d - \rho_{H_2O} \cdot V_{H_2O}^d}{V_{\text{skel}}^d} \tag{A.26}$$

Rework eq. (A.26) using eq. (A.19) to eliminate $V_{H_2O}^d$:

$$\rho_{\text{skel}} = \frac{m^d - \rho_{H_2O} V_{\text{skel}}^d C_H}{V_{\text{skel}}^d} \tag{A.27}$$

$$\Leftrightarrow \rho_{\text{skel}} V_{\text{skel}}^d = m^d - \rho_{H_2O} V_{\text{skel}}^d C_H \tag{A.28}$$

$$\Leftrightarrow V_{\text{skel}}^{d} = \frac{m^{d}}{\rho_{\text{skel}} + \rho_{H_2O} C_H} \tag{A.29}$$

Substitute eq.(A.29) in eq. (A.25) to eliminate V_{skel}^{d}:

$$(\bar{\mu}_k - \mu_{\text{hex}}) V_k = \frac{\bar{\mu}^{d} V^{d}}{C_V C_\mu} - \left(\frac{\mu_{H_2O} C_H}{C_V C_\mu} + \frac{\mu_{\text{hex}}}{C_V} \right) \cdot \frac{m^{d}}{\rho_{\text{skel}} + \rho_{H_2O} C_H} \tag{A.30}$$

$$\Leftrightarrow \left[(\bar{\mu}_k - \mu_{\text{hex}}) V_k - \frac{\bar{\mu}^{d} V^{d}}{C_V C_\mu} \right] \left(\rho_{\text{skel}} + \rho_{H_2O} C_H \right) = - \left(\frac{\mu_{H_2O} C_H}{C_V C_\mu} + \frac{\mu_{\text{hex}}}{C_V} \right) m^{d} \tag{A.31}$$

The term in the first bracket on the left-hand side of eq. (A.31) was abbreviated as α_k:

$$\alpha_k = (\bar{\mu}_k - \mu_{\text{hex}}) V_k - \frac{\bar{\mu}^{d} V^{d}}{C_V C_\mu} \tag{A.32}$$

Rewrite eq. (A.31) with eq. (A.32):

$$\alpha_k \left(\rho_{\text{skel}} + \rho_{H_2O} C_H \right) = - \left(\frac{\mu_{H_2O} C_H}{C_V C_\mu} + \frac{\mu_{\text{hex}}}{C_V} \right) m^{d} \tag{A.33}$$

$$\Leftrightarrow \left(\alpha_k \rho_{H_2O} + \frac{\mu_{H_2O} m^{d}}{C_V C_\mu} \right) C_H = -\alpha_k \rho_{\text{skel}} - \frac{\mu_{\text{hex}} m^{d}}{C_V} \tag{A.34}$$

$$\Leftrightarrow C_H = - \frac{\alpha_k \rho_{\text{skel}} + \frac{\mu_{\text{hex}} m^{d}}{C_V}}{\alpha_k \rho_{H_2O} + \frac{\mu_{H_2O} m^{d}}{C_V C_\mu}} \tag{A.35}$$

$$\Leftrightarrow C_H = - \frac{\alpha_k \rho_{\text{skel}} C_V C_\mu + \mu_{\text{hex}} m^{d} C_\mu}{\alpha_k \rho_{H_2O} C_V C_\mu + \mu_{H_2O} m^{d}} \tag{A.36}$$

Replace α_k in eq. (A.36):

$$C_H = - \frac{\left[(\bar{\mu}_k - \mu_{\text{hex}}) V_k - \frac{\bar{\mu}^{d} V^{d}}{C_V C_\mu} \right] \rho_{\text{skel}} C_V C_\mu + \mu_{\text{hex}} m^{d} C_\mu}{\left[(\bar{\mu}_k - \mu_{\text{hex}}) V_k - \frac{\bar{\mu}^{d} V^{d}}{C_V C_\mu} \right] \rho_{H_2O} C_V C_\mu + \mu_{H_2O} m^{d}} \tag{A.37}$$

$$\Leftrightarrow C_H = - \frac{\rho_{\text{skel}} \left[(\bar{\mu}_k - \mu_{\text{hex}}) V_k C_V C_\mu - \bar{\mu}^{d} V^{d} \right] + \mu_{\text{hex}} m^{d} C_\mu}{\rho_{H_2O} \left[(\bar{\mu}_k - \mu_{\text{hex}}) V_k C_V C_\mu - \bar{\mu}^{d} V^{d} \right] + \mu_{H_2O} m^{d}} \tag{A.38}$$

$$\Leftrightarrow C_H = \frac{\rho_{\text{skel}} \left[\bar{\mu}^{d} V^{d} - (\bar{\mu}_k - \mu_{\text{hex}}) V_k C_V C_\mu \right] - \mu_{\text{hex}} m^{d} C_\mu}{-\rho_{H_2O} \left[\bar{\mu}^{d} V^{d} - (\bar{\mu}_k - \mu_{\text{hex}}) V_k C_V C_\mu \right] + \mu_{H_2O} m^{d}} \tag{A.39}$$

The only time-dependent term was $(\bar{\mu}_k - \mu_{\text{hex}}) V_k$ and corresponds to the left-hand side of the mass conservation equation (see chapter 4.3). The time-dependent term was averaged over $k_1 \leq k \leq k_2$:

$$\beta = \sum_{k_1 \leq k \leq k_2} \frac{(\bar{\mu}_k - \mu_{\text{hex}})V_k}{N} \tag{A.40}$$

Where N is the number of scans for $k_1 \leq k \leq k_2$. The terms $(\bar{\mu}_k - \mu_{\text{hex}})V_k$ in eq. (A.39) were replaced by β and the final equation was derived:

$$C_H = \frac{\rho_{\text{skel}}\left[\bar{\mu}^d V^d - \beta C_V C_\mu\right] - \mu_{\text{hex}} m^d C_\mu}{-\rho_{H_2O}\left[\bar{\mu}^d V^d - \beta C_V C_\mu\right] + \mu_{H_2O} m^d} \tag{A.41}$$

This function has the form:

$$z = \frac{a_1 + a_2 y + a_3 xy}{1 + a_4 xy} \tag{A.42}$$

Eq. (A.41) shows that a decrease in skeleton volume is coupled to an increase in skeleton RAC at a constant water volume. This is expected since the condensation of hydroxyl groups to water leads to a higher fraction of silicon atoms in the silica skeleton, which has a higher attenuation coefficient than water[120]. The simulations were performed for $0.8 \leq C_V \leq 1.0$, $1.0 \leq C_\mu \leq 1.2$ and $0 \leq C_H \leq 0.1$ and computed in a python script. The results are available in Figure 4.8 and Figure A.18.

We were unable to evaluate at which point the condensation reactions occur during the drying. Assuming no volume change upon condensation reactions, the average attenuation coefficient of two silanol groups would be the same as the one of a siloxane group and a water molecule, leaving the μCT contrast unchanged at a voxel size of 11 μm. For similar reasons, it was not possible to consider the eventual evaporation of water because the impact of hexane and water evaporation on the global RAC cannot be decomposed into separate contributions. Water evaporation would result in a lower global RAC, which would be consistent with a lower plateau of $\bar{\mu}_k V_k$ at the end of the drying for the unmodified gels compared to the modified gels (Figure A.16e). An additional equation could further reduce the number of unknowns in the simulation. C_H may be fixed by comparing the weight of unmodified gels after the μCT measurement and after further drying, e.g. in a desiccator.

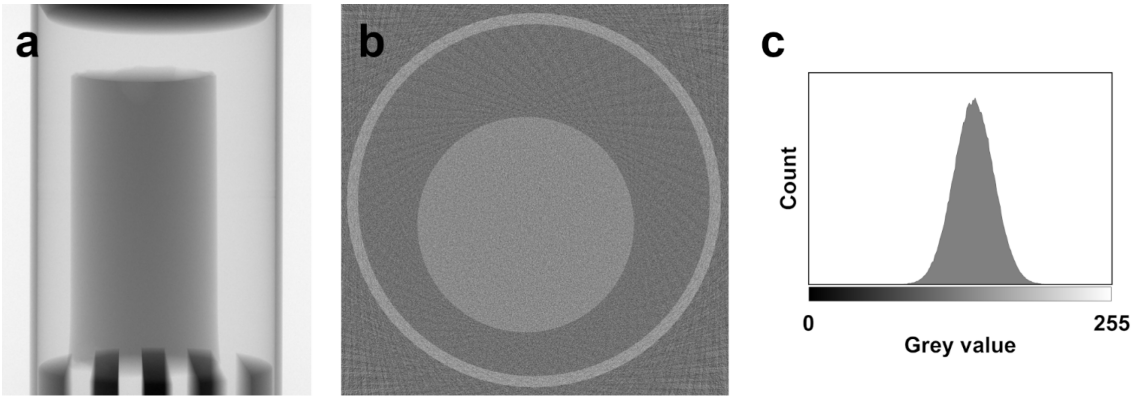

Figure A.10 (**a**) Example of a µCT projection of a drying gel. (**b**) Reconstructed slice of the µCT scan at mid-height of the gel. (**c**) Histogram of the gray values inside the gel on the reconstructed slice. Reprinted from ref.[102], CC BY 4.0 (https://creativecommons.org/licenses/by/4.0/)

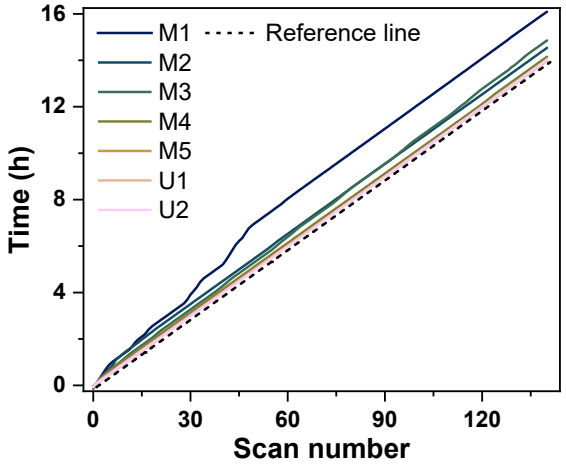

Figure A.11 Time at which a scan was performed versus the corresponding scan number (0 – 140) for the five modified gels (M1 – M5) and the two unmodified gels (U1 – U2). The dashed line is a theoretical reference if each µCT scan would be recorded exactly every 6 min. The error bands are too small and thus not visible. M1 deviates significantly from the reference, meaning that some acquisitions lasted longer than expected. Each curve consists of 141 data points. Reprinted from ref.[102], CC BY 4.0 (https://creativecommons.org/licenses/by/4.0/)

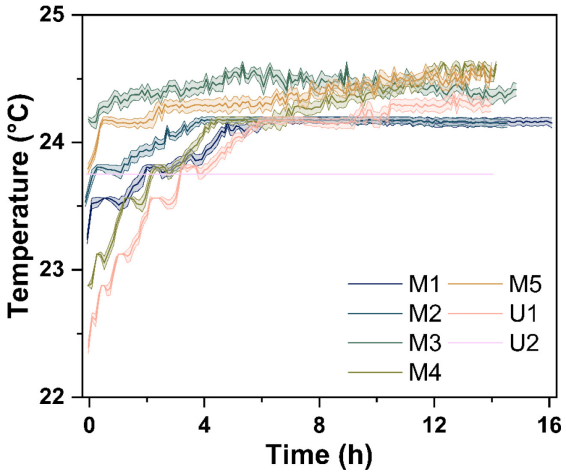

Figure A.12 Temperature recorded in the μCT instrument next to the drying chamber throughout all in-operando μCT experiments. The error bands stand for the standard deviation of 64 values recorded over a single tomography. The temperature for U2 was not recorded due to an instrument error. Each curve consists of 141 data points. Reprinted from ref.[102], CC BY 4.0 (https://creativecommons.org/licenses/by/4.0/)

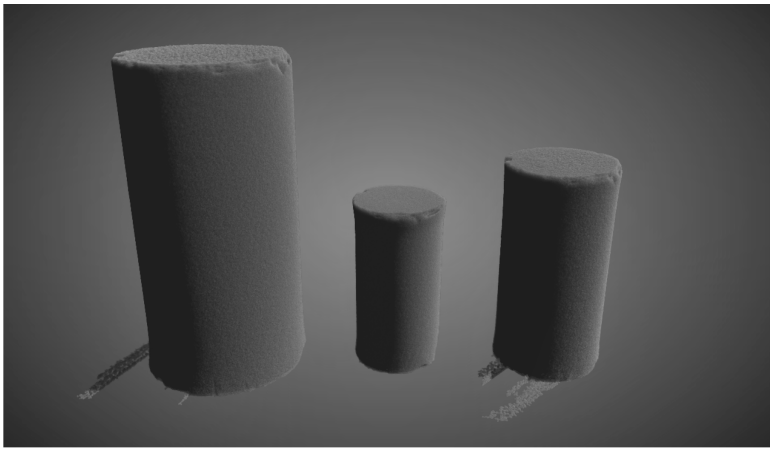

Figure A.13 3D rendering of a gel's volume (M4) at three drying stages generated by the automated segmentation procedure. (left) Alcogel before drying. (middle) Gel at the point of maximum shrinkage. (right) Aerogel after 14 h of drying. The bottom part of the drying chamber can be seen in the alcogel and the aerogel. Visualization done in Dragonfly software. Reprinted from ref.[102], CC BY 4.0 (https://creativecommons.org/licenses/by/4.0/)

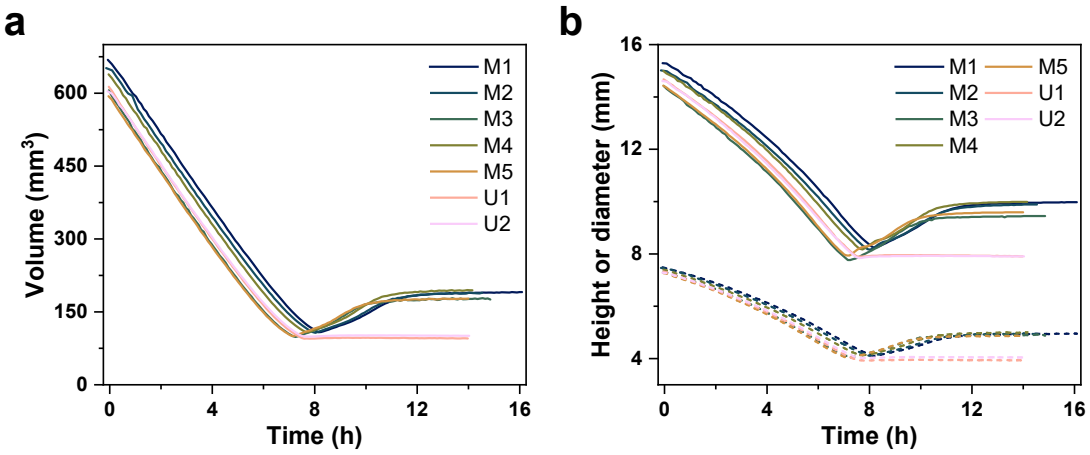

Figure A.14 (**a**) Volume of all modified (M1 – M5) and unmodified (U1 – U2) gels during ambient-pressure drying. The error on the volume at a given point in time is 0.578 % of that volume and is not shown to enhance visibility. (**b**) Height (full line) and diameter (dashed line) of the corresponding gels. Error bands of the height and diameter profiles are not shown. Each curve consists of 141 data points. Reprinted from ref.[102], CC BY 4.0 (https://creativecommons.org/licenses/by/4.0/)

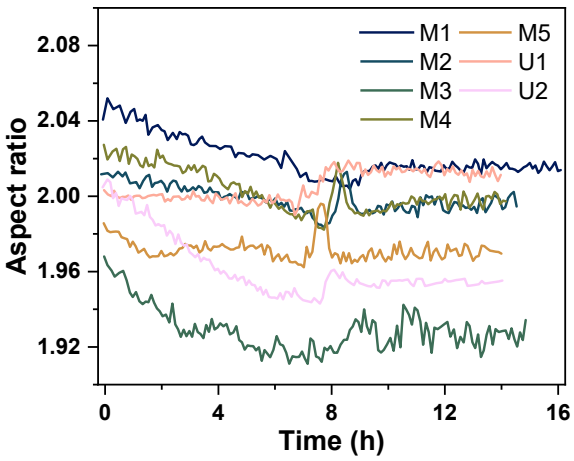

Figure A.15 Aspect ratio (height over diameter) of all modified (M1 – M5) and unmodified (U1 – U2) gels during ambient-pressure drying. The error bands are not shown. Each curve consists of 141 data points. Reprinted from ref.[102], CC BY 4.0 (https://creativecommons.org/licenses/by/4.0/)

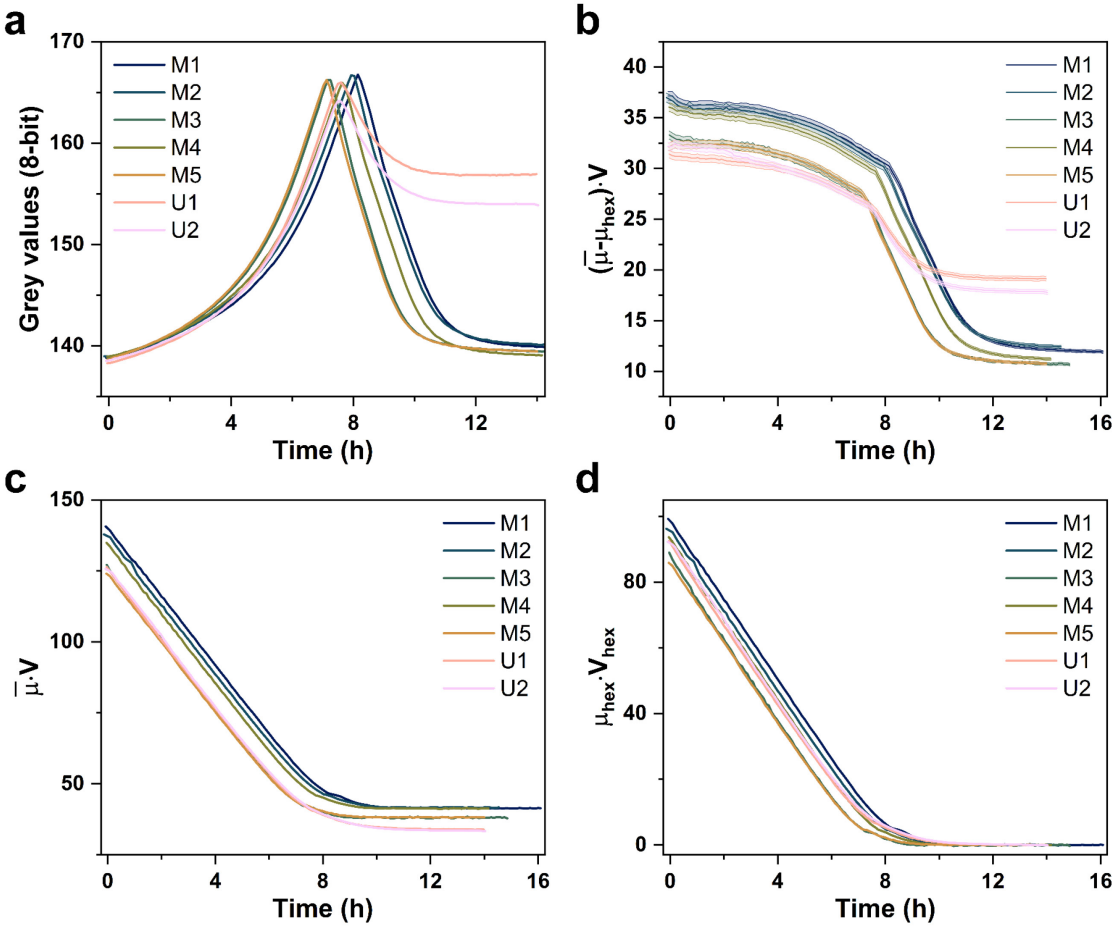

Figure A.16 Intermediate data from the µCT quantitative imaging procedure of all modified (M1 – M5) and unmodified (U1 – U2) gels during drying. (**a**) Global gray value. The error of the global gray values is 0.018. (**b**) $(\bar{\mu} - \mu_{hex}) \cdot V$ profiles. (**c**) $\bar{\mu} \cdot V$ profiles. (**d**) $\mu_{\mathrm{hex}} \cdot V_{\mathrm{hex}}$ profiles. Error bands are not shown in (**c**) and (**d**) to enhance readability. Each curve consists of 141 data points. Reprinted from ref.[102], CC BY 4.0 (https://creativecommons.org/licenses/by/4.0/)

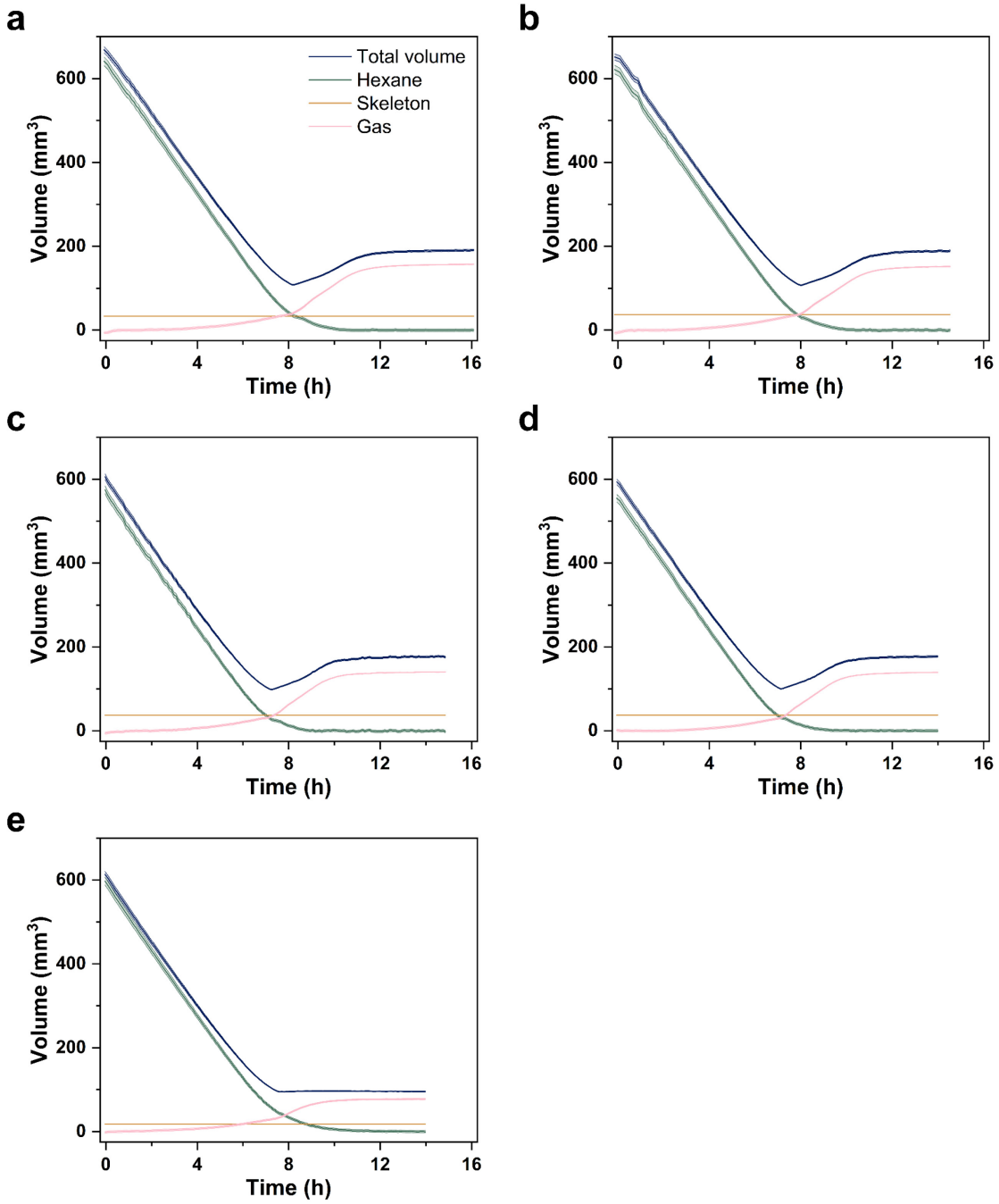

Figure A.17 Total volume, hexane volume, skeleton volume and gas volume of the five other gels. (**a**) Gel M1. (**b**) Gel M2. (**c**) Gel M3. (**d**) Gel M5. (**e**) Gel U1. The profiles of gels M4 and U2 are shown in Figure 4.6. Each curve consists of 141 data points. Reprinted from ref.[102], CC BY 4.0 (https://creativecommons.org/licenses/by/4.0/)

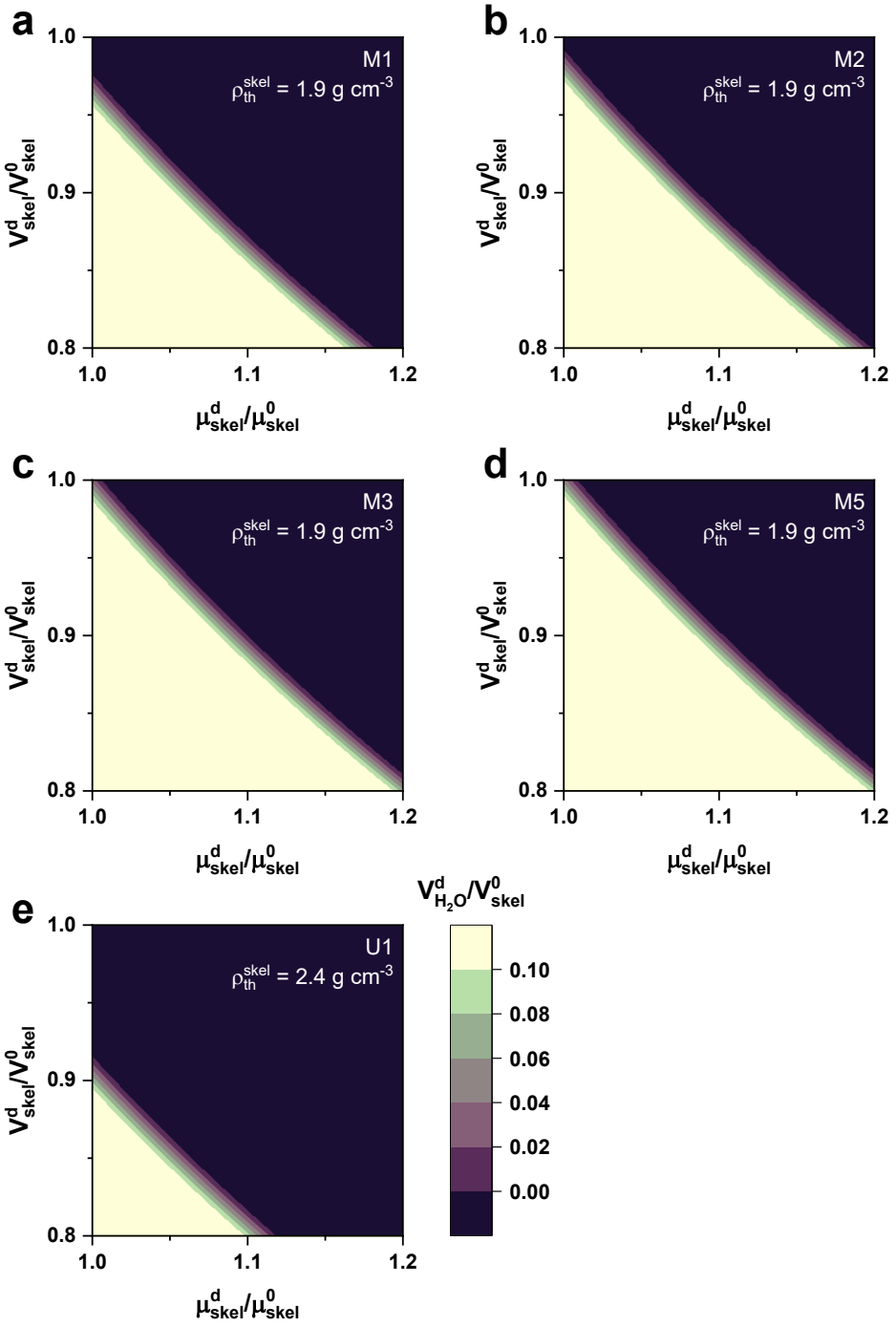

Figure A.18 Maps resulting from numerical simulations implementing condensation reactions during the drying of the four modified gels and the unmodified gel not presented in the main text. (**a**) Gel M1. (**b**) Gel M2. (**c**) Gel M3. (**d**) Gel M5. (**e**) Gel U1. A given skeleton density of $\rho_{\text{skel}}^{0} = 2.4$ and $\rho_{\text{skel}}^{0} = 1.9\ \text{g cm}^{-3}$ for the unmodified (U1) and the modified gels (M1, M2, M3, M5) was used in the simulations. The x-axis corresponds to the relative change in the skeleton RAC between the end and the beginning of the drying. The y-axis corresponds to the relative change in the skeleton volume. The colored scale bar shows the relative volume of water in the gel at the end of the drying. Each trio of values located on the contour surfaces within $0 \leq V_{H_2O}^{d}/V_{\text{skel}}^{0} \leq 0.1$ satisfies $\rho_{\text{skel}} = \rho_{\text{skel}}^{0}$. Points located outside of this range are not shown. The arrow highlights the theoretical point corresponding to no condensation reactions. The maps resolution is 100 x 100 data points. Reprinted from ref.[102], CC BY 4.0 (https://creativecommons.org/licenses/by/4.0/)

Table A.1 Parameters used in the quantitative imaging procedure for all modified (M1 – M5) and unmodified (U1 – U2) gels during drying. k_1 corresponds to the scan number from which the X-ray tube was stable; k_2 corresponds to the scan number from which the quantity $(\bar{\mu}_k - \mu_{\text{hex}})V_k$ (mass conservation equation) began to decrease; k_c is the scan number up to which the gradient of the gray value profiles $\tilde{g}_{i,k}$ in the reconstructed slices was linear; k_d is the scan number from which the changes in volume and global gray value of the gel were insignificant and where the quantity $\bar{\mu}^d V^d$ was calculated; i_p is the slice number corresponding to the pivot used in the correction procedure of the anode heel effect. Adapted from ref.[102], CC BY 4.0 (https://creativecommons.org/licenses/by/4.0/)

Sample	$t_{k=k_1}$ (h)	$t_{k=k_2}$ (h)	$t_{k=k_c}$ (h)	$t_{k=k_d}$ (h)	Pivot i_p (slice number)
M1	0.5	1.5	8.1	15.5	621
M2	0.6	2.3	7.9	13.9	605
M3	1.4	2.3	7.2	14.3	557
M4	1.3	2.0	7.6	13.6	628
M5	0.3	2.0	7.0	13.4	572
U1	0.1	1.0	7.4	13.4	569
U2	0.1	0.6	7.4	13.4	575

Appendix B. Solvent cavitation during ambient pressure drying

B.1 Data reduction procedure

The in operando μCT measurements generated a 4D dataset as 3D reconstructed volumes over time for each sample. This section describes the three reduction procedures used to reduce the 4D dataset. Note that in chapter 5.2, the notation was simplified and the 4D dataset was introduced as $g_{i,p,q,k}$, describing it as the gray values already corrected for the anode heel effect. In practice, the anode heel effect correction was performed after a preliminary integration.

The 4D gray values were referred to as $\tilde{g}_{i,p,q,k}$, with $i,p,q,k \in \mathbb{N}$. The tilde stands for uncorrected, the index i depicts the vertical position in the sample in voxels, the indexes p and q depict the horizontal positions in voxels and the index k stands for the scan number (time). Figure B.1 illustrates the three spatial axes and the time axis. Note that the index i was defined pointing downwards following the convention for digital pictures. The 4D dataset consisted of a series of images (the masked slices) indexed by i and k. As a reminder, the masked slices are 8-bit tif images that were generated upon segmentation of the reconstructed volume by replacing the value of the pixels outside of the sample by zero.

Azimuthal integration. The azimuthal integration generated the gray value maps showing the evolution of the gray values along the gel radius and height over time (GHR maps). The procedure was performed on the masked slices using the Python library DipLib.[190]

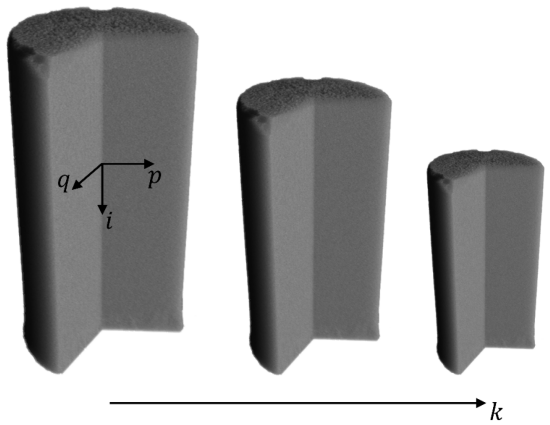

Figure B.1 Sketch of three reconstructed volumes along with the three spatial axes where the indexes i,p,q are defined and the time axis where the index k is defined. Reprinted from ref.[107], CC BY 4.0 (https://creativecommons.org/licenses/by/4.0/).

The center of the sample cross-section in the image was calculated as the center of mass (first order moments) of the image with the function *diplib.CenterOfMass()*. The azimuthal integration was then computed with the function *diplib.RadialMean()* using a bin size of one pixel. Integrated gray values at a radial distance from the center larger than 1.05 times the average radius of the gel at a given scan number were set at zero. This was done to limit the propagation of the imperfect segmentation at the bottom of the gel. Additionally, if the area of the sample in the image was less than half of the mean cross-section area of the gel, the integrated gray value of the masked slice was set to zero. This criterion allowed to exclude the noise at the top of the reconstructed volume due to imperfect segmentation. The mean cross-section area was calculated from the average diameter of the gel.

The profiles created by azimuthal integration of all masked slices at a given scan number k were then combined into a single map, referred to as $\tilde{g}_{i,j,k}$, where $j \in \mathbb{N}$ represents the radial distance to the center of the cylinder in pixels. The gray values were then corrected for the anode heel effect with:

$$g_{i,j,k} = \tilde{g}_{i,j,k} + (i_p - i) \cdot m^*(\tilde{g}_{i,j,k}), \tag{B.1}$$

where $g_{i,j,k}$ are the maps corrected for the anode heel effect, i_p is the pivot slice number and $m^*(g)$ is an exponential decay function. The parameters used in eq. (B.1) were the same as in appendix A.3.. The GHR maps were saved as npy files for further processing and as 8-bit tif images for illustration purposes. Figure B.2 illustrates the azimuthal integration procedure.

Azimuthal and vertical integration. The azimuthal and vertical integration generated a single radial gray value map (GR map) for a given sample, showing the evolution of the gray values along the gel radius over time. The GHR maps generated by azimuthal integration were further integrated along the index i (along the height of the gel) to compute the GR map:

$$g_{j,k} = \frac{1}{H_{\Omega_{j,k}}} \sum_{i \in \Omega_{j,k}} g_{i,j,k}, \tag{B.2}$$

where $g_{j,k}$ is the GR map, $H_{\Omega_{j,k}}$ is the height in pixel of the domain $\Omega_{j,k}$ which defines the range of i indexes belonging to the sample. Note that the domains $\Omega_{j,k}$ were cropped, so that the sum in eq. (B.2) was effectively done by excluding a top and bottom band of 70 pixels. This was done as an attempt to get a more representative evolution of the gray values along the gel radius over time. Moreover, since the GHR maps were already corrected for the anode heel effect, no additional correction procedure was required.

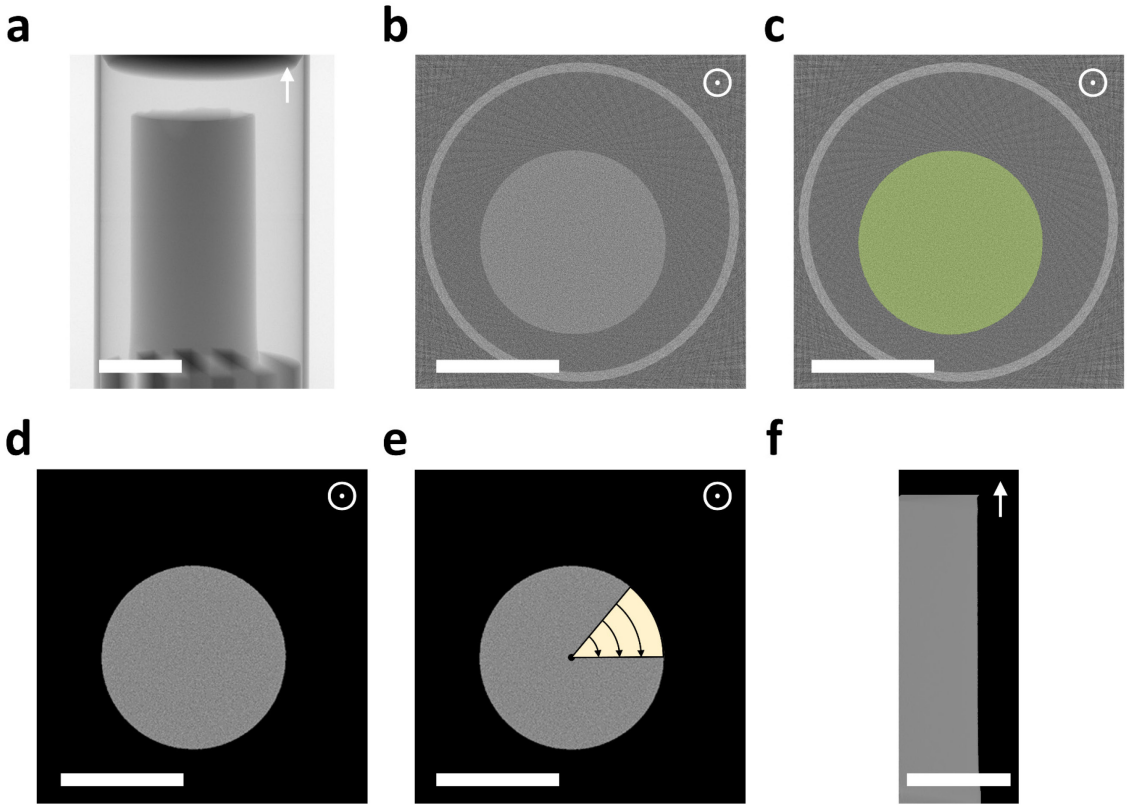

Figure B.2 Illustration of the reduction procedure by azimuthal integration on sample M2 at the start of drying. (**a**) µCT projection at the start of drying. (**b**) Reconstructed slice at $i = 300$. (**c**) Same slice overlaid with the ROI from the automated segmentation. (**d**) Corresponding masked slice. (**e**) Sketch of the azimuthal integration on the masked slice. (**f**) Final GHR map created by combining the radial gray value profiles generated by the azimuthal integration at each index i. The scale bar in each panel is 5 mm. The gray values are in 8-bit. The arrow in each panel stands for the vertical direction of the gel. Reprinted from ref.[107], CC BY 4.0 (https://creativecommons.org/licenses/by/4.0/).

Slice integration. The slice integration generated a single vertical gray value map (GH map) for a given sample, showing the evolution of the gray values along the gel height over time. In practice, this reduction procedure was carried out directly in the software Dragonfly[130] using the "slice analysis" plugin. The masked slices were integrated along the indexes p and q as follows:

$$\tilde{g}_{i,k} = \frac{1}{A_{\Omega_{i,k}}} \sum_{p,q \in \Omega_{i,k}} \tilde{g}_{i,p,q,k}, \tag{B.3}$$

where $\tilde{g}_{i,k}$ is the uncorrected GH map, $A_{\Omega_{i,k}}$ is the area in the masked slice within the domain $\Omega_{i,k}$ defining the range of p and q indexes belonging to the sample. The map $\tilde{g}_{i,k}$ was then corrected for the anode heel effect with a similar expression as in eq. (B.1).

B.2 Derivation of the μCT drying model

Here the μCT drying model is derived by developing the equations step-by-step, leading to the final expression for the spatial and temporal volume fraction maps of the three phases composing the gel. As mentioned in the main text, the reconstructed attenuation coefficient (RAC) of each pixel belonging to the sample in the MHR maps is given by:

$$\mu_{i,j,k} = \mu_{\mathrm{hex}} f_{\mathrm{hex},i,j,k} + \mu_{\mathrm{skel}} f_{\mathrm{skel},i,j,k}, \tag{B.4}$$

where μ_{hex} and μ_{skel} is the RAC of the hexane and skeleton phases, respectively and $f_{\mathrm{hex},i,j,k}$ and $f_{\mathrm{skel},i,j,k}$ are the volume fraction of hexane and skeleton in each pixel. $\mu_{\mathrm{hex}} = 0.155$ from separate measurements on hexane. Volume conservation within each pixel of the MHR maps reads:

$$f_{\mathrm{hex},i,j,k} + f_{\mathrm{skel},i,j,k} + f_{\mathrm{air},i,j,k} = 1. \tag{B.5}$$

Eqs. (B.4) and (B.5) were the main equations of the drying model.

To calculate the volume fraction maps of each phase, the same assumptions than those mentioned in chapter 4.2 were made. First, the total skeleton volume was assumed constant throughout drying: $V_{\mathrm{skel},k} = \mathrm{constant}$, which can be expressed locally as:

$$\sum_{(i,j)\in\Omega_k} f_{\mathrm{skel},i,j,k} V_{\mathrm{voxel}} = \mathrm{constant}. \tag{B.6}$$

Second, the content of hexane after a certain time was assumed to be zero everywhere in the gel, leading to: $f_{\mathrm{hex},i,j,k\geq k_d} = 0$. Lastly, the initial content of vapor/air was assumed to be zero everywhere in the gel, leading to: $f_{\mathrm{air},i,j,k_1\leq k\leq k_2} = 0$. k_d, k_1 and k_2 were the same as previously reported (Table A.1). Additionally, a variation of the skeleton volume conservation equation can be derived by taking the sum over the domain Ω_k of eq. (B.4):

$$\sum_{(i,j)\in\Omega_k} \mu_{i,j,k} - \mu_{\mathrm{hex}} f_{\mathrm{hex},i,j,k} - \mu_{\mathrm{skel}} f_{\mathrm{skel},i,j,k} = 0, \tag{B.7}$$

$$\Leftrightarrow \sum_{(i,j)\in\Omega_k} \mu_{i,j,k} - \mu_{\mathrm{hex}} f_{\mathrm{hex},i,j,k} = \mathrm{constant}. \tag{B.8}$$

Where eq. (B.8) was derived using the conservation of the skeleton volume. Taking eq. (B.5) for $k_1 \leq k \leq k_2$ gives:

$$f_{\mathrm{hex},i,j,k} = 1 - f_{\mathrm{skel},i,j,k}, \quad k_1 \leq k \leq k_2. \tag{B.9}$$

By replacing $f_{\mathrm{hex},i,j,k}$ in eq. (B.8) by its expression in eq. (B.9), we get:

$$\sum_{(i,j)\in\Omega_k} \mu_{i,j,k} - \mu_{\text{hex}}\left(1 - f_{\text{skel},i,j,k}\right) = \text{constant}, \quad k_1 \le k \le k_2, \tag{B.10}$$

$$\Leftrightarrow \sum_{(i,j)\in\Omega_k} \mu_{i,j,k} - \mu_{\text{hex}} = \text{constant}, \quad k_1 \le k \le k_2. \tag{B.11}$$

Eq. (B.11) was not an additional equation per se, but will be used later on.

Hexane volume fraction. We first derive the expressions used to calculate the hexane volume fraction maps throughout drying. To improve the statistics, the calculations were done on a MHR map representative of the dry gel for $k \ge k_d$. The hexane volume fraction $f_{\text{hex},i,j,k}$ is calculated by finding an expression for $\mu_{\text{skel}} f_{\text{skel},i,j,k}$ in eq. (B.4). For $k \ge k_d$, eq. (B.4) becomes:

$$\mu_{i,j,k} = \mu_{\text{skel}} f_{\text{skel},i,j,k}, \quad k \ge k_d, \tag{B.12}$$

because there was no more hexane in the gel at $k \ge k_d$. By combining the MHR maps $\mu_{i,j,k}$ over $k \ge k_d$, an artificial MHR map representative of the dry gel could be generated. However, the volume of the gel still changed at $k \ge k_d$, so did the domains Ω_k, preventing to average the MHR maps directly. We write formally:

$$\Omega_{k_a} \ne \Omega_{k_b}, \quad k_a \ne k_b. \tag{B.13}$$

This was solved by resizing one map onto another using bilinear interpolation so that the domain of the maps matched. The MHR map to be resized was referred to as the source and the map over which it was resized was referred to as the target. In this case, the target was unique and was set as the MHR map of the last scan ($k = k_f$), while the source scans were multiple ($k_d \le k < k_f$). Note that the target scan could have been any scan within $k \ge k_d$. We define:

$$\mu^*_{i,j,k\to k_f} = \mu^{\text{F}}_{i,j,k\to k_f} \cdot \gamma, \quad k_d \le k < k_f, \tag{B.14}$$

where $\mu^*_{i,j,k\to k_f}$ is the rescaled MHR map of scan k towards scan k_f, $\mu^{\text{F}}_{i,j,k\to k_f}$ is the interpolated map defined over the domain Ω_{k_f} and γ is a correction factor. Formally, we also define $\text{F}_{k\to k_f}$ as the bilinear interpolation function from a source k towards a target k_f:

$$\mu^{\text{F}}_{i,j,k\to k_f} = \text{F}_{k\to k_f}\left(\mu_{i,j,k}\right). \tag{B.15}$$

The algorithm for the bilinear interpolation function is described in appendix B.3. A series of rescaled maps $\mu^*_{i,j,k\to k_f}$ for $k_d \le k < k_f$ was thus obtained, each map being defined on the same domain Ω_{k_f}. To derive the scaling factor in eq. (B.14), let's consider a quantity that stays constant throughout drying. We recall the conservation of the skeleton volume:

$$\sum_{(i,j)\in\Omega_k} f_{\text{skel},i,j,k} V_{\text{voxel}} = \text{constant}. \tag{B.6}$$

By substituting $f_{\text{skel},i,j,k}$ in eq. (B.6) by its expression from eq. (B.12), we get:

$$\sum_{(i,j)\in\Omega_k} \frac{\mu_{i,j,k}}{\mu_{skel}} V_{\text{voxel}} = \text{constant}, \quad k \geq k_d, \tag{B.16}$$

$$\Leftrightarrow \sum_{(i,j)\in\Omega_k} \mu_{i,j,k} V_{\text{voxel}} = \text{constant}, \quad k \geq k_d. \tag{B.17}$$

Eqs. (B.16) and (B.17) were only defined for $k \geq k_d$ since they were derived using eq. (B.12). Let's consider eq. (B.17) between the rescaled MHR map from source scan $k = k_d$ onto target scan $k = k_f$, and the source MHR map at scan $k = k_d$:

$$\sum_{(i,j)\in\Omega_{k_f}} \mu^{\text{F}}_{i,j,k_d\to k_f} V_{\text{voxel}} \cdot \gamma = \sum_{(i,j)\in\Omega_{k_d}} \mu_{i,j,k} V_{\text{voxel}}, \tag{B.18}$$

$$\Rightarrow \bar{\mu}^{\text{F}}_{k_d\to k_f} V_{k_f} \cdot \gamma = \bar{\mu}_{k_d} V_{k_d}, \tag{B.19}$$

$$\Leftrightarrow \bar{\mu}^{\text{F}}_{k_d\to k_f} \cdot \gamma = \bar{\mu}_{k_d} \cdot \frac{V_{k_d}}{V_{k_f}}, \tag{B.20}$$

where $\bar{\mu}_k$ is the RAC averaged over the domain Ω_k. Since the average of all values of a MHR map (or any digital image) are conserved upon interpolation, we have that:

$$\bar{\mu}^{\text{F}}_{k_d\to k_f} = \bar{\mu}_{k_d}, \tag{B.21}$$

giving an expression for the scaling factor γ:

$$\gamma \equiv \gamma_{k_d\to k_f} = \frac{V_{k_d}}{V_{k_f}}. \tag{B.22}$$

The expression of the γ scaling factor can be generalized:

$$\gamma_{\text{source}\to\text{target}} = \frac{V_{\text{source}}}{V_{\text{target}}}. \tag{B.23}$$

The rescaled maps were averaged over the scans $k \geq k_d$, resulting in an artificial MHR map representative of the dry gel:

$$\mu^{\text{dry}}_{i,j,k_f} = \frac{1}{N_d}\left(\mu_{i,j,k_f} + \sum_{k_d\leq k<k_f} \mu^{\text{F}}_{i,j,k_d\to k_f} \cdot \gamma_{k\to k_f}\right), \tag{B.24}$$

where N_d is the number of scans in $k_d \leq k \leq k_f$. The quantity $\mu^{\text{dry}}_{i,j,k_f}$ was referred to as the dry MHR map. By recalling eq. (B.12), the MHR maps $\mu_{i,j,k\geq k_d}$ were equal to $\mu_{\text{skel}} f_{\text{skel},i,j,k\leq k_d}$ under the assumption of a zero hexane content in the gels at $k \geq k_d$. The dry MHR map

derived in eq. (B.24) was thus an expression of the quantity $\mu_{\text{skel}} f_{\text{skel},i,j,k}$ interpolated onto scan $k = k_f$. We set:

$$\mu_{\text{skel}} f_{\text{skel},i,j,k_f} = \mu^{\text{dry}}_{i,j,k_f}. \tag{B.25}$$

The dry MHR map was then used to calculate the HEXHR maps. Let's recall the expression of the local RAC:

$$\mu_{i,j,k} = \mu_{\text{hex}} f_{\text{hex},i,j,k} + \mu_{\text{skel}} f_{\text{skel},i,j,k}. \tag{B.4}$$

At $k = k_f$, the rightmost term in eq. (B.4) is equal to the dry MHR map. The change of the gel volume throughout drying implied that $\Omega_{k \neq k_f} \neq \Omega_{k_f}$. By assuming that the distribution of the silica skeleton within the gel's volume does not change throughout drying, an expression for $\mu_{\text{skel}} f_{\text{skel},i,j,k}$ for any scan k could be obtained by rescaling $\mu_{\text{skel}} f_{\text{skel},i,j,k_f}$ (which is known) from source scan $k = k_f$ to target scan $k \neq k_f$ using a similar methodology as before. In this case, the source is unique ($k = k_f$) and the targets are multiple ($k \neq k_f$). We thus set:

$$\mu_{\text{skel}} f^*_{\text{skel},i,j,k_f \to k} = \text{F}_{k_f \to k}\left(\mu_{\text{skel}} f_{\text{skel},i,j,k_f}\right) \cdot \gamma_{k_f \to k}, \tag{B.26}$$

$$\Leftrightarrow \mu_{\text{skel}} f^*_{\text{skel},i,j,k_f \to k} = \text{F}_{k_f \to k}\left(\mu^{\text{dry}}_{i,j,k_f}\right) \cdot \gamma_{k_f \to k}, \tag{B.27}$$

$$\Leftrightarrow \mu_{\text{skel}} f^*_{\text{skel},i,j,k_f \to k} = \mu^{\text{dry,F}}_{i,j,k_f \to k} \cdot \gamma_{k_f \to k}, \tag{B.28}$$

where $\mu_{\text{skel}} f^*_{\text{skel},i,j,k}$ is the rescaled map and the scaling factor is:

$$\gamma_{k_f \to k} = \frac{V_{k_f}}{V_k}. \tag{B.29}$$

The expression for the scaling factor was verified by recalling the conservation of the skeleton volume, considering the rescaled map at scan $k \neq k_f$ and the dry MHR map at scan $k = k_f$:

$$\sum_{(i,j) \in \Omega_k} f_{\text{skel},i,j,k} V_{\text{voxel}} = \text{constant}, \tag{B.6}$$

$$\Rightarrow \sum_{(i,j) \in \Omega_k} \frac{\mu^{\text{dry,F}}_{i,j,k_f \to k} \cdot \gamma_{k_f \to k}}{\mu_{\text{skel}}} V_{\text{voxel}} = \sum_{(i,j) \in \Omega_{k_f}} \frac{\mu^{\text{dry}}_{i,j,k_f}}{\mu_{\text{skel}}} V_{\text{voxel}}, \tag{B.30}$$

$$\Rightarrow \bar{\mu}^{\text{dry,F}}_{k_f \to k} \cdot \gamma_{k_f \to k} V_k = \bar{\mu}^{\text{dry}}_{k_f} V_{k_f}, \tag{B.31}$$

$$\Leftrightarrow \bar{\mu}^{\text{dry,F}}_{k_f \to k} = \bar{\mu}^{\text{dry}}_{k_f}, \tag{B.32}$$

where $\bar{\mu}^{\text{dry,F}}_{k_f \to k}$ and $\bar{\mu}^{\text{dry}}_{k_f}$ is the RAC of the maps averaged over the domains Ω_k and Ω_{k_f}, respectively. Finally, the quantity $\mu_{\text{skel}} f_{\text{skel},i,j,k}$ in eq. (B.4) was replaced by the expression in eq. (B.28), giving an expression for the hexane volume fraction maps at any scan:

$$f_{\mathrm{hex},i,j,k} = \frac{\mu_{i,j,k} - \mu^{\mathrm{dry,F}}_{i,j,k_f \to k} \cdot \gamma_{k_f \to k}}{\mu_{\mathrm{hex}}}. \tag{B.33}$$

Skeleton volume fraction. The SKELHR maps can be directly calculated at $k_1 \leq k \leq k_2$ using the volume conservation equation and the previously computed HEXHR maps. Similarly to the procedure adopted to calculate the hexane volume fraction maps, an artificial MHR map representative of the state of the gel at the beginning of drying was computed to improve the statistics upon calculating $f_{\mathrm{skel},i,j,k}$. This was done by rescaling and combining the MHR maps over $k_1 \leq k \leq k_2$. The rescaling was performed from source scans $k_1 < k \leq k_1$ onto target scan $k = k_1$. In this case, the target is unique and the sources are multiple. The rescaled maps are:

$$\mu^{*}_{i,j,k \to k_1} = \mu^{\mathrm{F}}_{i,j,k \to k_1} \cdot \gamma_{k \to k_1} + \beta, \;\; k_1 \leq k \leq k_2, \tag{B.34}$$

where $\mu^{\mathrm{F}}_{i,j,k \to k_1}$ is the interpolated map defined over the domain Ω_{k_1} and β is an additional scaling factor. An expression for β was found by considering a quantity that stays constant over $k_1 \leq k \leq k_2$ (similar strategy as the one employed to determine γ). Let's recall the 2nd conservation equation:

$$\sum_{(i,j) \in \Omega_k} \mu_{i,j,k} - \mu_{\mathrm{hex}} = \mathrm{constant}, \;\; k_1 \leq k \leq k_2. \tag{B.11}$$

Let's consider eq. (B.11) between a rescaled MHR map from scan $k \neq k_1$ to $k = k_1$ and the MHR map of source scan k:

$$\sum_{(i,j) \in \Omega_{k_1}} \mu^{*}_{i,j,k \to k_1} - \mu_{\mathrm{hex}} = \sum_{(i,j) \in \Omega_k} \mu_{i,j,k} - \mu_{\mathrm{hex}}, \tag{B.35}$$

$$\Leftrightarrow V_{\mathrm{voxel}} \sum_{(i,j) \in \Omega_{k_1}} \mu^{\mathrm{F}}_{i,j,k \to k_1} \cdot \gamma_{k \to k_1} + \beta - \mu_{\mathrm{hex}} = V_{\mathrm{voxel}} \sum_{(i,j) \in \Omega_k} \mu_{i,j,k} - \mu_{\mathrm{hex}}, \tag{B.36}$$

$$\Rightarrow \left(\bar{\mu}^{\mathrm{F}}_{k \to k_1} \cdot \gamma_{k \to k_1} + \beta - \mu_{\mathrm{hex}}\right) V_{k_1} = (\bar{\mu}_k - \mu_{\mathrm{hex}}) V_k, \tag{B.37}$$

where $\bar{\mu}^{\mathrm{F}}_{k \to k_1}$ and $\bar{\mu}_k$ are the MHR maps averaged over their domain Ω_{k_1} and Ω_k, respectively. Because bilinear interpolation conserves the average value of a MHR map, we have that:

$$\bar{\mu}^{\mathrm{F}}_{k \to k_1} = \bar{\mu}_k, \tag{B.38}$$

giving an expression for β:

$$\left(\bar{\mu}^{\mathrm{F}}_{k \to k_1} \cdot \frac{V_k}{V_{k_1}} + \beta - \mu_{\mathrm{hex}}\right) V_{k_1} = (\bar{\mu}_k - \mu_{\mathrm{hex}}) V_k, \tag{B.39}$$

$$\Leftrightarrow \bar{\mu}^{\mathrm{F}}_{k \to k_1} V_k + (\beta - \mu_{\mathrm{hex}}) V_{k_1} = \bar{\mu}_k V_k - \mu_{\mathrm{hex}} V_k, \tag{B.40}$$

$$\Leftrightarrow (\beta - \mu_{\text{hex}})V_{k_1} = -\mu_{\text{hex}}V_k, \tag{B.41}$$

$$\Rightarrow \beta = \mu_{\text{hex}}\frac{\left(V_{k_1} - V_k\right)}{V_{k_1}}, \tag{B.42}$$

$$\Leftrightarrow \beta = \mu_{\text{hex}}\left(1 - \gamma_{k\to k_1}\right). \tag{B.43}$$

The rescaled MHR maps were then averaged over $k_1 \le k \le k_2$, resulting in an artificial MHR map representative of the state of the alcogel referred to as the alco MHR map:

$$\mu^{\text{alco}}_{i,j,k_1} = \frac{1}{N_a}\left[\mu_{i,j,k_1} + \sum_{k_1<k\le k_2} \mu^{\text{F}}_{i,j,k\to k_1}\gamma_{k\to k_1} + \mu_{\text{hex}}\left(1 - \gamma_{k\to k_1}\right)\right], \tag{B.44}$$

where N_a is the number of scans between $k_1 \le k \le k_2$. The alco MHR map was used to compute a hexane volume fraction map representative of the alcogel at scan $k = k_1$. Eq. (B.33) was rewritten considering a target scan $k = k_1$ and by replacing the MHR map at scan k by the alco MHR map at scan $k = k_1$:

$$f^{\text{alco}}_{\text{hex},i,j,k_1} = \frac{\mu^{\text{alco}}_{i,j,k_1} - \mu^{\text{dry,F}}_{i,j,k_f\to k_1}\cdot\gamma_{k_f\to k_1}}{\mu_{\text{hex}}}, \tag{B.45}$$

where $f^{\text{alco}}_{\text{hex},i,j,k_1}$ is a hexane map representative of the state of the alcogel expressed at scan $k = k_1$. This expression was finally used to calculate the SKELHR map at scan $k = k_1$ from the conservation of the total volume:

$$f_{\text{skel},i,j,k_1} = 1 - f^{\text{alco}}_{\text{hex},i,j,k_1}. \tag{B.46}$$

The SKELHR maps at scans $k \ne k_1$ were determined by rescaling f_{skel,i,j,k_1}:

$$f_{skel,i,j,k} = f^{\text{F}}_{skel,i,j,k_1\to k}\cdot\gamma_{k_1\to k}, \tag{B.47}$$

where $f^{\text{F}}_{\text{skel},i,j,k_1\to k}$ is the interpolated map defined over the domain Ω_k.

Vapor/air volume fraction. The vapor/air volume fraction maps were directly computed using eq. (B.5) with the knowledge of $f_{\text{hex},i,j,k}$ and $f_{\text{skel},i,j,k}$:

$$f_{\text{air},i,j,k} = 1 - f_{\text{hex},i,j,k} - f_{\text{skel},i,j,k}. \tag{B.48}$$

B.3 Bilinear interpolation procedure

A key step in the local quantitative imaging procedure was the resizing of the maps between the different drying stages by bilinear interpolation. The resizing and rescaling of a GHR map from source scan $k_s = 140$ onto target scan $k_t = 0$ is illustrated in Figure B.3 as an example and consisted in: (i) conversion of the GHR maps into MHR maps (Figure B.3b), (ii) define

the edges of the domains Ω_{k_s} and Ω_{k_t} separating the sample from the background in the source and target MHR maps (Figure B.3c), (iii) compute the normalized vertical and radial coordinates of any pixel of the maps within the domain edges (not shown), (iv) bilinear interpolation of source map onto target map and correction of the RAC values by a scalar factor (Figure B.3d).

As mentioned in the main text and in appendix B.2, the domain of two GHR or MHR maps taken at different scans did not match, due to the shape change of the sample. To compare maps at different drying stages required establishing a correspondence between the two domains, which was done by bilinear interpolation of a source scan: k_s towards the domain of a target scan: k_t. The procedure described here is based on the GHR maps but can also be applied to a MHR map or a volume fraction map upon minor adaptations. First, the edges of

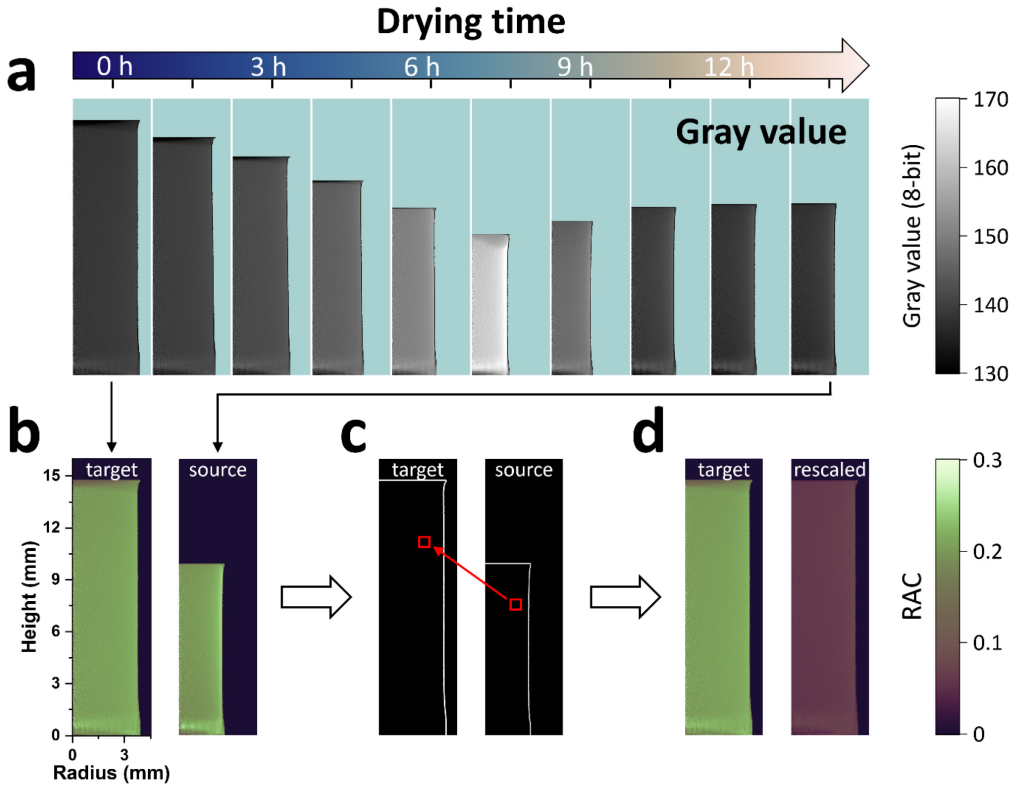

Figure B.3 Example of the bilinear interpolation procedure and rescaling. (**a**) GHR maps of sample M4 at 10 selected drying stages on top of a cyan background with the corresponding color scale on the right. The brightness and contrast in the images of the gray value maps was adjusted to improve visualization. (**b**) MHR maps converted from the GHR maps at the start of drying (target scan) and at the end of drying (source scan) (**c**) Domains defining the sample in the MHR maps (white line over black background) in target and source scans. The red squares illustrate the correspondence in the relative coordinates of two pixels in both scans. (**d**) Target MHR map and rescaled MHR map interpolated from the source scan domain onto the target scan domain. The color scale of the MHR maps in panels (**b**) and (**d**) is shown at the bottom right of the figure. The length axes of all maps is indicated in the first map of panel (**b**). Reprinted from ref.[107], CC BY 4.0 (https://creativecommons.org/licenses/by/4.0/).

the domains were defined as the limit where the gray values dropped to zero in the GHR maps (Figure B.3c). The top edge of the gel was called the north edge: $N_{j,k}$, and was defined as the i index where the gray values became non-zero, from top to bottom for each index j. The radial edge of the gel was called the east edge: $E_{i,k}$, and was similarly defined as the j index where the gray values became non-zero, from right to left for each index i. The bottom edge of the gel was called the south edge: S and was independent of the radial position and of the scan number. Figure B.4 depicts those edges of the GHR maps at scans k_t and k_s shown in Figure B.3.

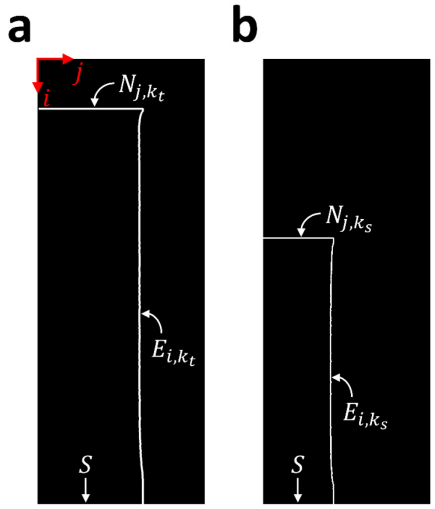

Figure B.4 . Edges (white lines) of the domains of two GHR maps from (**a**) a target scan at the start of drying ($k = 0$) and (**b**) a source scan at the end of drying ($k = 140$). The north edges are depicted with an arrow: N_{j,k_t} and N_{j,k_s} for target and source scans, respectively. The east edges are depicted accordingly: E_{i,k_t} and E_{i,k_s}. The south edge S is also shown and is independent of the j index and of the scan number k. The axes are shown in red on the top left of the figure in panel (**a**). Reprinted from ref.[107], CC BY 4.0 (https://creativecommons.org/licenses/by/4.0/).

We define the normalize coordinates within a domain Ω_k as:

$$h_{i,j} = \frac{i - N_{j,k}}{S - N_{j,k}}, \tag{B.49}$$

$$r_{i,j} = \frac{j}{E_{i,k}}, \tag{B.50}$$

with $h_{i,j} \in [0,1]$ and $r_{i,j} \in [0,1]$. For a given coordinate in the target map -abbreviated (i^*, j^*)- a corresponding coordinate was calculated in the source map -abbreviated (i, j)- by minimizing the difference between the normalized coordinates, defined as $\delta_h = |h^* - h|$ and $\delta_r = |r^* - r|$. (h^*, r^*) is short for $(h_{i^*,j^*}, r_{i^*,j^*})$ and is the normalized coordinates of the target map (known). (h, r) is short for $(h_{i,j}, r_{i,j})$ and is the normalized coordinate of the source map (unknown). The following algorithm was developed to find (h, r) at a given (h^*, r^*):

1) Define the vertical and radial tolerance:

$$\epsilon_h = 0.1 \cdot \left(S - N_{k_s}^{\min}\right), \tag{B.51}$$

$$\epsilon_r = 0.1 \cdot E_{k_s}^{\max}, \tag{B.52}$$

where $N_{k_s}^{\min}$ is the minimum of N_{j,k_s} and $E_{k_s}^{\max}$ is the maximum of E_{i,k_s}.

2) Set a starting point in the source map (h_0, r_0) as:

$$h_0 = \left\lfloor h^* \cdot \left(S - N_{k_s}^{\min}\right) + N_{k_s}^{\min} \right\rceil, \tag{B.53}$$

$$\epsilon_r = 0.1 \cdot E_{k_s}^{max}, \tag{B.54}$$

where the notation $\lfloor x \rceil$ stands for rounding x to the nearest integer (0.5 is rounded down to 0).

3) Compute the normalized radial coordinate in the source map r_1 the closest to the target coordinate r^* at $h = h_0$:

$$r_1 = \underset{i|h_{i,j}=h_0}{\operatorname{argmin}}\left(\left|r^* - r_{i,j}\right|\right). \tag{B.55}$$

The function **argmin** is the argument of the minima taken over a series of coordinates (i, j), where i is such that $h_{i,j} = h_0$. This represents a relatively horizontal line.

4) Do the same for the normalized vertical coordinate h_1 at $r = r_1$:

$$r_1 = \underset{i|h_{i,j}=h_0}{\operatorname{argmin}}\left(\left|r^* - r_{i,j}\right|\right). \tag{B.56}$$

where the coordinates j is such that $r_{i,j} = r_1$.

5) Compute the difference $\delta_h = |h^* - h_1|$ and $\delta_r = |r^* - r_1|$.

6) If $\delta_h \geq \epsilon_h$ or $\delta_r \geq \epsilon_r$, assign the current value of h_1 to h_0 and r_1 to r_0, and repeat steps 3) to 6). After five iterations, or if $\delta_h < \epsilon_h$ and $\delta_r < \epsilon_r$, set $h = h_1$ and $r = r_1$ and exit the loop.

Once the correspondence between the normalized coordinates in the source map (h, r) and in the target map (h^*, r^*) was established, an empty map with the domain of the target map Ω_{k_t} was created. The gray values in the empty map were filled using a bilinear interpolation algorithm. For any pixel with the coordinates (i^*, j^*) in the empty map, its gray value was determined by:

1) Calculate the virtual position in the source map corresponding to the normalized coordinates (h^*, r^*) of the empty map:

$$I = h^* \cdot \left(S - N_{j,k_s}\right) + N_{j,k_s}, \tag{B.57}$$

$$J = r^* \cdot E_{i,k_s}, \tag{B.58}$$

where I and J are not pixel indexes but a virtual position in between pixels. (i,j) are known from $(h_{i,j}, r_{i,j})$ determined in the previous calculations.

2) Find the four pixels the closest to the virtual position (I,J):

$$i_1 = \begin{cases} i, & I \geq i \\ i-1, & I < i \end{cases}, \tag{B.59}$$

$$i_2 = \begin{cases} i+1, & I \geq i \\ i, & I < i \end{cases}, \tag{B.60}$$

$$j_1 = \begin{cases} j, & J \geq j \\ j-1, & J < j \end{cases}, \tag{B.61}$$

$$j_2 = \begin{cases} j+1, & J \geq j \\ j, & J < j \end{cases}. \tag{B.62}$$

3) The gray value in the empty map at the coordinates (i^*,j^*) is given by the bilinear interpolation formula:

$$g_{i^*,j^*,k_s \to k_t} = \begin{pmatrix} i_2 - I & I - i_1 \end{pmatrix} \begin{pmatrix} g_{i_1,j_1,k_s} & g_{i_1,j_2,k_s} \\ g_{i_2,j_1,k_s} & g_{i_2,j_2,k_s} \end{pmatrix} \begin{pmatrix} j_2 - J \\ J - j_1 \end{pmatrix}. \tag{B.63}$$

By construction, the interpolated map $g_{i^*,j^*,k_s \to k_t}$ was defined over the same domain as the target map g_{i,j,k_t}. After interpolation, depending on the nature of the interpolated map (GHR, MHR or volume fraction map), the interpolated map was corrected with one or more scaling factor (see appendix B.2).

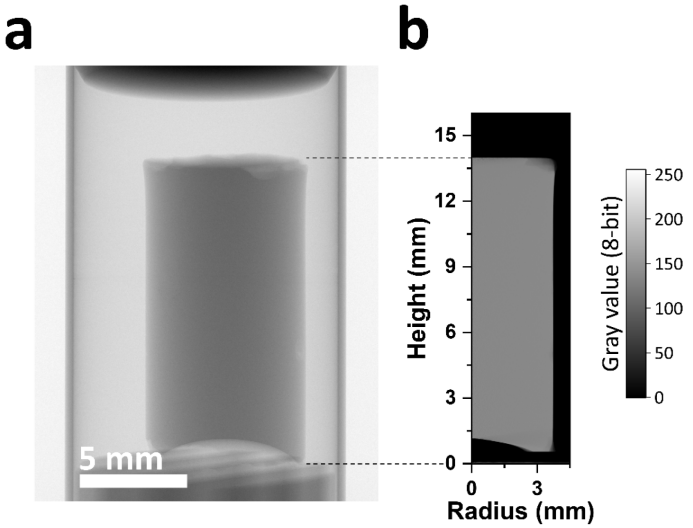

Figure B.5 (**a**) μCT projection of sample M3 at the start of drying, the meniscus in the gel is visible at the gel's bottom. (**b**) GHR map of the same μCT scan on a black background, where artifacts can be seen at the bottom of the sample. Those artifacts resulted in errors in the bilinear interpolation algorithm, preventing to compute volume fraction maps for that sample. Reprinted from ref.[107], CC BY 4.0 (https://creativecommons.org/licenses/by/4.0/).

B.4 Gel diameter during X-ray scattering measurements

Here we describe how the local diameter of the gels was calculated during their drying at the µSpot beamline at BESSY. The digital pictures were correlated with the µCT data and with the time stamps of the scattering data. Figure B.6 shows a series of digital pictures at selected drying stages, where the maximum shrinkage occurred after ca. 4.4 h of drying, which was faster than in the µCT experiments. Due to the insufficient contrast in the image, the dimensions of the gel could not be retrieved by automated image processing. Instead, the height of the gel in pixel was measured manually from 14 pictures using the software Fiji.[106] It must be noted that during the first 2 h of drying, the height of the gel could not be measured because its top was hidden by the measurement cell (Figure B.6).

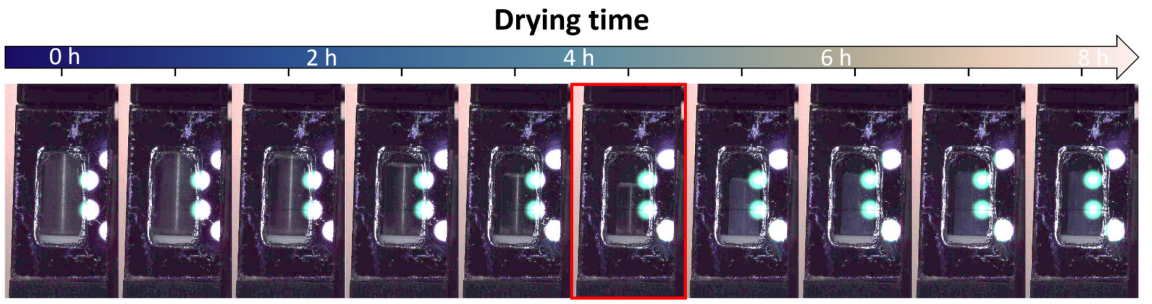

Figure B.6 Digital pictures of the gel dried in the measurement cell during the in operando SAXS/WAXS measurement. The picture corresponding to the maximum shrinkage is outlined in red. The bright spots are due to the reflection of the camera lamp on the museum glass. The brightness and contrast of the images are adjusted for better visualization. Reprinted from ref.[107], CC BY 4.0 (https://creativecommons.org/licenses/by/4.0/).

The diameter of the gel in pixel was derived by dividing the height by a factor 2 assuming an aspect ratio of 2, and was normalized by the diameter of the gel at the maximum shrinkage. We define:

$$\nu_{\mathrm{PI}}(t_{\mathrm{PI}}) = d(t_{\mathrm{PI}})/d\left(t_{\mathrm{PI}} = t_{\mathrm{PI,MS}}\right), \tag{B.64}$$

with $\nu_{\mathrm{PI}}(t_{\mathrm{PI}})$ the normalized diameter from the digital pictures, $d_{PI}(t_{\mathrm{PI}})$ the diameter of the gel in pixels and $t_{\mathrm{PI,MS}}$ the time of maximum shrinkage. t_{PI} is the time at which the digital pictures were recorded. $\nu_{\mathrm{PI}}(t_{\mathrm{PI}})$ is shown in Figure B.7. Because the diameter of the gel at $t_{\mathrm{PI}} < 2\ \mathrm{h}$ could not be measured, the diameter from the digital pictures was fitted using µCT data, allowing to extrapolate the diameter of the gel at the start of drying.

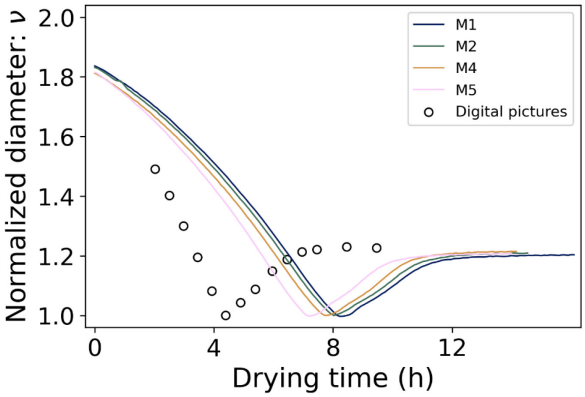

Figure B.7 Diameter of a gel normalized over its diameter at the maximum shrinkage: $\boldsymbol{\nu}$ from the μCT measurements (M1, M2, M4 and M5) and from the digital pictures versus the drying time. Reprinted from ref.[107], CC BY 4.0 (https://creativecommons.org/licenses/by/4.0/).

During the in operando X-ray scattering experiment, the X-ray beam probed the gel at a vertical height of ca. 4 mm from the bottom of the gel. That location can be seen in Figure B.6 as a slight darker line on the museum glass. The diameter of the gels dried by μCT at the same location was extracted from the masked images and was normalized by its value at the maximum shrinkage as in eq. (B.64). The corresponding normalized diameters of samples M1, M2, M4 and M5 are shown in Figure B.7. Note that the drying rate within these samples differed because of slightly different starting volume of the gels and possibly drying conditions

The μCT normalized diameter was taken as the average among samples M1, M2, M3 and M4 to improve the accuracy of the fit. To do so, the μCT time scale was also normalized:

$$x_{\mathrm{CT},m} = t_{\mathrm{CT},m}/t_{\mathrm{CT,MS},m}, \tag{B.65}$$

where $x_{\mathrm{CT},m}$ is a time scale normalized over the time of the maximum shrinkage $t_{\mathrm{CT,MS},m}$ for a sample m. The average μCT normalized diameter was then: $\nu_{\mathrm{CT}}(x_{\mathrm{CT}})$, where $x_{\mathrm{CT}} = 0$ and $x_{\mathrm{CT}} = 1$ corresponded to the start of drying and to the maximum shrinkage, respectively.

The normalized diameter from the digital pictures was also expressed as a function of a normalized time scale. However, the first recorded image was taken a few minutes after the gel started drying due to experimental limitations. We defined the time difference between the first recorded image and the effective start of drying of the gel as Δt_1. Therefore, we can express $\nu_{\mathrm{PI}} = \nu_{\mathrm{PI}}(x_{\mathrm{PI}})$ with x_{PI} as:

$$x_{\mathrm{PI}} = \frac{t_{\mathrm{PI}} + \Delta t_1}{t_{\mathrm{PI,MS}} + \Delta t_1}. \tag{B.66}$$

By minimizing the difference of $(\nu_{\mathrm{CT}}(x_{\mathrm{CT}}) - \nu_{\mathrm{PI}}(x_{\mathrm{PI}}))^2$, Δt_1 could be determined at ca. 3.5 min, which was reasonable. After a time scale normalization, $\nu_{\mathrm{PI}}(x_{\mathrm{PI}})$ was in good agreement

with the normalized diameter from the μCT data (see Figure B.8). $\nu_{\mathrm{PI}}(x_{\mathrm{PI}})$ was then interpolated at the points x_{CT}.

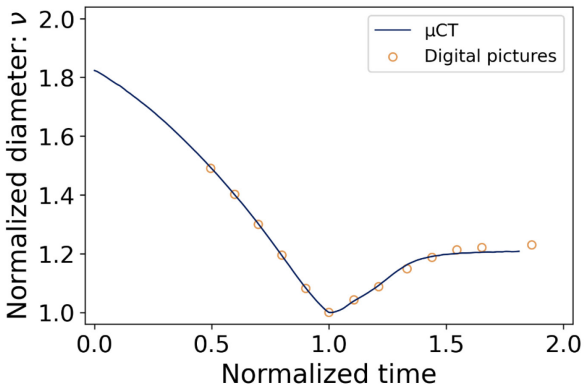

Figure B.8 Normalized diameter ν from the μCT and digital pictures expressed as a function of a normalized time scale. Reprinted from ref.[107], CC BY 4.0 (https://creativecommons.org/licenses/by/4.0/).

The last step was to interpolate the diameter of the gel with the time of the scattering data. The scattering intensity could be expressed as $I(q, x_{\mathrm{XS}})$ with:

$$x_{\mathrm{XS}} = \frac{t_{\mathrm{XS}} + \Delta t_2}{t_{\mathrm{XS,MS}} + \Delta t_2}. \tag{B.67}$$

where x_{XS} is the normalized time scale of the X-ray scattering data frames, t_{XS} the time in h, $t_{\mathrm{XS,MS}}$ the time of maximum shrinkage and Δt_2 a time shift. $t_{\mathrm{XS,MS}}$ was set by visual inspection of the scattering profiles (see Figure B.19). Δt_2 was known, it corresponded to the delay between the first scattering data frame recorded and the first digital pictures that was taken. $\nu_{\mathrm{PI}}(x_{\mathrm{PI}})$ was then interpolated at the points x_{XS}. The diameter in absolute units was calculated with: $d_{\mathrm{XS}}(x_{\mathrm{XS}}) = \nu_{\mathrm{PI}}(x_{\mathrm{XS}}) \cdot d_{\mathrm{CT,MS}}$, from which the diameter of the gel during drying was found by converting x_{XS} back to the absolute time scale t_{XS}.

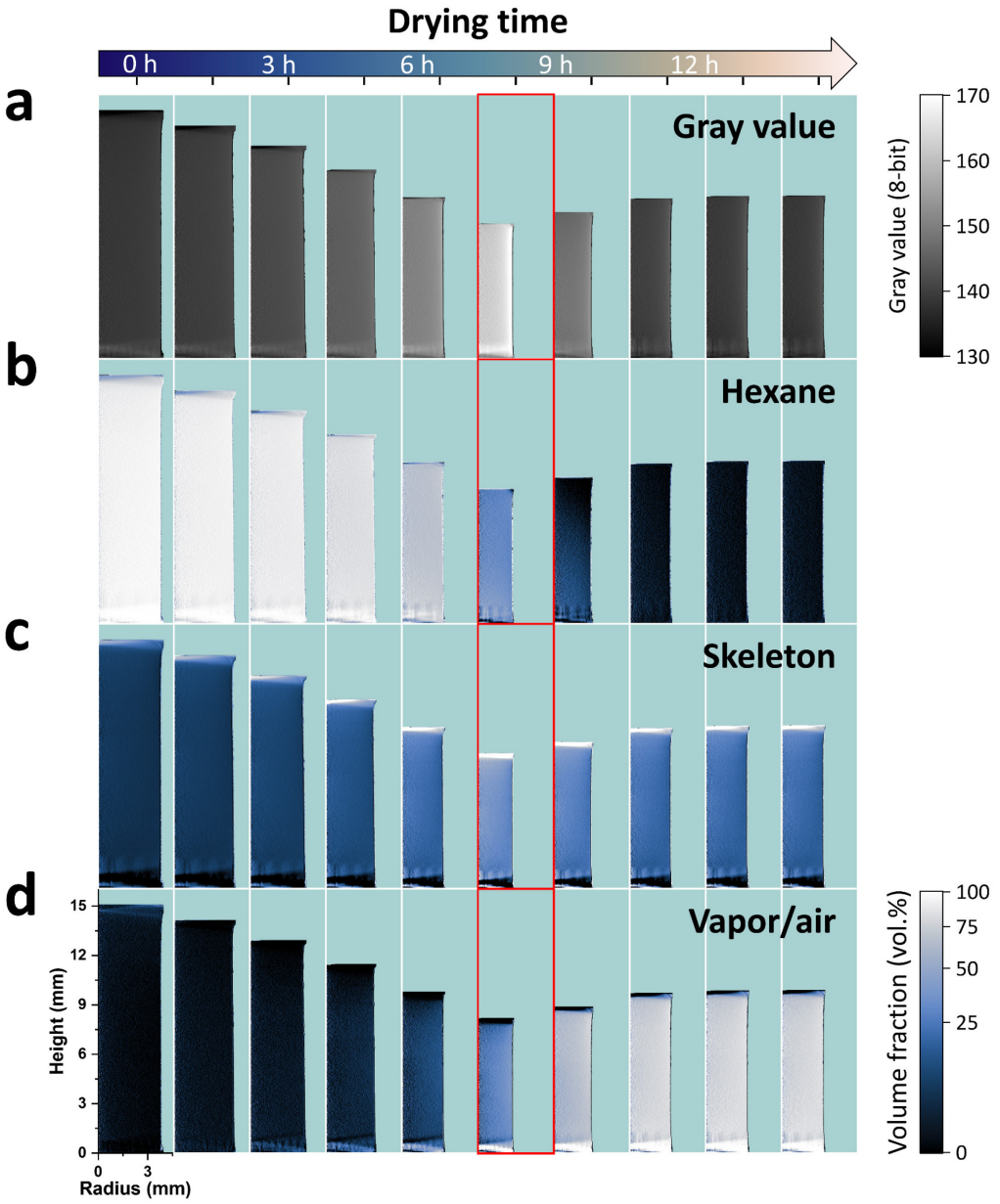

Figure B.9 GHR and volume fraction maps of sample M1 at 10 selected drying stages on top of a cyan background. (**a**) GHR maps with the corresponding gray value scale on the right. The brightness and contrast in the images of the GHR maps are adjusted to improve visualization. (**b**) HEXHR maps. (**c**) SKELHR maps. (**d**) AIRHR maps. The color scale of the volume fraction maps is shown at the bottom right of the figure. The volume fraction maps are normalized between 0 % and 100 %. The images of the volume fraction maps are encoded with a gamma value of 0.5 to improve visualization. The time scale is illustrated with an arrow on top of the figure and the time gap between the maps in a given panel is 1.64 ± 0.04 h. The length scale of all maps is indicated in the first map of panel (**d**). The maps corresponding to the maximum shrinkage are outlined in red. Each map consists in 410 x 1455 non-interpolated data points. Reprinted from ref.[107], CC BY 4.0 (https://creativecommons.org/licenses/by/4.0/).

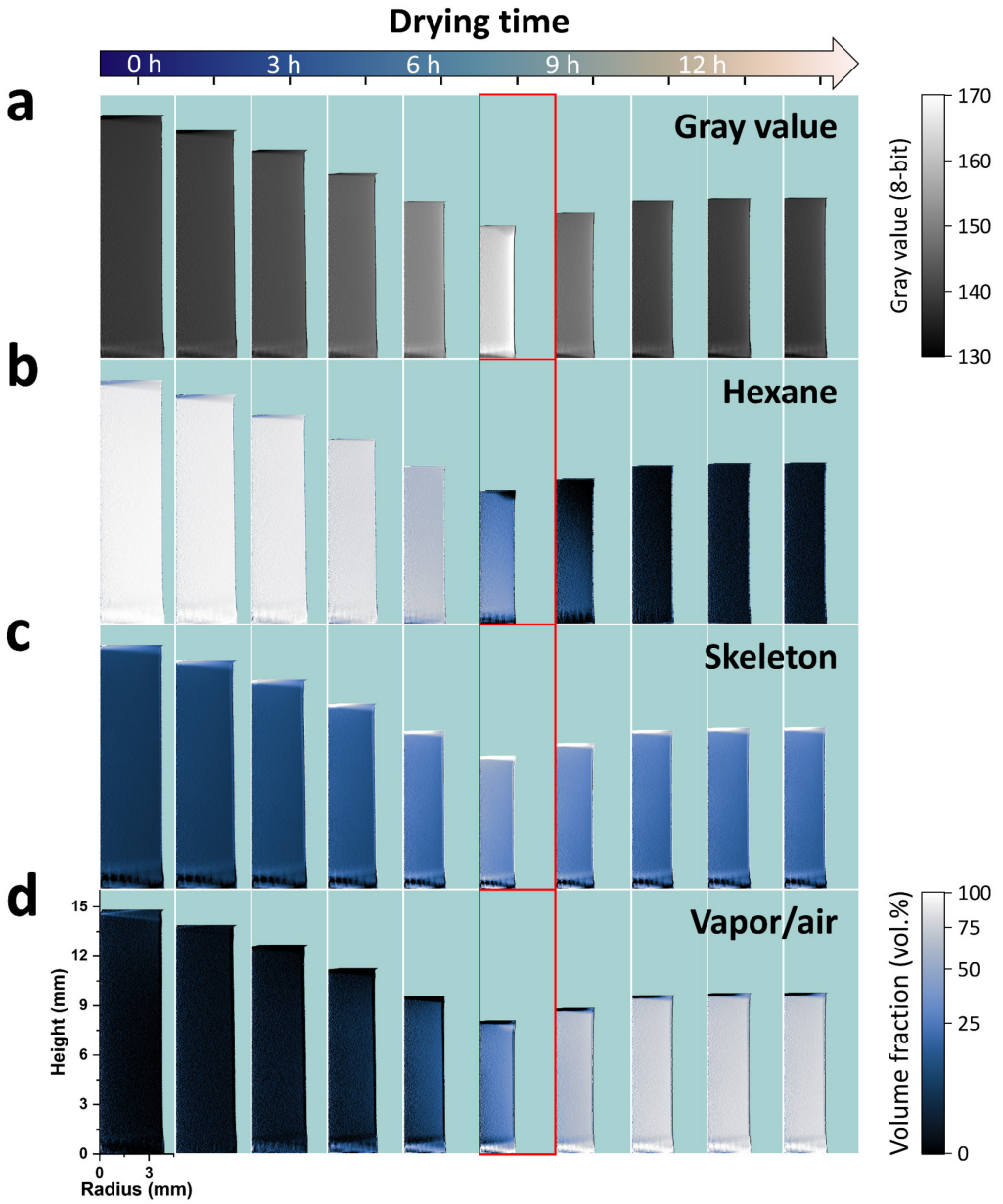

Figure B.10 GHR and volume fraction maps of sample M2 at 10 selected drying stages on top of a cyan background. (**a**) GHR maps with the corresponding gray value scale on the right. The brightness and contrast in the images of the GHR maps are adjusted to improve visualization. (**b**) HEXHR maps. **(c**) SKELHR maps. (**d**) AIRHR maps. The color scale of the volume fraction maps is shown at the bottom right of the figure. The volume fraction maps are normalized between 0 % and 100 %. The images of the volume fraction maps are encoded with a gamma value of 0.5 to improve visualization. The time scale is illustrated with an arrow on top of the figure and the time gap between the maps in a given panel is 1.63 ± 0.04 h. The length scale of all maps is indicated in the first map of panel (**d**). The maps corresponding to the maximum shrinkage are outlined in red. Each map consists in 410 x 1455 non-interpolated data points. Reprinted from ref.[107], CC BY 4.0 (https://creativecommons.org/licenses/by/4.0/).

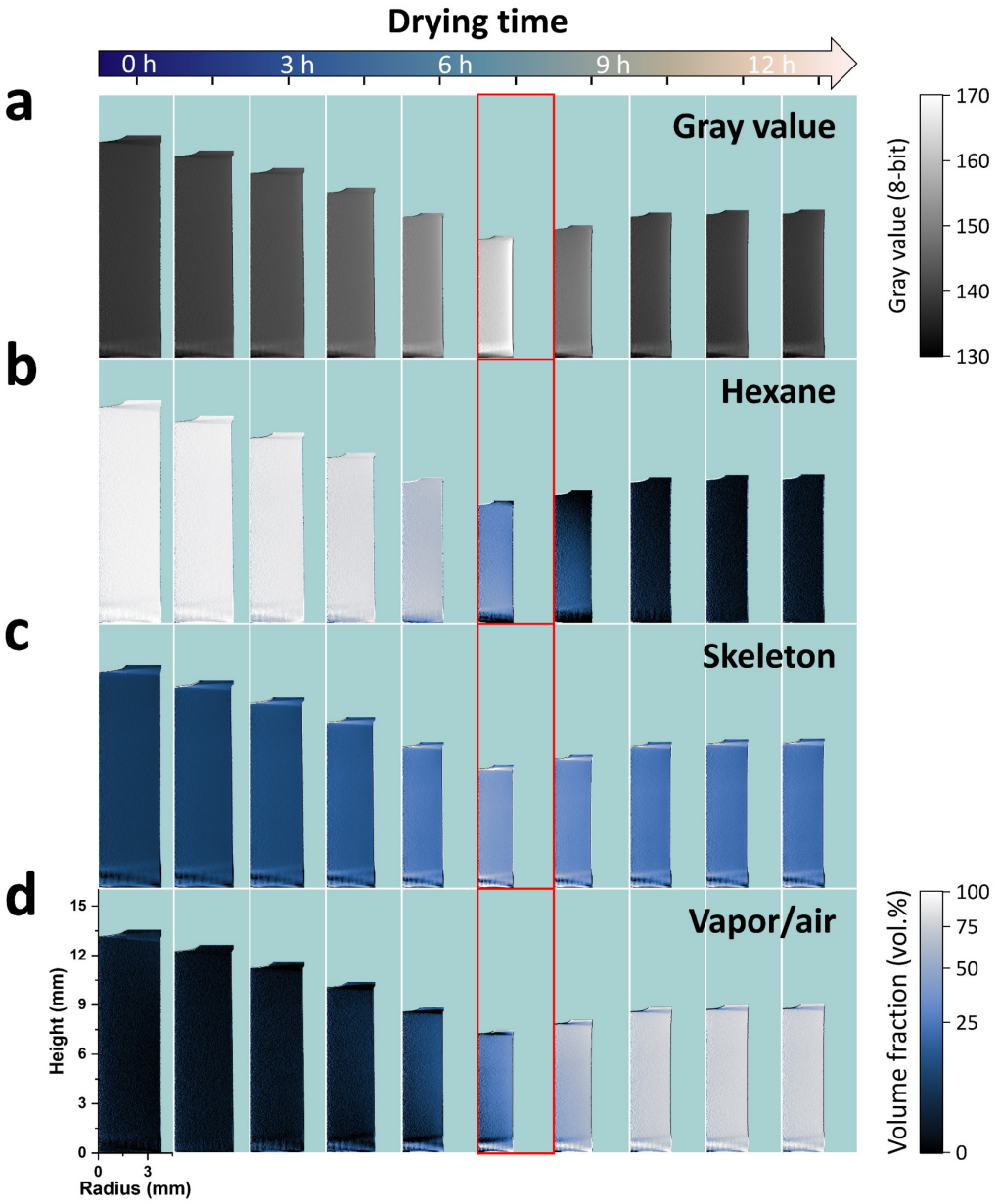

Figure B.11 GHR and volume fraction maps of sample M5 at 10 selected drying stages on top of a cyan background. (**a**) GHR maps with the corresponding gray value scale on the right. The brightness and contrast in the images of the GHR maps are adjusted to improve visualization. (**b**) HEXHR maps. (**c**) SKELHR maps. (**d**) AIRHR maps. The color scale of the volume fraction maps is shown at the bottom right of the figure. The volume fraction maps are normalized between 0 % and 100 %. The images of the volume fraction maps are encoded with a gamma value of 0.5 to improve visualization. The time scale is illustrated with an arrow on top of the figure and the time gap between the maps in a given panel is 1.43 ± 0.04 h. The length scale of all maps is indicated in the first map of panel (**d**). The maps corresponding to the maximum shrinkage are outlined in red. Each map consists in 410 x 1455 non-interpolated data points. Reprinted from ref.[107], CC BY 4.0 (https://creativecommons.org/licenses/by/4.0/).

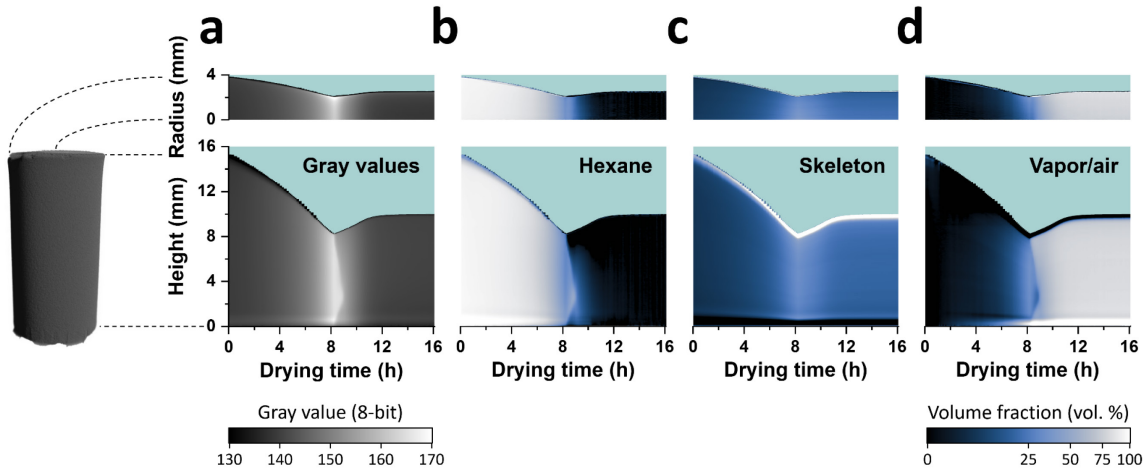

Figure B.12 Radial and vertical maps of the gray values and volume fraction of sample M1 on top of a cyan background. The 3D image on the left of the figure depicts the segmented volume of M1 at the beginning of drying and the dashed lines illustrate the radial and vertical axes of the cylinder against which the radial and vertical maps are shown. (**a**) GR and GH maps. The gray value scale is shown at the bottom of panel (**a**). The brightness and contrast in the images of the GR and GH maps are adjusted to improve visualization. (**b**) HEXR and HEXH maps. (**c**) SKELR and SKELH maps. (**d**) AIRR and AIRH maps. The images of the volume fraction maps are encoded with a gamma value of 0.5 to improve visualization. The time axis is shown in each vertical map and the length scale is shown in the radial and vertical maps of panel (**a**). The radial maps consist in 1663 x 410 data points and the vertical maps in 1663 x 1455 points. In all maps, the horizontal time resolution is interpolated from 141 time stamps onto 1663 points. Reprinted from ref.[107], CC BY 4.0 (https://creativecommons.org/licenses/by/4.0/).

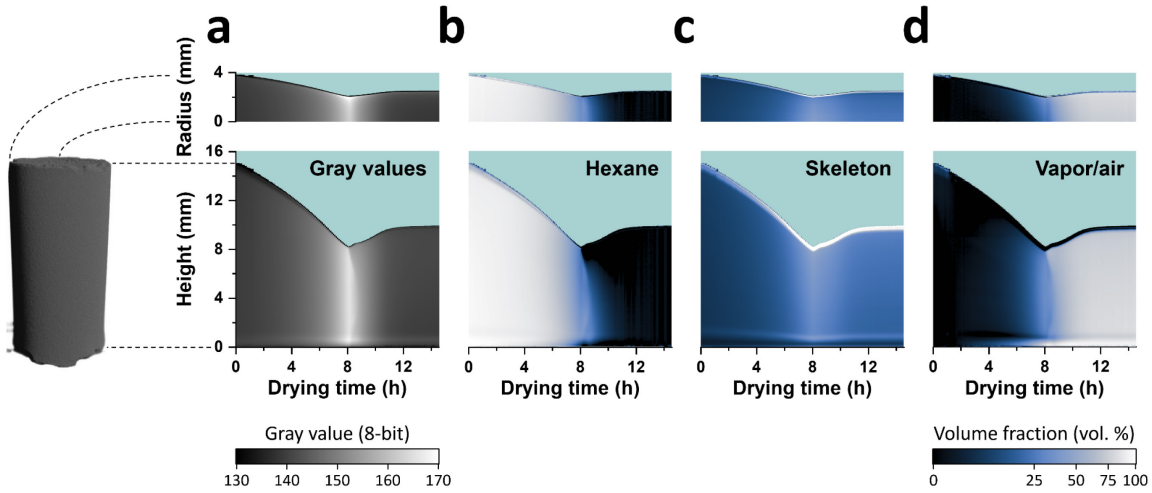

Figure B.13 Radial and vertical maps of the gray values and volume fraction of sample M2 on top of a cyan background. The 3D image on the left of the figure depicts the segmented volume of M2 at the beginning of drying and the dashed lines illustrate the radial and vertical axes of the cylinder against which the radial and vertical maps are shown. (**a**) GR and GH maps. The gray value scale is shown at the bottom of panel (**a**). The brightness and contrast in the images of the GR and GH maps are adjusted to improve visualization. (**b**) HEXR and HEXH maps. (**c**) SKELR and SKELH maps. (**d**) AIRR and AIRH maps. The images of the volume fraction maps are encoded with a gamma value of 0.5 to improve visualization. The time axis is shown in each vertical map and the length scale is shown in the radial and vertical maps of panel (**a**). The radial maps consist in 1509 x 410 data points and the vertical maps in 1509 x 1455 points. In all maps, the horizontal time resolution is interpolated from 141 time stamps onto 1509 points. Reprinted from ref.[107], CC BY 4.0 (https://creativecommons.org/licenses/by/4.0/).

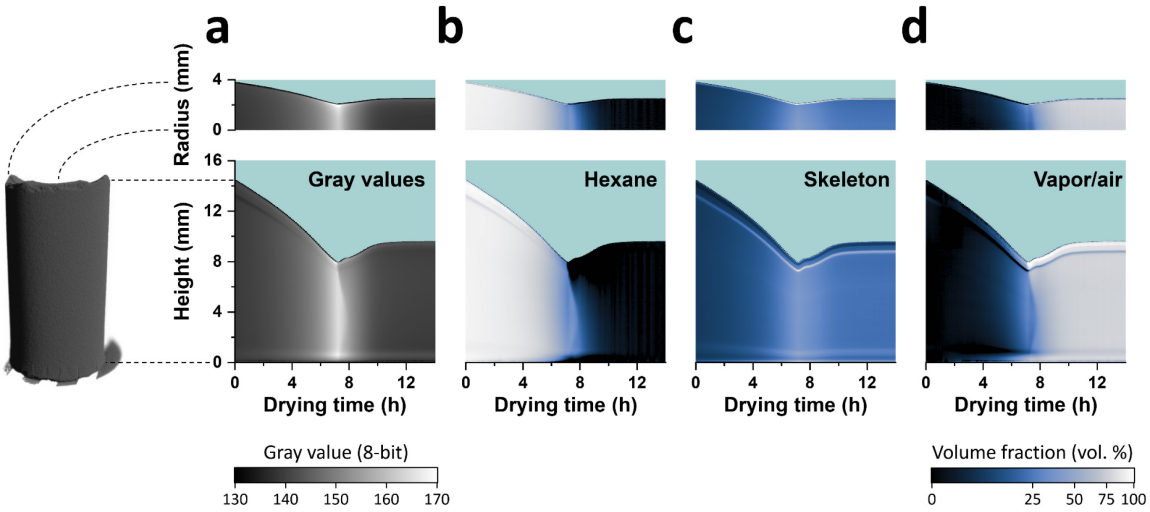

Figure B.14 Radial and vertical maps of the gray values and volume fraction of sample M5 on top of a cyan background. The 3D image on the left of the figure depicts the segmented volume of M5 at the beginning of drying and the dashed lines illustrate the radial and vertical axes of the cylinder against which the radial and vertical maps are shown. (**a**) GR and GH maps. The gray value scale is shown at the bottom of panel (**a**). The brightness and contrast in the images of the GR and GH maps are adjusted to improve visualization. (**b**) HEXR and HEXH maps. (**c**) SKELR and SKELH maps. (**d**) AIRR and AIRH maps. The images of the volume fraction maps are encoded with a gamma value of 0.5 to improve visualization. The time axis is shown in each vertical map and the length scale is shown in the radial and vertical maps of panel (**a**). The radial maps consist in 1444 x 410 data points and the vertical maps in 1444 x 1455 points. In all maps, the horizontal time resolution is interpolated from 141 time stamps onto 1444 points. Reprinted from ref.[107], CC BY 4.0 (https://creativecommons.org/licenses/by/4.0/).

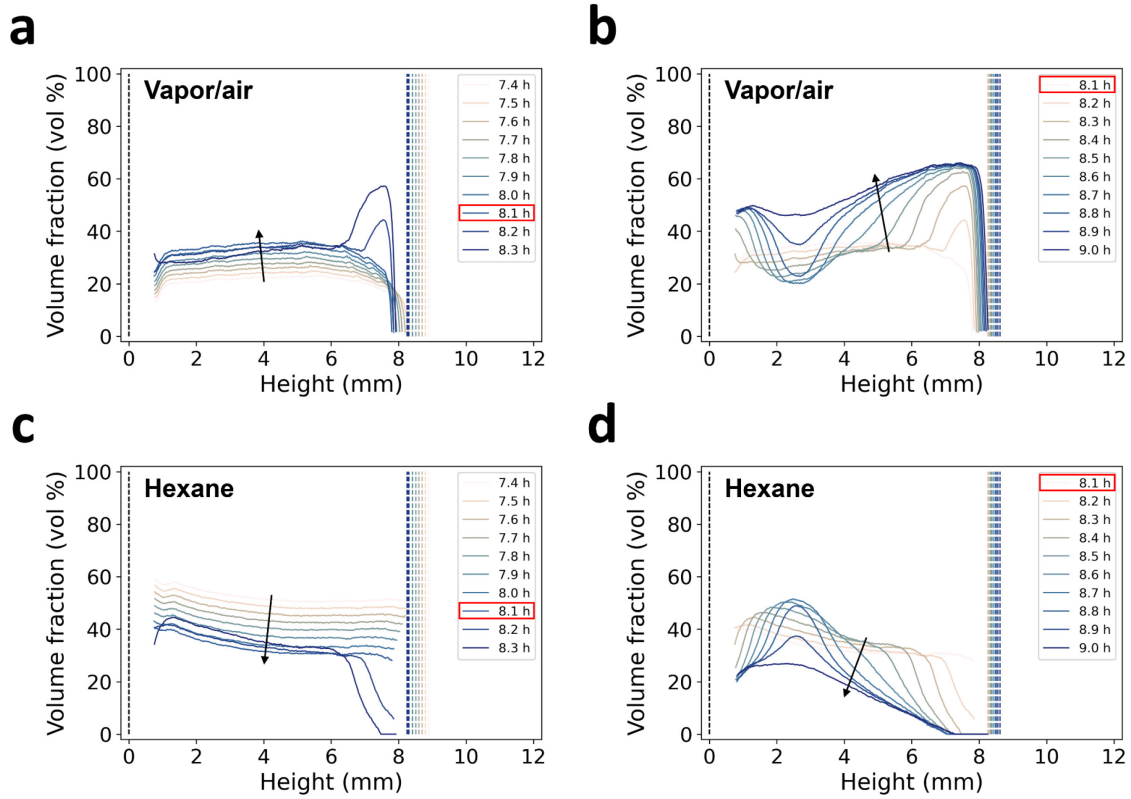

Figure B.15 Volume fraction profiles of hexane and vapor/air along the height of sample M1 at selected time stamps. Vapor/air profiles between 7.4 and 8.3 h (**a**) and between 8.1 and 9.0 h (**b**). Hexane profiles between 7.4 and 8.3 h (**c**) and between 8.1 and 9.0 h (**d**). The profiles in panels (**a**) and (**c**) correspond to the μCT scans before the maximum shrinkage and shortly after, while the profiles in panels (**b**) and (**d**) correspond to the μCT scans at the maximum shrinkage and after. The dashed lines correspond to the bottom (h = 0 mm) and to the top of the sample. The time of maximum shrinkage is highlighted in red in the legends. The spacing between the profiles in each panel corresponds to a single μCT scan. The profiles were extracted from the AIRH and HEXH maps by excluding the values affected by the artifacts at the edges for better visualization. Reprinted from ref.[107], CC BY 4.0 (https://creativecommons.org/licenses/by/4.0/).

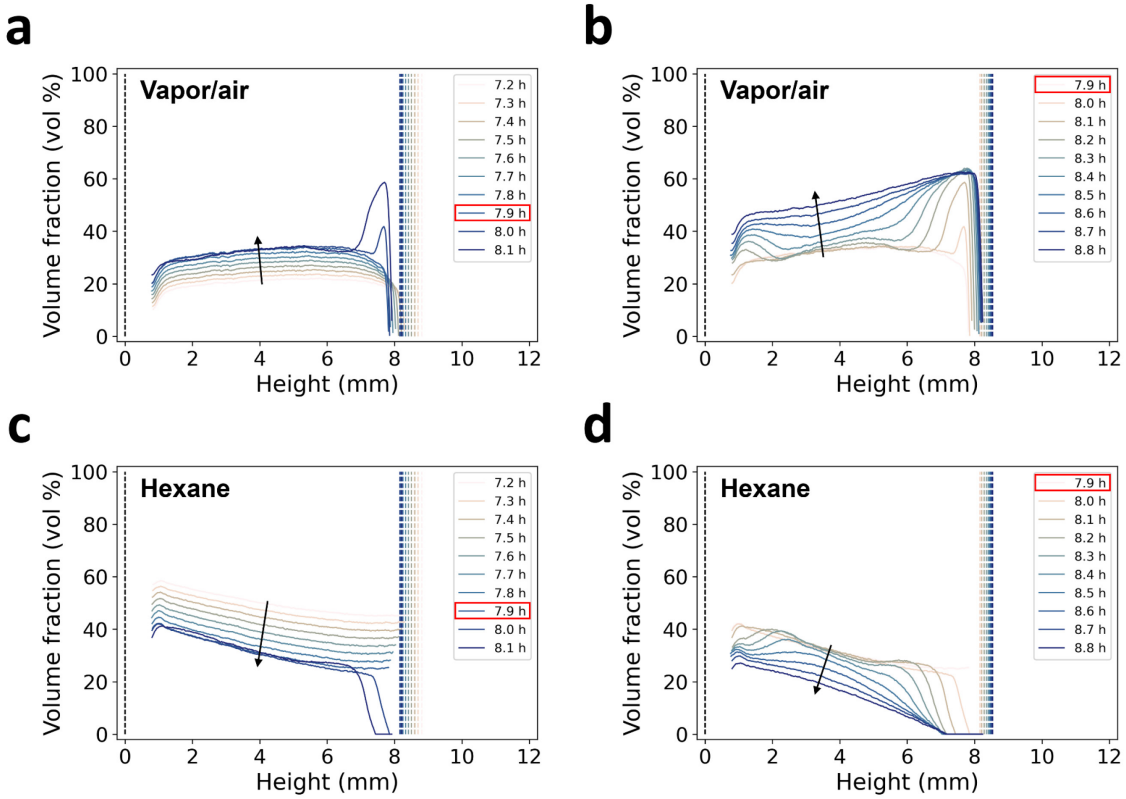

Figure B.16 Volume fraction profiles of hexane and vapor/air along the height of sample M2 at selected time stamps. Vapor/air profiles between 7.2 and 8.1 h (**a**) and between 7.9 and 8.8 h (**b**). Hexane profiles between 7.2 and 8.1 h (**c**) and between 7.9 and 8.8 h (**d**). The profiles in panels (**a**) and (**c**) correspond to the μCT scans before the maximum shrinkage and shortly after, while the profiles in panels (**b**) and (**d**) correspond to the μCT scans at the maximum shrinkage and after. The dashed lines correspond to the bottom (h = 0 mm) and to the top of the sample. The time of maximum shrinkage is highlighted in red in the legends. The spacing between the profiles in each panel corresponds to a single μCT scan. The profiles were extracted from the AIRH and HEXH maps by excluding the values affected by the artifacts at the edges for better visualization. Reprinted from ref.[107], CC BY 4.0 (https://creativecommons.org/licenses/by/4.0/).

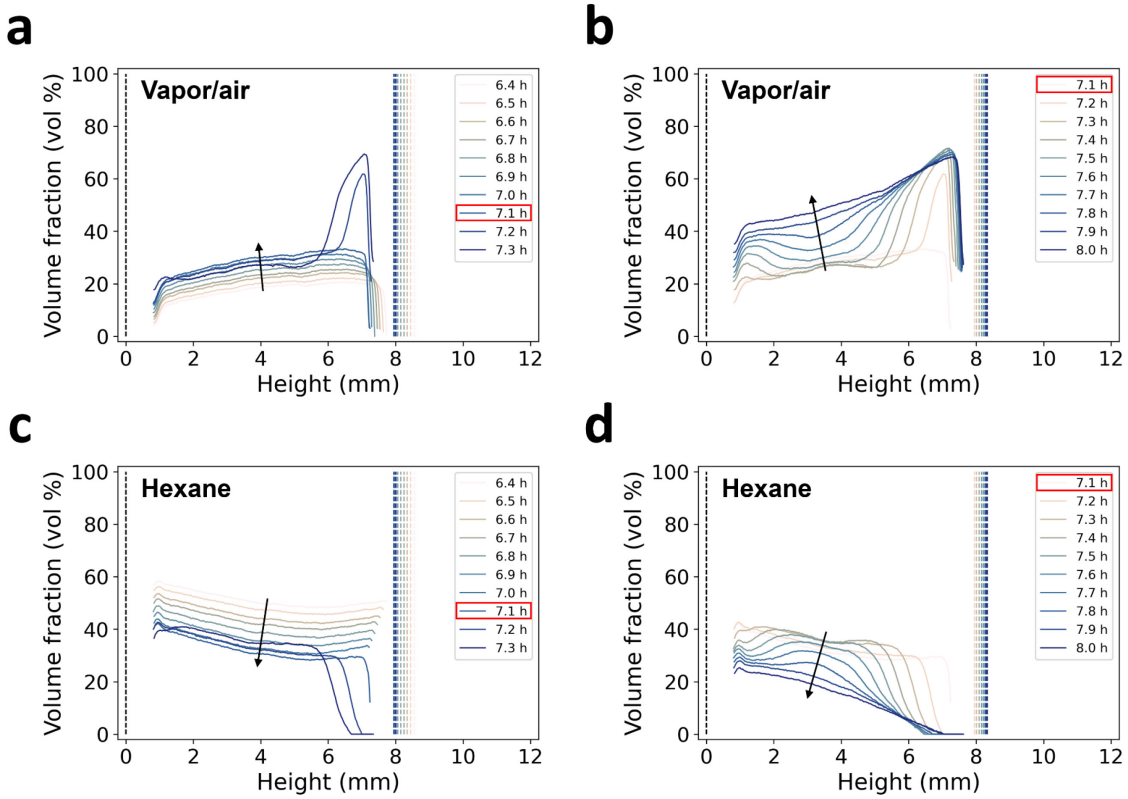

Figure B.17 Volume fraction profiles of hexane and vapor/air along the height of sample M5 at selected time stamps. Vapor/air profiles between 6.4 and 7.3 h (**a**) and between 7.1 and 8.0 h (**b**). Hexane profiles between 6.4 and 7.3 h (**c**) and between 7.1 and 8.0 h (**d**). The profiles in panels (**a**) and (**c**) correspond to the μCT scans before the maximum shrinkage and shortly after, while the profiles in panels (**b**) and (**d**) correspond to the μCT scans at the maximum shrinkage and after. The dashed lines correspond to the bottom (h = 0 mm) and to the top of the sample. The time of maximum shrinkage is highlighted in red in the legends. The spacing between the profiles in each panel corresponds to a single μCT scan. The profiles were extracted from the AIRH and HEXH maps by excluding the values affected by the artifacts at the edges for better visualization. Reprinted from ref.[107], CC BY 4.0 (https://creativecommons.org/licenses/by/4.0/).

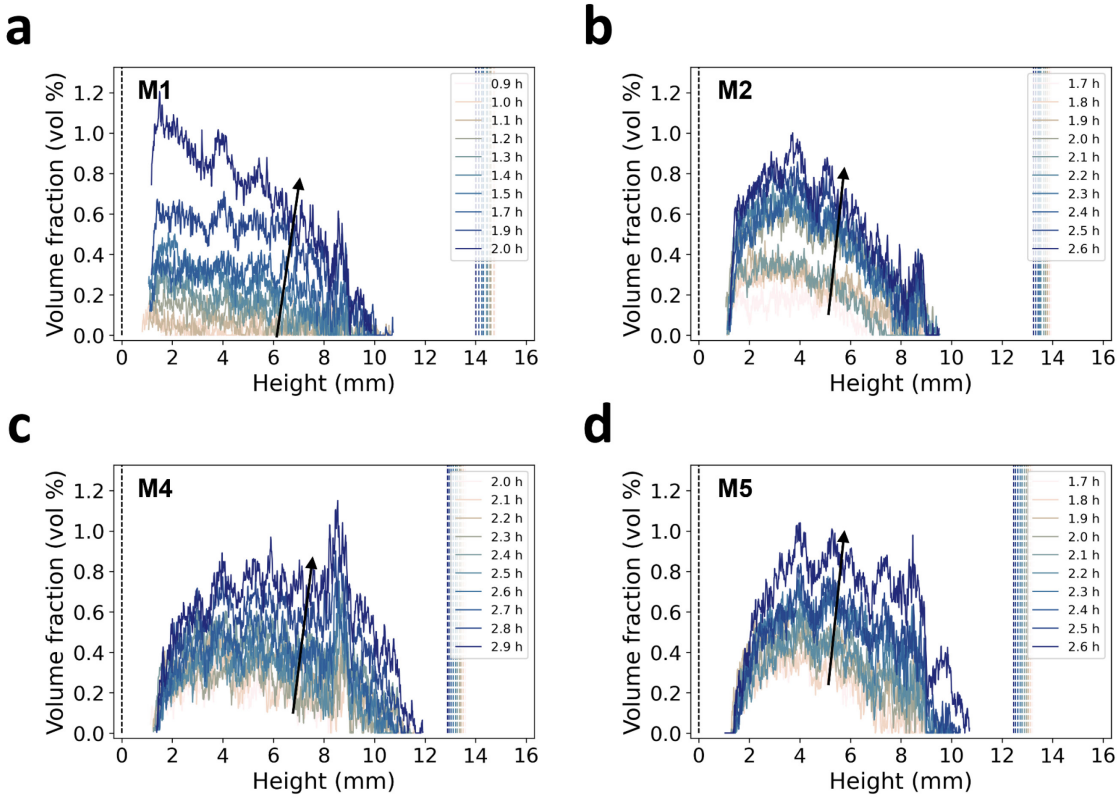

Figure B.18 Vertical vapor/air profiles extracted from the AIRH maps of all samples at selected drying stages. (**a**) Sample M1 between 0.9 and 2.0 h. (**b**) Sample M2 between 1.7 and 2.6 h. (**c**) Sample M4 between 2.0 and 2.9 h (as shown in the main text). (**d**) Sample M5 between 1.7 and 2.6 h. The dashed lines correspond to the bottom (h = 0 mm) and to the top of the sample. The spacing between each profile corresponds to a single µCT scan. Reprinted from ref.[107], CC BY 4.0 (https://creativecommons.org/licenses/by/4.0/).

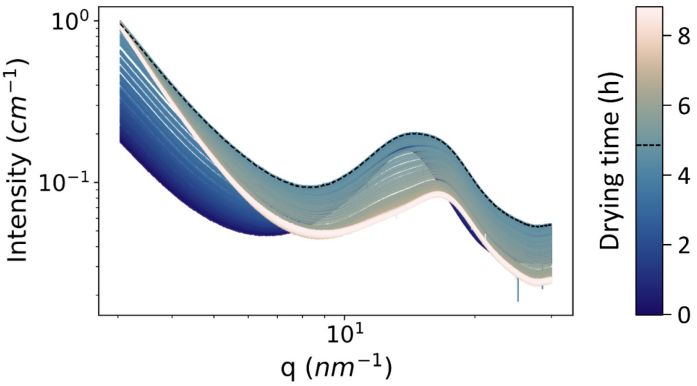

Figure B.19 Scattering patterns of gel M6 throughout drying within 3 – 30 nm^{-1}. Only 100 profiles were shown until ca. 8.5 h to enhance visualization. The scattered intensity of the gel at the maximum shrinkage is highlighted with black dashed lines. The color scale is shown on the right and also depicts the time of maximum shrinkage. The data are plotted as bands including the standard deviation. Reprinted from ref.[107], CC BY 4.0 (https://creativecommons.org/licenses/by/4.0/).

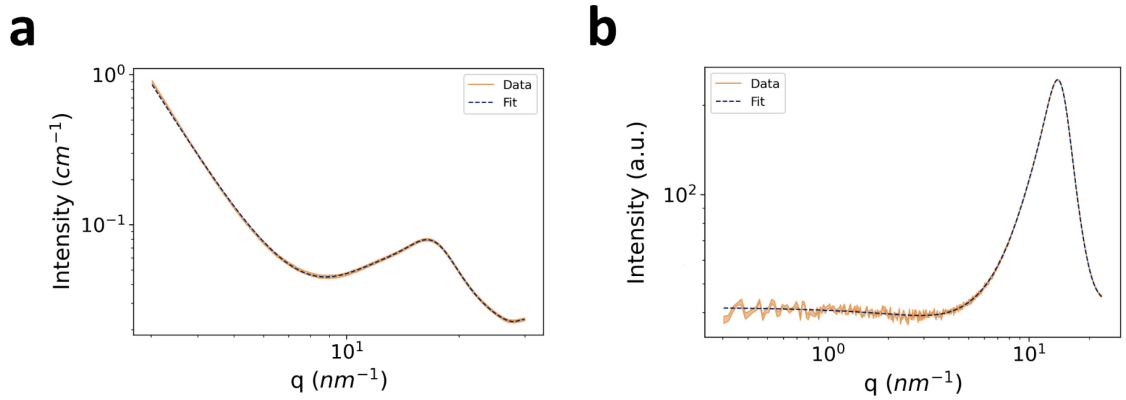

Figure B.20 (**a**) Scattering pattern of sample M6 at the end of drying in the region 3 – 30 nm^{-1} along with the corresponding fit. The scattered intensity is in absolute units. (**b**) Scattering pattern of a hexane capillary in the region 0.3 – 3.3 nm^{-1} along with the fit of the data. Here the scattered intensity is in arbitrary units as the data frames on the hexane reference samples were not normalized by the sample thickness. The data are plotted as bands including the standard deviation. Reprinted from ref.[107], CC BY 4.0 (https://creativecommons.org/licenses/by/4.0/).

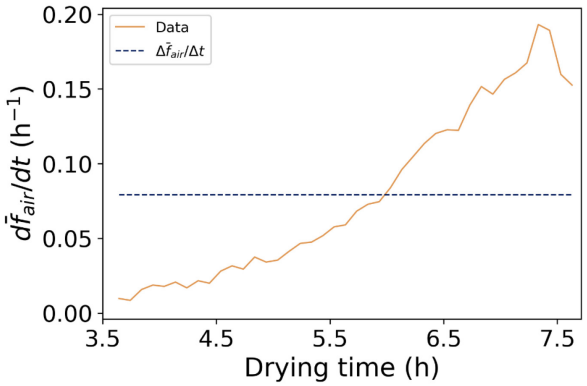

Figure B.21 Numerical derivative of the average vapor/air volume fraction in gel M4 versus the drying time: $d\bar{f}_{\mathrm{air}}/dt$ from the cavitation onset ($t_{\mathrm{cav}} = 3.64$ h) until the time of maximum shrinkage ($t_{\mathrm{MS}} = 7.63$ h). The dashed line indicates the value $\Delta\bar{f}_{\mathrm{air}}/\Delta t$ used in the manuscript. These results were produced using the µCT global quantitative imaging results reported in chapter 4. Reprinted from ref.[107], CC BY 4.0 (https://creativecommons.org/licenses/by/4.0/).

B.5 Spatial variability analysis

Vertical and radial distributions. This section reports the spatial variability analysis of the gray values in the GHR and GR maps and discusses their origin. A heterogeneous distribution of the gray values was observed in the GHR maps (Figure 5.3, Figure B.9 – Figure B.11). To further quantify these variations, gray value profiles were extracted from the GHR maps of sample M4 across the gel height and radius as shown in Figure B.22. Three vertical profiles were extracted at a relative radius of 0.25, 0.5 and 0.75 (from the center of the gel to its radial

edge) and three radial profiles were extracted at a relative height of 0.25, 0.5 and 0.75 (from the bottom to the top of the gel).

The gray values remained relatively constant across the gel's height throughout drying, suggesting a homogeneous composition (Figure B.22a-c). Variations were only observed during the spring-back effect (visible in Figure B.22c at 7 – 8 mm and 7.6 h of drying) and at the edges of the sample, regardless of the radial coordinate. The small peak at a height of about

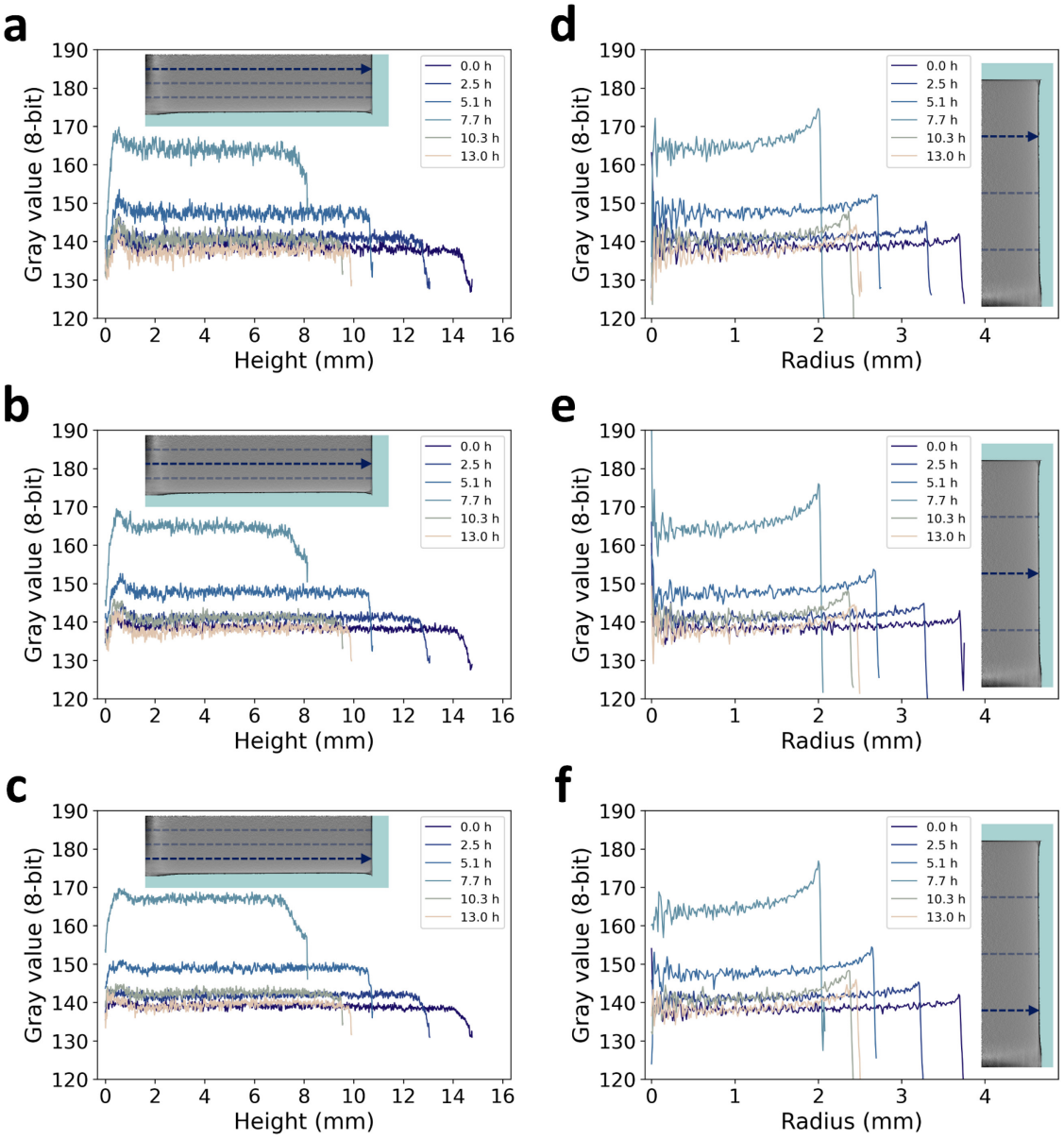

Figure B.22 Gray value profiles extracted from the GHR maps of sample M4. Each panel presents the gray value profiles at six drying stages. Each panel includes a GHR map as an inset with an arrow illustrating the region where the gray value profiles are extracted. The regions (lines) are fixed at a relative height or relative radius regarding to the maximum height or radius at each drying stage. (a-c) Gray value profiles along the height of the gel at a relative radius of (**a**) 0.25, (**b**) 0.5 and (**c**) 0.75. (d-f) Gray value profiles along the radius of the gel at a relative height of (**d**) 0.75, (**e**) 0.5 and (**f**) 0.25. Reprinted from ref.[107], CC BY 4.0 (https://creativecommons.org/licenses/by/4.0/).

0.5 mm was seemingly caused by under-sampling artifacts in the masked slices[132] due to the low number of projections taken and the proximity of the sample with the drying chamber. This region with locally higher gray values can clearly be seen in the GHR maps (Figure 5.3, Figure B.9 – Figure B.11). The lower gray values before the peak at the bottom of the gel (at a height of 0 mm), as well as the lower gray values at the top of the gel (Figure B.22a-c) were due to imperfect segmentation at the edges which included some of the background in the ROIs.

Across the gel's radius, the gray values followed an exponential growth with the radius regardless of the vertical coordinate (Figure B.22d-f). After reaching a maximum near the edge of the sample, the gray values decreased due to imperfect segmentation that included some of the background in the masked slices. The exponential dependency of the gray values on the gel's radius was coherent with beam hardening artifacts in cylindrical samples.[131] Beam hardening artifacts are caused by a higher attenuation of the soft X-rays in the center of the sample than at its periphery with polychromatic radiations. Beam hardening was expected in our in operando experiments given the relatively high voltage (135 kV) and the absence of a filter. The change in amplitude and curvature of the radial variations was quantified throughout drying by fitting the gray value profiles to compare the variations with a simplified beam hardening model.

RAC radial profiles were extracted from the MR map of sample M4 at each scan number. The edges effect were excluded by considering the profiles until the maximum of the RAC values. The RAC radial profiles were then fitted with an exponential function defined as $f(r) = Ae^{r/B} + C$, where r is the gel's radius in mm and A, B and C are fitting parameters. Figure B.23a shows the fitted radial profiles at selected drying stages. The amplitude of the radial variations was quantified by δ_μ, defined as the difference of the RAC at the outer radius of the gel and the RAC at the center of the gel:

$$\delta_\mu = A\left(e^{r_{\max}/B} - 1\right), \tag{B.68}$$

where $r_{\max}$ is the maximum radius of the gel. The curvature was quantified with the inverse of the B parameter, the lower B the more the profiles were curved, compared to flat profiles as $B \to \infty$.

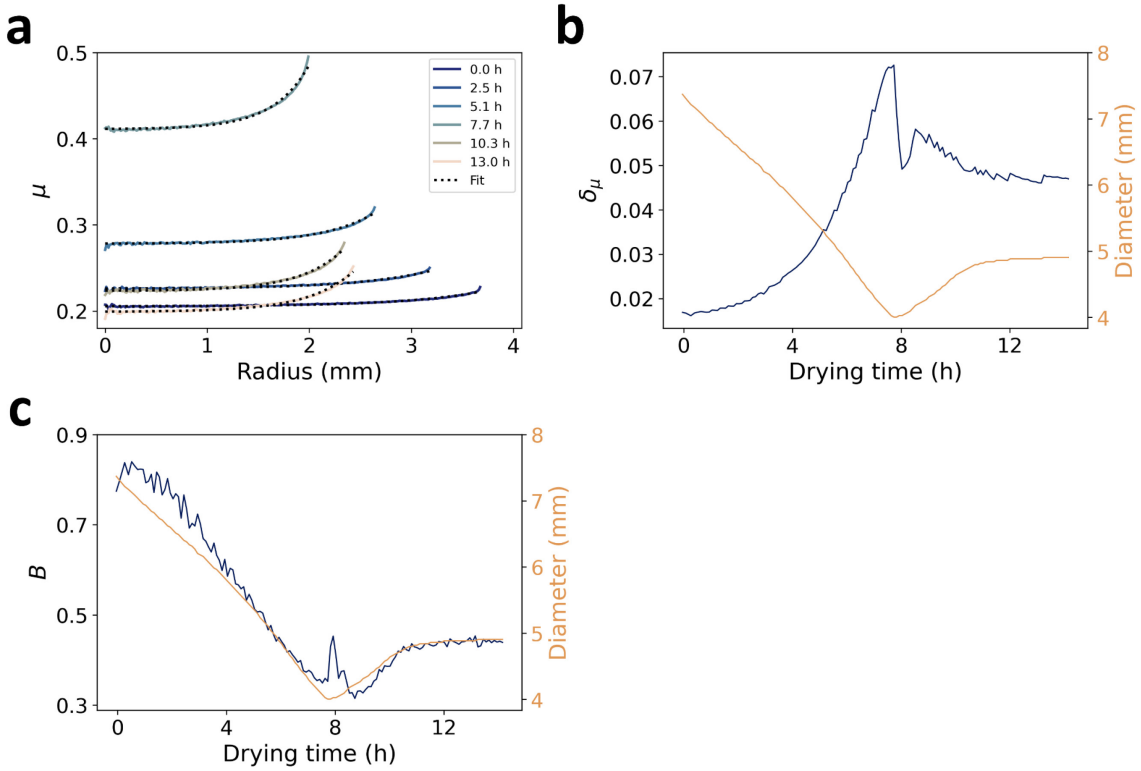

Figure B.23 (**a**) Example of the fitting results on the radial profiles extracted from the MR maps of sample M4 at six drying stages. (**b**) Amplitude of the gray value variations: δ_μ parameter (blue) and average diameter of the gel (orange). (**c**) Curvature of the gray value variations (blue) and average diameter of the gel (orange). The smaller B, the more curved the radial profiles. Reprinted from ref.[107], CC BY 4.0 (https://creativecommons.org/licenses/by/4.0/).

The fitting of the radial profiles generated 141 values of δ_μ and B shown in Figure B.23b,c along the average diameter of the gel. δ_μ was inversely proportional to the gel diameter: the amplitude of the radial variations increased as the gel diameter decreased. The maximum amplitude corresponded to the maximum shrinkage and the steep drop afterwards was likely caused by the heterogeneous spring-back of the gel. A similar behavior was observed for the curvature of the spatial variations. The evolution of the B parameter throughout drying was comparable to the gel diameter with a higher curvature the smaller the diameter was. Identical conclusions were made from spatial variability analyses on samples M1, M2 and M4. This procedure was also performed on the hr-maps and provided similar results in terms of amplitude, but the curvature could not be accurately determined due to the noise in the GHR maps.

The correlation between the amplitude (δ_μ) and the curvature ($1/B$) of the variations with the diameter of the gel was consistent with beam hardening. Considering a large cylindrical sample, most of the soft X-rays are absorbed except a relatively small portion at the sample edges resulting in virtually higher RAC in these regions. In a smaller cylindrical sample of the

same material, the difference in the extent of soft X-rays absorbed in the center and at the edge is more pronounced due to the exponential dependency of X-ray transmission with the sample thickness[108] (see chapter 3.1), resulting in stronger beam hardening and in increased amplitude and curvature of the variations in the gray values and RAC along the gel radius.

Besides beam hardening artifacts, a potential gradient of the hexane composition along the radial direction of the gel could also generate the radial variations observed in Figure B.22d-f and Figure B.23a. However, the amplitude of the variations would then vanish in the dry gel, which was not the case in our experiments. Additionally, the value of δ_μ was inversely proportional to the diameter of the gel and not on the hexane content. Eventual radial variations caused by a different hexane content should decrease in amplitude as the hexane evaporates, whereas δ_μ had the same value after 6 h of drying and at the end of drying (Figure B.23b). On the other hand, heterogeneities of the silica skeleton composition in the gel could produce variations of the gray values and RAC along the gel radius. A denser shell of silica skeleton could have formed in the samples during gelation in the molds. Such variations would not vanish in the dry gel and would be consistent with the increase in curvature with the gel diameter. While this hypothesis could not be ruled out, the significant increase in the amplitude of the variations between the maximum shrinkage and the start of drying could not be solely explained by a higher content of skeleton at the edge of the gel.

The spatial variability analysis leaned towards the occurrence of beam hardening to explain the observed variations along the gel radius, with possible effects related to a heterogeneous composition of the gels. Given those remarks, the evaluation of the evaporation mechanisms was performed on the GH map and the derived vertical volume fraction maps, as beam hardening artifacts were not observed along the gel height.

Radial variations in the volume fraction maps. Upon modeling the phase composition from the GHR and GR maps, similar radial variations as the ones attributed to beam hardening appeared in the corresponding volume fraction maps. As a result, the phase composition of the gel seemed to vary along its radius. This can be slightly seen in the HEXR and AIRR maps shortly before the maximum shrinkage (Figure 5.4, Figure B.12 – Figure B.14). Figure B.24 shows the radial volume fraction profiles extracted from the HEXR, SKELR and AIRR maps at three selected drying stages, where variations along the gel radius could clearly be seen. These were attributed to the propagation of beam hardening artifacts present in the gray value maps. It was worth noting that the amplitude and curvature of the variations observed in the HEXR, SKELR and AIRR radial maps were not directly proportional to the RAC variations shown in Figure B.23. This was due to the way the drying model was defined:

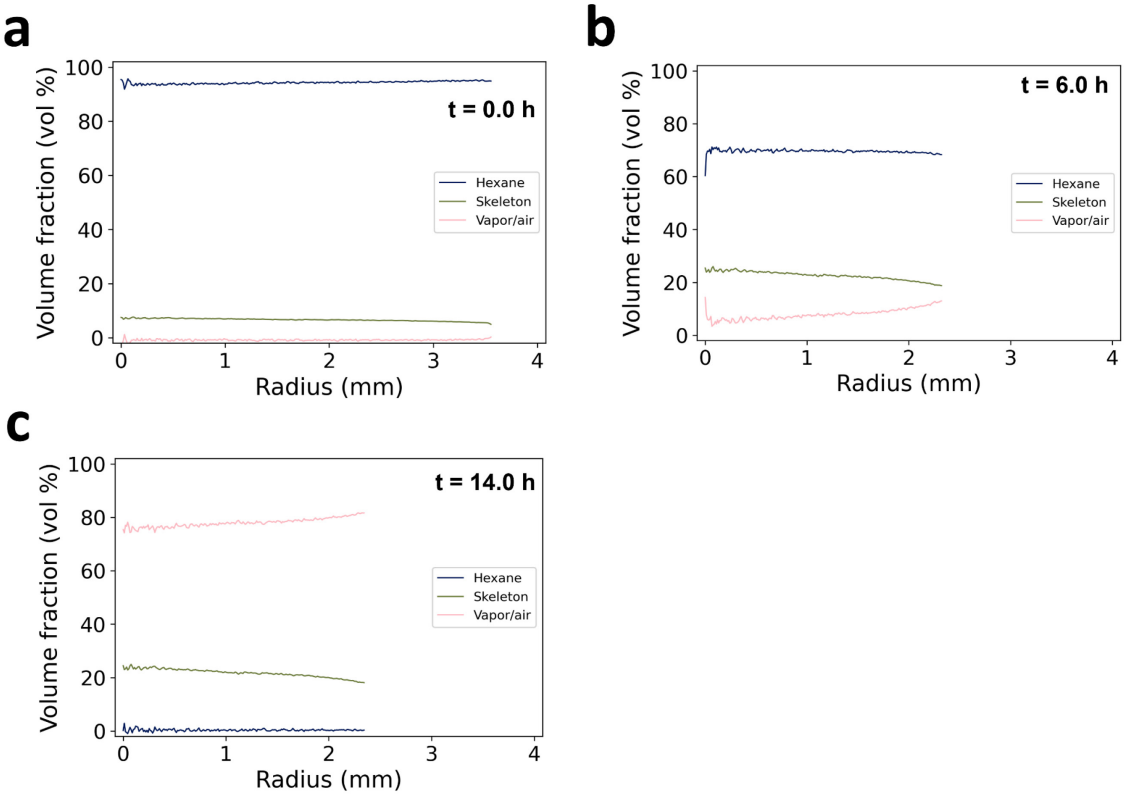

Figure B.24 Hexane, skeleton and vapor/air radial profiles extracted from the HEXR, SKELR and AIRR maps of sample M4 at three selected drying stages: (**a**) 0.0 h, (**b**) 6.0 h and (**c**) 14.0 h. The time is indicated in each panel on the top right corner. Reprinted from ref.[107], CC BY 4.0 (https://creativecommons.org/licenses/by/4.0/).

the quantity $\mu_{\mathrm{skel}} f_{\mathrm{skel},i,j,k}$ was calculated from the μCT scans of the dry gel and interpolated and rescaled to the other scans (appendix B.2).

Azimuthal variations. This section presents the spatial variability analysis on the gray values along the azimuth of the cylindrical samples to evaluate potential heterogeneities in the gel composition during drying. To do so, selected masked slices were integrated radially with a custom Python script to produce azimuthal gray value profiles. For each scan number, a masked slice was selected at a given relative height of the cylinder. The center of each masked slice was defined as the center of mass as described in appendix B.1. The pixels in the masked slices were separated into 100 bins depending on their azimuth from 0 to 2π and were radially integrated. The resulting gray value maps were defined as the azimuthal maps $g_{\chi,k}$, where χ stands for the azimuthal range with $0 \leq \chi \leq 99$ and k for the scan number. Rather than evaluating the azimuthal map, the difference of the gray values compared to the average at a given scan was computed:

$$\delta_{\chi,k} = g_{\chi,k} - \frac{1}{100}\sum_{\chi} g_{\chi,k}, \tag{B.69}$$

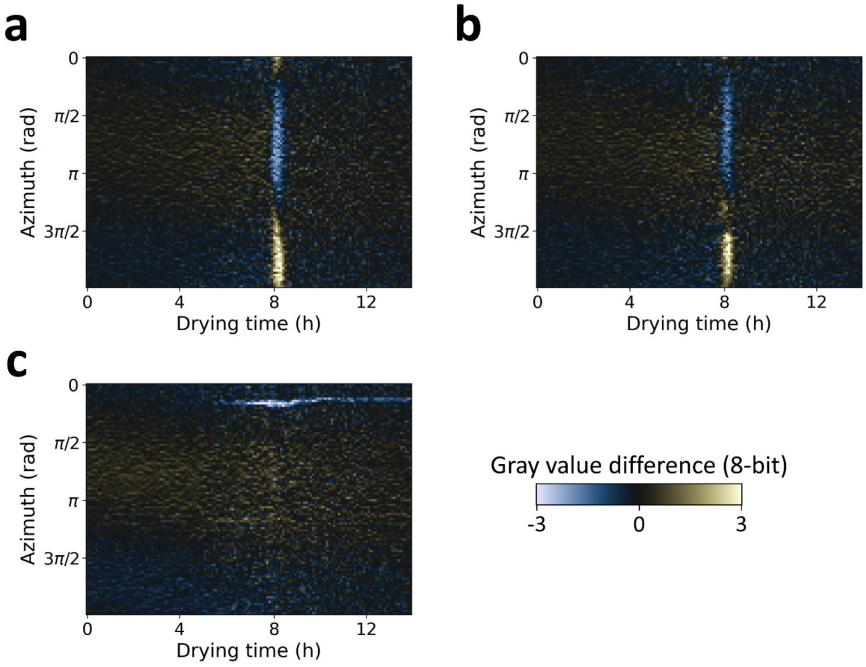

Figure B.25 $\delta_{\chi,k}$ maps (gray value difference) of sample M4 throughout drying. The maps in panels (**a**-**c**) refer to the radial integration performed at a relative height of (**a**) 0.25 (near the bottom), (**b**) 0.5 and (**c**) 0.75 (near the top) in the gels. Each panel share the same color scale that is indicated at the bottom right of the figure. Each map consists in 100x141 data points and the horizontal axis is linearly interpolated in time. Reprinted from ref.[107], CC BY 4.0 (https://creativecommons.org/licenses/by/4.0/).

where $\delta_{\chi,k}$ is also a map. Figure B.25 shows the final results at three relative heights: 0.25, 0.5 and 0.75.

Slight variations in the gray values (± 1 gray value) were consistently observed along the azimuth regardless of the drying stage and relative height. The gray values were higher than the average between $\pi/2$ and π and lower between $3\pi/2$ and 2π. Similar variations were observed in the other samples at different angles, and the minimum of the variations systematically occurred in the regions the closest to the wall of the drying chamber while the maximum occurred at the opposite location (Figure B.26). Those spatial variations were attributed to reconstruction artifacts but could not be clearly identified to a specific μCT artifact. A combination of undersampling and beam hardening artifacts may have created these variations. Nevertheless, the established dependency of the azimuthal variations with the proximity of the gel to the chamber suggested that they did not originate from heterogeneities in the composition of the gels. Stronger azimuthal variations appeared shortly after the maximum shrinkage in samples M2, M4 and M5 (Figure B.25a,b and Figure B.26). The time at which the variations increased corresponded to the time where the drying front reached the relative height of the gel at which the azimuthal maps were produced, which suggested that

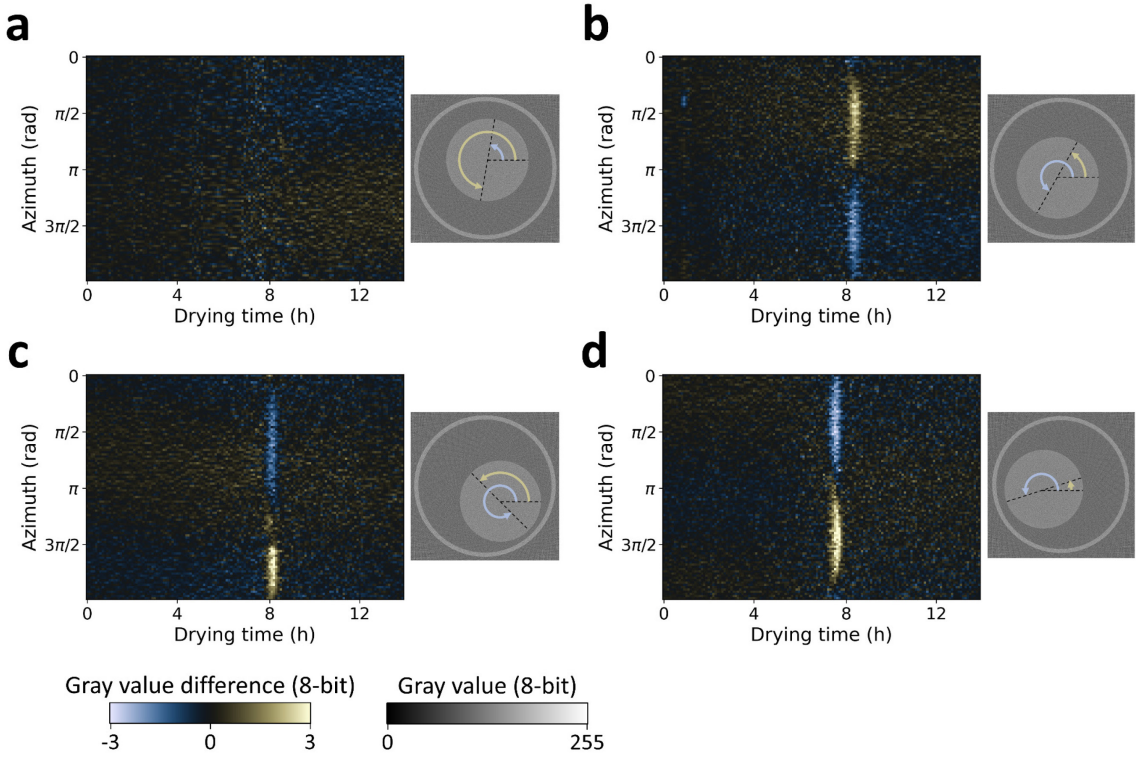

Figure B.26 $\delta_{\chi,k}$ maps (gray value difference) at a relative height of 0.5 throughout drying. The maps in panels (**a**), (**b**), (**c**) and (**d**) refer to the samples M1, M2, M4 and M5, respectively. Each panel contains an inset on the right of the map showing the masked slice at the relative height of 0.5 at the beginning of drying. The angle corresponding to the maximum (yellow) and minimum (blue) of $\delta_{\chi,k}$ are depicted on the masked slice with arrows. Each map consists in 100x141 data points and the horizontal axis was linearly interpolated in time. Reprinted from ref.[107], CC BY 4.0 (https://creativecommons.org/licenses/by/4.0/).

the spring-back effect was slightly heterogeneous along the azimuthal direction of the gels. This feature was not observed in sample M1, which may be related to the fact that M1 stayed relatively well centered during drying. Sample M5 moved during drying, resulting in a change of direction of the variations before and after maximum shrinkage (Figure B.26d).

B.6 Comparative analysis of the quantitative imaging approaches

This section reports a comparative analysis between the quantitative imaging results presented in chapter 5 (local analysis, composition maps) and in chapter 4 (global analysis, average composition) to evaluate the reliability of the local quantitative imaging approach. The gray value and volume fraction maps from the three reduction procedures were integrated along their corresponding spatial domains to calculate a spatially averaged quantity representative of the gel throughout drying. The integration of the volume fraction maps was performed over a

partial domain of the corresponding maps and was consistent with the global quantitative imaging approach. For a given map $M_{i,j,k}$, the integration was defined as:

$$\bar{M}_k = \frac{1}{N_{\Omega'_k}} \sum_{(i,j)\in\Omega'_k} M_{i,j,k} \cdot n_j, \tag{B.70}$$

where $\bar{M}_k$ is the average value of the map $M_{i,j,k}$ integrated over the partial domain Ω'_k, with $M_{i,j,k}$ a GHR, HEXHR, SKELHR or AIRHR map, $N_{\Omega'_k}$ is the number of pixels within Ω'_k and n_j is a radial weight factor depending on the radial distance given by the index j. As a reminder to the reader: the GHR maps were computed by azimuthal integration of the masked slices, thus the values in $g_{i,j,k}$ at a large index j were calculated from more pixels in the masked slices than the values at a small j. The radial weight factor n_j accounted for this and was defined as $n_j = \pi[(j+1)^2 - j^2]$. The averaging of the GH, HEXH, SKELH, AIRH, GR, HEXR, SKELR and AIRR maps was done similarly as in eq. (B.70). Depending on the nature of the map (i.e. on the reduction procedure used), the domains were further cropped to mitigate the contribution of the artifacts at the edges of the maps originating from improper segmentation. Those edges effects did not have a large impact on the integration of the gray value maps because the variations were in the order of 10-20 gray values out of 255 over a relatively small domain. However, upon calculating the volume fraction maps from the gray value maps, these variations were significantly amplified sometimes resulting in volume fraction at the edges of ± 500 %, which were not representative of the state of the gel.

Figure B.27 – Figure B.30 show the average quantities calculated in this study for samples M1, M2, M4 and M5, respectively (referred to as local maps) along with the results of the global quantitative imaging procedure. The gray values were in good agreement in all samples and all three data reduction procedures between the local and global approaches, besides a slight shift of the maximum gray value. The evolution of the hexane volume fraction was also consistent between both workflows, although some variations were observed at and shortly after the maximum shrinkage, especially in the HEXR maps (e.g. in Figure B.27d). The content of vapor/air showed comparable variations at the maximum shrinkage. Overall, the average skeleton volume fraction profiles from the local approach were systematically higher than the one calculated in the global approach, while the average vapor/air profiles from the local approach were lower than in the global one. It was not possible to link the differences between the two workflows to a specific aspect of the two quantitative imaging approaches, as they were fundamentally different. Whereas the global quantitative imaging approach consisted mainly of two steps: integration of the gray values and calculations, the local quantitative

imaging approach in this work consisted in: partial integration of the gray values (appendix B.1), bilinear interpolation and rescaling (appendix B.3), calculations (appendix B.2) and partial integration for the comparative analysis (appendix B.6). It could notably not be ruled out that the averaging procedure described here was responsible for the observed variations. Nonetheless, the evolution of the average local volume fraction throughout drying appeared consistent with our previous study.

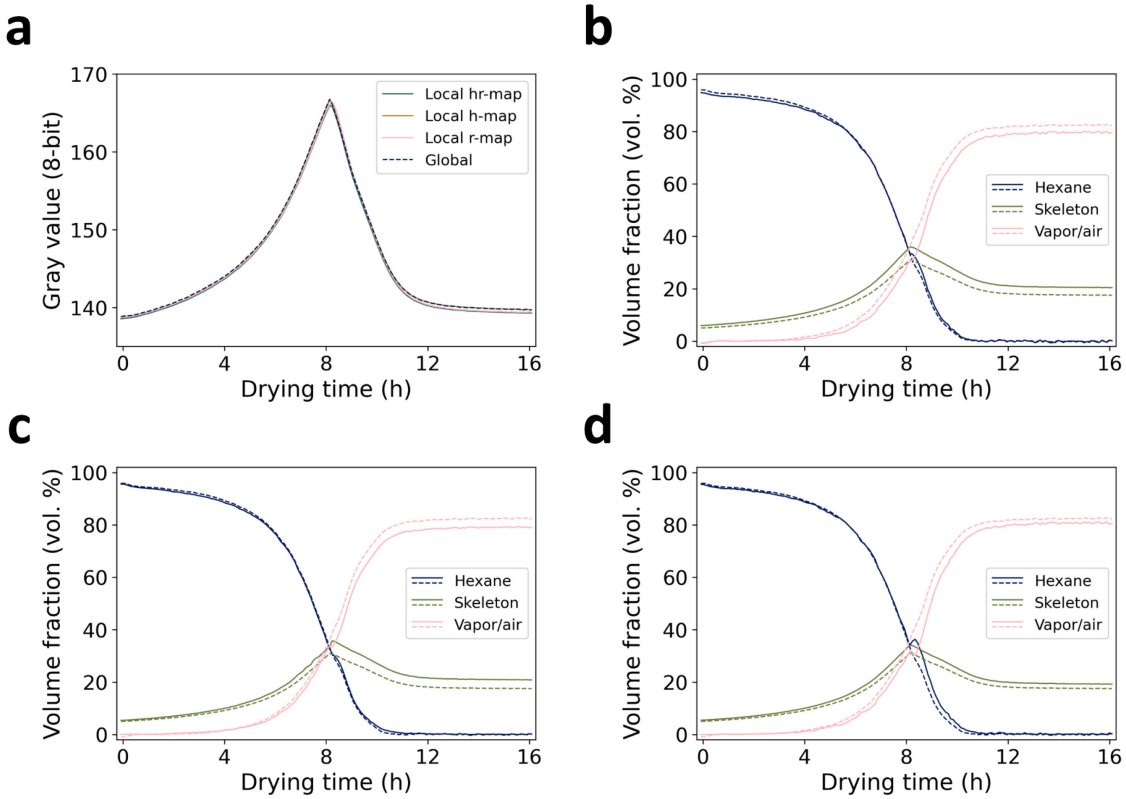

Figure B.27 Comparison between the local and global quantitative imaging approaches in sample M1. (**a**) Global gray values and averaged local gray value in the three reduction procedures. (**b**-**d**) Global volume fraction (dashed lines) and averaged local volume fraction (full lines) of the three phases for the azimuthal integration (**b**), slice integration (**c**) and azimuthal + vertical integration (**d**) reduction procedures. Reprinted from ref.[107], CC BY 4.0 (https://creativecommons.org/licenses/by/4.0/).

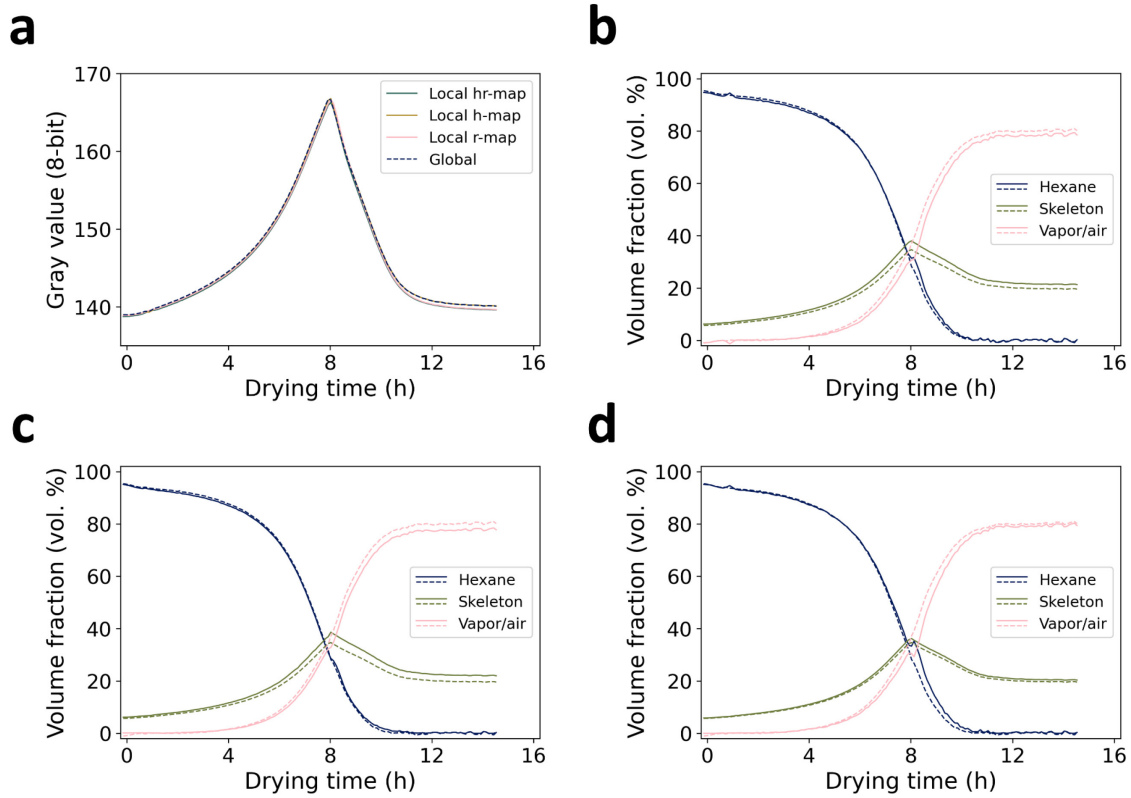

Figure B.28 Comparison between the local and global quantitative imaging approaches in sample M2. (**a**) Global gray values and averaged local gray value in the three reduction procedures. (**b**-**d**) Global volume fraction (dashed lines) and averaged local volume fraction (full lines) of the three phases for the azimuthal integration (**b**), slice integration (**c**) and azimuthal + vertical integration (**d**) reduction procedures. Reprinted from ref.[107], CC BY 4.0 (https://creativecommons.org/licenses/by/4.0/).

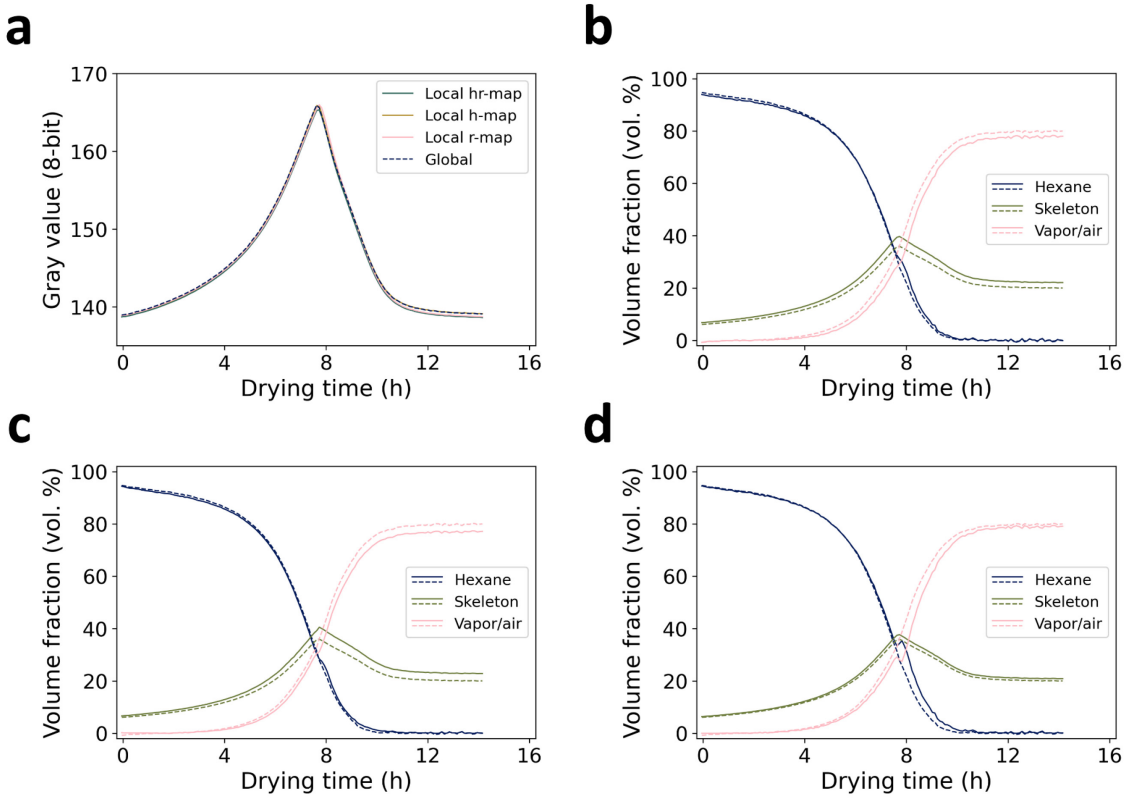

Figure B.29 Comparison between the local and global quantitative imaging approaches in sample M4. (**a**) Global gray values and averaged local gray value in the three reduction procedures. (**b**-**d**) Global volume fraction (dashed lines) and averaged local volume fraction (full lines) of the three phases for the azimuthal integration (**b**), slice integration (**c**) and azimuthal + vertical integration (**d**) reduction procedures. Reprinted from ref.[107], CC BY 4.0 (https://creativecommons.org/licenses/by/4.0/).

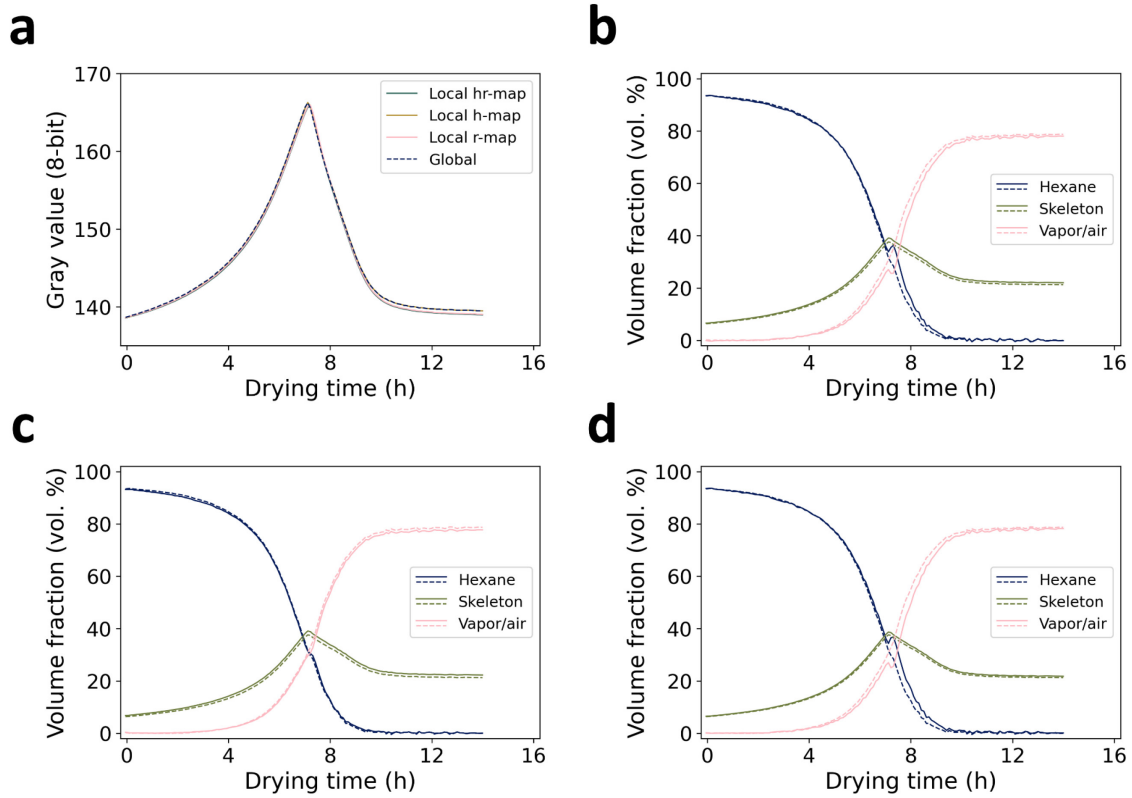

Figure B.30 Comparison between the local and global quantitative imaging approaches in sample M5. (**a**) Global gray values and averaged local gray value in the three reduction procedures. (**b**-**d**) Global volume fraction (dashed lines) and averaged local volume fraction (full lines) of the three phases for the azimuthal integration (**b**), slice integration (**c**) and azimuthal + vertical integration (**d**) reduction procedures. Reprinted from ref.[107], CC BY 4.0 (https://creativecommons.org/licenses/by/4.0/).

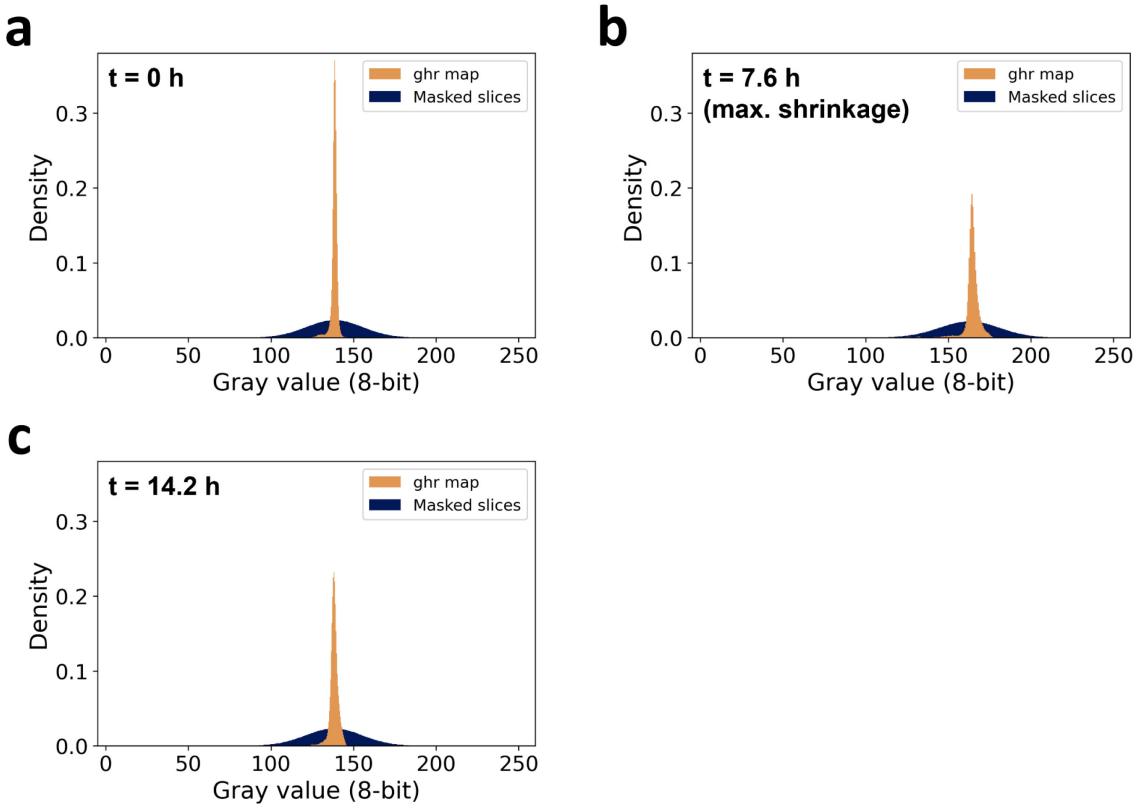

Figure B.31 Gray value density histograms of a GHR map (orange) and of all the masked slices (blue) at three selected drying stages: (**a**) t = 0 h, (**b**) t = 7.6 h (maximum shrinkage) and (**c**) t = 14.2 h. Upon azimuthal integration, the distribution of the gray values became narrower. Reprinted from ref.[107], CC BY 4.0 (https://creativecommons.org/licenses/by/4.0/).

Appendix C. Plastic deformation and heat-enabled structural recovery

C.1 μCT quantitative imaging

The average phase composition of the sample HT1 throughout drying was computed using a similar quantitative imaging approach as in chapter 4. Selected projections of HT1 during drying are shown in Figure C.1. The reconstructed μCT volumes were segmented in the software Dragonfly[130] using an automated script written in Python. The global gray values of the sample in each μCT scan were computed after correction for the anode heel effect, and the volume of the gel was corrected taking into account the estimated error on the automated segmentation algorithm.

In this study, the hexane RAC was computed from the 10 scans done on a reference hexane sample, resulting in $\mu_{\text{hex}} = 0.1543$, which was very similar to the value of 0.1548 found in chapter 4 by averaging 140 scans with the same acquisition and reconstruction parameters. The calculations were performed with threshold scan numbers related to the assumption of zero vapor/air content at the start of drying (within scan numbers k_1 and k_2) and the assumption of zero hexane content at the end of drying (from scan number k_d). The threshold scan numbers were determined by visual inspection of the quantities $(\bar{\mu}_k - \mu_{\text{hex}})V_k$ and $\bar{\mu}_k V_k$, which gave: $k_1 = 0, k_2 = 27$ and $k_d = 130$, corresponding to a drying time of 0, 2.7 and 13.1 h, respectively. The standard deviation on the gray values was calculated from the 10 scans performed on the hexane reference sample and was 0.015 (in 8-bit). All the error bands were computed based on two standard deviations (95$^{\text{th}}$ percentile) using the same approach as previously reported. The last μCT scan of the sample after annealing was reconstructed with the same parameters as the in-operando series of scans, and the gel volume was computed by manual segmentation of the 3D reconstructed volume. Manual segmentation was required for the annealed sample, as the automated script resulted in an inaccurate segmentation. The reason for this was low contrast between the sample and the background (Figure C.1d). The vapor/air volume in the gel after annealing was then calculated by assuming a hexane content of zero and that the skeleton volume was conserved upon annealing. It is worth noting that the drying model did not account for the weight difference attributed to residual hexane in sample HT1 as it was negligible compared to the initial hexane volume in the alcogel. At the start of drying, the hexane volume was 664.4 ± 10.6 mm^3, corresponding to 437.8 ± 7.0 mg of

hexane (ρ_{hex} = 0.659 g cm^{-3} at 20 °C)[226]. The residual hexane amount was measured at 0.4 ± 0.2 mg, which represented less than 0.1 wt % of the initial weight of hexane in the alcogel, confirming that it could be neglected.

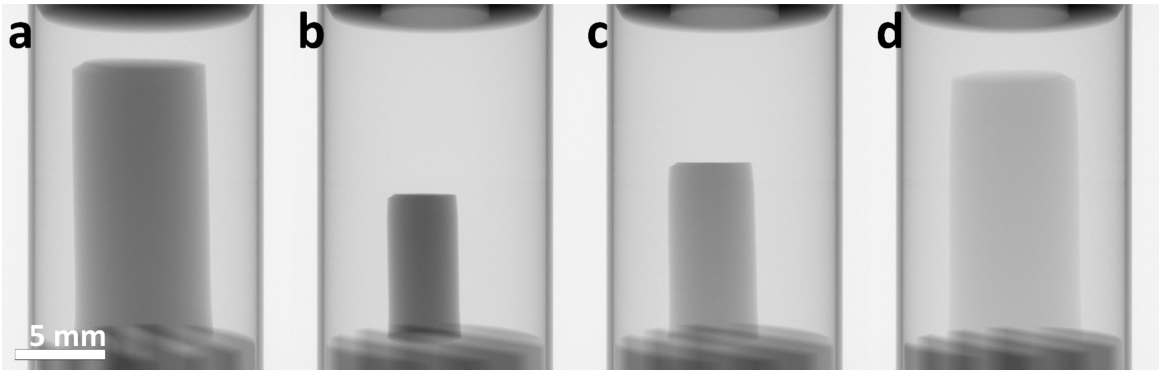

Figure C.1 µCT projections of HT1 at the start of drying (**a**), at the maximum shrinkage (**b**), at the end of drying (**c**) and after annealing (**d**).

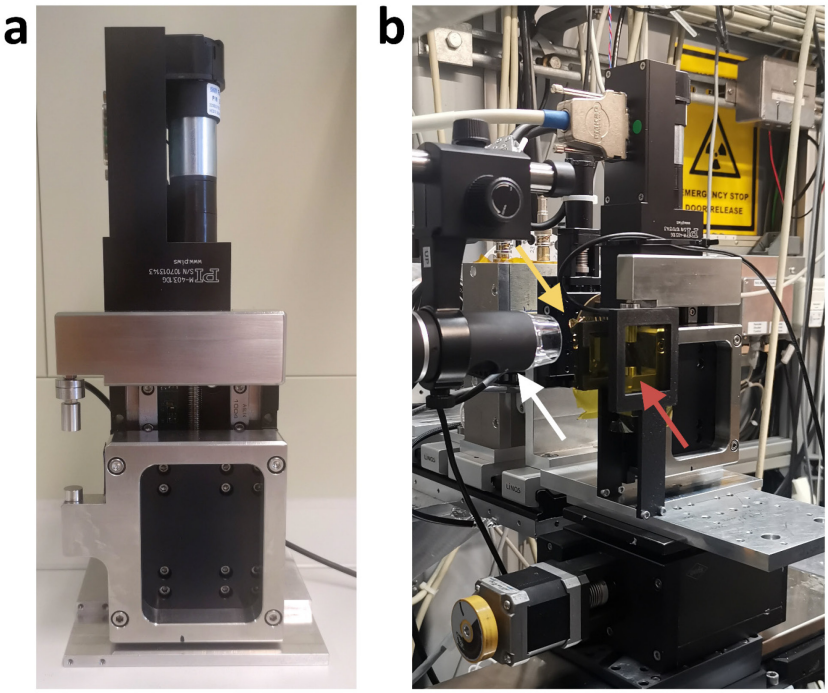

Figure C.2 (**a**) Micromechanical tester used for the uniaxial compression experiments. (**b**) Setup at the µSpot beamline: the digital camera (white arrow) is placed perpendicular to the X-ray beam (yellow arrow) directed at the sample placed on the micromechanical tester and protected by two kapton windows (red arrow).

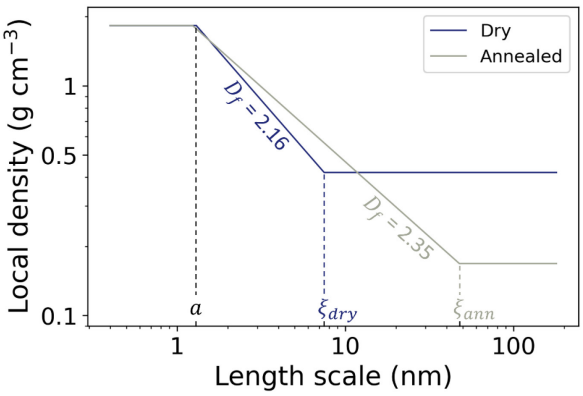

Figure C.3 Log-log plot of the local density of the fractal clusters versus the length scale for sample nHT3 in the dry and annealed states. The figure is inspired from ref.[146] The fractal dimension is depicted in the linear decay region, which correspond to the fractal range. The cut-off distances correspond to the particle radius (a) and the mean cluster size of the dry (ξ_{dry}) and annealed gel (ξ_{ann}).

C.2 Fracture strain

This section presents the fracture strain upon uniaxial compression of a dry and an annealed gel. The main motivation to measure the fracture strain was to derive values of maximum strains that would ensure the mechanical stability of the aerogels over a complete loading-unloading cycle. The compression tests conditions were identical to those reported in the main text. Pictures were recorded every 10 sec for the dry gel and every 2 sec for the annealed gel. The stress-strain curves are shown in Figure C.4a. The true stress and Poisson's ratio were not calculated in those experiments. The dry gel was synthesized from another batch than the other samples presented in this study but with the same synthesis route. The annealed gel had a slight cross-section reduction at the bottom (Figure C.4b). The fracture strain of the dry gel was determined at 36.1 % and that for the annealed gel was at 47.7 %. The mechanical failure was rather similar between both gels. Although the time resolution of the digital pictures was not high enough to capture the rupture mechanism, the development of cracks was observed in the dry gel shortly before fracture (Figure C.4b). This suggests that the dry gel failed due to the propagation of cracks, upon which the sample burst out of the stage. While no cracks were observed in the annealed gel, the mechanical failure also resulted in the ejection of a large piece of the sample out of the stage. This fracture by cracking was consistent with the brittle nature of silica aerogels.

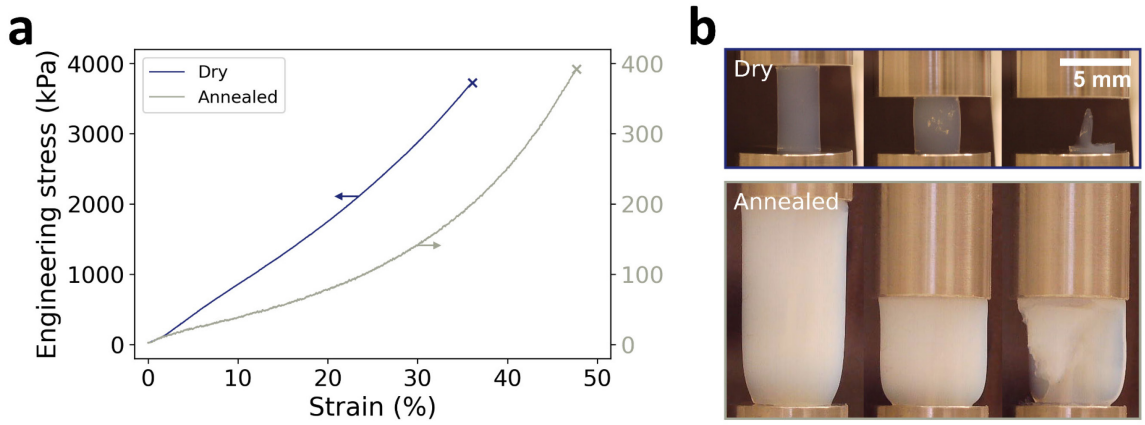

Figure C.4 (**a**) Engineering stress versus absolute strain of a dry and annealed sample compressed until fracture (x symbol). (**b**) Digital pictures of the dry and annealed samples at 0 % strain (left), just before fracture (middle) and after fracture (right). The length scale of all pictures is depicted at the top right corner of panel (**b**).

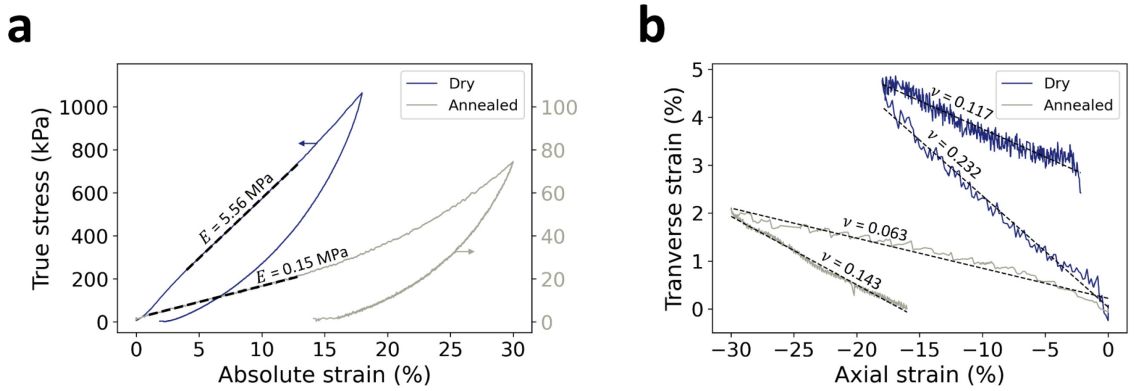

Figure C.5 (**a**) True stress versus absolute strain for samples nHT2 and HT2 including a relaxation of about 30 min for nHT2 and 20 min for HT2. The maximum strain is 18 and 30 % for nHT2 and HT2, respectively. The Young's modulus E is depicted on the corresponding profiles. (**b**) Transverse versus axial strain for nHT2 and HT2 during loading (starts at the point (0,0)) and unloading. The fit of the loading and unloading curves is shown in black dashed lines and the Poisson's ratio ν is depicted on top of the fitting curves. The error on Poisson's ratio is maximum 0.001.

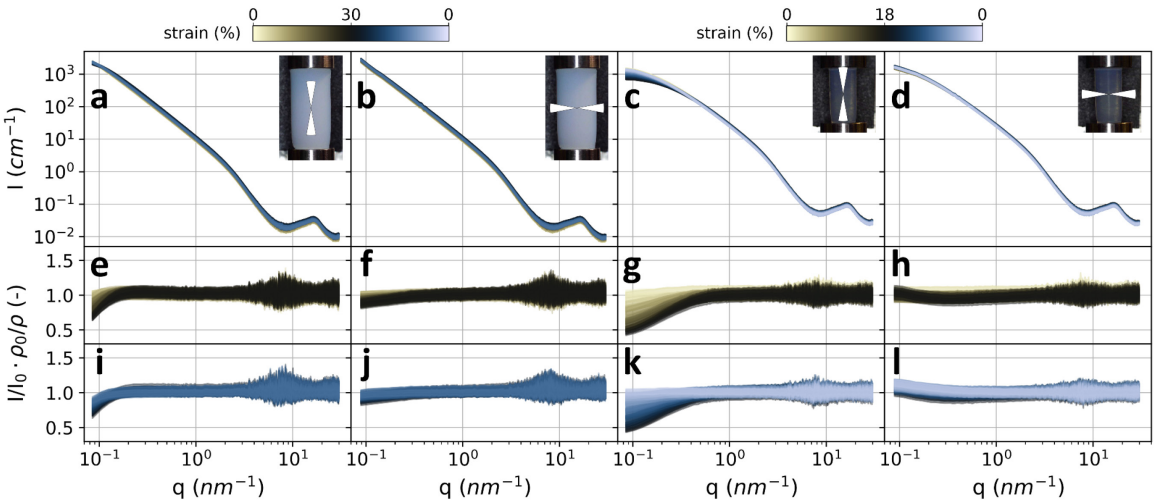

Figure C.6 Scattering profiles of HT2 in the axial (**a**) and transverse (**b**) direction to the load and scattering profiles of nHT2 in the axial (**c**) and transverse (**d**) direction. Panels (**e**-**j**) display the ratio of the intensity at a given strain $I(q)$ relative to the native intensity before compression $I_0(q)$, and normalized by the apparent density of the sample by multiplying the scalar ρ_0/ρ. The intensity ratio plots are split into the loading (**e**-**h**) and unloading (**i**-**l**) parts of the mechanical test corresponding to the HT2 and nHT2 samples in both axial and transverse directions. The strain value is indicated with a diverging colormap shown on top of panels (**a**,**b**) for HT2 data, and on top of panels (**c**,**d**) for nHT2 data. The insets in panels (**a**-**d**) are images of the sample depicting the integration cake used to reduce the scattering data (axial or transverse directions).

C.3 Correlation between scattering intensity and bulk density

To assess the impact of the increased bulk density of the samples during compression on the azimuthally integrated scattering profiles, the latter were fitted in the wide-angle region to evaluate their overall evolution. The scattering signal in the wide-angle region was attributed to the molecular structure of the silica skeleton.[18,145] The peak at ca 20 nm^{-1} was fitted on the first data frame of the scattering profiles (unloaded sample) using a sum of Pseudo-Voigt functions and a linear background and omitting the contributions beyond Porod's regime using a similar approach as in chapter 5. The resulting function was labelled $I_0^*(q)$. The data frames at a given strain ε were then expressed as a scalar $\alpha(\varepsilon)$ multiplying $I_0^*(q)$, and the scalar was computed by minimizing the residue for each strain value:

$$\delta(\varepsilon) = \int_q [I(q,\varepsilon) - \alpha(\varepsilon) \cdot I_0^*(q)]^2 \, dq. \tag{0.1}$$

The scalar α was referred to as the fit ratio. The evolution of $\alpha(\varepsilon)$ along with the evolution of the bulk density during uniaxial compression is shown in Figure C.7 for HT1, nHT1, HT2 and nHT2.

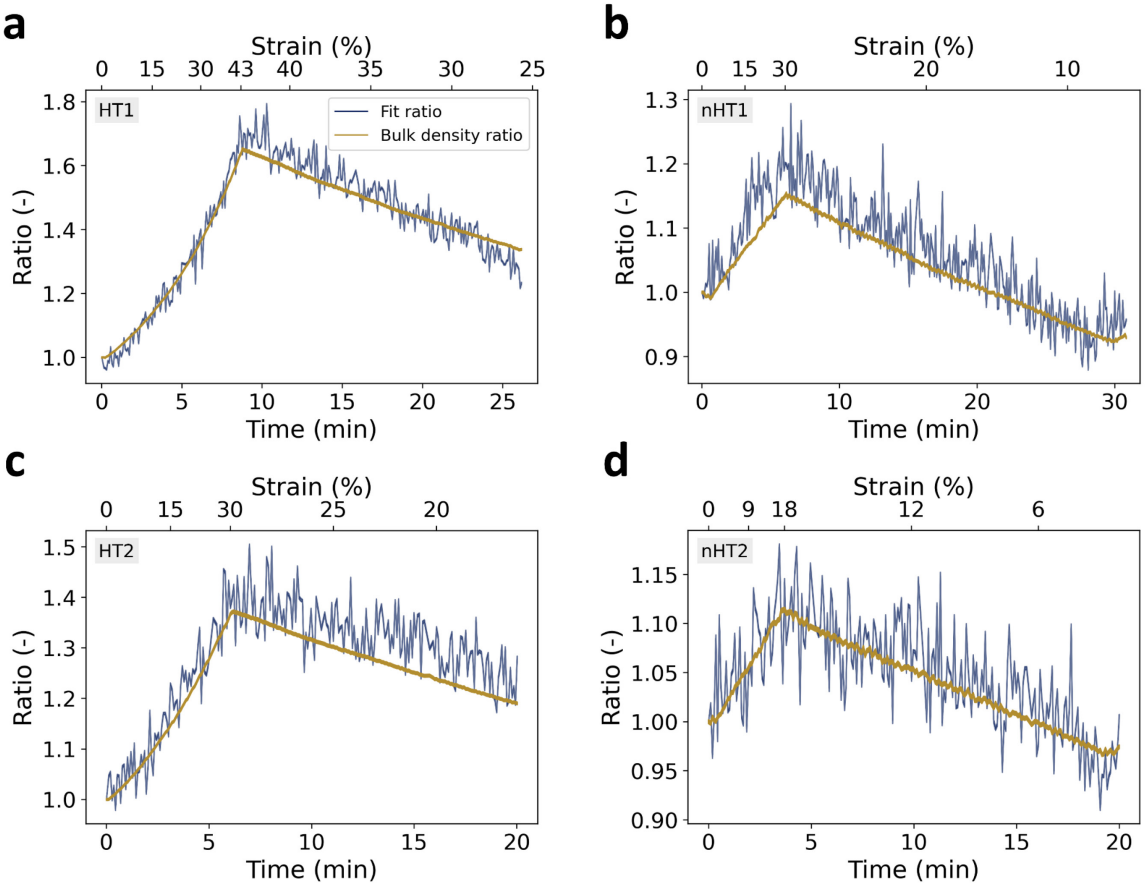

Figure C.7 Fit ratio α (blue) and ratio of the bulk density (orange) during uniaxial compression of samples HT1 (**a**), nHT1 (**b**), HT2 (**c**) and nHT2 (**d**).

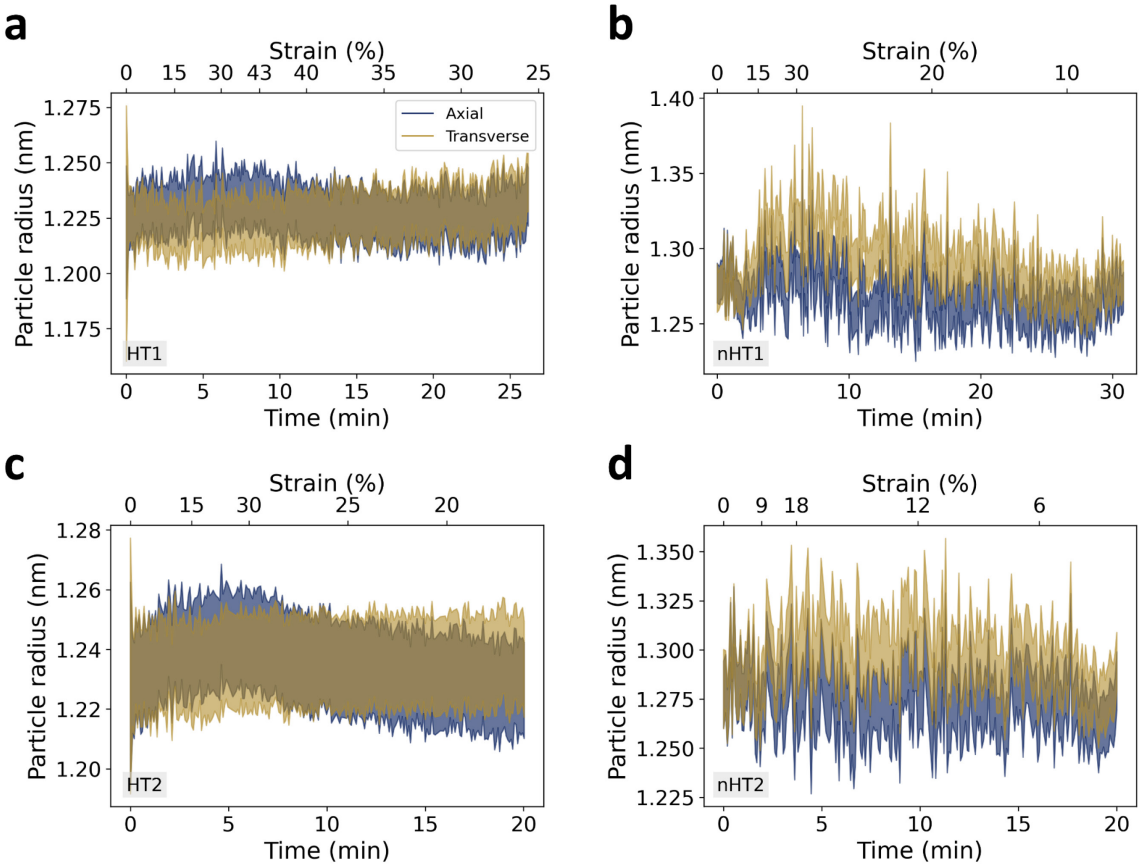

Figure C.8 Radius of the silica particles during uniaxial compression derived from the mean chord length of the skeleton for samples HT1 (**a**), nHT1 (**b**), HT2 (**c**) and nHT2 (**d**).

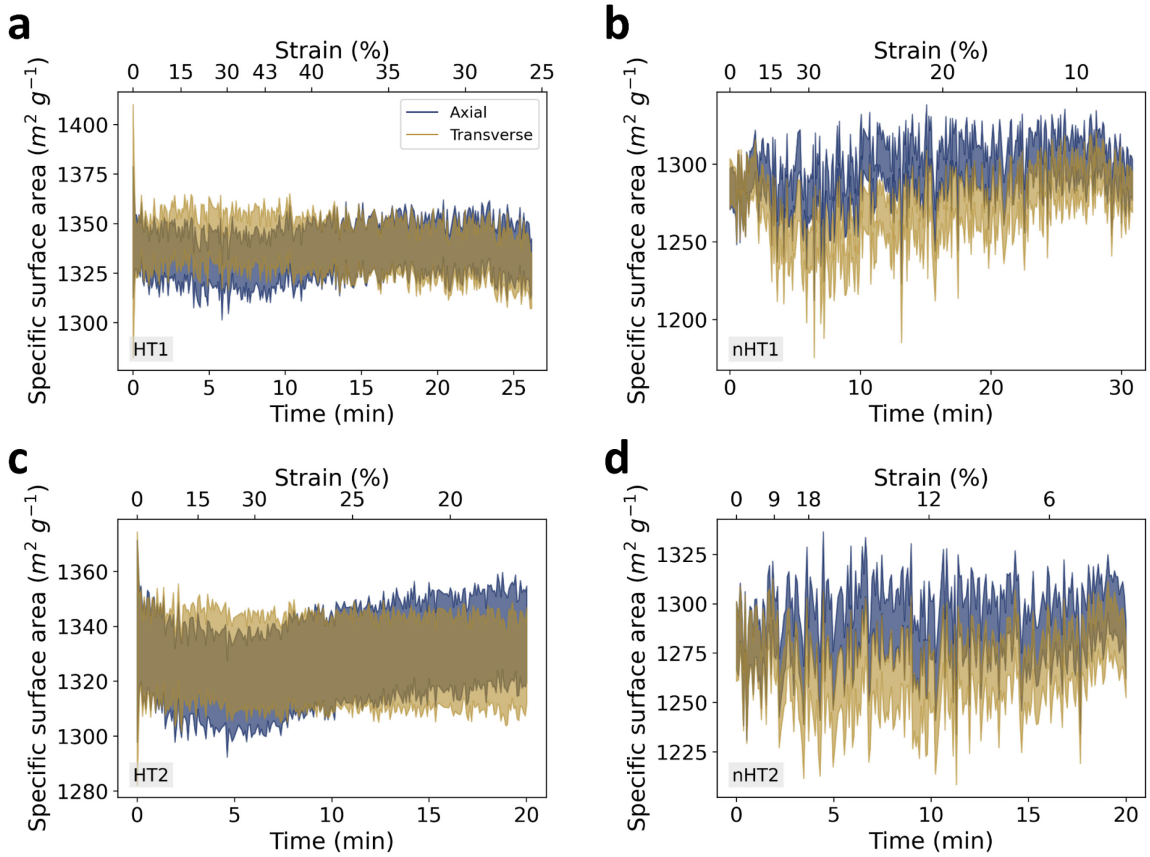

Figure C.9 Specific surface area (SSA) during uniaxial compression of samples HT1 (**a**), nHT1 (**b**), HT2 (**c**) and nHT2 (**d**).

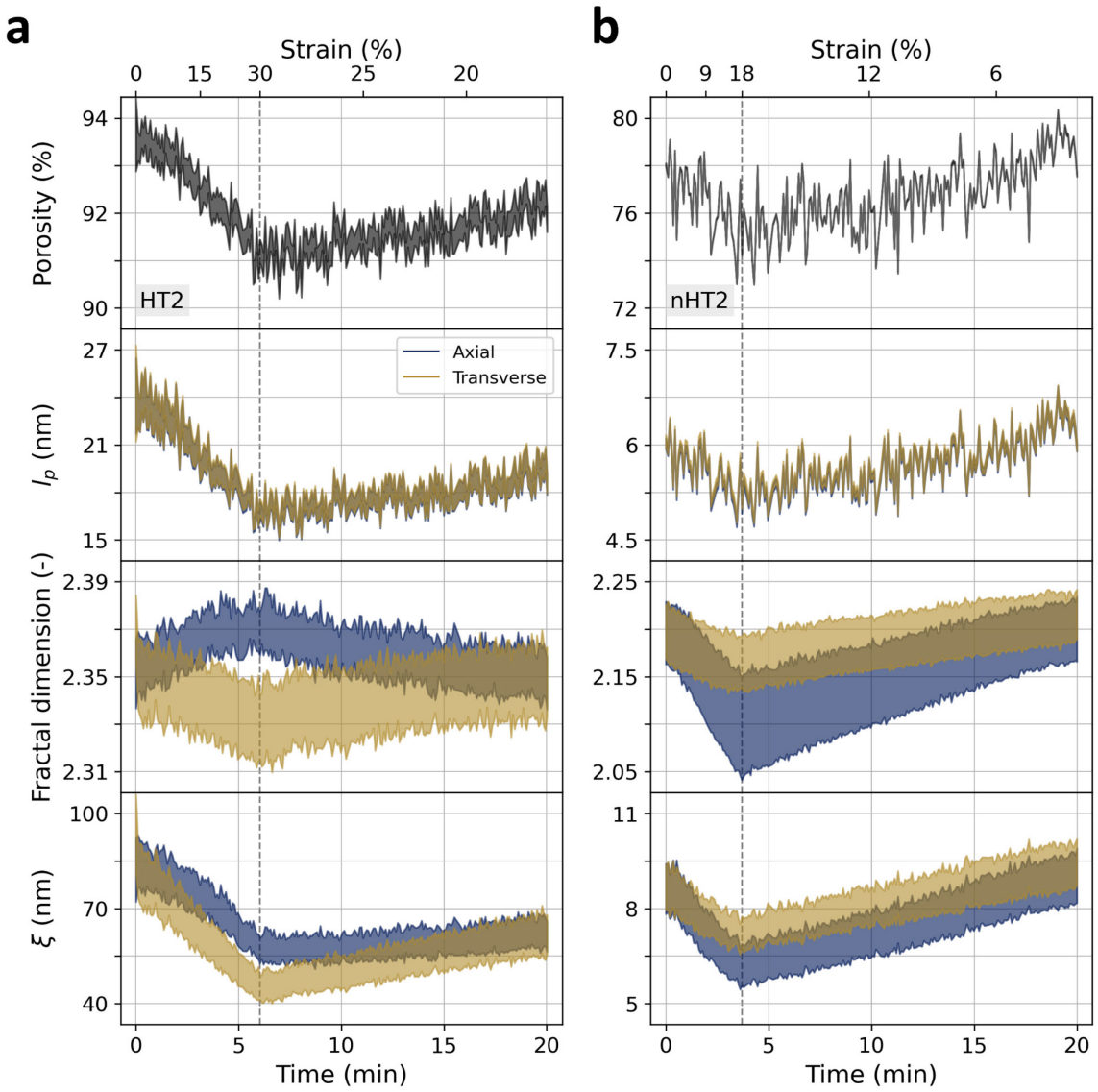

Figure C.10 Porosity, mean free path within the pores (l_p), fractal dimension and mean length of the fractal cluster (ξ) of samples (**a**) HT2 and (**b**) nHT2 during uniaxial compression. Time is represented on the bottom x-axis and the corresponding strain is depicted on the top x-axis with a non-linear scale. All data are shown in the axial and transverse directions except for the porosity. The error of nHT2 porosity is lower than 0.07 %. The data points corresponding to the relaxation are not shown for clarity.

C.4 Sensitivity analysis on determination of the fractal slope

The q-range used to fit the fractal region of the scattering patterns was varied within 0.1 to 1.77 nm^{-1} using a constant range in the log space corresponding to $q_2 = 2.5q_1$, where q_2 and q_1 are respectively the right and left limits for the fitting range. The results are shown in Figure C.11. The fitting region within 0.4 – 1 nm^{-1} resulted in the most stable fractal dimensions in the axial and transverse directions and it was in agreement with visual estimations of the fractal

range in the scattering profiles. Therefore, the fractal dimension was calculated within 0.4 – 1 nm^{-1}.

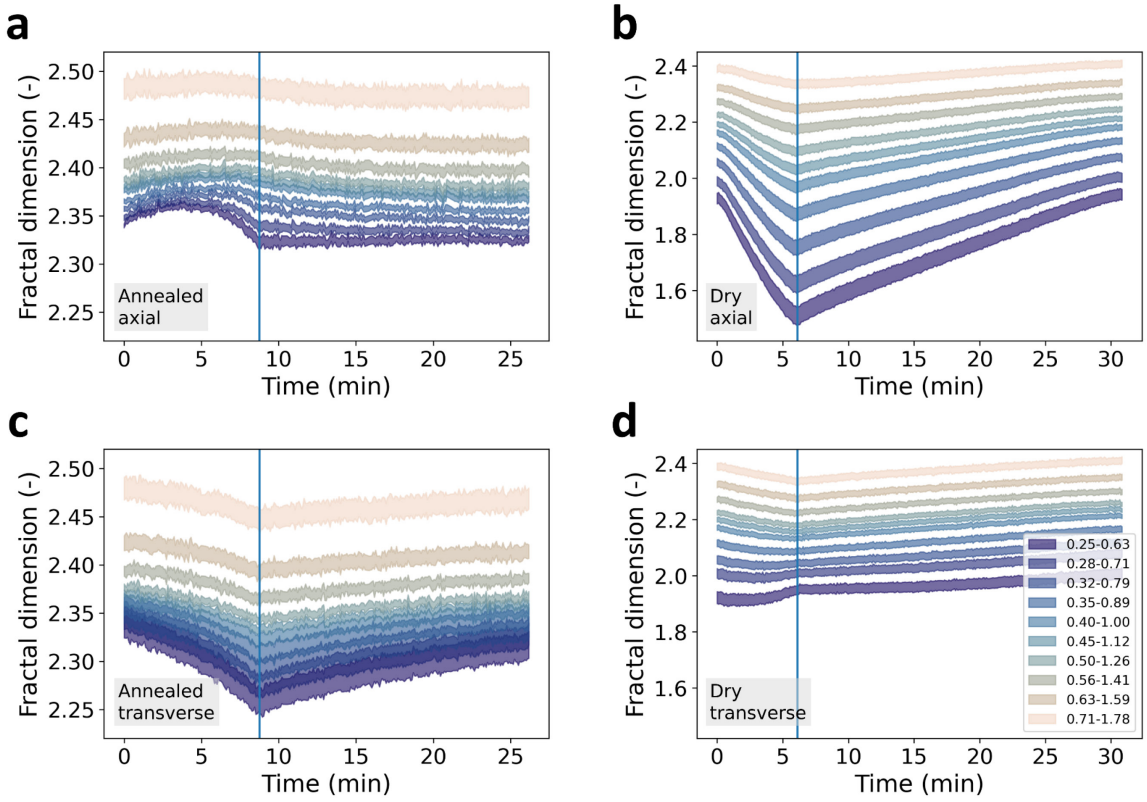

Figure C.11 Fractal slope determined from the mechanical tests done on HT1 (**a**,**c**) and nHT1 (**b**,**d**) along the axial direction (**a**,**b**) and the transverse direction (**c**,**d**). The q-range used is depicted in the legend of panel (**d**). The range used in the publication was 0.4 – 1.0 nm^{-1}.

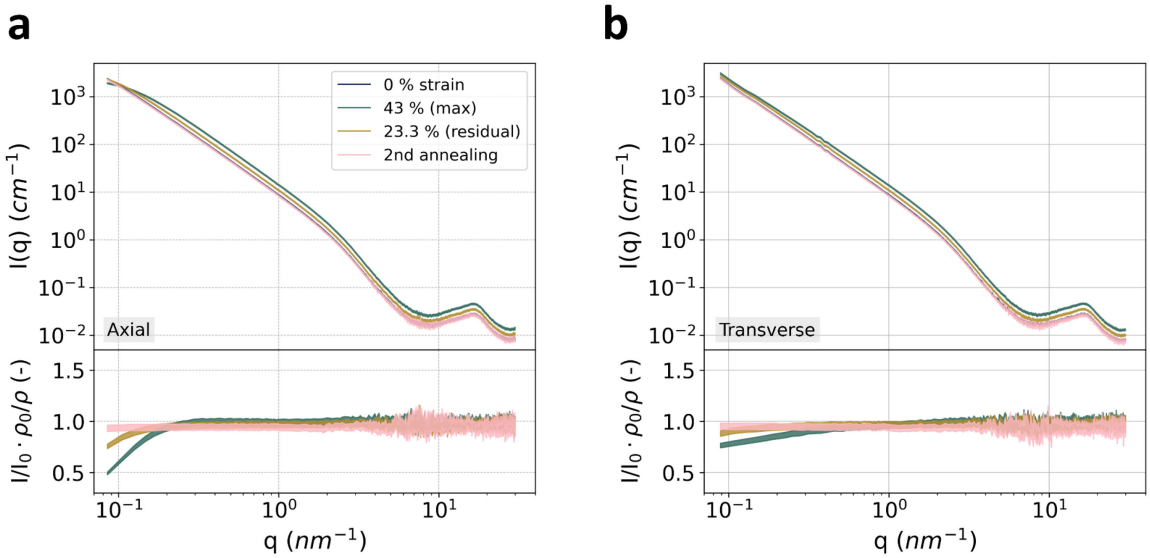

Figure C.12 Scattering patterns and relative intensity normalized by the apparent density of sample HT1 in the axial (**a**) and transverse (**b**) directions to the load. The profiles correspond to different stages of the gel: unloaded (0 % strain), maximum strain (43 %), after unloading (23.3 %) and after a 2nd annealing process.

References

1 Union, E. *EU Energy in Figures – Statistical Pocketbook 2023*; Publications Office of the European Union, 2023.

2 Eurostat. *Disaggregated final energy consumption in households - quantities*. accessed 15.03.2024. https://doi.org/10.2908/NRG_D_HHQ.

3 Ashby, M. F.; Shercliff, H.; Cebon, D. Chapitre 12. Agitation Des Atomes: Matériaux et Chaleur. In *Matériaux - Ingénierie, Science, Procédé et Conception*; Presses polytechniques et universitaires romandes: Lausanne, 2013; 261–292.

4 Koebel, M.; Rigacci, A.; Achard, P. Aerogel-Based Thermal Superinsulation: An Overview. *J. Sol-Gel Sci. Technol.* **2012**, *63* (3), 315–339.

5 Malfait, W. J.; Ebert, H.-P.; Brunner, S.; Wernery, J.; Galmarini, S.; Zhao, S.; Reichenauer, G. The Poor Reliability of Thermal Conductivity Data in the Aerogel Literature: A Call to Action! *J. Sol-Gel Sci. Technol.* **2024**, *109* (2), 569–579.

6 Kadoya, K.; Matsunaga, N.; Nagashima, A. Viscosity and Thermal Conductivity of Dry Air in the Gaseous Phase. *J. Phys. Chem. Ref. Data* **1985**, *14* (4), 947–970.

7 Li, C.; Chen, Z.; Dong, W.; Lin, L.; Zhu, X.; Liu, Q.; Zhang, Y.; Zhai, N.; Zhou, Z.; Wang, Y.; Chen, B.; Ji, Y.; Chen, X.; Xu, X.; Yang, Y.; Zhang, H. A Review of Silicon-Based Aerogel Thermal Insulation Materials: Performance Optimization through Composition and Microstructure. *J. Non. Cryst. Solids* **2021**, *553*, 120517.

8 Smirnova, I.; Gurikov, P. Aerogel Production: Current Status, Research Directions, and Future Opportunities. *J. Supercrit. Fluids* **2018**, *134*, 228–233.

9 Berardi, U. The Development of a Monolithic Aerogel Glazed Window for an Energy Retrofitting Project. *Appl. Energy* **2015**, *154*, 603–615.

10 Carroll, M. K.; Anderson, A. M.; Mangu, S. T.; Hajjaj, Z.; Capron, M. Aesthetic Aerogel Window Design for Sustainable Buildings. *Sustainability* **2022**, *14* (5), 2887.

11 Ganobjak, M.; Malfait, W. J.; Just, J.; Käppeli, M.; Mancebo, F.; Brunner, S.; Wernery, J. Get the Light & Keep the Warmth - A Highly Insulating, Translucent Aerogel Glass Brick for Building Envelopes. *J. Build. Eng.* **2023**, *64*, 105600.

12 Wernery, J.; Mancebo, F.; Malfait, W. J.; O'Connor, M.; Jelle, B. P. The Economics of Thermal Superinsulation in Buildings. *Energy Build.* **2021**, *253*, 111506.

13 Vareda, J. P.; Lamy-Mendes, A.; Durães, L. A Reconsideration on the Definition of the Term Aerogel Based on Current Drying Trends. *Microporous Mesoporous Mater.* **2018**, *258*,

211–216.

14 Kohns, R.; Torres-Rodríguez, J.; Euchler, D.; Seyffertitz, M.; Paris, O.; Reichenauer, G.; Enke, D.; Huesing, N. Drying of Hierarchically Organized Porous Silica Monoliths–Comparison of Evaporative and Supercritical Drying. *Gels* **2023**, *9* (1), 71.

15 Smith, D. M.; Scherer, G. W.; Anderson, J. M. Shrinkage during Drying of Silica Gel. *J. Non. Cryst. Solids* **1995**, *188* (3), 191–206.

16 Prakash, S. S.; Sankaran, C. J.; Hurd, A. J.; Rao, S. M. Silica Aerogel Films Prepared at Ambient Pressure by Using Surface Derivatization to Induce Reversible Drying Shrinkage. *Nature* **1995**, *374* (6521), 439–443.

17 Zemke, F. Insights into the Springback Effect in Ambient-Pressure-Dried Silica Aerogels by in-Situ Synchrotron X-Ray Scattering, Technische Universität Berlin, 2024. https://doi.org/10.14279/depositonce-19594.

18 Zemke, F.; Scoppola, E.; Simon, U.; Bekheet, M. F.; Wagermaier, W.; Gurlo, A. Springback Effect and Structural Features during the Drying of Silica Aerogels Tracked by In-Situ Synchrotron X-Ray Scattering. *Sci. Rep.* **2022**, *12* (1), 7537.

19 Zemke, F.; Gonthier, J.; Scoppola, E.; Simon, U.; Bekheet, M. F.; Wagermaier, W.; Gurlo, A. Origin of the Springback Effect in Ambient-Pressure-Dried Silica Aerogels: The Effect of Surface Silylation. *Gels* **2023**, *9* (2), 160.

20 Zemke, F.; Scoppola, E.; Simon, U.; Bekheet, M. F.; Wagermaier, W.; Gurlo, A. Springback Effect of Ambient-Pressure-Dried Silica Aerogels: Nanoscopic Effects of Silylation Revealed by in Situ Synchrotron X-Ray Scattering. *Nanoscale Adv.* **2023**, *6* (1), 111–125.

21 Scherer, G. W.; Smith, D. M. Cavitation during Drying of a Gel. *J. Non. Cryst. Solids* **1995**, *189* (3), 197–211.

22 Crameri, F. Scientific Colour Maps. Zenodo October 2023. https://doi.org/10.5281/zenodo.8409685.

23 Crameri, F.; Shephard, G. E.; Heron, P. J. The Misuse of Colour in Science Communication. *Nat. Commun.* **2020**, *11* (1), 5444.

24 Liebner, F.; Aigner, N.; Schimper, C.; Potthast, A.; Rosenau, T. Bacterial Cellulose Aerogels: From Lightweight Dietary Food to Functional Materials. *ACS Symp. Ser.* **2012**, *1107*, 57–74.

25 Hüsing, N.; Schubert, U. Aerogels - Airy Materials: Chemistry, Structure, and Properties. *Angew. Chemie - Int. Ed.* **1998**, *37* (1–2), 22–45.

26 Kistler, S. S. Coherent Expanded Aerogels. *J. Phys. Chem.* **1932**, *36* (1), 52–64.

27 Yang, H.; Zhu, W.; Sun, S.; Guo, X. Preparation of Monolithic Titania Aerogels with High Surface Area by a Sol–Gel Process Combined Surface Modification. *RSC Adv.* **2014**, *4* (62), 32934–32940.

28 Tokudome, Y.; Nakanishi, K.; Kanamori, K.; Fujita, K.; Akamatsu, H.; Hanada, T. Structural Characterization of Hierarchically Porous Alumina Aerogel and Xerogel Monoliths. *J. Colloid Interface Sci.* **2009**, *338* (2), 506–513.

29 Walker, R. C.; Potochniak, A. E.; Hyer, A. P.; Ferri, J. K. Zirconia Aerogels for Thermal Management: Review of Synthesis, Processing, and Properties Information Architecture. *Adv. Colloid Interface Sci.* **2021**, *295*, 102464.

30 Sen, S.; Singh, A.; Bera, C.; Roy, S.; Kailasam, K. Recent Developments in Biomass Derived Cellulose Aerogel Materials for Thermal Insulation Application: A Review. *Cellulose* **2022**, *29* (9), 4805–4833.

31 Yanagi, R.; Takemoto, R.; Ono, K.; Ueno, T. Light-Induced Levitation of Ultralight Carbon Aerogels via Temperature Control. *Sci. Rep.* **2021**, *11* (1), 12413.

32 Wen, M.; Ren, B.; Ye, X.; He, J.; Jiang, H.; Xiong, C. Hierarchical Loading of CuO on SiO2 Aerogel@high Crystalline TiO2 Nanofibers for Efficiently Photocatalytic Reduction of CO2 without Sacrificial Agent. *Nano Res.* **2022**, *15* (5), 3872–3879.

33 Maleki, H.; Huesing, N. Silica-Silk Fibroin Hybrid (Bio)Aerogels: Two-Step versus One-Step Hybridization. *J. Sol-Gel Sci. Technol.* **2021**, *98* (2), 430–438.

34 Vakifahmetoglu, C.; Semerci, T.; Gurlo, A.; Soraru, G. D. Polymer Derived Ceramic Aerogels. *Curr. Opin. Solid State Mater. Sci.* **2021**, *25* (4), 100936.

35 Mohammadi, A.; Moghaddas, J. Mesoporous Starch Aerogels Production as Drug Delivery Matrices: Synthesis Optimization, Ibuprofen Loading, and Release Property. *Turkish J. Chem.* **2020**, *44* (3), 614–633.

36 Zhang, H.; Xu, G.; Wang, F.; Su, S.; Wang, J.; Shen, H. A Theoretical and Experimental Study of Oil Wicking Behavior via "Green" Superabsorbent. *Cellulose* **2021**, *28* (16), 10517–10529.

37 James, A.; Yadav, D. Bioaerogels, the Emerging Technology for Wastewater Treatment: A Comprehensive Review on Synthesis, Properties and Applications. *Environ. Res.* **2022**, *212*, 113222.

38 MacMinn, C. W.; Dufresne, E. R.; Wettlaufer, J. S. Large Deformations of a Soft Porous Material. *Phys. Rev. Appl.* **2016**, *5* (4), 44020.

39 Rennhofer, H.; Plappert, S. F.; Lichtenegger, H. C.; Bernstorff, S.; Fitzka, M.; Nedelec, J.-M.; Liebner, F. W. Insight into the Nanostructure of Anisotropic Cellulose Aerogels

upon Compression. *Soft Matter* **2019**, *15* (41), 8372–8380.

40 Woignier, T.; Primera, J.; Alaoui, A.; Etienne, P.; Despestis, F.; Calas-Etienne, S. Mechanical Properties and Brittle Behavior of Silica Aerogels. *Gels* **2015**, *1* (2), 256–275.

41 Wong, J. C. H.; Kaymak, H.; Brunner, S.; Koebel, M. M. Mechanical Properties of Monolithic Silica Aerogels Made from Polyethoxydisiloxanes. *Microporous Mesoporous Mater.* **2014**, *183*, 23–29.

42 Zhao, S.; Siqueira, G.; Drdova, S.; Norris, D.; Ubert, C.; Bonnin, A.; Galmarini, S.; Ganobjak, M.; Pan, Z.; Brunner, S.; Nyström, G.; Wang, J.; Koebel, M. M.; Malfait, W. J. Additive Manufacturing of Silica Aerogels. *Nature* **2020**, *584* (7821), 387–392.

43 Xu, X.; Zhang, Q.; Hao, M.; Hu, Y.; Lin, Z.; Peng, L.; Wang, T.; Ren, X.; Wang, C.; Zhao, Z.; Wan, C.; Fei, H.; Wang, L.; Zhu, J.; Sun, H.; Chen, W.; Du, T.; Deng, B.; Cheng, G. J.; Shakir, I.; Dames, C.; Fisher, T. S.; Zhang, X.; Li, H.; Huang, Y.; Duan, X. Double-Negative-Index Ceramic Aerogels for Thermal Superinsulation. *Science* **2019**, *363* (6428), 723–727.

44 Brinker, C. J.; Scherer, G. W. *Sol-Gel Science: The Physics and Chemistry of Sol-Gel Processing*; Elsevier, 1990.

45 Innocenzi, P. Overview of the Sol–Gel Process. In *Springer Handbook of Aerogels*; Aegerter, M. A., Leventis, N., Koebel, M., Steiner III, S. A., Eds.; Springer International Publishing: Cham, 2023; 53–69.

46 Griffin, J. S.; Nelson, R. T.; Gurikov, P.; Smirnova, I.; Steiner, S. A. Gel-Phase Processing and Solvent Exchange. In *Springer Handbook of Aerogels*; Aegerter, M. A., Leventis, N., Koebel, M., Steiner III, S. A., Eds.; Springer International Publishing: Cham, 2023; 71–92.

47 Alemán, J. V; Chadwick, A. V; He, J.; Hess, M.; Horie, K.; Jones, R. G.; Kratochvíl, P.; Meisel, I.; Mita, I.; Moad, G.; Penczek, S.; Stepto, R. F. T. Definitions of Terms Relating to the Structure and Processing of Sols, Gels, Networks, and Inorganic-Organic Hybrid Materials (IUPAC Recommendations 2007). *Pure Appl. Chem.* **2007**, *79* (10), 1801–1829.

48 Al-Oweini, R.; El-Rassy, H. Synthesis and Characterization by FTIR Spectroscopy of Silica Aerogels Prepared Using Several Si(OR)4 and R"Si(OR')3 Precursors. *J. Mol. Struct.* **2009**, *919* (1), 140–145.

49 Soleimani Dorcheh, A.; Abbasi, M. H. Silica Aerogel; Synthesis, Properties and Characterization. *J. Mater. Process. Technol.* **2008**, *199* (1), 10–26.

50 Pierre, A. C. History of Aerogels. In *Aerogels Handbook*; Aegerter, M. A., Leventis, N., Koebel, M. M., Eds.; Springer New York: New York, NY, 2011; 3–18.

51 Wei, T. Y.; Chang, T. F.; Lu, S. Y.; Chang, Y. C. Preparation of Monolithic Silica Aerogel of Low Thermal Conductivity by Ambient Pressure Drying. *J. Am. Ceram. Soc.* **2007**, *90* (7), 2003–2007.

52 Prakash, S. S.; Brinker, C. J.; Hurd, A. J. Silica Aerogel Films at Ambient Pressure. *J. Non. Cryst. Solids* **1995**, *190* (3), 264–275.

53 Venkateswara Rao, A.; Bhagat, S. D. Synthesis and Physical Properties of TEOS-Based Silica Aerogels Prepared by Two Step (Acid–Base) Sol–Gel Process. *Solid State Sci.* **2004**, *6* (9), 945–952.

54 Tillotson, T. M.; Hrubesh, L. W. Transparent Ultralow-Density Silica Aerogels Prepared by a Two-Step Sol-Gel Process. *J. Non. Cryst. Solids* **1992**, *145*, 44–50.

55 Brinker, C. J.; Scherer, G. W. Chapter 6 - Aging of Gels. In *Sol-Gel Science*; Brinker, C. J., Scherer, G. W., Eds.; Academic Press: San Diego, 1990; 356–405.

56 Iswar, S.; Malfait, W. J.; Balog, S.; Winnefeld, F.; Lattuada, M.; Koebel, M. M. Effect of Aging on Silica Aerogel Properties. *Microporous Mesoporous Mater.* **2017**, *241*, 293–302.

57 Bisson, A.; Rigacci, A.; Lecomte, D.; Rodier, E.; Achard, P. Drying of Silica Gels to Obtain Aerogels:Phenomenology and Basic Techniques. *Dry. Technol.* **2003**, *21* (4), 593–628.

58 Scherer, G. W. Syneresis in Silica Gel. In *MRS Online Proceedings Library*; 1988; Vol. 121, 179–186.

59 Hwang, S.-W.; Jung, H.-H.; Hyun, S.-H.; Ahn, Y.-S. Effective Preparation of Crack-Free Silica Aerogels via Ambient Drying. *J. Sol-Gel Sci. Technol.* **2007**, *41* (2), 139–146.

60 Steiner, S. A.; Anderson, A. M.; Brock, S. L.; Buckwalter, M. C.; Carroll, M. K.; De Pooter, S.; Downey, S. L.; Eychmüller, A.; Georgi, M.; Griffin, J. S.; Grogan, M. D. W.; Gurikov, P.; Hiekel, K.; Hrubesh, L. W.; Kanamori, K.; Milow, B.; Nelson, R. T.; Rao, A. V.; Schwan, M.; Silva, K. L.; Worsley, M. A.; Zhao, S. Recipes and Designs for Aerogels. In *Springer Handbook of Aerogels*; Aegerter, M. A., Leventis, N., Koebel, M., Steiner III, S. A., Eds.; Springer International Publishing: Cham, 2023; 1643–1728.

61 Vincent, O.; Sessoms, D. A.; Huber, E. J.; Guioth, J.; Stroock, A. D. Drying by Cavitation and Poroelastic Relaxations in Porous Media with Macroscopic Pores Connected by Nanoscale Throats. *Phys. Rev. Lett.* **2014**, *113* (13), 134501.

62 Liu, H.; Cao, G. Effectiveness of the Young-Laplace Equation at Nanoscale. *Sci. Rep.* **2016**, *6* (1), 23936.

63 Imre, A.; Martinás, K.; Rebelo, L. P. N. Thermodynamics of Negative Pressures in Liquids. *J. Non-Equilibrium Thermodyn.* **1998**, *23* (4), 351–375.

64 Kanduč, M.; Schneck, E.; Loche, P.; Jansen, S.; Schenk, H. J.; Netz, R. R. Cavitation in Lipid Bilayers Poses Strict Negative Pressure Stability Limit in Biological Liquids. *Proc. Natl. Acad. Sci.* **2020**, *117* (20), 10733–10739.

65 Brinker, C. J.; Scherer, G. W. Chapter 8 - Drying. In *Sol-Gel Science*; Brinker, C. J., Scherer, G. W., Eds.; Academic Press: San Diego, 1990; 452–513.

66 Weissmüller, J.; Duan, H.-L.; Farkas, D. Deformation of Solids with Nanoscale Pores by the Action of Capillary Forces. *Acta Mater.* **2010**, *58* (1), 1–13.

67 Kucheyev, S. O.; Stadermann, M.; Shin, S. J.; Satcher Jr., J. H.; Gammon, S. A.; Letts, S. A.; van Buuren, T.; Hamza, A. V. Super-Compressibility of Ultralow-Density Nanoporous Silica. *Adv. Mater.* **2012**, *24* (6), 776–780.

68 Sivaraman, D.; Zhao, S.; Iswar, S.; Lattuada, M.; Malfait, W. J. Aerogel Spring-Back Correlates with Strain Recovery: Effect of Silica Concentration and Aging. *Adv. Eng. Mater.* **2021**, *23* (10), 2100376.

69 Scherer, G. W. Drying Gels: VIII. Revision and Review. *J. Non. Cryst. Solids* **1989**, *109* (2), 171–182.

70 Klein, T.; Yan, S.; Cui, J.; Magee, J. W.; Kroenlein, K.; Rausch, M. H.; Koller, T. M.; Fröba, A. P. Liquid Viscosity and Surface Tension of N-Hexane, n-Octane, n-Decane, and n-Hexadecane up to 573 K by Surface Light Scattering. *J. Chem. Eng. Data* **2019**, *64* (9), 4116–4131.

71 Ahn, W. S.; Jhon, M. S.; Pak, H.; Chang, S. Surface Tension of Curved Surfaces. *J. Colloid Interface Sci.* **1972**, *38* (3), 605–608.

72 Rao, A. P.; Rao, A. V.; Pajonk, G. M. Hydrophobic and Physical Properties of the Two Step Processed Ambient Pressure Dried Silica Aerogels with Various Exchanging Solvents. *J. Sol-Gel Sci. Technol.* **2005**, *36* (3), 285–292.

73 Zhang, Z.; Scherer, G. W. Physical and Chemical Effects of Isopropanol Exchange in Cement-Based Materials. *Cem. Concr. Res.* **2021**, *145*, 106461.

74 Smith, D. M.; Stein, D.; Anderson, J. M.; Ackerman, W. Preparation of Low-Density Xerogels at Ambient Pressure. *J. Non. Cryst. Solids* **1995**, *186*, 104–112.

75 Deshpande, R.; Smith, D. M.; Brinker, C. J. Preparation of High Porosity Xerogels by Chemical Surface Modification. 5565142, 1996. https://patents.google.com/patent/US5565142A/en.

76 Rao, A. P.; Pajonk, G. M.; Rao, A. V. Effect of Preparation Conditions on the Physical and Hydrophobic Properties of Two Step Processed Ambient Pressure Dried Silica Aerogels. *J. Mater. Sci.* **2005**, *40* (13), 3481–3489.

77 Malfait, W. J.; Zhao, S.; Verel, R.; Iswar, S.; Rentsch, D.; Fener, R.; Zhang, Y.; Milow, B.; Koebel, M. M. Surface Chemistry of Hydrophobic Silica Aerogels. *Chem. Mater.* **2015**, *27* (19), 6737–6745.

78 Shewale, P. M.; Rao, A. V.; Rao, A. P. Effect of Different Trimethyl Silylating Agents on the Hydrophobic and Physical Properties of Silica Aerogels. *Appl. Surf. Sci.* **2008**, *254* (21), 6902–6907.

79 Stojanovic, A.; Paz Comesaña, S.; Rentsch, D.; Koebel, M. M.; Malfait, W. J. Ambient Pressure Drying of Silica Aerogels after Hydrophobization with Mono-, Di- and Tri-Functional Silanes and Mixtures Thereof. *Microporous Mesoporous Mater.* **2019**, *284* (October 2018), 289–295.

80 Jeong, A. Y.; Koo, S. M.; Kim, D. P. Characterization of Hydrophobic SiO2 Powders Prepared by Surface Modification on Wet Gel. *J. Sol-Gel Sci. Technol.* **2000**, *19* (1–3), 483–487.

81 Xian-lang, Q.; Min, Y.; Hong, L.; Jia-wen, X.; Mu-su, R.; Jin-liang, S. Optimized Preparation of Thermal Insulation Hydrophobic SiO2 Aerogel Based on Orthogonal Design Method. *J. Porous Mater.* **2022**, *29* (4), 1027–1037.

82 Bangi, U. K. H.; Ransing, A. A.; Dhavale, R. P.; Park, H.-H.; Patil, V. B. Improvement in the Characteristics of Ambient Pressure Dried Silica Aerogels for Thermal Insulation Purpose. *J. Porous Mater.* **2024**, *31* (1), 115–123.

83 Hwang, S.-W.; Kim, T.-Y.; Hyun, S.-H. Effect of Surface Modification Conditions on the Synthesis of Mesoporous Crack-Free Silica Aerogel Monoliths from Waterglass via Ambient-Drying. *Microporous Mesoporous Mater.* **2010**, *130* (1), 295–302.

84 Bangi, U. K. H.; Venkateswara Rao, A.; Parvathy Rao, A. A New Route for Preparation of Sodium-Silicate-Based Hydrophobic Silica Aerogels via Ambient-Pressure Drying. *Sci. Technol. Adv. Mater.* **2008**, *9* (3), 35006.

85 Kang, S. K.; Choi, S. Y. Synthesis of Low-Density Silica Gel at Ambient Pressure: Effect of Heat Treatment. *J. Mater. Sci.* **2000**, *35* (19), 4971–4976.

86 Shi, F.; Wang, L.; Liu, J. Synthesis and Characterization of Silica Aerogels by a Novel Fast Ambient Pressure Drying Process. *Mater. Lett.* **2006**, *60* (29), 3718–3722.

87 Bangi, U. K. H.; Pandit, S. S.; Bagal, D. B.; Park, H.-H. Preparation of Sodium Silicate–Based Aerogels Using a Two-Step Sol–Gel Process and Ambient Pressure Drying. *Macromol. Symp.* **2019**, *387* (1), 1800226.

88 Balkis Ameen, K.; Rajasekar, K.; Rajasekharan, T.; Rajasekharan, M. V. The Effect of Heat-Treatment on the Physico-Chemical Properties of Silica Aerogel Prepared by Sub-

Critical Drying Technique. *J. Sol-Gel Sci. Technol.* **2008**, *45* (1), 9–15.

89 Liu, G.; Zhou, B.; Ni, X.; Shen, J.; Wu, G.; Du, A.; Zu, G. Influence of Thermal Process on Microstructural and Physical Properties of Ambient Pressure Dried Hydrophobic Silica Aerogel Monoliths. *J. Sol-Gel Sci. Technol.* **2012**, *62* (2), 126–133.

90 Hamelin, G.; Jauffrés, D.; Martin, C. L.; Meille, S.; Foray, G. Mechanical Properties of Milimetric Silica Aerogel Particles Produced through Evaporative Drying: A Coupled Experimental and Discrete Element Approach. *J. Non. Cryst. Solids* **2021**, *560*, 120727.

91 Zhao, J.; Qin, F.; Kang, Q.; Derome, D.; Carmeliet, J. Pore-Scale Simulation of Drying in Porous Media Using a Hybrid Lattice Boltzmann: Pore Network Model. *Dry. Technol.* **2021**, 1–16.

92 Bentz, D. P.; Garboczi, E. J.; Quenard, D. A. Modelling Drying Shrinkage in Reconstructed Porous Materials: Application to Porous Vycor Glass. *Model. Simul. Mater. Sci. Eng.* **1998**, *6* (3), 211–236.

93 Lesov, I.; Tcholakova, S.; Denkov, N. Drying of Particle-Loaded Foams for Production of Porous Materials: Mechanism and Theoretical Modeling. *RSC Adv.* **2014**, *4* (2), 811–823.

94 Hu, L. B.; Péron, H.; Hueckel, T.; Laloui, L. Desiccation Shrinkage of Non-Clayey Soils: Multiphysics Mechanisms and a Microstructural Model. *Int. J. Numer. Anal. Methods Geomech.* **2013**, *37* (12), 1761–1781.

95 Rastogi, M.; Müller, A.; Haha, M. Ben; Scrivener, K. L. The Role of Cavitation in Drying Cementitious Materials. *Cem. Concr. Res.* **2022**, *154*, 106710.

96 Hayase, G.; Kanamori, K.; Maeno, A.; Kaji, H.; Nakanishi, K. Dynamic Spring-Back Behavior in Evaporative Drying of Polymethylsilsesquioxane Monolithic Gels for Low-Density Transparent Thermal Superinsulators. *J. Non. Cryst. Solids* **2016**, *434*, 115–119.

97 Gurikov, P.; S. P., R.; Griffin, J. S.; Steiner, S. A. I. I. I.; Smirnova, I. 110th Anniversary: Solvent Exchange in the Processing of Biopolymer Aerogels: Current Status and Open Questions. *Ind. Eng. Chem. Res.* **2019**, *58* (40), 18590–18600.

98 Subrahmanyam, R.; Selmer, I.; Bueno, A.; Weinrich, D.; Lölsberg, W.; Fricke, M.; Movahhed, S.; Gurikov, P.; Smirnova, I. Supercritical Drying of Aerogels. In *Springer Handbook of Aerogels*; Aegerter, M. A., Leventis, N., Koebel, M., Steiner III, S. A., Eds.; Springer International Publishing: Cham, 2023; 93–120.

99 Pons, A.; Casas, L.; Estop, E.; Molins, E.; Harris, K. D. M.; Xu, M. A New Route to Aerogels: Monolithic Silica Cryogels. *J. Non. Cryst. Solids* **2012**, *358* (3), 461–469.

100 Jones, D. P.; Leach, D. C.; Moore, D. R. Mechanical Properties of Poly(Ether-Ether-

Ketone) for Engineering Applications. *Polymer* **1985**, *26* (9), 1385–1393.

101 Shi, X.; Wu, C.; Rong, M.; Czigany, T.; Ruan, W.; Zhang, M. Improvement of Creep Resistance of Polytetrafluoroethylene Films by Nano-Inclusions. *Chinese J. Polym. Sci.* **2013**, *31* (3), 377–387.

102 Gonthier, J.; Rilling, T.; Scoppola, E.; Zemke, F.; Gurlo, A.; Fratzl, P.; Wagermaier, W. In Operando μCT Imaging of Silylated Silica Aerogels during Ambient Pressure Drying and Spring-Back. *Chem. Mater.* **2023**, *35* (18), 7683–7693.

103 Stroud, R. M.; Long, J. W.; Pietron, J. J.; Rolison, D. R. A Practical Guide to Transmission Electron Microscopy of Aerogels. *J. Non. Cryst. Solids* **2004**, *350*, 277–284.

104 Chal, B.; Roiban, L.; Masenelli-Varlot, K.; Baeza, G. P.; Yrieix, B.; Foray, G. 3D Multi-Scale Quantification of Industrially Relevant Ultra-Porous Silicas by Low-Dose Electron Tomography Combined with SANS. *J. Non. Cryst. Solids* **2021**, *557*, 120577.

105 Li, T.; Du, A.; Zhang, T.; Ding, W.; Liu, M.; Shen, J.; Zhang, Z.; Zhou, B. Continuous Adjustment of Fractal Dimension of Silica Aerogels. *J. Non. Cryst. Solids* **2018**, *499*, 159–166.

106 Schindelin, J.; Arganda-Carreras, I.; Frise, E.; Kaynig, V.; Longair, M.; Pietzsch, T.; Preibisch, S.; Rueden, C.; Saalfeld, S.; Schmid, B.; Tinevez, J.-Y.; White, D. J.; Hartenstein, V.; Eliceiri, K.; Tomancak, P.; Cardona, A. Fiji: An Open-Source Platform for Biological-Image Analysis. *Nat. Methods* **2012**, *9* (7), 676–682.

107 Gonthier, J.; Scoppola, E.; Rilling, T.; Gurlo, A.; Fratzl, P.; Wagermaier, W. Solvent Cavitation during Ambient Pressure Drying of Silica Aerogels. *Langmuir* **2024**, *40* (25), 12925–12938.

108 Withers, P. J.; Bouman, C.; Carmignato, S.; Cnudde, V.; Grimaldi, D.; Hagen, C. K.; Maire, E.; Manley, M.; Du Plessis, A.; Stock, S. R. X-Ray Computed Tomography. *Nat. Rev. Methods Prim.* **2021**, *1* (1), 18.

109 Spaeker, O.; Taylor, G. J.; Wilts, B. D.; Slabý, T.; Abdel-Rahman, M. A. K.; Scoppola, E.; Schmitt, C. N. Z.; Sztucki, M.; Liu, J.; Bertinetti, L.; Wagermaier, W.; Scholtz, G.; Fratzl, P.; Politi, Y. Gradients of Orientation, Composition, and Hydration of Proteins for Efficient Light Collection by the Cornea of the Horseshoe Crab. *Adv. Sci.* **2022**, *9* (33), 2203371.

110 Amini, S.; Razi, H.; Seidel, R.; Werner, D.; White, W. T.; Weaver, J. C.; Dean, M. N.; Fratzl, P. Shape-Preserving Erosion Controlled by the Graded Microarchitecture of Shark Tooth Enameloid. *Nat. Commun.* **2020**, *11* (1), 5971.

111 Schemenz, V.; Gjardy, A.; Chamasemani, F. F.; Roschger, A.; Roschger, P.; Zaslansky,

P.; Helfen, L.; Burghammer, M.; Fratzl, P.; Weinkamer, R.; Brunner, R.; Willie, B. M.; Wagermaier, W. Heterogeneity of the Osteocyte Lacuno-Canalicular Network Architecture and Material Characteristics across Different Tissue Types in Healing Bone. *J. Struct. Biol.* **2020**, *212* (2), 107616.

112 Pylkkänen, R.; Werner, D.; Bishoyi, A.; Weil, D.; Scoppola, E.; Wagermaier, W.; Safeer, A.; Bahri, S.; Baldus, M.; Paananen, A.; Penttilä, M.; Szilvay, G. R.; Mohammadi, P. The Complex Structure of Fomes Fomentarius Represents an Architectural Design for High-Performance Ultralightweight Materials. *Sci. Adv.* **2023**, *9* (8), eade5417.

113 Zorzetto, L.; Scoppola, E.; Raguin, E.; Blank, K. G.; Fratzl, P.; Bidan, C. M. Induced Mineralization of Hydroxyapatite in Escherichia Coli Biofilms and the Potential Role of Bacterial Alkaline Phosphatase. *Chem. Mater.* **2023**, *35* (7), 2762–2772.

114 Yu, B.; Fan, W.; Dijkstra, T. A.; Wei, Y. N.; Deng, L. S. Heterogeneous Evolution of Pore Structure during Loess Collapse: Insights from X-Ray Micro-Computed Tomography. *Catena* **2021**, *201*, 105206.

115 Finegan, D. P.; Scheel, M.; Robinson, J. B.; Tjaden, B.; Di Michiel, M.; Hinds, G.; Brett, D. J. L.; Shearing, P. R. Investigating Lithium-Ion Battery Materials during Overcharge-Induced Thermal Runaway: An Operando and Multi-Scale X-Ray CT Study. *Phys. Chem. Chem. Phys.* **2016**, *18* (45), 30912–30919.

116 Chung, S.-Y.; Kim, J.-S.; Stephan, D.; Han, T.-S. Overview of the Use of Micro-Computed Tomography (Micro-CT) to Investigate the Relation between the Material Characteristics and Properties of Cement-Based Materials. *Constr. Build. Mater.* **2019**, *229*, 116843.

117 Withers, P. J. X-Ray Nanotomography. *Mater. Today* **2007**, *10* (12), 26–34.

118 Vásárhelyi, L.; Kónya, Z.; Kukovecz, Á.; Vajtai, R. Microcomputed Tomography–Based Characterization of Advanced Materials: A Review. *Mater. Today Adv.* **2020**, *8*, 100084.

119 Yada, N.; Onishi, H. Validation of Computed Tomography-Based Attenuation Correction of Deviation between Theoretical and Actual Values for Four Computed Tomography Scanners. *Asia Ocean. J. Nucl. Med. Biol.* **2016**, *4* (2), 81–89.

120 Hubbell, J. H.; Seltzer, S. M. *X-ray Mass Attenuation Coefficients*. NIST Standard Reference Database 126. https://doi.org/10.18434/T4D01F.

121 Radon, J. Über Die Bestimmung von Funktionen Durch Ihre. Integralwerte Längs Gewisser Mannigfaltigkeiten. *Ber. Vor Sächs. Akad. Wiss.* **1917**, *69*, 262–277.

122 Meaney, A. Cone-Beam Computed Tomography Dataset of a Walnut. Zenodo August 2022. https://doi.org/10.5281/zenodo.6986012.

123 Sedigh Rahimabadi, P.; Khodaei, M.; Koswattage, K. R. Review on Applications of Synchrotron-Based X-Ray Techniques in Materials Characterization. *X-Ray Spectrom.* **2020**, *49* (3), 348–373.

124 Kumar, U.; Ramakrishna, G. S.; Pendharkar, A. S.; Singh, G. Behaviour of Reconstructed Attenuation Values with X-Ray Tube Voltage in an Experimental Third-Generation Industrial CT System Using Xscan Linear Detector Array. *Nucl. Instruments Methods Phys. Res. Sect. A Accel. Spectrometers, Detect. Assoc. Equip.* **2002**, *490* (1), 379–391.

125 Sittner, J.; Godinho, J. R. A.; Renno, A. D.; Cnudde, V.; Boone, M.; De Schryver, T.; Van Loo, D.; Merkulova, M.; Roine, A.; Liipo, J. Spectral X-Ray Computed Micro Tomography: 3-Dimensional Chemical Imaging. *X-Ray Spectrom.* **2021**, *50* (2), 92–105.

126 *Tescan UniTOM XL Spectral*. accessed 24.03.2024. https://info.tescan.com/micro-ct/products/tescan-spectral-ct.

127 Otsu, N. A Threshold Selection Method from Gray-Level Histograms. *IEEE Trans. Syst. Man. Cybern.* **1979**, *9* (1), 62–66.

128 Thangadurai, S.; Majkut, M.; Milgram, J.; Zaslansky, P.; Shahar, R.; Raguin, E. Focused Ion Beam-SEM 3D Study of Osteodentin in the Teeth of the Atlantic Wolfish Anarhichas Lupus. *J. Struct. Biol.* **2024**, *216* (1), 108062.

129 Stalling, D.; Westerhoff, M.; Hege, H.-C. Amira: A Highly Interactive System for Visual Data Analysis. In *Visualization Handbook*; Hansen, C. D., Johnson, C. R. B. T.-V. H., Eds.; Butterworth-Heinemann: Burlington, 2005; 749–767.

130 Object Research Systems (ORS) Inc. Dragonfly [Computer Software]. (Version 2022.2). 2022. http://www.theobjects.com/dragonfly.

131 Davis, G. R.; Elliott, J. C. Artefacts in X-Ray Microtomography of Materials. *Mater. Sci. Technol.* **2006**, *22* (9), 1011–1018.

132 Schulze, R.; Heil, U.; Groβ, D.; Bruellmann, D. D.; Dranischnikow, E.; Schwanecke, U.; Schoemer, E. Artefacts in CBCT: A Review. *Dentomaxillofacial Radiol.* **2011**, *40* (5), 265–273.

133 Kusk, M. W.; Jensen, J. M.; Gram, E. H.; Nielsen, J.; Precht, H. Anode Heel Effect: Does It Impact Image Quality in Digital Radiography? A Systematic Literature Review. *Radiography* **2021**, *27* (3), 976–981.

134 Fritz, S. L.; Livingston, W. H. The Effect of Anode Curvature on Radiographic Heel Effect. *Med. Phys.* **1985**, *12* (4), 443–446.

135 Zhang, H.; Lin, C.; Han, T.; Du, F.; Zhao, Y.; Li, X.; Sun, Y. Visualization of the Formation and 3D Porous Structure of Ag Doped MnO2 Aerogel Monoliths with High

Photocatalytic Activity. *ACS Sustain. Chem. Eng.* **2016**, *4* (12), 6277–6287.

136 *Phoenix v|tome|x M Data Sheet*. accessed 08.04.2024. https://www.jwjndt.com/product/phoenix-vtomex-m/.

137 Phillips, D. H.; Lannutti, J. J. Measuring Physical Density with X-Ray Computed Tomography. *NDT E Int.* **1997**, *30* (6), 339–350.

138 Borisenko, N. G.; Nazarov, W.; Musgrave, C. S. A.; Merkuliev, Y. A.; Orekhov, A. S.; Borisenko, L. A. Characterization of Divinyl Benzene Aerogels with Density Gradient Using X-Ray Tomography Technique. *J. Radioanal. Nucl. Chem.* **2014**, *299* (2), 961–964.

139 Borisenko, N. G.; Akunets, A. A.; Artyukov, I. A.; Gorodnichev, K. E.; Merkuliev, Y. A. X-Ray Tomography of Growing Silica Gel with a Density Gradient. *Fusion Sci. Technol.* **2009**, *55* (4), 477–483.

140 Welborn, S. S.; Detsi, E. Small-Angle X-Ray Scattering of Nanoporous Materials. *Nanoscale Horizons* **2020**, *5* (1), 12–24.

141 Jeffries, C. M.; Ilavsky, J.; Martel, A.; Hinrichs, S.; Meyer, A.; Pedersen, J. S.; Sokolova, A. V; Svergun, D. I. Small-Angle X-Ray and Neutron Scattering. *Nat. Rev. Methods Prim.* **2021**, *1* (1), 70.

142 Mertens, H. D. T.; Svergun, D. I. Structural Characterization of Proteins and Complexes Using Small-Angle X-Ray Solution Scattering. *J. Struct. Biol.* **2010**, *172* (1), 128–141.

143 Schaefer, D. W. Polymers, Fractals, and Ceramic Materials. *Science* **1989**, *243* (4894), 1023–1027.

144 Schitco, C.; Bazarjani, M. S.; Riedel, R.; Gurlo, A. NH3-Assisted Synthesis of Microporous Silicon Oxycarbonitride Ceramics from Preceramic Polymers: A Combined N2 and CO2 Adsorption and Small Angle X-Ray Scattering Study. *J. Mater. Chem. A* **2015**, *3* (2), 805–818.

145 Emmerling, A.; Fricke, J. Small Angle Scattering and the Structure of Aerogels. *J. Non. Cryst. Solids* **1992**, *145*, 113–120.

146 Woignier, T.; Phalippou, J.; Vacher, R.; Pelous, J.; Courtens, E. Different Kinds of Fractal Structures in Silica Aerogels. *J. Non. Cryst. Solids* **1990**, *121* (1), 198–201.

147 Peterlik, H.; Fratzl, P. Small-Angle X-Ray Scattering to Characterize Nanostructures in Inorganic and Hybrid Materials Chemistry. *Monatshefte für Chemie / Chem. Mon.* **2006**, *137* (5), 529–543.

148 Brotherton, E. E.; Hatton, F. L.; Cockram, A. A.; Derry, M. J.; Czajka, A.; Cornel, E. J.; Topham, P. D.; Mykhaylyk, O. O.; Armes, S. P. In Situ Small-Angle X-Ray Scattering

Studies During Reversible Addition–Fragmentation Chain Transfer Aqueous Emulsion Polymerization. *J. Am. Chem. Soc.* **2019**, *141* (34), 13664–13675.

149 Ping, H.; Wagermaier, W.; Horbelt, N.; Scoppola, E.; Li, C.; Werner, P.; Fu, Z.; Fratzl, P. Mineralization Generates Megapascal Contractile Stresses in Collagen Fibrils. *Science* **2022**, *376* (6589), 188–192.

150 Gommes, C.; Blacher, S.; Goderis, B.; Pirard, R.; Heinrichs, B.; Alié, C.; Pirard, J.-P. In Situ SAXS Analysis of Silica Gel Formation with an Additive. *J. Phys. Chem. B* **2004**, *108* (26), 8983–8991.

151 Emmerling, A.; Petricevic, R.; Beck, A.; Wang, P.; Scheller, H.; Fricke, J. Relationship between Optical Transparency and Nanostructural Features of Silica Aerogels. *J. Non. Cryst. Solids* **1995**, *185* (3), 240–248.

152 Reichenauer, G. Structural Characterization of Aerogels. In *Springer Handbook of Aerogels*; Aegerter, M. A., Leventis, N., Koebel, M., Steiner III, S. A., Eds.; Springer International Publishing: Cham, 2023; 151–195.

153 Wagermaier, W.; Zander, T.; Hofmann, D.; Kratz, K.; Narendra Kumar, U.; Lendlein, A. In Situ X-Ray Scattering Studies of Poly(ε-Caprolactone) Networks with Grafted Poly(Ethylene Glycol) Chains to Investigate Structural Changes during Dual- and Triple-Shape Effect. *Macromol. Rapid Commun.* **2010**, *31* (17), 1546–1553.

154 Allen, A. J.; Zhang, F.; Kline, R. J.; Guthrie, W. F.; Ilavsky, J. NIST Standard Reference Material 3600: Absolute Intensity Calibration Standard for Small-Angle X-Ray Scattering. *J. Appl. Crystallogr.* **2017**, *50* (2), 462–474.

155 Pauw, B. R.; Smith, A. J.; Snow, T.; Terrill, N. J.; Thünemann, A. F. The Modular Small-Angle X-Ray Scattering Data Correction Sequence. *J. Appl. Crystallogr.* **2017**, *50* (6), 1800–1811.

156 Woignier, T.; Primera, J.; Alaoui, A.; Dieudonne, P.; Duffours, L.; Beurroies, I.; Calas-Etienne, S.; Despestis, F.; Faivre, A.; Etienne, P. Fractal Structure in Silica and Composites Aerogels. *Gels* **2021**, *7* (1), 1–16.

157 Omote, K.; Iwata, T. Real-Space Modeling for Complex Structures Based on Small-Angle X-Ray Scattering. *J. Appl. Crystallogr.* **2021**, *54* (5), 1290–1297.

158 Marlière, C.; Despetis, F.; Etienne, P.; Woignier, T.; Dieudonné, P.; Phalippou, J. Very Large-Scale Structures in Sintered Silica Aerogels as Evidenced by Atomic Force Microscopy and Ultra-Small Angle X-Ray Scattering Experiments. *J. Non. Cryst. Solids* **2001**, *285* (1), 148–153.

159 Beaucage, G.; Kammler, H. K.; Pratsinis, S. E. Particle Size Distributions from Small-

Angle Scattering Using Global Scattering Functions. *J. Appl. Crystallogr.* **2004**, *37* (4), 523–535.

160 Ashby, M. F.; Shercliff, H.; Cebon, D. Chapitre 4. Rigidité et Poids: Densité et Module Élastique. In *Matériaux - Ingénierie, Science, Procédé et Conception*; Presses polytechniques et universitaires romandes: Lausanne, 2013; 51–85.

161 Carroll, M. K.; Anderson, A. M.; Gorka, C. A. Preparing Silica Aerogel Monoliths via a Rapid Supercritical Extraction Method. *JoVE* **2014**, No. 84, e51421.

162 Pollanen, J.; Shirer, K. R.; Blinstein, S.; Davis, J. P.; Choi, H.; Lippman, T. M.; Halperin, W. P.; Lurio, L. B. Globally Anisotropic High Porosity Silica Aerogels. *J. Non. Cryst. Solids* **2008**, *354* (40), 4668–4674.

163 Hamad, A. J. Size and Shape Effect of Specimen on the Compressive Strength of HPLWFC Reinforced with Glass Fibres. *J. King Saud Univ. - Eng. Sci.* **2017**, *29* (4), 373–380.

164 Tam, C. T.; Babu, D. S.; Li, W. EN 206 Conformity Testing for Concrete Strength in Compression. *Procedia Eng.* **2017**, *171*, 227–237.

165 Darvell, B. W. Uniaxial Compression Tests and the Validity of Indirect Tensile Strength. *J. Mater. Sci.* **1990**, *25* (2), 757–780.

166 Andreev, K.; Tadaion, V.; Koster, J.; Verstrynge, E. Cyclic Fatigue of Silica Refractories – Effect of Test Method on Failure Process. *J. Eur. Ceram. Soc.* **2017**, *37* (4), 1811–1819.

167 Smith, C. W.; Wootton, R. J.; Evans, K. E. Interpretation of Experimental Data for Poisson's Ratio of Highly Nonlinear Materials. *Exp. Mech.* **1999**, *39* (4), 356–362.

168 Walsh, J. B. The Effect of Cracks on the Uniaxial Elastic Compression of Rocks. *J. Geophys. Res.* **1965**, *70* (2), 399–411.

169 Ashby, M. F.; Shercliff, H.; Cebon, D. Chapitre 6. Au-Delà de l'élasticité: Plasticité et Ductilité. In *Matériaux - Ingénierie, Science, Procédé et Conception*; Presses polytechniques et universitaires romandes: Lausanne, 2013; 119–148.

170 Woignier, T.; Phalippou, J. Mechanical Strength of Silica Aerogels. *J. Non. Cryst. Solids* **1988**, *100* (1), 404–408.

171 Kucheyev, S. O.; Wang, Y. M.; Hamza, A. V; Worsley, M. A. Light-Ion-Irradiation-Induced Thermal Spikes in Nanoporous Silica. *J. Phys. D. Appl. Phys.* **2011**, *44* (8), 85406.

172 Brinker, C. J.; Scherer, G. W. Chapter 9 - Structural Evolution during Consolidation. In *Sol-Gel Science*; Brinker, C. J., Scherer, G. W., Eds.; Academic Press: San Diego, 1990; 514–615.

173 Pierre, A. C.; Rigacci, A. SiO2 Aerogels. In *Aerogels Handbook*; Aegerter, M. A., Leventis,

N., Koebel, M. M., Eds.; Springer New York: New York, NY, 2011; 21–45.

174 Thiery, J.; Rodts, S.; Weitz, D. A.; Coussot, P. Drying Regimes in Homogeneous Porous Media from Macro- to Nanoscale. *Phys. Rev. Fluids* **2017**, *2* (7), 74201.

175 Ichilmann, S.; Rücker, K.; Haase, M.; Enke, D.; Steinhart, M.; Xue, L. Adiabatic Burst Evaporation from Bicontinuous Nanoporous Membranes. *Nanoscale* **2015**, *7* (20), 9185–9193.

176 Scherer, G. W. Effect of Drying on Properties of Silica Gel. *J. Non. Cryst. Solids* **1997**, *215* (2), 155–168.

177 Doebele, V.; Benoit-Gonin, A.; Souris, F.; Cagnon, L.; Spathis, P.; Wolf, P. E.; Grosman, A.; Bossert, M.; Trimaille, I.; Rolley, E. Direct Observation of Homogeneous Cavitation in Nanopores. *Phys. Rev. Lett.* **2020**, *125* (25), 255701.

178 Vincent, O.; Marmottant, P. On the Statics and Dynamics of Fully Confined Bubbles. *J. Fluid Mech.* **2017**, *827*, 194–224.

179 Vincent, O. Dynamique de Bulles de Cavitation Dans de l'eau Micro-Confinée Sous Tension. Application à l'étude de l'embolie Dans Les Arbres, Université de Grenoble, 2012. https://theses.hal.science/tel-00807749.

180 Leonov, K.; Akhatov, I. Dynamics of an Externally Driven Cavitation Bubble in an Elastic Microconfinement. *Phys. Rev. E* **2021**, *104* (1), 15105.

181 Bossert, M.; Grosman, A.; Trimaille, I.; Souris, F.; Doebele, V.; Benoit-Gonin, A.; Cagnon, L.; Spathis, P.; Wolf, P.-E.; Rolley, E. Evaporation Process in Porous Silicon: Cavitation vs Pore Blocking. *Langmuir* **2021**, *37* (49), 14419–14428.

182 Morishige, K.; Tateishi, M.; Hirose, F.; Aramaki, K. Change in Desorption Mechanism from Pore Blocking to Cavitation with Temperature for Nitrogen in Ordered Silica with Cagelike Pores. *Langmuir* **2006**, *22* (22), 9220–9224.

183 Ravikovitch, P. I.; Neimark, A. V. Experimental Confirmation of Different Mechanisms of Evaporation from Ink-Bottle Type Pores: Equilibrium, Pore Blocking, and Cavitation. *Langmuir* **2002**, *18* (25), 9830–9837.

184 Bossert, M.; Trimaille, I.; Cagnon, L.; Chabaud, B.; Gueneau, C.; Spathis, P.; Wolf, P. E.; Rolley, E. Surface Tension of Cavitation Bubbles. In *Proceedings of the National Academy of Sciences of the United States of America*; 2023; Vol. 120, e2300499120.

185 Rasmussen, C. J.; Vishnyakov, A.; Thommes, M.; Smarsly, B. M.; Kleitz, F.; Neimark, A. V. Cavitation in Metastable Liquid Nitrogen Confined to Nanoscale Pores. *Langmuir* **2010**, *26* (12), 10147–10157.

186 Rasmussen, C. J.; Gor, G. Y.; Neimark, A. V. Monte Carlo Simulation of Cavitation in

Pores with Nonwetting Defects. *Langmuir* **2012**, *28* (10), 4702–4711.

187 Wang, S.; Kirkbir, F.; Chaudhuri, S. R.; Sarkar, A. Accelerated Subcritical Drying of Large Alkoxide Silica Gels. In *Sol-Gel Optics II*; 1992; Vol. 1758, 113.

188 Sarkar, A.; Chaudhuri, S. R.; Wang, S.; Kirkbir, F.; Murata, H. Drying of Alkoxide Gels—Observation of an Alternate Phenomenology. *J. Sol-Gel Sci. Technol.* **1994**, *2* (1), 865–870.

189 Murata, H.; Meyers, D. E.; Kirkbir, F.; Ray Chaudhuri, S.; Sarkar, A. Drying and Sintering of Bulk Silica Gels. *J. Sol-Gel Sci. Technol.* **1997**, *8* (1), 397–402.

190 DIPlib [Computer Software]. 2023. https://github.com/DIPlib/diplib.

191 Hunter, J. D. Matplotlib: A 2D Graphics Environment. *Comput. Sci. Eng.* **2007**, *9* (3), 90–95.

192 Harris, C. R.; Millman, K. J.; van der Walt, S. J.; Gommers, R.; Virtanen, P.; Cournapeau, D.; Wieser, E.; Taylor, J.; Berg, S.; Smith, N. J.; Kern, R.; Picus, M.; Hoyer, S.; van Kerkwijk, M. H.; Brett, M.; Haldane, A.; del Río, J. F.; Wiebe, M.; Peterson, P.; Gérard-Marchant, P.; Sheppard, K.; Reddy, T.; Weckesser, W.; Abbasi, H.; Gohlke, C.; Oliphant, T. E. Array Programming with NumPy. *Nature* **2020**, *585* (7825), 357–362.

193 Clark, A. Pillow (PIL Fork) [Computer Software]. 2015. https://buildmedia.readthedocs.org/media/pdf/pillow/latest/pillow.pdf.

194 Virtanen, P.; Gommers, R.; Oliphant, T. E.; Haberland, M.; Reddy, T.; Cournapeau, D.; Burovski, E.; Peterson, P.; Weckesser, W.; Bright, J.; van der Walt, S. J.; Brett, M.; Wilson, J.; Millman, K. J.; Mayorov, N.; Nelson, A. R. J.; Jones, E.; Kern, R.; Larson, E.; Carey, C. J.; Polat, \.Ilhan; Feng, Y.; Moore, E. W.; VanderPlas, J.; Laxalde, D.; Perktold, J.; Cimrman, R.; Henriksen, I.; Quintero, E. A.; Harris, C. R.; Archibald, A. M.; Ribeiro, A. H.; Pedregosa, F.; van Mulbregt, P.; SciPy 1.0 Contributors. SciPy 1.0: Fundamental Algorithms for Scientific Computing in Python. *Nat. Methods* **2020**, *17*, 261–272.

195 Zizak, I. The MySpot Beamline at BESSY II. *J. large-scale Res. Facil.* **2016**, *2*.

196 Benecke, G.; Li, C.; Roth, S. V.; Rothkirch, A.; Kracht, T.; Paris, O.; Wagermaier, W.; Gourrier, A.; Burghammer, M.; Riekel, C.; Fratzl, P. Directly Programmable Data Analysis Kit (DPDAK) for Online Analysis of High Throughput 2D Scattering Data. In *Emerging Themes in Analysis of Grazing Incidence Small-Angle Scattering Data*; 2013; 18.

197 Ashiotis, G.; Deschildre, A.; Nawaz, Z.; Wright, J. P.; Karkoulis, D.; Picca, F. E.; Kieffer, J. The Fast Azimuthal Integration Python Library: PyFAI. *J. Appl. Crystallogr.* **2015**, *48* (2), 510–519.

198 Brunetti, A.; Sanchez del Rio, M.; Golosio, B.; Simionovici, A.; Somogyi, A. A Library for X-Ray–Matter Interaction Cross Sections for X-Ray Fluorescence Applications. *Spectrochim. Acta Part B At. Spectrosc.* **2004**, *59* (10), 1725–1731.

199 Schoonjans, T.; Brunetti, A.; Golosio, B.; Sanchez del Rio, M.; Solé, V. A.; Ferrero, C.; Vincze, L. The Xraylib Library for X-Ray–Matter Interactions. Recent Developments. *Spectrochim. Acta Part B At. Spectrosc.* **2011**, *66* (11), 776–784.

200 Shimizu, T.; Kanamori, K.; Maeno, A.; Kaji, H.; Doherty, C. M.; Falcaro, P.; Nakanishi, K. Transparent, Highly Insulating Polyethyl- and Polyvinylsilsesquioxane Aerogels: Mechanical Improvements by Vulcanization for Ambient Pressure Drying. *Chem. Mater.* **2016**, *28* (19), 6860–6868.

201 Bonnet, F.; Melich, M.; Puech, L.; Anglès d'Auriac, J.-C.; Wolf, P.-E. On Condensation and Evaporation Mechanisms in Disordered Porous Materials. *Langmuir* **2019**, *35* (15), 5140–5150.

202 Maillet, B.; Dittrich, G.; Huber, P.; Coussot, P. Diffusionlike Drying of a Nanoporous Solid as Revealed by Magnetic Resonance Imaging. *Phys. Rev. Appl.* **2022**, *18* (5), 54027.

203 Blander, M.; Katz, J. L. Bubble Nucleation in Liquids. *AIChE J.* **1975**, *21* (5), 833–848.

204 Or, D.; Tuller, M. Cavitation during Desaturation of Porous Media under Tension. *Water Resour. Res.* **2002**, *38* (5), 14–19.

205 Liu, X. Y. Heterogeneous Nucleation or Homogeneous Nucleation? *J. Chem. Phys.* **2000**, *112* (22), 9949–9955.

206 Doinikov, A. A.; Marmottant, P. Natural Oscillations of a Gas Bubble in a Liquid-Filled Cavity Located in a Viscoelastic Medium. *J. Sound Vib.* **2018**, *420*, 61–72.

207 Tyree, M. T.; Dixon, M. A. Cavitation Events in Thuja Occidentalis L.? 1: Utrasonic Acoustic Emissions from the Sapwood Can Be Measured. *Plant Physiol.* **1983**, *72* (4), 1094–1099.

208 Page, J. H.; Liu, J.; Abeles, B.; Herbolzheimer, E.; Deckman, H. W.; Weitz, D. A. Adsorption and Desorption of a Wetting Fluid in Vycor Studied by Acoustic and Optical Techniques. *Phys. Rev. E* **1995**, *52* (3), 2763–2777.

209 Smarsly, B.; Mascotto, S.; Wallacher, D.; Brandt, A.; Zickler, G.; Timmann, A. Mechanism of Desorption of Fluids from Mesoporous Silica Followed by In-Situ SANS and SAXS: A Direct Proof of the Cavitation Pore Empyting Mechanism. In *Deutsche Tagung für Forschung mit Synchrotronstrahlung, Neutronen und Ionenstrahlen an Großgeräten*; 2010.

210 Reichenauer, G.; Scherer, G. W. Nitrogen Sorption in Aerogels. *J. Non. Cryst. Solids*

2001, *285* (1), 167–174.

211 Jánosi, A. Neue Aspekte Der Phasenbestimmung an Festkörpern Mittels Röntgenkleinwinkelstreuung. *Zeitschrift für Phys. B Condens. Matter* **1986**, *63* (3), 375–381.

212 Zarzycki, J. Structural Aspects of Sol-Gel Synthesis. *J. Non. Cryst. Solids* **1990**, *121* (1), 110–118.

213 Scherer, G. W.; Smith, D. M.; Qiu, X.; Anderson, J. M. Compression of Aerogels. *J. Non. Cryst. Solids* **1995**, *186*, 316–320.

214 Gross, J.; Reichenauer, G.; Fricke, J. Mechanical Properties of SiO2 aerogels. *J. Phys. D. Appl. Phys.* **1988**, *21* (9), 1447–1451.

215 Guo, J.; Fu, S.; Deng, Y.; Xu, X.; Laima, S.; Liu, D.; Zhang, P.; Zhou, J.; Zhao, H.; Yu, H.; Dang, S.; Zhang, J.; Zhao, Y.; Li, H.; Duan, X. Hypocrystalline Ceramic Aerogels for Thermal Insulation at Extreme Conditions. *Nature* **2022**, *606* (7916), 909–916.

216 Jia, C.; Li, L.; Liu, Y.; Fang, B.; Ding, H.; Song, J.; Liu, Y.; Xiang, K.; Lin, S.; Li, Z.; Si, W.; Li, B.; Sheng, X.; Wang, D.; Wei, X.; Wu, H. Highly Compressible and Anisotropic Lamellar Ceramic Sponges with Superior Thermal Insulation and Acoustic Absorption Performances. *Nat. Commun.* **2020**, *11* (1), 3732.

217 Bhupathi, P.; Jaworski, L.; Hwang, J.; Tanner, D. B.; Obukov, S.; Lee, Y.; Mulders, N. Optical Birefringence in Uniaxially Compressed Aerogels. *New J. Phys.* **2010**, *12* (10), 103016.

218 Rosa-Fox, N. de la; Morales-Flórez, V.; Toledo-Fernández, J. A.; Piñero, M.; Esquivias, L.; Keiderling, U. SANS Study of Hybrid Silica Aerogels under "in Situ" Uniaxial Compression. *J. Sol-Gel Sci. Technol.* **2008**, *45* (3), 245–250.

219 Wang, W.; Murthy, N. S.; Grubb, D. T. 'Butterfly' Small-Angle X-Ray Scattering Patterns in Semicrystalline Polymers Are Double-Elliptical. *Polymer* **2007**, *48* (12), 3393–3399.

220 Malekian, A.; Salari, S.; Stumper, J.; Djilali, N.; Bahrami, M. Effect of Compression on Pore Size Distribution and Porosity of PEM Fuel Cell Catalyst Layers. *Int. J. Hydrogen Energy* **2019**, *44* (41), 23396–23405.

221 Alcañiz-Monge, J.; Trautwein, G.; Pérez-Cadenas, M.; Román-Martínez, M. C. Effects of Compression on the Textural Properties of Porous Solids. *Microporous Mesoporous Mater.* **2009**, *126* (3), 291–301.

222 Marlière, C.; Woignier, T.; Dieudonné, P.; Primera, J.; Lamy, M.; Phalippou, J. Two Fractal Structures in Aerogel. *J. Non. Cryst. Solids* **2001**, *285* (1–3), 175–180.

223 Tartakovsky, D. M.; Dentz, M. Diffusion in Porous Media: Phenomena and

Mechanisms. *Transp. Porous Media* **2019**, *130* (1), 105–127.

224 Luo, J.; Demchuk, Z.; Zhao, X.; Saito, T.; Tian, M.; Sokolov, A. P.; Cao, P.-F. Elastic Vitrimers: Beyond Thermoplastic and Thermoset Elastomers. *Matter* **2022**, *5* (5), 1391–1422.

225 Wagermaier, W.; Kratz, K.; Heuchel, M.; Lendlein, A. Characterization Methods for Shape-Memory Polymers. In *Shape-Memory Polymers*; Lendlein, A., Ed.; Springer Berlin Heidelberg: Berlin, Heidelberg, 2009; 97–145.

226 Findenegg, G. H. Dichte Und Ausdehnungskoeffizient Einiger Flüssiger Alkane. *Monatshefte für Chemie* **1970**, *101* (4), 1081–1088.

Symbols and abbreviations

Symbols

Symbol	Quantity	Unit
a	Size or radius of the primary particles	nm
	or minimum attenuation value (custom contrast parameter)	-
A	Cross-section area of a specimen	m^2
b	Maximum attenuation value (custom contrast parameter)	-
C_H	Ratio between the water volume and the silica skeleton volume in the dry gel	-
C_μ	Ratio of the silica skeleton reconstructed attenuation coefficient between the dry gel and the alcogel	-
C_V	Silica skeleton volume ratio between the dry gel and the alcogel	-
d, D	Specimen diameter or thickness	m
D_f	Fractal dimension	-
E	Energy	J
	or Young's modulus	Pa
f	Volume fraction	-
F	Force	N
$\tilde{g}$	Uncorrected gray value of a voxel	8-bit
g	Gray value of a voxel	8-bit
G	Gray value averaged over a domain	8-bit
h	Specimen height	m
i	µCT slice number	-
I	Transmitted intensity	a.u.
$I(q)$	Scattered intensity	cm^{-1}
j	Voxel radial coordinate	-
J	Nucleation rate	$cm^{-3}\ s^{-1}$
k	µCT scan number	-

K	Porod's constant	cm^{-5}
$\bar{l}$	Mean chord length	nm
l_p	Mean chord length of the pores	nm
l_s	Mean chord length of the silica skeleton	nm
m	Weight	g
M_w	Molar mass	$g\ mol^{-1}$
N	Number of slices or number of scans	-
p	Pressure or voxel coordinate in the reconstructed volume	Pa -
q	Modulus of the scattering vector or voxel coordinate in the reconstructed volume	nm^{-1} -
Q	Q invariant	cm^{-4}
r_c	Capillary radius	m
t	Time	s
T	Temperature	K
V_0, V^0	Volume of the alcogel	m^3
V_d, V^d	Volume of the dry gel	m^3
$\tilde{V}$	Uncorrected specimen volume by µCT	m^3

Greek letters

Symbol	Quantity	Unit
χ	Azimuthal angle in scattering patterns	°
Δp	Capillary pressure	Pa
$\varepsilon, \varepsilon_{ax}, \varepsilon_z$	Axial strain	-
ε_{tr}	Transverse strain	-
γ	Surface tension of the liquid-vapor interface or scaling factor in the µCT drying model (volume ratio)	$N\ m^{-1}$ -
λ	Light wavelength	m

μ	Attenuation coefficient	m^{-1}
	or reconstructed attenuation coefficient	-
$\overline{\mu}$	Reconstructed attenuation coefficient averaged over a domain	-
μ^F	Interpolated reconstructed attenuation coefficient	-
ν	Poisson's ratio	-
Ω	Domain of pixels belonging to the sample	-
ϕ	Porosity	-
ρ, ρ_a	Apparent density	$g\ cm^{-3}$
$\rho_{\text{skel}}, \rho_s$	Skeletal density	$g\ cm^{-3}$
ρ_{SLD}	Scattering length density	cm^{-2}
σ	Engineering stress or true stress	Pa
θ	Contact angle between a solid and a liquid	°
	or scattering angle	°
ξ	Mean cluster size	nm

Acronyms

AIRH	Vapor/air map along the height of a gel and versus time
AIRHR	Vapor/air map along the height and radius of a gel
AIRR	Vapor/air map along the radius of a gel and versus time
APD	Ambient-pressure drying
CNT	Classical nucleation theory
CT	X-ray computed tomography
EtOH	Ethanol
FD	Freeze-drying
FTIR	Fourier transform infrared spectroscopy
GH	Gray values map along the height of a gel and versus time
GHR	Gray values map along the height and radius of a gel
GR	Gray values map along the radius of a gel and versus time

HEXH	Hexane map along the height of a gel and versus time
HEXHR	Hexane map along the height and radius of a gel
HEXR	Hexane map along the radius of a gel and versus time
μCT	X-ray micro-computed tomography
MHR	Map of the reconstructed attenuation coefficient along the height and radius of a gel
nanoCT	X-ray nanotomography
PEEK	Polyether ether ketone
PTFE	Polytetrafluoroethylene
RAC	Reconstructed attenuation coefficient
ROI	Region of interest
SAXS	Small-angle X-ray scattering
SBE	Spring-back effect
SCD	Supercritical drying
SDD	Source-to-detector distance
SKELH	Silica skeleton map along the height of a gel and versus time
SKELHR	Silica skeleton map along the height and radius of a gel
SKELR	Silica skeleton map along the radius of a gel and versus time
SOD	Source-to-object distance
SSA	Specific surface area in $m^2\ g^{-1}$
TEM	Transmission electron microscopy
TEOS	Tetraethyl orthosilicate
TMCS	trimethylchlorosilane
WAXS	Wide-angle X-ray scattering

This list does not include symbols and abbreviations that are specific to the appendices.

Acknowledgements

I would like to thank my supervisor Dr. habil. Wolfgang Wagermaier for his guidance during these three years. Wolfgang is a formidable leader and open-minded person; he has always given me invaluable advice not only in science but also in management, communication and conflict resolution. I hope I can one day provide as much guidance to someone as he did to me.

I would also like to express my deepest gratitude to Prof. Dr. Peter Fratzl, Dr. Ernesto Scoppola and Dr. Fabian Zemke who made substantial contributions to the work presented in this thesis by their ideas, resources, support and discussions. I am grateful to Prof. Dr. Aleksander Gurlo for his feedback and for the leeway that he accorded me to conduct my research. I sincerely thank Tilman Rilling for his work, innovative ideas and enthusiasm. I am also grateful to the Deutsche Forschungsgemeinschaft (DFG) for financing this project.

The experiments performed in this thesis could not have been done without the work of Tobias Schmidt and Marco Bott who designed and manufactured the micromechanical tester, molds and drying chambers with the help of Petra Leibner. Many thanks to Klaus Bienert, Dr. Friedrich Reppe and Martin Niedermeier for their assistance on the microcontroller software, to Dr. Chenghao Li for his support in the SAXS experiments, to Daniel Werner and Nikolai Rosenthal for their help and valuable discussion on μCT experiments and analysis, to Dr. Peter Werner and Dr. habil. Nadezda Tarakina for their guidance in electron microscopy measurements, to Dr. Mateusz Odziomek for the interesting discussions on aerogels, to Jeannette Steffen for her assistance on the FTIR measurements, and to Ralf Ditsch, Dr. Angelo Valleriani, Annette Pape, Jan von Szada-Borryszkowski and Aslı Güngör for their overall help. I would also like to acknowledge Solène Valton from RX Solutions for her expert tips on the μCT reconstruction and Dr. Mike Marsh and Dr. Mathieu Gendron from Object Research Systems for their help on the automated segmentation script.

I am grateful to Prof. Dr. Claudia Fleck for accepting to be the chair of the doctoral committee and to Dr. Wim Malfait for accepting to be a reviewer of this dissertation.

I would like to kindly thank Dr. Émeline Raguin, Dr. Patrick Kwon, Dr. Hannes Zschiesche, Dr. Macarena Siri, Dr. Agustin Mangiarotti, Clémentine Ferrari, Anne Seewald and Efe Yavuzsoy for the good time spent in your company. My family has always supported me in my life choices, which has constantly inspired me to surpass myself. Finally, my partner Dr. Jing Hou has supported me in so many aspects during my PhD, regardless of my mood,

of the distance between us and of the challenges along the path. Thank you for making everything possible.